AGRICULTURAL UNIVERSITY OF ATHENS
DEPARTMENT OF NATURAL RESOURCES MANAGEMENT & AGRICULTURAL ENGINEERING
LABORATORY OF FARM MACHINE SYSTEMS

PhD Thesis

Extracting and assessing plant features spatio-temporally by means of 3D sensing in apple trees

Nikolaos K. Tsoulias

Supervisor:
Spyros Fountas, Associate Professor AUA

Three-member Committee:
Spyros Fountas, Associate Professor AUA
Manuela Zude-Sasse, Prof. Dr. habil ATB-Leibniz Institute
George Xantopoulos, Assistant Professor AUA

Athens
2021

AGRICULTURAL UNIVERSITY OF ATHENS
DEPARTMENT OF NATURAL RESOURCES MANAGEMENT & AGRICULTURAL ENGINEERING
LABORATORY OF FARM MACHINE SYSTEMS

PhD Thesis

Extracting and assessing plant features spatio-temporally by means of 3D sensing in apple trees

"Χωροχρονική εξαγωγή και εκτίμηση χαρακτηριστικών των φυτών με χρήση 3D αισθητήρα σε μηλεώνες"

Nikolaos K. Tsoulias

Seven-member Examination Committee:
Spyros Fountas, Associate Professor AUA (Supervisor)
Manuela Zude-Sasse, Prof. Dr. habil ATB-Leibniz Institute
George Xantopoulos, Assistant Professor AUA
Dimitrios Stergios Paraforos, Professor, Geisenheim University
Konstantinos Arvanitis, Professor AUA
Dionysios Kalyvas, Professor AUA
Peter Anargyros Roussos, Associate Professor AUA

Extracting and assessing plant features spatio-temporally by means of 3D sensing in apple trees

Department of Natural Resources & Agricultural Engineering
Laboratory of Farm Machine Systems

Abstract

Knowledge of tree structural characteristics is gaining importance in advanced fruit growing, especially when implementing precision horticulture techniques. Accurate extraction and processing of tree structure is critical for precision horticulture, whereas spatio-temporal crop monitoring aim to optimize farm management practices such as pruning, thinning, selective harvest, chemical and fertilizer spraying. Growers have traditionally obtained this information by using manual sampling techniques, which tend to be laborious, spatially sparse, expensive, inaccurate and prone to subjective biases. Three-dimensional (3D) sensing, offers new possibilities for a more efficient agricultural practice with the use of highly advanced technological instruments and methodologies. Essential reasons contributing to this possibility include the increasing computational processing power of computers, the decrease in cost and size of electronics, the increase of efficiency in laser emitting diodes. Therefore, the demand for advanced knowledge of individual crops, requires robust and accurate data processing techniques needed by the grower to support precision agriculture protocols.

In the present study, precision horticulture techniques were applied in apple orchards. The aim of this study was to extract 3D structural information of apple trees spatially and to associate this information with soil properties, microclimate, tree physiology, yield and fruit quality. To meet this end, a light detection and ranging (LiDAR) system was mounted on a commercial tractor to scan tree rows of the orchard.

The first contribution of this thesis is the development of a tree segmentation methodology to detect individual trees in 3D domain, based on stem position in high density orchards. The approach focuses on trees trained as slender spindled, which presents unique challenges for segmentation algorithms due to their intertwined nature. Initially, the accuracy of the LiDAR system assessed using a metal-box with known dimensions in field conditions. Tree stem position of each tree was estimated based on a bivariate point density histogram. Each tree was segmented using a cylindrical boundary projected around the estimated stem positions. Therefore, geometrical parameters of the segmented tree point clouds were estimated and compared with manual measurements. The assessment of the LiDAR system considering the metal box exhibited enhanced error due to points with enhanced

distance between laser aperture and the object. The coefficient of determinations were achieved between the measurements and estimated data from the segmented point clouds in terms of tree height, stem diameter and canopy volume.

The second contribution considers the implementation of structural parameters in a water balance model for observing their interaction with microclimate and soil properties over growing season. In particular, leaf area (LA) and height of trees, estimated LiDAR system, with daily weather data and soil variables are utilized to estimate the daily tree water needs different areas of soil electrical conductivity (ECa). The results revealed that tree geometry interacts with ECa. Furthermore, the utilization of 3D plant and microclimate informationincreased the spatial resolution of the water balance model, and its accuracy. Furthermore, the estimated LA by the LiDAR presented high correlations with ECa at different areas. In parallel, a correlation was observed between the ECa and total available water content in the root zone. Whereas, the implementation of LA information from different ECa areas pointed to the reasonability of spatially resolved water balance, allowing to estimate daily tree water needs.

Moreover, the study emphasized in the spatio-temporal estimation of tree geometry in 3D using the LiDAR system at different growth stages. Firstly, the spatial impact of ECa and orchard landscape in the growth of tree volume was analyzed, indicating high variation over the season and its significant dependence with the soil properties. The LiDAR system was used to monitor the whole field repeatedly over the growth season. The estimated canopy volume related negatively with ECa areas (low, mid, and high) of the orchard, indicating that tree growth was approximately 30% higher in low ECa compared to mid and high ECa areas. These results suggest that the canopy growth varies spatially, whereas the terrestrial laser scanning offers a feasible method for implementation in decision support systems, in precision horticulture.

Additionally, LiDAR-based estimation of LA was achieved using LA of defoliated trees with the corresponding points per tree. In parallel, linearity and backscattered reflectance of LiDAR, which suggested in fruit detection methodology, were utilized to segment the woody parts from points per tree (PPT) at different growth stages, improving the relationship with LA. The spatial responses of LA were investigated with the ECa and yield over the season. Whereas, a k-nearest neighbor model, was built to predict the fruit fresh mass (FM) and soluble solids content by means of soil ECa and LA. These results confirm spatio-temporal variation of canopy growth.

Furthermore, the results suggest the value of LA data in decision support systems aimed at optimizing orchard management practices, particularly addressing the impact of orchard management on fruit quality.

Estimation of LA was improved when points of woody parts were removed from points per tree, providing higher adjusted coefficient of determination at 55 days after bud break. ECa and LA were positively correlated with fruit size. Motivated by these correlations, k-nearest neighbor models were built to predict fruit quality at harvest. Validation was performed by applying the model of one year on data of the subsequent year. Based on geoposition and ECa, classification accuracy in the test set validation was 39.7 %, whereas classification with geoposition and LA resulted in increased accuracy by 63.3 %. Results confirm spatio-temporal variation of canopy growth as was expected.

Tree structural parameters can impact on fruit size, number and quality parameters. Therefore, in the final part of the study, fruit detection algorithms using the LiDAR system were proposed to estimate fruit diameter at different growth stages. Trees were scanned pre and after defoliation at each individual date. Fruit segmentation was based on threshold values of LiDAR calibrated backscattered reflectance and the geometrical features of linearity and curvature. The high complexity of tree structure highlights the need to set up an assessment pipeline considering fruits from defoliated trees as reference points. Therefore, evaluation of fruit number and position founded on foliated trees is performed by comparison against the reference labels on defoliated. The results show the high efficacy of LiDAR to localize and estimate fruit size in 3D domains, overpassing imaging systems limitations susceptible to highly variable external factors that lead to significant appearance variations.

An analysis of LiDAR calibrated backscattered reflectance of tree elements was performed, exhibiting discrete values for leaves, woody parts and apple fruits, respectively. The diameter of apple fruits estimated from the foliated trees was related to the reference values based on the perimeter of the fruits, revealing high adjusted coefficient of determination at $DAFB_{120}$. When comparing the results obtained on foliated and defoliated tree's data, the estimated number of fruit's on foliated trees at 120 days after full bloom 94.8% of the ground truth values. The algorithm resulted in maximum values of 88.2% precision, 91.0% recall, and 89.5 F1 score at 120 days after full bloom.

The components of this thesis have been designed to address to future machine vision challenges under the local variable environmental conditions identified in high density apple orchards. Regarding tree segmentation, the

accuracy of the proposed methodology should be evaluated at different perennial trees and planting systems. Future research should further investigate the implementation of 3D temporal plant information (e.g. LA, volume) from high density orchards in variable rate applications such as irrigation, fertilisation. The inner relationship of fruit quality and LA should be observed at different cultivars and climates to improve decision making in orchards. Estimating fruit number over the growing season can optimise crop load and selective harvesting. In the future, the detection accuracy of the proposed methodology should be assessed under different apple cultivars and LiDAR sensors potential and architecture.

Scientific area: Precision horticulture

Keywords: 3D data, leaf area, fruit size, tree geometry

Χωροχρονική εξαγωγή και εκτίμηση χαρακτηριστικών των φυτών με χρήση 3D αισθητήρα σε μηλεώνες

Τμήμα Αξιοποίησης Φυσικών Πόρων & Γεωργική Μηχανικής
Εργαστήριο Γεωργικής Μηχανολογίας

Περίληψη

Τα δομικά χαρακτηριστικά των δέντρων αποκτούν ολοένα και μεγαλύτερη σημασία στην καλλιέργεια των οπωροφόρων δέντρων, ιδίως κατά την εφαρμογή των τεχνικών της δενδροκομίας ακριβείας. Κρίσιμα στοιχεία για την πληρέστερη εφαρμογή της αποτελούν η ακριβής εξαγωγή και επεξεργασία της δομής των δέντρων καθώς και η χωρική και χρονική παρακολούθηση των καλλιεργειών, μέσω της οποίας επιτυγχάνεται η βελτιστοποίηση των πρακτικών διαχείρισης, όπως το κλάδεμα, το αραίωμα, η επιλεκτική συγκομιδή, ο ψεκασμός με φυτοφάρμακα και λιπάσματα, του οπωρώνα. Παραδοσιακά, η συλλογή των παραπάνω πληροφοριών γινόταν μέσω χειρωνακτικής δειγματοληψίας, η οποία χαρακτηριζόταν από υψηλό κόστος εργασίας, χρόνο διεκπεραίωσης και μεγάλη πιθανότητα σφάλματος. Προς επίλυση των εν λόγω προβλημάτων, αναπτύχθηκε η τρισδιάστατη (3D) ανίχνευση, προσφέροντας νέες δυνατότητες στις γεωργικές πρακτικές και αυξάνοντας την απόδοση τους μέσω της χρήσης κατάλληλων αισθητήρων. Υπό το πλαίσιο αυτό, οι κύριοι παράγοντες που συμβάλλουν σε αυτή τη δυνατότητα είναι η συνεχιζόμενη αύξηση της επεξεργαστικής ισχύος των υπολογιστών, η μείωση κόστους και μεγέθους των ηλεκτρονικών συσκευών, η ενίσχυση της απόδοσης των διόδων εκπομπής λέιζερ. Συνεπώς, η ανάγκη για κατανόηση και φροντίδα των επιμέρους καλλιεργειών απαιτεί ακριβείς και αξιόπιστες τεχνικές επεξεργασίας δεδομένων για την εξαγωγή πληροφοριών υψηλής ευκρίνειας που χρειάζεται ο καλλιεργητής για την υποστήριξη της δενδροκομίας ακριβείας.

Στην παρούσα μελέτη εφαρμόστηκαν τεχνικές δενδροκομίας ακριβείας σε μηλεώνες. Στόχος της μελέτης ήταν η εξαγωγή και ανάλυση τρισδιάστατων (3D) δομικών πληροφοριών των δέντρων σε συνάρτηση με τη φυσιολογία τους, τις ιδιότητες του εδάφους, του μικροκλίματος, την απόδοση και την ποιότητα των καρπών. Για την εκπλήρωση αυτού του στόχου, τοποθετήθηκε ένα σύστημα light detection and range (LiDAR) πάνω σε ένα τρακτέρ για τη σάρωση των σειρών του οπωρώνα.

Η πρώτη συνεισφορά της παρούσας διατριβής είναι η ανάπτυξη μεθοδολογίας κατάτμησης των δέντρων με σκοπό τον εντοπισμό του εκάστοτε δέντρου σε 3D απεικόνιση, με βάση τη θέση του κορμού του σε οπωρώνες πυκνής φύτευσης. Η προσέγγιση εστιάζει σε μηλιές συστήματος παλμέτας, τα οποία χαρακτηρίζονται ως ιδιαίτερα

απαιτητικά στην ανάπτυξη αλγορίθμων κατάτμησης εξαιτίας των διακλαδώσεων μεταξύ των φυτών. Αρχικά, η ακρίβεια του συστήματος LiDAR αξιολογήθηκε στον οπωρώνα χρησιμοποιώντας ένα μεταλλικό κουτί συγκεκριμένων διαστάσεων. Εν συνεχεία, ένα ιστόγραμμα πυκνότητας σημείων χρησιμοποιήθηκε για τον εντοπισμό των δέντρων με βάση τη θέση του κορμού τους, ενώ ένας κύλινδρος τοποθετήθηκε γύρω από το κορμό για την κατάτμηση του εκάστοτε δέντρου. Κατά συνέπεια, για των εξαγωγή των συμπερασμάτων της παρούσας, εκτιμήθηκαν δομικές πληροφορίες των δέντρων, όπως το ύψος, ο όγκος και η διάμετρος του κορμού. Κρίσιμο στοιχείο για την εξαγωγή των εν λόγω συμπερασμάτων αποτέλεσε ο σημαντικός συντελεστής συσχέτισης μεταξύ των χειρωνακτικών μετρήσεων επί των στοιχειών αυτών και των 3D δεδομένων που ελήφθησαν με τη χρήση του συστήματος LiDAR. Ωστόσο, αξιομνημόνευτο καθίσταται το γεγονός ότι μέσω της χρήσης του συστήματος LiDAR με το προαναφερόμενο μεταλλικό κουτί, παρουσιάστηκε αυξημένη πιθανότητα σφάλματος επί των σημείων που βρίσκονταν σε μεγαλύτερη απόσταση μεταξύ του ανοίγματος λέιζερ και του αντικειμένου.

Η δεύτερη συνεισφορά σχετίζεται με την εφαρμογή των δομικών παραμέτρων εντός ενός μοντέλου υδατικού ισοζυγίου, αποσκοπώντας στην παρατήρηση της αλληλεπίδρασής τους με το μικρόκλιμα και τις ιδιότητες του εδάφους κατά τη διάρκεια της καλλιεργητικής περιόδου. Συγκεκριμένα, η φυλλική επιφάνεια (LA) και το ύψος των δέντρων, όπως αυτά υπολογίστηκαν μέσω του συστήματος LiDAR, συνδυάστηκαν με τα μετεωρολογικά δεδομένα και τις εδαφικές μεταβλητές για την εκτίμηση των ημερήσιων αναγκών των δέντρων σε νερό σε διαφορετικές περιοχές ηλεκτρικής αγωγιμότητας του εδάφους (ECa). Τα αποτελέσματα έδειξαν ότι η γεωμετρία των δέντρων αλληλοεπιδρά με την ECa, καθώς και ότι η αξιοποίηση 3D δεδομένων των φυτών και του μικροκλίματος αύξησε τη χωρική ευκρίνεια του μοντέλου υδατικού ισοζυγίου, παρέχοντας μεγαλύτερη ακρίβεια σε αντίθεση με τις παραδοσιακές μεθόδους. Επιπλέον, η εκτιμώμενη LA με το LiDAR παρουσίασε υψηλούς συσχετισμούς με το ECa σε διαφορετικές περιοχές. Παράλληλα, παρατηρήθηκε συσχέτιση μεταξύ του ECa και της συνολικής διαθέσιμης περιεκτικότητας σε νερό επί του ριζικού συστήματος, ενώ ο συνδυασμός του ECa και του LA ανέδειξε την έννοια της χωρικής επίλυσης του ισοζυγίου νερού, επιτρέποντας την πληρέστερη εκτίμηση των ημερήσιων αναγκών των δένδρων σε νερό.

Εν συνεχεία, ιδιαίτερη έμφαση δόθηκε στη χωρική και χρονική εκτίμηση της γεωμετρίας των δέντρων σε 3D με τη χρήση του συστήματος LiDAR κατά τα στάδια ανάπτυξης τους. Αρχικά αναλύθηκε η χωρική επίδραση της ECa και μορφολογίας του οπωρώνα στην ανάπτυξη του όγκου των δέντρων, παρουσιάζοντας υψηλή διακύμανση

κατά τη διάρκεια της καλλιεργητικής περιόδου και σημαντική εξάρτησή της από τις ιδιότητες του εδάφους. Το σύστημα LiDAR χρησιμοποιήθηκε για τους σκοπούς της επίβλεψης της καλλιέργειας ολόκληρου του οπωρώνα κατά τη διάρκεια της περιόδου ανάπτυξης. Ο εκτιμώμενος όγκος των δένδρων συσχετίστηκε αρνητικά με την ECa σε όλες τις περιοχές του οπωρώνα (χαμηλές, μεσαίες και υψηλές), εμφανίζοντας ότι η ανάπτυξη των δέντρων σε χαμηλά επίπεδα ECa αυξήθηκε κατά περίπου 30% σε σύγκριση με τις μεσαίες και υψηλές περιοχές ECa. Αυτά τα αποτελέσματα υποδηλώνουν ότι η ανάπτυξη του δένδρου κυμαίνεται χωρικά, καθιστώντας έτσι την επίγεια σάρωση με λέιζερ μια χρήσιμη μέθοδο για τη λήψη αποφάσεων στην δενδροκομία ακριβείας.

Στη συνέχεια, πραγματοποιήθηκε η εκτίμηση της LA με βάση το LiDAR συσχετίζοντας την LA των αποφυλλωμένων δέντρων με τα αντίστοιχα σημεία ανά δέντρο (PPT). Παράλληλα, η γραμμικότητα και η βαθμονομημένη ανάκλαση του LiDAR, χρησιμοποιήθηκαν για την κατάτμηση των ξυλώδων τμημάτων από τα PPT στα διαφορετικά στάδια ανάπτυξης, βελτιώνοντας τη σχέση με την χειρωνακτική LA. Οι χωρικές συσχετίσεις της LA διερευνήθηκαν με την ECa και την απόδοση κατά τη διάρκεια της περιόδου, ενώ κατασκευάστηκε ένα μοντέλο k-nearest neighbour για την πρόβλεψη της νωπής μάζας των καρπών, της διαμέτρου και ης περιεκτικότητας σε διαλυτά στερεά, μέσω της ECa και LA. Τα αποτελέσματα αυτά επιβεβαιώνουν τη χωρική και χρονική διακύμανση της ανάπτυξης του φυλλώματος, υποδηλώνοντας παράλληλα την αξία των δεδομένων της LA σε συστήματα υποστήριξης αποφάσεων που στοχεύουν στη βελτιστοποίηση της διαχείρισης των οπωρώνων.

Η εκτίμηση του LA βελτιώθηκε όταν εντοπίστηκαν και αφαιρέθηκαν τα σημεία των ξυλωδών μερών, παρέχοντας υψηλότερο προσαρμοσμένο συντελεστή συσχέτισης στις 55 ημέρες μετά το σπάσιμο των οφθαλμών. Επιπρόσθετα, παρατηρήθηκε ότι η ECa και η LA συσχετίστηκαν θετικά με το μέγεθος των φρούτων. Με κίνητρο αυτούς τους συσχετισμούς, δημιουργήθηκαν μοντέλα k- nearest neighbour για να προβλέψουν την ποιότητα των φρούτων κατά τη συγκομιδή, εφαρμόζοντας το μοντέλο πρώτου έτους της μελέτης στα δεδομένα του επόμενου έτους. Με βάση τη γεωγραφική θέση και τη ECa, η ακρίβεια ταξινόμησης στην επαλήθευση του συνόλου των δεδομένων ήταν 39.7%, ενώ η ταξινόμηση με βάση τη γεωγραφική θέση και το LA οδήγησε στο 63.3%. Τα αποτελέσματα επιβεβαιώνουν τη χωρική και χρονική μεταβολή της ανάπτυξης του δένδρου.

Στο τελικό τμήμα της παρούσας μελέτης, παρατηρήθηκε ότι οι δομικές παράμετροι των δέντρων μπορούν να επηρεάσουν το μέγεθος, τον αριθμό και τις ποιοτικές παραμέτρους των καρπών. Ως εκ τούτου, προτάθηκαν αλγόριθμοι ανίχνευσης των καρπών με τη χρήση του συστήματος LiDAR για την εκτίμηση της διαμέτρου τους

κατά τα στάδια ανάπτυξης του δένδρου. Σε κάθε μέτρηση, τα δέντρα σαρώθηκαν πριν και μετά την αποφύλλωση. Ο διαχωρισμός των καρπών βασίστηκε στις οριακές τιμές της βαθμονομημένης ανάκλασης του LiDAR και στα γεωμετρικά χαρακτηριστικά της γραμμικότητας και της καμπυλότητας . Η υψηλή πολυπλοκότητα της δομής των δέντρων επιβάλλει την ανάγκη δημιουργίας μιας μεθόδου αξιολόγησης που θα λαμβάνει υπόψη τους καρπούς από τα αποφυλλωμένα δέντρα ως σημείο αναφοράς. Συνεπώς η αξιολόγηση του αριθμού και της θέσης των καρπών που εντοπίζονται σε δέντρα με φύλλα πραγματοποιείται. Συγκρίνονται αυτά με τα σημεία αναφοράς που βρέθηκαν στα αποφυλλωμένα δένδρα. Τα αποτελέσματα έδειξαν την υψηλή ικανότητα του LiDAR να εντοπίζει και να υπολογίζει το μέγεθος των καρπών σε 3D, ξεπερνώντας τους περιορισμούς των συστημάτων εικόνας, τα οποία είναι ευαίσθητα στους μεταβλητούς εξωτερικούς παράγοντες που οδηγούν σε σημαντικές διακυμάνσεις στα δεδομένα.

Συγκεκριμένα, πραγματοποιήθηκε ανάλυση της βαθμονομημένης ανάκλασης του LiDAR επί των στοιχείων του δέντρου, δείχνοντας διακριτές τιμές για φύλλα, ξυλώδη μέρη και καρπούς. Η διάμετρος των μήλων που υπολογίστηκε από τα φυλλωμένα δέντρα συσχετίστηκε σημαντικά με τα σημεία αναφοράς των αποφυλλωμένων δένδρων κατά τη συγκομιδή. Παράλληλα, στη σύγκριση των αποτελεσμάτων που προέκυψαν από τα δεδομένα του φυλλώματος και του αποφυλλωμένου δέντρου, ο εκτιμώμενος αριθμός των φρούτων στα φυλλωμένα δέντρα στις 120 ημέρες μετά την πλήρη άνθηση, αποτέλεσε το 94.8% των πραγματικών τιμών αναφοράς. Ο αλγόριθμος είχε ως αποτέλεσμα μέγιστες τιμές ακρίβειας 88.2%, ανάκλησης 91.0% και 89.5 F1 score σε 120 ημέρες μετά την πλήρη άνθηση.

Τα μέρη αυτής της διατριβής έχουν σχεδιαστεί για την αντιμετώπιση του μελλοντικού μηχανικού οράματος υπό το πρίσμα των δύσκολων περιβαλλοντικών συνθήκων που παρατηρούνται σε οπωρώνες υψηλής πυκνότητας. Όσον αφορά την κατάτμηση των δέντρων, η ακρίβεια της προτεινόμενης μεθοδολογίας θα πρέπει να αξιολογηθεί σε διάφορα πολυετή δέντρα και συστήματα φύτευσης για την παροχή πληρέστερων αποτελεσμάτων. Η μελλοντική έρευνα θα πρέπει να διερευνήσει περαιτέρω την εφαρμογή τρισδιάστατων χωρικών και χρονικών πληροφοριών επί φυτών (π.χ. LA, όγκος) από οπωρώνες υψηλής πυκνότητας σε συστήματα εφαρμογής μεταβλητής δόσης όπως η άρδευση και η λίπανση. Σε κάθε περίπτωση, η σχέση της ποιότητας των φρούτων και του LA θα πρέπει να παρατηρηθεί σε διαφορετικές ποικιλίες και κλίματα, στοχεύοντας στη βελτίωση λήψης αποφάσεων σε οπωρώνες. Εν κατακλείδι, η εκτίμηση του αριθμού των φρούτων κατά τη διάρκεια της καλλιεργητικής περιόδου μπορεί να

συνεισφέρει στο αραίωμα των καρπών και την επιλεκτική συγκομιδή. Για την ορθότερη και πληρέστερη αξιολόγηση της προτεινόμενης μεθοδολογίας, θα πρέπει αυτή να κριθεί μελλοντικά με διαφορετικές ποικιλίες μήλων και αισθητήρες LiDAR.

Επιστημονική περιοχή: Δενδροκομία ακριβείας

Λέξεις κλειδιά: 3D δεδομένα, φυλλική επιφάνεια, μέγεθος καρπού, γεωμετρία δέντρου

Table of contents

Acknowledgments

I express my deepest gratitude to my chief supervisor A/Prof. Spyros Fountas for his excellent guidance, encouragement, and criticism throughout my study. He is so caring about both my academic and personal achievements. He always encourages me to utilize my full potential and helps me with his invaluable technical, physical and moral supports. I consider most fortunate to have him as my chief supervisor.

To my supervisor, Prof. Dr. habil. Manuela Zude-Sasse, you have been an excellent mentor. I greatly admire your proficiency in providing guidance and support through all aspects of my candidature, from exploring results long discussions on conceptualizing research goals. Thank you for always providing me with the resources that I have needed, the opportunity to be part of numerous field trials. I have also always appreciated your constructive feedback on my writing and approach to research. The skills that I have learnt under your supervision will continue to play a big role well into the future.

I would like to express my heartfelt gratitude to my supervisor A/Prof. George Xanthopoulos for his supervision and guidance in this research work. He contributed a lot in planning and discussion of research work, scientific advice, and the tremendous help with manuscripts.

I wish to give my sincere gratitude to Dr. habil. Dimitrios Stergios Paraforos for his patient and constructive, yet friendly, guidance. He has also shared with me his expertise in the area of 3D point clouds analysis. Without you Dimitri, I would not had the chance to explore trees in 3D. Also, his support and flexibility has greatly reduced frustration while running experiments.

I would also like to thank the members of the seven-member committee, Associate Professors Dionysios Kalyvas Konstantinos Arvanitis and Peter A. Roussos for their immense contribution to the review of this dissertation.

A big thanks to my teammates and friends from Farm Machinery lab at Agricultural University of Athens and from ATB Leibniz Institure, Thanos Balafoutis, Evangelos Anastasiou, Aikaterini Kasimati, Martin Penzel, Kowshik Kumar Saha, Nicole Brandes for been so encouraging and always being there for all matters, personal or work-related. I would like to kindly thank and express my appreciation to Nele Handtke, Evgeny Gubin, Andreas Giakoumatos, Giannis Tsakos and Tzenni Georgiadi for helping me with field and labouratory measurements. I would like to express my gratitude to Achilleas Anastasiou, David Sakowsky, Stephan Elwert, Corina Rolleczek,

Gabi Wegner, Ingo Trupel, Christian Regen who assisted me in the lab. I would like to thank all the other people in my department and institute who in some way or the other influenced my life and made this journey simple. All of them provided a wonderful work environment.

Table of publications

Journal articles	
J.1	**N. Tsoulias**, G. Xanthopoulos, S. Fountas & M. Zude-Sasse (2021). Effects of soil ECa and LiDAR-derived leaf area on yield and fruit quality in apple production. (Submitted)
J.2	**N. Tsoulias**, D. S. Paraforos, G. Xanthopoulos, & M. Zude-Sasse (2020). Apple shape detection based on geometric and radiometric features using a LiDAR laser scanner. *Remote Sensing*, *12*(15), 2481.
J.3	**N. Tsoulias**, D. S. Paraforos, S. Fountas, & M. Zude-Sasse (2019). Estimating canopy parameters based on the stem position in apple trees using a 2D lidar. *Agronomy*, *9*(11), 740.
International conference proceedings with a full-paper review	
IC.1	Tsoulias, N., S. Fountas & Zude-Sasse, M. (2021). Estimating the canopy volume using a 2D LiDAR in apple trees. virtual 4th International Symposium on Horticulture in Europe (SHE/Virtual), 8. -11.03, Stuttgart, Germany. (In print)
IC.2	**N. Tsoulias,** G. Xanthopoulos, S. Fountas, & M. Zude (2020, November). In-situ detection of apple fruit using a 2D LiDAR laser scanner. In *2020 IEEE International Workshop on Metrology for Agriculture and Forestry (MetroAgriFor)* (pp. 278-282). IEEE.
IC.3	**N. Tsoulias**, D. Paraforos, S. Fountas, M. Zude-Sasse. (2019). "Calculating the water deficit spatially using LiDAR laser scanner in an apple orchard". *In European Conference of Precision Agriculture (ECPA). 8-11 July, Montpelier, France.*
IC.4	**N. Tsoulias**, D. Paraforos, N. Brandes, S. Fountas, M. Zude-Sasse. (2018)." Calculating the Water Deficit of Apple Orchard by Means of Spatially Resolved Approach", *In 14th International Conference on Precision Agriculture (ICPA),* 24-27 June, Montreal, Quebec, Canada.
This thesis contributed in other studies (results not shown)	
C.1	Penzel, M., **Tsoulias, N**., Herppich, W. B., Weltzien, C., & Zude-Sasse, M. (2021). Modelling the tree-individual fruit bearing capacity aimed at optimising fruit quality of Malus x domestica BORKH. 'Gala'. Frontiers in plant science (Accepted)
C.2	Penzel, M., Lakso, A. N., **Tsoulias, N.**, & Zude-Sasse, M. (2020). Carbon consumption of developing fruit and the fruit bearing capacity of individual RoHo 3615 and Pinova apple trees. *Int. Agrophys.*, *34*, 409-423.

Abbreviations

3D	Three-dimensional
2D	Two-dimensional
C	Curvature estimated by eigenvalues [%]
$\tilde{C}$	Mean value of curvature in defoliated trees [%]
C_A	Curvature of apple class [%]
C_L	Curvature of leaf class [%]
C_W	Curvature of wood class [%]
C_{th}	Curvature threshold with the highest likelihood within the apple class [%]
Cov	Covariance matrix of the *k*-nearest neighbors points, Pi
D_{Manual}	Manually measured diameter of apples [mm]
D_{LiDAR}	Estimated diameter of apple cluster or subcluster [mm]
$D_{r,i}$	Actual reference dimension of the metal box profile [mm]
$D_{LiDAR,\ i}$	Dimension of the metal box estimated by the LiDAR for time instance i [mm]
$D_{r,\ i}$	Water depletion in the root zone at the end of day i [mm]
$D_{e,i}$	Daily cumulative depth of water depleted from the surface of day i [mm]
DAFB	Days after full bloom
DABB	Days after bud break
DP_i	Water loss out of the root zone by deep percolation on day i [mm]
ECa	Apparent soil electrical conductivity [mS m^{-1}]
$ECa_{,\ Low}$	Areas within the orchard with low ECa values
$ECa_{,\ Mid}$	Areas within the orchard with middle ECa values
$ECa_{,\ High}$	Areas within the orchard with high ECa values
ECEF	Earth-centered earh fixed coordinate system
ENU	East north up coordinate system of IMU
ET_a	Actual evapotranspiration [mm]
ET_0	Potential evapotranspiration [mm]
ET_c	Crop evapotranspiration [mm]
$ET_{c,RF}$	Crop evapotranspiration adjusted to soil texture and plant height considering mean root depth of 1 according to Allen et al., (1998)
$ET_{c,LiDAR}$	Crop evapotranspiration adjusted to soil texture, LiDAR measured leaf area and considering mean root depth of 1 m
e	First numerical eccentricity of the earth ellipsoid
e_a	Actual vapour pressure [kPa]
e_s	Saturation vapour pressure [kPa]
FN	False negatives
FP	False positives
G	Soil heat flux [MJ $m^{-2}d^{-1}$]
G_{LA}	Estimated LA at t [m^2]
H_{LiDAR}	LiDAR estimated tree height [mm]
H_{manual}	Manually measured tree height [mm]
h	Mean tree height [m]
I_i	Irrigation on day i [mm]
ICP	Iterative closest point algorithm
IMU	Inertial measurement unit
K	Total number of point set defined from k- nearest neighbors algorithm
K_{cb}	Basal crop coefficient
$K_{cb,ini}$	Basal crop coefficient during bud break and full bloom, adjusted to field conditions
$K_{cb,mid}$	Basal crop coefficient during full bloom and harvest, adjusted to field conditions
$K_{cb,end}$	Basal crop coefficient after harvest, adjusted to field conditions
$K_{c,\ min}$	Minimum crop coefficient for bare soil
$K_{cb,mid,RF}$	$K_{cb,mid}$ according table 12 (Allen et al., 1998)
$K_{cb,end,RF}$	$K_{cb,end}$ according table 12 (Allen et al., 1998)
$K_{cb,\ full,mid}$	Crop coefficient based on daily weather conditions and h during bud break and full bloom
$K_{cb,full,end}$	Crop coefficient based on daily weather conditions and h after harvest
$K_{cb,full,max}$	Maximum value of K_{cb} during the cultivation period

K_e	Soil surface evaporation coefficient
K_{LA}	Growth rate of LA at t [$m^2\,day^{-1}$]
K_s	Soil water stress coefficient
K_v	was the V_{LiDAR} growth rate [$m^3\,day^{-1}$]
K_r	Soil evaporation reduction coefficient (Allen et al., 1998)
K-dtree	K-dimensional space
L_A	Linearity of apple class [%]
L_L	Linearity of leaf class [%]
L_W	Linearity of wood class [%]
L_{th}	Linearity threshold with the highest likelihood within apple class [%]
LA	LiDAR estimated leaf area considering PPT [m^2]
LA_{Manual}	Manually measured leaf area [m^2]
LAI	Leaf area index [$m^2\,m^{-2}$]
LAST	Least absolute residuals
LiDAR	Light detection and ranging
LLA	Geodetic latitude longitude altitude in spherical coordinate
M_D	Center of fruit points created by *k*-means clustering in defoliated trees
M_L	Center of apple created by *k*-means clustering in foliated trees
MAE	Mean absolute error [mm]
MBE	Mean bias error [mm]
N	The sum of true positives, true negatives, false positives, false negatives
n	Total number of samples
n_D	Total number of apple clusters in defoliated trees.
n_{Manual}	Total number of manually counted apples
NED	North East down coordinate system of IMU
p	The average fraction of TAW that can be depleted from the root zone before the revealing of moisture stress [mm]
p_{tab}	Tabulated p values (Allen et al., 1998)
$\bar{P}$	Average of set of points defined from *k*- nearest neighbors algorithm
P	Precipiation on day i [mm]
P_i	Set of points defined from *k*- nearest neighbors algorithm
PPT	Segmented points per tree
r	Radius used in the *k*- nearest neighbors [mm]
$\widetilde{R}$	Mean value of apparent reflectance intensity in defoliated trees [%]
r	Pearson coefficient of determination
R^2	Coefficient of determination
R^2_{adj}	Adjusted coefficient of determination
$R^2_{adj,C}$	Adjusted coefficient of determination of calibration
$R^2_{adj,CV}$	Adjusted coefficient of determination of leave-one-out cross validation
R_A	Apparent reflectance intensity of apple class [%]
R_L	Apparent reflectance intensity of leaf class [%]
R_{LA}	Relative growth rate at t [$m^2\,day^{-1}$]
R_n	Solar radiation [$W\,m^{-2}$]
R_{min}	Reflectance of board target coated with urethane [%]
R_{max}	Reflectance of board target coated with barium sulphate [%]
R_{ToF}	Apparent reflectance intensity at 905 nm of LiDAR laser scanner [%]
R_{th}	Apparent reflectance intensity threshold with the highest likelihood within the apple class [%]
R_W	Apparent reflectance intensity of wood class [%]
RAW	Readily available water content in the root zone [mm]
RAW_{Low}	Readily available water content in the root zone in low ECa regions [mm]
RAW_{Mid}	Readily available water content in the root zone in depth in mid ECa regions [mm]
RAW_{High}	Readily available water content in the root zone in high ECa regions [mm]
RANSAC	Random sample consensus algorithm
REW	Cumulative depth of evaporation [mm]
RH	daily relative humidity [%]
RMSE	Root mean square error [%]
$RMSE_{CV}$	Cross validation root mean square error [%]

$RMSE_C$	Calibration root mean square error [%]
RO_i	Run off at the end of day i [mm]
Rot	Rotation matrix for three-dimensional tilt orientations in the point cloud considering the LiDAR timestamp *t*
RTK-GNSS	Real time kinematic -global navigation satellite system
S	Slope of the saturation vapour pressure [kPa °C^{-1}]
S_{manual}	Manually measured tree stem diameter [mm]
S_{LiDAR}	LiDAR estimated tree stem diameter [mm]
SSC	Fruit soluble solids content [%]
SOR	Statistical outlier removal
T_D	Trees after defoliation
T_L	Trees before defoliation
T_m	Mean temperature
T_{max}	Max temperature [°C]
T_{min}	Min temperature [°C]
TAW	Total available water for the root zone assuming field-homogeneous root depth of 1 m [mm]
TEW	Maximum cumulative of depletion from the soil surface [mm]
ToF	Time of flight
TN	True negatives
TP	True positives
Trans	Translation matrix for three-dimensional tilt orientations in the point cloud considering the LiDAR timestamp t
t	Days after bud break
T_e^n	Transformation matrix from the ECEF to the ENU coordinate system
$T_{LiDAR}^{sensor\text{-}frame}$	Transformation matrix from the coordinate system of the LiDAR sensor to the coordinate system of the RTK-GNSS
T_{LiDAR}^{ts-geo}	Transformation matrix considering three-dimensional tilt of the IMU data
u	Wind speed [m s^{-1}]
V_0	Initial horizontal asymptote of V_{LiDAR} [m^3]
V_{manual}	Manually measured tree volume [m^3]
V_n	Upper horizontal asymptote of V_{LiDAR} [m^3]
V_{LiDAR}	LiDAR estimated tree volume [m^3]
$V_{LiDAR, FB}$	LiDAR estimated tree volume during full bloom [m^3]
$V_{LiDAR, FS}$	LiDAR estimated tree volume during fruit set [m^3]
$V_{LiDAR, BH}$	LiDAR estimated tree volume during before harvest [m^3]
V_{Manual}	Manually calculated volume of apples [mm^3]
V_{LiDAR}	Estimated volume of apple clusters [mm^3]
V_t	Estimated V_{LiDAR} at time t and Δt
W_{LiDAR}	LiDAR estimated tree width [mm]
W_{manual}	Manually measured tree width [mm]
WB_{RF}	Water balance model [mm] soil-adjusted
WB_{LA}	Water balance model [mm] considering tree leaf area.
W_1,W_2, W_3, W_4	Four horizontally parallel wires supporting the trees
Z	Uniform root depth of 1 m (Allen et al., 1998) for apple trees
Z_e	Effective depth of soil evaporation layer [m]
α	Semi-major axis length of the earth [m]
γ	Psychrometric coefficient [kPa °C $^{-1}$]
γ	Acceleration and deceleration constant rate of approximation to the two asymptotes
ΔW	Tree region between the ground and W1, W2, W3, W4
Θ_{FC}	Volumetric soil water content at field capacity (FC) [m^3 m^{-3}]
Θ_{WP}	Volumetric soil water content at WP_0 [m^3 m^{-3}]
Δt	Time interval between the measurements
v	Distance from earth's surface to the z-axis along the ellipsoid normal

Π_e	Position in ECEF coordinates
Π_n	Position in the local ENU coordinate system
ρ	apparent soil resistivity [Ω m]
x_{min}	Initial horizontal asymptote of extracted features
x_{max}	Upper horizontal asymptote of extracted features
$[\psi,\theta,\varphi]$	[Yaw, pitch, roll] angles [°] from IMU
$[x_i, y_i, z_i]$	Points in three dimensions
$[\varphi, \lambda, h]$	[Latitude, longitude, altitude] in ECEF coordinate system

1. Introduction

1.1. *Precision agriculture*

Definition

The term *precision agriculture* refers to the spatio-temporal management of crops, to improve harvest efficiency and minimize environmental impacts (Gemtos et al., 2013). What differentiates precision agriculture from the conventional agriculture lies on the spatial variability of the field management based on the particular demands of each field segment. precision agriculture is that management during the cultivation tasks varies for each part of the field, according to the needs of that particular part. This allows for the accurate and optimized use of inputs relevant to each individual field parts, which minimizes costs and environmental impacts (Stafford, 2000). Lowenberg-DeBoer and Swinton (1997) defined *precision agriculture* as the digital control of data acquisition, processing of information and decision making by means of spatial and temporal inputs of agricultural production. *Precision agriculture* is a production system that involves crop management according to field variability and site-specific conditions. Precision agricultural technologies are technologies used either separately or in combination as the means to realize precision agriculture (Tey and Brindal, 2012). Recently, the International Society of Precision Agriculture specified precision agriculture as a management strategy; it gathers, processes and analyzes temporal, spatial and individual data and combines it with other information to support management decisions according to estimated variability for improved resource use, efficiency, productivity, quality and sustainability of agricultural production (ISPA Newsletter, 2019).

1.2. *Technologies in precision agriculture*

1.2.1. *Real time kinematic- global navigation satellite system (GNSS)*

The first step in precision agriculture concerns the acquisition of data related to the crop, orchard, and environment. To achieve this, precision agriculture utilises various sensors and technologies such as: global navigational systems (GPS), remote sensing, wireless sensors and networks, etc. Usually, data processing in precision agriculture deals with spatio-temporal data (maps, management zones, geostatistics) and as a consequence, the use of global navigational satellite systems (GNSS) is necessary to acquire the location corresponding to each measurement.

The GNSS was first developed in the early 70s to improve navigation using satellites (Lasisi and Chris, 2021). GNSS provides the position (latitude, longitude and elevation) of the object on the surface of the Earth in real time, by using the signal code and/or carrier phase and, therefore, measuring the distance (pseudorange) from the receiver antenna to the orbital position of at last four satellites within a certain time (Catania et al., 2020). Therefore, each individual measurement in precision agriculture is marked with a location and can be georeferenced. The main satellite constellations from which the antenna of the various GNSS receivers can receive signals are Galileo, operated by the European Union; global positioning system (GPS), operated by the US Department of Defense and using 31 satellites; global navigation satellite system (GLONASS), operated by the Russian Federation and using 23 satellites and BeiDou, operated by China and using 49 satellites (Balafoutis et al., 2017). The GNSS systems receiver antenna (rover) presents different levels of accuracy ranging from 1 m to 1 cm, which depends on the differential information or corrections provided by a nearby reference GNSS station or network of such stations (Perez-Ruiz and K., 2012). Due to its accuracy, GNSS can be implemented in numerous applications in agriculture, such as auto-steering (Groth et al., 2013), navigation of robotic platforms (Fountas et al., 2020) and variable rate applications (Bourodimos et al., 2019; Colaço and Molin, 2017).

Field positioning in agriculture is necessary to perform site specific applications related to precision agriculture. Based on the aforementioned information, various field applications require high accuracy for calculating the location or navigation within the field. Over the last decade, the use of the real time kinematic-global navigation satellite system (RTK-GNSS), which offers position accuracy dow to cm level, has been broadly expanded,

introducing new possibilities related to agricultural applications. Apart from the satellite signal, the antenna (rover) receives an additional corrective signal from the base. Therefore, GPS accuracy can reach accuracy down to 2 cm, rendering application in demanding tasks (e.g. navigation) feasible. One of such tasks was the development of auto-steering systems, which have thoroughly been assessed for their accuracy (Easterly et al., 2010; Groth et al., 2013).

1.2.2. *Satellite imaging*

Earth observation satellites have found application in precision agriculture. They can be categorized based on the trajectory height (low, middle and geosynchronous), purpose (meteorological, environmental and mapping), and the equipped sensor (active or passive). A series of satellites, such as Landsat, SPOT 1, IRS-1A were launched during the past decades to provide high quality images to end users. Satellite products from these missions were employed for land use and crop classification in many large earth regions, however the spatiotemporal resolution was not adequate (< 30 m) for applications in precision agriculture.

A plethora of satellites, such as IKONOS, ResourceSat-1, KOMPSAT-2 were launched after 1999, improving the spatial resolution (~ 4m) of image acquisition in visible and near infra-red bands with a revisit period of up to five days (Mulla, 2013). Imageries collected from IKONOS have been used for multiple purposes in precision agriculture, including soil mapping, crop growth and yield prediction, nutrient management, and evapotranspiration estimation (Enclona et al., 2004; Sullivan et al., 2005; Yang et al., 2014).

Numerous nanosatellite constellations have been launched during the past decade (GeoEye-1, Pleiades-1A, Superview-1), addressing further limitations associated with high spatial (< 2m), spectral, and temporal (daily) resolution of satellite imagery (Sishodia et al., 2020; Zare et al., 2020). Nanosatellite constellations consist of clusters of small satellites bearing compact sensors that are cheaper and replaceable. Several data fusion approaches have been proposed for the combination of high/moderate spatial resolution data with high temporal resolution data (and vice-versa) in order to generate high spatial–temporal resolution data products with the aim of taking advantage of a wide variety of publicly available satellite data (Knipper et al., 2019; Xiaolin Zhu et al., 2018). This technology was substantially applied in arable crops enabling the monitoring of biotic (e.g. weeds, diseases) and

abiotic (e.g. deficiency of water, nutrients) parameters that can influence the plant (Janareva, 1978; Sishodia et al., 2020; Vinh et al., 2019). The recent launch of the ICESat-2 LiDAR satellite (September 2018) and the attachment of the GEDI LiDAR sensor to the international space station (December 2018) has opened up many new avenues for research, providing opportunities to map vegetation structure at a global scale and at high resolutions (Prins and Van Niekerk, 2020).

1.2.3. *RGB cameras*

Colour images with red, green and blue channels (RGB) are utilized in precision agriculture for the detection of a great number of agricultural parameters related with plant vigour, water stress, diseases and soil properties. The cost effectiveness of RGB cameras combined with the development of image analysis and computer vision techniques has led to their extensive use in precision agriculture. These applications include the estimation of plant vigour (Z. Khan et al., 2018; Vollmann et al., 2011), yield (Fernandez-Gallego et al., 2018; M. Zhang et al., 2020) weed detection (Bosilj et al., 2018; Hamuda et al., 2017; Kounalakis et al., 2018), diseases detection (Ali et al., 2017; Zhou et al., 2015) and insects detection (Ebrahimi et al., 2017; Rustia et al., 2020). This type of camera owes its potential to the use of efficient image analysis algorithms and image resolution. However, the captured images are sensitive to light variation and detection can be biased in cases where the fruit, leaves and branches are of the same color (Kurtulmus et al., 2011; Linker et al., 2012). Thus, image processing is rather challenging, given that intensity is not decoupled from chromaticity, resulting in a high correlation between the components R, G and B (Garcia-Lamont et al., 2018).

1.2.4. *Spectral cameras*

Plant and soil particles absorb, transmit and reflect the sun's electromagnetic radiation in a unique way, which is determined by chemical and morphological characteristics of the object's surface. It is well known that the water content of plant particles (wood, leaves, tissues, fruits) varies and so does the reflectance of light spectra. Although numerous studies that have been conducted in agriculture using low-cost passive imagery sensors, such as visible and near infrared, many applications require higher spectral fidelity that only multispectral and hyperspectral

sensors can offer (Kitić et al., 2019; Zarate-Valdez et al., 2012; Zude, 2003). Both of the indicated spectral-based methods consist of the acquisition of images where, for each of the image's spatially distributed elements, a spectrum of the energy reaching the respective sensor is measured. The main difference between them is the number of bands (also referred as channels) and their width. There are nondestructive, contactless optical methods, widely adopted and recognized as an option for routine monitoring of photosynthetic activity and plant status (Behmann et al., 2015; Gonzalez-Dugo et al., 2015). These optical methods include hyperspectral imaging, spectroscopy, and fluorescence, and are based on the analysis of the plant's optical signature in visible and near infrared region, i.e. on the analysis of the light reflectance from the plants' surface (Bauriegel and Herppich, 2014; Behmann et al., 2015; Kitić et al., 2019; Peñuelas and Filella, 1998).

Multispectral imaging systems acquire a small number of spectral bands by using parallel sensor arrays (M. J. Khan et al., 2018). Three to six spectral bands with large optical band intervals are typically utilized ranging from visible to near infrared regions of the electromagnetic spectrum. The most used and implemented indices of plant vigour from multispectral wavebands in precision agriculture is the normalized difference vegetation index (NDVI) and normalized difference red edge (NDRE) derived either from multispectral camera (Candiago et al., 2015; Geipel et al., 2016) or dedicated sensors (e.g., GreenSeeker, CropCircle) (Reyniers et al., 2006; Scotford and Miller, 2004) These sensors have been used to determine biophysical parameters, such as the green biomass and leaf area index (Fitzgerald, 2010; Flynn et al., 2008), and the nitrogen (N) status (Shaver et al., 2011; Tremblay et al., 2009). Furthermore, the NDVI has been related with vine vigor (Tagarakis et al., 2018; Trought and Bramley, 2011), yield (Matese and Di Gennaro, 2015) and quality (Anastasiou et al., 2019; Tagarakis et al., 2018). Berni et al. (2009) used a multispectral camera MCA-6 (Tetracam Inc., CA, USA) in an unmanned aerial vehicle to produce vegetation indices in corn plants and olive trees.

Hyperspectral cameras, as opposed to multispectral cameras, can collect image data in tens to hundreds of very narrow (5–20 nm, each), continuous spectral bands throughout the visible and infrared ranges. As a result, hyperspectral cameras can produce a larger number of vegetation indices than multispectral ones. Yang et al. (2009, 2007) derived NDVI from 102-band hyperspectral images and related them to yield. They also applied spectral angle mapper and linear spectral unmixing techniques to the 102-band hyperspectral images to generate single-

layer spectral angle images and plant cover fraction images, respectively, in order to map the variation in crop yields. Their results showed that the spectral angle images and plant cover fraction images provided better correlations with yield than most of the narrow-band NDVIs derived from the hyperspectral images. Ye et al. (2007) used partial least squares (PLS) regression models to predict the yields of citrus trees based on their canopy features obtained from airborne hyperspectral imagery as compared with vegetation indices and multiple linear regression models. Their results showed that vegetation indices and multispectral regression models failed to predict citrus yield, but PLS models successfully predicted citrus yield with r-squared values of 0.51–0.90. Zarco-Tejada et al. (2013) used the hyperspectral camera, which was adapted onto a UAV to calculate carotenoids in vineyards with a 0.84 linear regression coefficient (R^2). Calderon et al. (2013) used a multispectral and a hyperspectral camera mounted on a UAV to locate olives infected by the pathogen *Verticillium* wilt through various by applying vegetation indices. Okamoto and Lee (2009) utilized a hyperspectral imaging system to detect green immature citrus fruit of three different varieties, and reported 80–89 % correct identification of foreground fruit by employing pixel discriminant function and applying spatial image processing steps.

1.2.5. *Thermal cameras*

Thermal cameras can generate images related to object temperature, because they operate in the infrared wavelength ranging from 3-35 μm. However, day images between 3 and 5 μm overlap with solar reflection producing noise, whereas 17 - 25 μm regions have not yet been well investigated (Ishimwe et al., 2014). As a consequence, 8 - 14 μm regions have been of greatest interest for thermal remote sensing since this is where the atmosphere is fairly transparent and the signal is only lightly attenuated by atmospheric absorption (Prakash, 2000).

Several studies used thermal imaging techniques to measure the crop water status by means of the crop water stress index (Jones, 1999; Käthner et al., 2017). While thermal imaging is easily applied in the laboratory, the technique has also been developed for field studies, particularly in the semi-arid and arid sub-tropics (Ben-Gal et al., 2009; Cohen et al., 2012). Consequently, thermal cameras are frequently mounted on tractors or unmanned aerial vehicles to estimate the crop water stress index spatially (Gan et al., 2018; Zarco-Tejada et al., 2013). In

peach and apple orchards located in a semi-arid environment, the crop water stress index was found to vary significantly between different irrigation treatments (Bellvert et al., 2016; Nagy, 2015).

In addition, thermal imaging has been applied in fruit detection. Bulanon et al. (2009) built a multi-modal system using a thermal camera and a color camera to detect mature citrus fruit. Similarly, thermal cameras produced 90.4 % recall rates and 95.5 % precision rates in immature green citrus fruit detection (Gan et al., 2018). Stajnko et al. (2004) demonstrated the applicability of thermal imaging for predicting the number and diameter of apple (Malus domestica) fruits to calculate the yield in an apple orchard. They demonstrated that image fusion of the two types of images improved fruit detection compared to using a thermal image alone,while recently the method was utilized in the detection of sunburn in apple trees (Ranjan et al., 2020).

1.2.6.*Robotic platforms*

In an effort to decrease labor costs and automate agricultural tasks to address the constant rise of demand for higher yields, several small field robots have been proposed for specific purposes, such as automated weeding or field data collection. Weed control can be applied electrically using electrodes (Blasco et al., 2002; Reiser et al., 2019), mechanically (Åstrand and Baerveldt, 2002) or by utilizing weed map information (Bak and Jakobsen, 2004). Robotic weed management systems have also been reported (Kunz et al., 2018), aiming at maximizing the weed treatment efficiency and success rate using a combination of tactics. Bawden et al. (2017) proposed a heterogeneous weed management system that is capable of selectively applying a mechanical or chemical control method based on the species of the weeds. Chang and Lin (2018) developed a small scale agricultural robot that can automatically weed and perform variable rate irrigation within a cultivated field. In general, weed detection precision recorded with mechanical weeding robots was < 25 mm (Bakker et al., 2006) or higher of 3 cm (Bochtis et al., 2011; Jørgensen et al., 2007).

Yield monitoring and harvesting are two more repetitive tasks where robotic systems have been implemented. However, these are complex tasks due to the non-uniform maturation of the crop/fruit due to the biotic and abiotic factors affecting plant growth and cause high variation in-field. Harvesting robots in horticulture and specifically in apple trees exhibited picking speeds of 7.5 to 9 sec (Baeten et al., 2008; Silwal et al., 2016) per apple and even 90 % accuracy detection (De-An et al., 2011). Similar systems have been developed for horticultural products,

such as tomatoes (L. L. Wang et al., 2017), sweet pepper (Arad et al., 2020; Ringdahl et al., 2019) and cucumber (Van Henten et al., 2006).

1.3. *Data Processing*

1.3.1. *Geographical information systems*

Geographical information systems (GIS) have grown exponentially over the past decades and in nowadays are considered a potential geographic-based information processing tool for spatial data analysis and management (Braud et al., 2005; Malczewski, 2006). Upon the implementation of GIS in agriculture, spatiotemporal variability of biotic and abiotic parameters became feasible, thus improving the management of natural resources and environmental protection, regional and urban planning and development, and the management of utilities (Montgomery et al., 2016). Spatiotemporal information can mainly be quantified with geostatistics, allowing the observation of autocorrelations within parameters and the creation of maps. The data type can be either continuous, creating more robust models or point data (e.g. soil data) to reduce the sampling cost (Aggelopoulou et al., 2011; Liaghat and Balasundram, 2010). GIS supports high level decision making for effective management of fertilizers and pesticides, stress mapping, and irrigation (Ali et al., 2017; Clay and Shanahan, 2011; Knipper et al., 2019). Crop and soil bio-physical attributes and data derived remotely are used with the help of GIS for radical improvement of agricultural productivity (Anastasiou et al., 2018; Knipper et al., 2019).

1.3.2. *Machine learning*

There are two types of machine learning techniques, supervised and unsupervised learning. They require less prior information and are applicable to a wider range of tasks as they derive the underlying distributions and model assumptions implicitly from training data (Behmann et al., 2015). In supervised learning, data are presented with training example inputs and the corresponding outputs, and the objective is to construct a training model which can be used to predict test data. In some cases, inputs may be only partially available with some of the target outputs missing or given only as feedback to the actions in a dynamic environment (Liakos et al., 2018). Supervised machine learning techniques, such as Principal components analysis (PCA), are often used to learn patterns from

big-data, reducing high dimensionality in datasets so that computational speed and classification accuracy could potentially be improved (Kamilaris et al., 2017;Zhang et al., 2020). Karkee (et al., 2009) adopted PCA to reduce the dimensionality of normalised differential vegetation index (NDVI) datasets. The results indicated that PCA could effectively remove the redundant information either to preserve a high classification accuracy or to decrease the calculating time. Crop area fractions within a pixel were predicted with an RMSE of 1.3% and an average estimated emergence date error of 4 days.

Some of the most efficient algorithms in machine learning that are applied in precision agriculture are: support vector machine, K-nearest neighbor (KNN) and neural networks. For example, Linker et al. (2012) used KNN for detection of apples. Apple surface was detected using growing region based on color and texture information, then contour of each region was segmented into an arc so that the apple could be recognized. The authors reported that 85.0% of apples were detected under direct lighting conditions. They also claimed that 95.0% of green apples were detected under diffused lighting conditions. Whereas, Wachs et al. (2010) used thermal images and color images for green apple detection. Support vector machine was used to identify the shape of apples on trees based on pixels value of apples in hue, luminance, and saturation color space (Ji et al., 2012; Wang et al., 2009). Furthermore, neural networks models were built up from multispectral images to predict the spatial variability of stem water potential in vines, resulting in an R^2 between 0.57- 0.87 when the bands 550, 570, 670, 700 and 800 nm were included (Poblete et al., 2017).

1.3.3.*Variable rate*

The method of variable rate application is a vital component of precision agriculture. More specifically, it can adjust treatment rates based on the vehicle's spatial location (water, fertilizer, pesticides, etc.) according to maps or management zones (Roberson et al., 2000). This optimum utilization of resources helps to maintain economic profit ensuring sustainability and environmental safety. Various sensors mounted on a platforms(tractor, UAV, satellites) have been to dynamically measureto measure the crop indexes and transmitted the signal to the controller in real time so that the appropriate dose to be adjusted. Optical reflectance canopy sensors mounted on agricultural machines, such as Greenseeker®, N-Sensor®, and Crop Circle®, enable real-time reflectance monitoring with high spatial resolution, allowing variable rate nitrogen fertilization. Raun et al.(2005) showed that the use of the

Greenseeker sensor for N fertilizer recommendation for wheat resulted in 15% increase in N use efficiency. The use of these sensors as a tool in N management involves the development of algorithms that estimate the N dose to be applied at variable rates based on different vegetation indexes evaluated by the canopy sensors, such as the NDVI (Clay et al., 2018; Sun et al., 2020). Moreover, applying variable rate on herbicides can reduce the amount of herbicide by 29 % (Carrara et al., 2004) or lead to savings up to 60 % (Dammer, 2016). Another variable rate application approach is based on variability maps of the crop or the soil. This approach can be implemented after grid sampling or delineation of management zone. Implementation of this approach in corn, wheat and grapes has shown that the technology can increase profits (Chen et al., 2008; Kitchen et al., 2005; Liakos et al., 2020). Currently, the latter two technologies are exploited by numerous agricultural machinery (market ready), including fertilizers (Forouzanmehr and Loghavi, 2012; Liakos et al., 2020), sprayers (Colaço and Molin, 2017), seeding machines (Velandia et al., 2013) and irrigation systems (Sanchez et al., 2017) for orchards and arable crops.

1.4. *Precision horticulture*

Precision horticulture targets individual trees or zones of tree blocks adaptively to its apparent status that shall trim down environmental footprint of fruit and vegetables production through enhanced resource efficiency and improved production (Zude-Sasse et al., 2016). Digital horticulture is a recent terminology that refers to the use of a range of digital technologies (including plant sensing devices) used in different horticultural applications such as the high-throughput phenotyping and precision horticulture (often referred as site-specific management) (Colaço et al., 2018).

However, horticultural products are characterized by high value, therefore quality analysis of the product is more important than in any other crop. In contrast to arable crops, the size of orchards is usually small with low plant density and trees are treated individually. Furthermore, the planting system remains stable over years, with canopy morphology and rooting system to be adapted according to the environment and soil system . The first step includes data acquisition of parameters related to the orchard and fruit trees. More specifically, data acquisition of soil, plant physiology, yield and quality, is monitored throughout the season within the orchards with manual measurements, using in situ sensors or in the laboratory. In perennial fruit trees, are necessary additional, e.g.,

thinning of flowers and fruits, pruning. In orchards, structures for irrigation, hail nets or frost protection limit, the use of methods for soil mapping, e.g. for electromagnetic measurements, which are disturbed by iron installations (Gebbers et al., 2009). Time data series, is a significant source of information throughout the growth season, revealing parameters exhibiting temporal stability and the causes which lead to temporal variability.

1.4.1. *Soil mapping*

Soil is a key factor that determines the growth and vigour of perennial trees and therefore the yield and fruit quality. Spatial variability of soil properties affects the variance of plant data (Aggelopooulou et al., 2013), whereas the necessity of soil variability in orchard management has not been proven so far leaving for future studies. Soil influences fruit trees at least to down the depth covered by the roots, and soil electrical conductivity (ECa) measurements should be extended to the same depth. This type of sensors emit several electromagnetic signals at different soil depths, which may reveal properties of the topsoil or even the whole profile depending on the sensor range or the user adjustment. Thus, spatial maps of ECa or soil properties can be produced and ultimately used by farmers.

The electrical conductivity (EC) and apparent electrical conductivity (ECa) of soil are influenced by numerous factors such as salinity or mechanical composition (Corwin and Plant, 2005), the content of humidity, soil depth (Tsoulias et al., 2020a) and the content of organic matter (Gemtos et al., 2013; Shaner et al., 2008). Therefore, EC and ECa can provide valuable information about the variation of soil properties and for the deliniation of management zones.

The spatial variability of soil can be derived by the ECa measurement even if many potentially influential factors need to be considered (e.g. soil humidity, temperature). A methodology for guided soil sampling using ECa data was suggested (Horney et al. 2005) for targeting samples of each ECa zone. The steps are to map ECa, delineate zones, and identify the locations for soil sampling (Shaner et al. 2008). This method has been successfully applied in fields, orchards, and vineyards (Daccache et al. 2014; Hedley and Yule 2009; Oldoni and Bassoi 2016). Also, ECa mapping has been frequently used for guided soil sampling and the mapping of available water content by means of clustering algorithms (Haghverdi et al. 2015; Peeters et al. 2015). However, when measuring at field

capacity, ECa is assumed to be influenced mainly by soil texture and soil water content. This is interesting considering the plant water supply.

Mapping ECa [mS m^{-1}] can be used as a key sensing system to understand and evaluate how soil varies spatially in the framework of precision fruticulture (Shaner et al., 2008; Trought and Bramley, 2011). As ECa varies on a similar spatial scale as many soil physico-chemical properties (Sudduth et al., 2003; Carroll and Oliver, 2005), these soil monitoring systems have been widely accepted. Specifically, good correlations with soil salinity, soil water content and soil texture have been widely documented (Heil and Schmidhalter, 2012; Lesch et al., 2005). Other soil properties affecting conductivity may be the organic C (Sudduth et al., 2003; Martinez et al., 2009), cation exchange capacity (Sudduth et al., 2005) and the $CaCO_3$ content (Kühn et al., 2009). Additionally, ECa was used to predict the content of Na^{+}, Mg^{+2} in salty and clay soils (Rodríguez-Pérez et al., 2011). Valente et al. (2012), evaluating soil physical and chemical properties in coffee fields, used geostatistical analysis combined with fuzzy c-means clustering analysis to define management zones within coffee fields. Fountas et al. (2011) delineated management zones for fertilization in olive trees orchards, using soil chemical properties. Aggelopoulou et al. (2010) produced fertilization maps for apple trees fields, based on the amount of nutrients that were removed from the soil with the previous year yield. Mapping the thickness or depth to a contrasting textural layer using ECa has been also referenced in several studies to detect clay horizons (Doolittle et al., 1994; Saey et al., 2009), or estimate topsoil depth explored by roots (Khan et al., 2016). Finally, the elevation, slope and the soil depth of the field are frequently correlated with the historical yield in vineyards (Tagarakis et al., 2018).

Käthner and Zude-Sasse (2015) show that even in small orchards there may be differences in soil properties that relate to tree growth and fruit size. The authors concluded that more than one soil variable should be used to define management zones. In an apple orchard in Greece, Aggelopooulou et al. (2013) delineated management zones combining ECa, soil properties and plant attributes (e.g., SSC, Hue, Firmness, yield), dividing the apple orchard into four zones and suggesting the potential of site specific management of soil fertility, irrigation and cultural practices. Furthermore, yield and fruit quality of peach fruits were affected by soil texture and water content spatiotemporally, enabling the creation of stable management zones and site-specific management. However, the quality parameters of apples are highly variated with reduced spatial stability resulting in poor relation to ECa

(Aggelopoulou et al., 2010). Manfrini et al., (2020) observed no effectamong the spatial patterns of ECa, crop load and fruit weight, suggesting the necessity of over time spatial plant data to improve site specific management within the orchard. Despite the relation of fruit yield and quality to the growth of perennial trees, their spatial interaction during the growth season has been rarely investigated.

1.4.2. *Tree water needs*

Irrigation scheduling is the core of irrigation management and precision irrigation, increasing grower profitability while protecting and improving our environment. The latter is of great importance in agriculture due to global warming effect which affects tree water needs, fruit quality (e.g. fruit sunburn) and consequently the yield. Furthermore, water in plants plays an essential role in supporting photosynthesis, regulating plant temperature via evaporative cooling, maintaining structure through cell turgor pressure (i.e. maintaining leaf orientation), and transporting nutrients into and throughout the plant, thereby supporting its growth.

Irrigation scheduling is usually applied by the farmer based on basic estimations or recommendations from the federal agriculture organization (FAO) (Allen et al., 1998; Pereira et al., 2015) regarding the field. Irrigation calculators provide growers with a practical tool to compute their irrigation needs based on their growing practices, types of soil and vegetation, and to specify their precision management plans based on the calculated needs.

For purposes of irrigation scheduling, plant water requirements are estimated according to the guidelines of FAO56 (Allen et al., 1998) using weather data based Penman-Monteith reference evapotranspiration (ETo) and crop coefficients (Kc). To calculate ETo the following data are needed: solar radiation, air temperature, humidity and wind speed measured at 2m (or converted to that height) above an extensive surface of green grass, shading the ground and not short of water (Gu et al., 2020). ETo can be estimated at different time intervals adjusted for the cultivation requirements and field. Among various approaches of irrigation scheduling, theevapotranspiration combined with soil properties and plant data can be utilized for estimating thedaily tree water needs.

Hedley and Yule (2009), reported that spatial variation in soil water retention characteristics was strongly correlated with spatial variation in soil texture across a field, noting that obviously, areas with heavier soil zones within a field had increased water-holding capacity in comparison to those with light textured soils, presenting higher percentage of enhanced particle size related to sand. Therefore, when calculating the water balance of an

orchard, texture determines field capacity which is crucial for calculating the total available water content of the soil (TAW). So, ECa maps might be used for precision irrigation if they mainly represent the TAW. Another significant factor that should be considered is the water needs of the trees in the orchard. This dynamic parameter also depends on soil properties, microclimate, and tree physiology. Thus, it is important to understand the spatial variability of soil texture as this remains the most stable property and could be interpreted as a key parameter for the estimation of water needs (Hedley et al., 2009). Understanding temporal and spatial variability of readily available water content (RAW) is a factor of major significance as it indicates the threshold inducingwater stress (Jensen et al., 1990; Allen et al., 1998). Calculation of water needs during the cultivation period could improve management in orchards (Alexandridis et al., 2014). The spatial variability of TAW was calculated based on the ECa and soil texture in cereals (Haghverdi et al., 2015). An example of variable rate irrigation based on ECa maps and TAW was shown earlier (Hedley et al., 2010).

Furthermore, trees may respond to short-term changes of TAW in the root zone: In drought stress situations, the root water potential may be affected by means of physiological mechanisms such as decreased osmotic potential (Blum, 2017; Herppich et al., 2001). Such decrease would lead to reduced root water potential and resulting enhanced capability of the root to obtain water from the soil. By definition, root water potential represents the actual wilting point in the calculation of readily available water content (RAW). Both, TAW and RAW are calculated considering the field capacity and wilting point. TAW and RAW are used for analyzing the actual evapotranspiration (ET_a), aimed at calculating the water balance of an orchard. The methods that are used for the estimation of ET_a are either empirical (Courault et al., 2005) or climate data driven (Verstraeten et al., 2008). The second category utilizes meteorological data from weather stations. As mentioned before, the Penman–Monteith method is commonly used to calculate ET_a (Allen et al.,1998; Jensen et al., 1990). For orchard management, only water balance methods can provide the required level of detail (Alexandridis et al., 2014; Hunink et al., 2015). However, water balance at an even finer spatial scale might be desirable, when the soil presents with spatial variability and response of trees to the growth factors can be demonstrated.

Beside soil parameters determining water supply, water consumption is affected by plant properties, such as the rootstock (Tworkoski et al., 2016), developmental stage (Allen et al. 1998), crop load (Haberle and Svoboda, 2015;

Hunsaker et al., 2015), and plant response to drought stress, such as the change in solute content per cell (osmotic adjustment) (Dodd et al., 2010; Lauri et al., 2014). Thus, plant parameters need to be considered during the calculation of TAW (Allen et al. 1998; Haberle and Svoboda 2015; Hunsaker et al. 2015). A water balance model based on observed and calculated TAW considering root depth and water depletion was developed for several annual crops, such as potatoes, maize, cereals, sugar beet, and oil seed rape (Haberle and Svoboda 2015) in temperate climate. When calculating TAW in orchards, particularly in perennial fruit trees, root depth should be considered, since the effects of soil texture and available water on root growth accumulate (Pérez-Pastor et al., 2014).

However, tree water needs are affected also by morphological and physiological parameters, such as the development stage, height and leaf area. It should be noted that the canopy volume in fruit trees is influenced by the tree water needs throughout the cultivation period (Naor et al., 2006; Bustan et al., 2016). Furthermore, a positive relationship of leaf area index (LAI) and evapotranspiration rate was found in citrus and olive trees (Ayyoub et al.,2017). Thus, these parameters and weather variables need to be considered during the calculation of ET_c and subsequently in the water balance model. Additionally to the yield, fruit quality can potentially be influenced by the spatial variability of TAW (Hunsaker et al., 2015). The relationship between soil water status and tree growth parameters has been specified in arid and semi-arid conditions (Blum, 2017; Käthner et al., 2017).

Advances in precision irrigation will improve retention of soluble fertigated nutrients in the root-zone of irrigated orchards. Traditionally, fertigation has ignored soil and crop variability, making uniform applications across an orchard. Improved understanding of soil variability and use of geostatistical techniques may allow for the creation of several irrigation management zones within fields, allowing variable rate irrigation and improving the overall match between water required and applied. Furthermore, decision support systems may facilitate the effective monitoring of the spatial variability of tree water status. For example, thermal sensors installed on unmanned airborne vehicles can be also provided field measurements for variable rate irrigation methods refinement (Gonzalez-Dugo et al., 2015).

The pro and cons of ground-based thermal remote sensing techniques regarding the estimation of evapotranspiration and drought stress have been reviewed (Maes and Steppe, 2012). Ideal, it would be the

development of a system that could allow individual nutrient and water applications to be made to single trees according to their requirements. Engineering limitations, including imprecision in emitter discharge rates, fluid travel times, sloping orchard soil surfaces and the high cost of wireless networked sensors and valves, prevent the use of a large number of simultaneously operating hydrozones (Coates *et al*., 2012).

1.4.3. *3D sensing*

Two-dimensional (2D) vision systems have been an integral part of the successful implementation of agricultural automation and robotics in the food production chain. Nevertheless, the development of most horticultural plants, such as of fruit trees, takes place in 3 dimensions (3D). The advancement in machine vision systems over the last decade allowed the acquisition of 3D data from plants. The number of publications related to horticultural 3D vision systems are increasing exponentially. The increase of computers' processing power in relation with the continuous decrease of cost and size of electronics are some of the main factors that allowed the implementation of such systems in agriculture. In comparison with the traditional systems, 3D sensing techniques ensure:

- Faster data acquisition
- Larger datasets
- More representative data
- Data of high resolution
- Less labour intensive techniques
- New type of data, inconceivable to be obtained before

More specifically, higher temporal resolution data along with increased temporal variability became available. Furthermore, larger datasets with improved quality allowed the acquisition of high resolution spatial data. Manual methods for estimating structural parameters (e.g., leaf area, height, width) or fruit detection were destructive and cost-effective. The implementation of 3D sensing improved accuracy and objectivity of the measurement, since plants could be monitored from different sides, remotely and spatially. Complex parameters (e.g., volume) with less measuring uncertainty as compared to manual measurements became available.

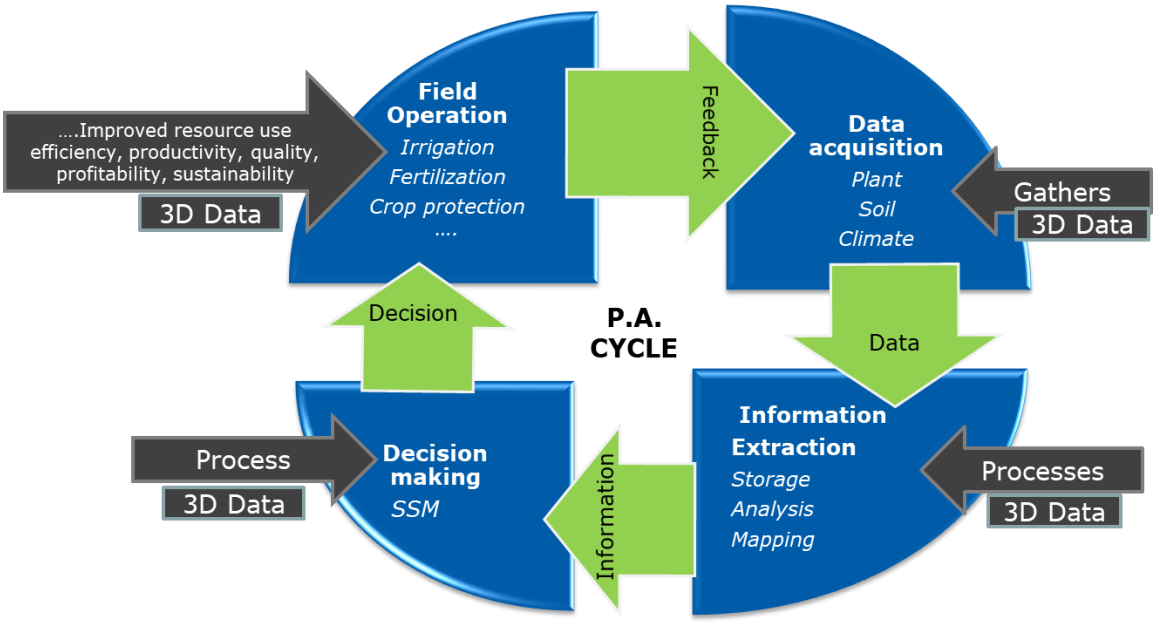

Figure 1. Implementing 3D data in the cycle of precision agriculture (P.A.) (Zhang et al., 2002).

1.4.4. *Time of flight (ToF) sensors in horticulture*

Among others, triangulation and time of flight (ToF) principles are probably the most important techniques of 3D data acquisition in agriculture. Triangulation is a geometrical calculation of a target point in 3D which belongs in a triangle with the other two points are known parts of the measurement system (Vázquez-Arellano et al., 2016). Therefore, depth can be determined. There are digital photogrammetry (passive), structured light (active) (Saudreau et al., 2007; Zhang et al., 2018), shading, focus and theodolite measuring techniques of triangulation (Hsu et al., 2004).

A stereo vision system was used to detect the 3D shape of apples for yield monitoring (Wang et al., 2012). The measurement was carried out at night using ring flashes to illuminate the site, reported problems due to occlusion, specular reflections, colour heterogeneity, and a bias in the shape-from-stereo algorithm that caused the apple location to be estimated closer to the camera. In a different study, the location and size of fruits was determined by a single camera mounted on a robot platform (Mehta and Burks, 2014) . The position of fruit was obtained by transforming the coordinates from the camera to robot base reference coordinate system using extrinsic camera parameters, achieving 15 mm accuracy in estimating the position. Zhao et al. (2012) obtained the 3D shape of zucchini leaves using a light beam triangulation sensor mounted on a 2-D scanning platform, in order to detect the

plant's water stress by tracing its morphological traits. Research on an automatic process for ground vineyard yield estimation by acquiring five images with an off-the-shelf camera and reconstructing the grape clusters at a close range reported that the main constrains concern weather conditions and suggested the use of artificial light and light diffusers to overcome them (Herrero-Huerta et al., 2015). The combination of RGB cameras with depth information was utilized in red sweet pepper, performing 90.9 % of true positive rates under natural light conditions (Vitzrabin and Edan, 2016).

On the other hand, ranging sensors such as ultrasonic, ToF, RGB-D cameras but mostly light detection and ranging (LiDAR) laser scanners are applied in fruit trees. These types of sensors are designed to monitor using ToF principle. More specifically, a range sensing unit consists of a laser source to emit pulsed laser beams and a sensor to receive the beam reflected back from the objects. The time required for the laser beam to reflect back from the objects is proportional to the distance between the object and the sensor (Bufton, 1991; Gokturk et al., 2004) ToF cameras were mounted on a mobile platform and driven along the rows of an apple orchard for fruit detection (Gongal et al., 2015). The error derived from varying lighting conditions was reduced using LED lights, producing an identification accuracy of 79.8 %. The research did not assess absolute location accuracy with this camera system but observed that some of the errors in the system were due to errors in registering 3D location information based on the apples identified in the color camera images. Whereas in sequence of this experiment, the size of apples based on the 3D coordinates from a 3D camera was obtained, resulting in 30.9 % MAE, which dropped to 15.2 % when pixel information from an RGB camera was considered (Gongal et al., 2018). Gene-Mola et al. (2019) used range corrected data capturing color, depth and backscattered reflectance in the near-infrared wavelength range from an RGB-D camera to detect the apple shape at the tree, resulting in 0.89 F1-score and 94.8 % average precision. The authors pointed out that the depth and backscattered reflectance provided the most robust variables in the calibration model, while RGB was highly influenced by light shading in the canopy. In mango, RGB-D imaging enabled the detection of mangoes with 81% precision, and the estimation of the length and width of the fruit, achieving a root mean square error (RMSE) of 4.9 mm and 4.3 mm, respectively (Wang et al., 2017). Both studies were conducted after sunset to achieve consistent lighting conditions. It was noticed that the sensor failed to acquire distance information over 3.5 m. However, ToF cameras available in the market have lower resolution

and are expensive. Data acquisition and processing for 3D localization can be faster with 3D cameras compared to other 3D sensing systems such as a stereovision camera. These cameras are also believed to provide better accuracy in 3D reconstruction as compared to stereovision systems (Beder et al., 2007).

The initial applications of ranging sensors in horticulture, deployed ultrasonic sensors (Giles et al., 1988; O'Connell et al., 2006). The sensors were arranged at different heights along a vertical pole, facing a side of the tree row. Each ultrasonic unit measured its distance to the canopy as the system moved along the row at constant speed for the calculation of height, width and tree row volume (TRV). This system was utilized to control variable rate application in real-time, resulting in spray volume savings up to 52 % in apples, 28 % in peaches (Giles et al., 1988), 30% and 37% in citrus (Moltó et al., 2000). In a similar study, actual tree width measured by the ultrasonic sensorwas used in spray application, reducing by 70 %, 28 % and 39 % the spray deposits in olive, pear and apple orchard, respectively (Solanelles et al., 2006). Moreover, Zaman et al. (2005) developed a real time variable application method of nitrogen fertilizer in citrus, considering the TRV and the nitrogen concentration of leaves, reducing costs by 40 %. However, ultrasonic sensors exhibited lower resolution, higher inaccuracies due to sound divergence or distance within the sensors and slower sampling rate in comparison with LiDAR sensors (Tumbo et al., 2002).

The implementation of LiDAR sensors enabled the detection of structural and geometrical parameters of fruit trees with higher accuracy. The LiDAR sensors, mimicking the arrangement of the ultrasonic, were mounted on a vehicle and moved along the tree rows to generate 3D point clouds. In earlier studies, the structural parameters of apple and citrus trees had been described by simplified geometrical equations (Lee and Ehsani, 2009; Walklate et al., 2002). Rosell Polo et al. (2009), after analyzing the TRV in 3D, obtained a significant correlation with the leaf area in pear trees (R^2= 0.84), apple trees (R^2 = 0.81) and vineyards (R^2=0.80). In a similar experiment, a logarithmic equation was used to describe the relationship of the TRV with the leaf area density (R^2 = 0.89) in pear trees, apple trees and vineyards denoting the reciprocal relation of these two parameters (Sanz et al., 2018). The LAI, which is one of the most widely used indices to characterize grapevine vigor, was well estimated using the TAI (tree area index) from LiDAR scanning (R^2 = 0.91 (Rosell Polo et al., 2009) ; and R^2 = 0.92 (Arnó et al., 2013). Escola et al. (2017) developed tools for point cloud data analysis from the LiDAR-based system which are proposed to extract

further geometrical and structural information, enabling the creation of maps with high spatial resolution. Spatial dependence between soil electrical conductivity and leaf area has been observed in apple trees (N. Tsoulias et al., 2019a). Moreover, the spatial information of leaf area was implemented in a water balance model, revealing variation in water needs according to the soil electrical conductivity zone. In another study, direct root-zone irrigation treatments showed a significant effect on canopy growth in grapevines, due to the high soil moisture content (Tagarakis et al., 2018).

Currently, LiDAR intensity data are being applied for feature extraction, classification, and object detection and recognition on rural and urban areas (Kashani et al., 2015). In forestry applications LiDAR's backscattered reflectance intensity (R_{ToF}) and geometric features such as the linearity (L) and other were used, based on decomposed eigenvalues of the covariance matrix, to discriminate LA from woody parts of trees (Ma et al., 2016; Xi Zhu et al., 2018). Thresholding methodology by means of R_{ToF} and L was proposed to segment and label tree point cloud components as LA or wood (Wang et al., 2018). Beland et al. (2014) suggested a voxel methodology (Béland et al., 2011) to develop thresholds based on R_{ToF} frequency for retrieving the LA per tree. The results are sensitive to voxel size, and the choice of voxel size is influenced by occlusion. Hackel et al. (2016) analysed several geometric features, including L, to extract and select contour surfaces. Their method was based in the eigenvalues, eigenvectors and the angles (e.g. tangle) of points in 3D space. Similarly, Lin et al. (2014) calculated geometric features using a weighted principle component analysis (PCA) a with a geometric median. In each point was assigned a weight to represent its spatial contribution in the weighted PCA and to estimate the geometric median, which can be regarded as a localized center of a certain shape. In fruit production, working in a 3D space allows for the identification of geometric tree features such as shape and size, aiming at fruit localization (Barnea et al., 2016). The spatial distribution of geometric features can be illustrated by the decomposition of the covariance matrix from a set of points in 3D. Brodu and Lague (2012) proposed that the set of points within the spherical neighborhood can be utilized to define whether the geometric structure of points is closer to a line, plane surface, or a random cluster. Several researchers in forestry applications used the method to include reflectance intensity (R_{ToF}) and geometric features such as linearity to discriminate foliage from woody parts (Ma et al., 2016; Xi Zhu et al., 2018) or to estimate leaf angle (Kuo et al., 2019). Whereas in agriculture, Gene-Mola et al. (2019a) proposed

a methodology that combines backscattered reflectance intensity with a geometric factor for spherical shapes based on the eigenvalues of clusters in apple trees to localize the fruits. The method achieved 87.5 % localization success, 82.4 % identification success, and a F1-score of 0.86 in relation to the total number of fruits. Moreover, eigenvalues of geometric data on curvature and linearity have been computed to distinguish cotton balls from branches, achieving 90 % detection accuracy (Sun et al., 2020). Similarly, intensity and geometric features have been exploited to train harvesting robots in greenhouse applications (Lin et al., 2020; Tao and Zhou, 2017).

1.4.5. *Monitoring and mapping yield of apples*

Spatial information of historical yield is essential for analysis and evaluation in precision horticulture. This information indicates regions of the field with different performance, enabling the site-specific management within the orchard (Bramley and Ouzman, 2019). Harvesting machine equipped with flow sensors or hand-held devices, are frequently used for yield mapping. Geographic coordinates are acquired through a GNSS receiver. Rains et al. (2002) used a moving platform equipped with load cells and GPS to acquire the weight and the location of yield in pecans orchard. The collected samples were weighed every second corresponding to 1 m of row. A prototype platformhas been developed in Spain to measure, in situ, the yield and quality parameters (e.g., colour, size) of oranges (González-González et al., 2020). The platform monitored the variables' spatial variability, creating thematic maps in real time. Furthermore, high density olive trees were mechanically harvested when maximum oil content was achieved with harvest efficiency of 92 and 90 % for 'Barnea' and 'Frantoio' varieties and a mean 2.5 % slight damages in the canopy (Ravetti and Robb, 2010). Applications in mechanically harvested vegetables have also been presented: Pelletier and Upadhyaya (1999) developed a yield monitor for processed tomato using load cells under the conveying chains of the machine.

However, most horticultural crops are not mechanically harvested and therefore many customised approaches for specific horticultural crops have been tested for yield mapping. In Florida citrus plantations, Schueller et al. (1999) used a system to weigh palette bins where oranges were collected manually. It was assumed that each bin represented the yield of the surrounding trees, since workers would empty their bags into the nearest bin. Yield

was estimated by dividing the weight by the area covered by each bin. Position and yield were used to prepare yield maps. In a different study adopting a similar approach, Colaço et al., (2020), compared two types of data processing for calculating the yield variability of oranges in Brazil. The two types of data processing tested in this study – one based on the coverage area of each bag and another based on bag distribution across an area – performed similarly in normal field situations. Maps were able to reproduce general spatial variability patterns, but their accuracy varied (between 5 and 11 Mg ha^{-1}) depending on the yield spatial variability. In fact, yield varied spatially even in small citrus orchards (< 3.6 ha) (Peeters et al., 2015; ÜNLÜ et al., 2014).

In the contex of experiments of mapping apple yield, Aggelopoulou et al. (2010) handpicked apples, and placed in 20-kg plastic bins along rows of spindle-formed trees. Each bin was weighed and geo-referenced using DGPS. The bins, corresponding to 5 or 10 trees, were grouped to represent their yield. Similarly, Tsoulias et al., 2021 measured the yield of 500 trees in a conventional apple orchard for two consecutive years. The yield was related to ECa and leaf area at different growth stages in both seasons. Manfrini et al., (2020) observed no effect among the spatial patterns of ECa, crop load and fruit weight, suggesting the necessity of over time spatial plant data to improve site specific management within the orchard. Results pointed to low correlation of elevation, soil ECa and generative plant growth (Käthner and Zude-Sasse, 2015). Despite the correlation of fruit yield and quality with the growth of perennial trees, their spatial interaction during the growth season has been rarely investigated.

The same procedure for yield mapping was also pursued for pears in a small field of less than 1 ha by Vatsanidou et al., (2017). Oldoni et al., (2019) mapped yield in a peach orchard of 1.5 ha size. Selective harvest was performed (n =101), over three consecutive years, by weighting all fruits per tree and recording fruit firmness, TSS, and soil properties. Results showed high spatial variability of yield and quality of peaches, while the TSS was related with the yield. In an different study for the same crop, RFID tags were placed on the collecting bins, while a weighting machine with RFID reader and GPS was used to record weight and position of each bin (Ampatzidis et al., 2009). Similarly, Taylor et al. (2007) used barcodes on bins to monitor yield in kiwifruits. Fountas et al. (2011) monitored yield variation in olive tree orchards. Olives in conventional orchards were picked by hitting fruit branches with sticks. Olives dropped on plastic sheets placed underneath each tree. The olives were placed in bags and categorised in groups where they were filled, for loading on platform. Each bag was weighed and geo-referenced using DGPS.

Each cluster of bags was considered to represent the yield of surrounding trees and was the basis for yield mapping. the previous experimental procedure highlighted the spatial variability on the olive field.

Pozdnyakova et al. (2005) analysed spatial variability of yield in a cranberry plantation. They used 0.3 x 0.3 m frames to measure the number of fruits before harvesting. Using mean berry mass, they estimated the yield. High spatial variability was also observed here. With regard to hand-picked vegetables, Qarallah et al. (2008) developed an impact type sensor for yield mapping of dry onions. The sensor was used in the laboratory to weigh individual bulbs. In another study, a harvesting machine was used for the harvest of carrots, to remove the soil, cut the leaves and place the carrots on the left side of the harvester. Damaged roots or roots that did not fit market standards were removed by experienced collectors, while the rest were placed in plastic boxes measuring 0.30 m × 0.33 m × 0.55 m and with a capacity of 52 L (Wei et al., 2020). The box location was acquired by a GNSS receiver and the yield map was created. Saldana et al. (2006) developed a yield monitoring system mounted on a platform used as a harvesting aid for broccoli. During the harvesting process, four load cells were placed on the lane of the platform to weight the broccoli. Yield variation from 1 to 8 t ha^{-1} was observed. Fountas et al (2015) measured yield of watermelons for two years, dividing the field into blocks and monitoring the yield of each block by weighing the platforms carrying watermelons from each block. At the same time, quality (e.g. maximum penetration force of the fruit flesh) and ECa were measured and mapped, resulting in a positive correlation between the yield, sugar content and the piercing force.

As mentioned above, advances in machine vision have been implemented in precision horticulture allowing for the development of yield prediction systems. Aggelopoulou et al. (2011) demonstrated a positive correlation between image based flower density estimates (using pixel counts of classified flower regions) about individual trees and the measured fruit weight. An autonomous platform has been developed in Australia for measuring plant features and soil parameters in almond trees. The 3D canopy volume calculated by a LiDAR laser scanner of individual trees and was correlated with yield measurements (Underwood et al., 2016). Recently, ground hyperspectral images were combined with a LiDAR laser scanner to count and predict the number of mango fruits (Anderson et al., 2019). The models were validated and tested on hundreds of trees and subsequently mapped. Colaço et al. (2019) observed the spatial relationship of canopy V and height (using a LiDAR) with the historical

yield and soil electrical conductivity (ECa) in three different orange groves. The V was spatially and temporally related to yield and ECa in 2 of the 3 orchards, suggesting that V information can improve the identification of management zones in yield and soil attributes. Recent studies in viticulture showed that vegetative and reproductive growth can have similar spatial patterns with the final yield and ECa at different years but not with the quality parameters of the grape (Tagarakis et al., 2018).

1.4.6.*Management zones*

Upon creation of thematic maps, the next step in precision horticulture is the determination of management zones. The farmers can select which plant parameters should be employed in order to adapt site specific management e.g., pruning, irrigation, fertilization, pesticides, selective harvest.

Several studies have been conducted in arable crops, where variable rate application is employed and management zones can vary in terms of size, shape and location (Gavioli et al., 2016; Haghverdi et al., 2015; Peralta et al., 2015). However, perennial trees require a different approach in the delineation of management zones, due to the stable planting system throughout the years, while morphological adaptation of canopy and root varies according and adapt to the micro-climate and soil properties. Fountas et al. (2011) adopted data fusion from soil characteristics and yield maps in an olive orchard to quantify spatial variation through semivariogram parameters and to apply site-specific fertilization management using two management zones, based on kriging maps. Principal component and fuzzy c-means clustering analyses were used to delineate the management zones in a peach orchard (Oldoni et al., 2019). Yield and fruit quality depicted high spatial variability compared to soil attributes. It was found that the optimal number of management zones for the experimental peach orchard was two and most of the soil and tree attributes exhibited statistical differences in each defined management zone.

Aggelopoulou et al. (2013) used a multivariate approach to delineate management zones in apple trees. The results showed that the spatial patterns of yield and fruit quality (SSC, fruit firmness) were consistent, contributing positively in the delineation of management zones. A similar methodology was suggested for delineating management zones in grapefruits using hot spot analysis to present tree-based data spatially (Peeters et al., 2015). However, Manfrini et al., (2020) observed no effect of the spatial patterns of ECa, crop load and fruit weight, suggesting the necessity of over time series of spatial plant data to improve site specific management within the

orchard. Despite the relation of fruit yield and quality to the growth of perennial trees, their spatial interaction during the growth season has been rarely investigated.

Tagarakis et al. (2013) applied fuzzy clustering in a vineyard to delineate management zones, using ECa, slope, soil depth, NDVI, yield and grape composition as reference parameters. The vineyard was divided in cells, therefore comparing matching cells between zone maps was a useful way to evaluate relationships between soil and production parameters. An ultrasonic sensor was utilized to estimate the tree canopy volume in a citrus orchard, revealing a correlation coefficient of 0.85 with yield and explaining 73 % of its variation (Mann et al., 2011). Therefore, tree canopy volume was used to classify grove productivity into management zones. Colaço et al. (2019) observed the spatial relationship of canopy V and height with the historical yield and soil electrical conductivity (ECa) in three different orange groves. The V was spatially and temporally related with the yield and ECa in 2 of the 3 orchards, suggesting that V information can improve the identification of management zones in yield and soil attributes.

1.4.7. *Decision support systems*

Another technology that contributes to decision making in precision agriculture applications is Decision Support Systems (DSS). The DSS systems utilize computational models and databases to provide information concerning decision making in the context of optimum management (Lindblom et al., 2017). In other words, decision making systems is the connection between the farmer and precision agriculture, converting data into decision (McBratney et al., 2005). Data can derive from a single or various types of sensors as mentioned above, such as satellites, spectral cameras, spatial maps and manual measurements. Several decision support systems have been developed for crop monitoring, plant protection, irrigation scheduling, yield prediction (Rupnik et al., 2019; Zhang et al., 2017). However, research is not successful in the implementation of decision support systems in the field. The lack of functional decision-making tools explains, to a certain extent, why rapid and widespread adoption of precision agriculture is difficult. Kitchen et al. (2005) indicated that more precise crop models in precision agriculture might help in the development of successful decision support systems. The inadequate development of control and decision support systems for implementing PA decisions has been identified as a major stumbling block to the adoption of precision agriculture (McBratney et al., 2005).

1.4.8. *Apple trees*

Apples are the fourth most cultivated fruit crop following citrus types, grapes and bananas. According to FAOSTAT (2019), apple production increased worldwide from 82 mega tones (mt) in 2015 to 87 mt in 2019. More specifically, China was the largest producer with 40 mt, representing 48 % of the total production in 2019. During the same year, the USA was the second largest producer with 5 mt, with Poland and Turkey holding the fourth and the fifth place, respectively, with approximately 3 megatones each. The reason for this development lies in the physiological value of the apple fruit, which is high in vitamin, antioxidant and mineral content. The comparison between countries in terms of the average annual production volume and productivity (Fig. 1) reveals a large difference in the average prosduction per hectare. The reasons for these differences are the diverse climate conditions (Lakso et al., 2001), growing systems (Robinson et al., 1991), and intensities of production.

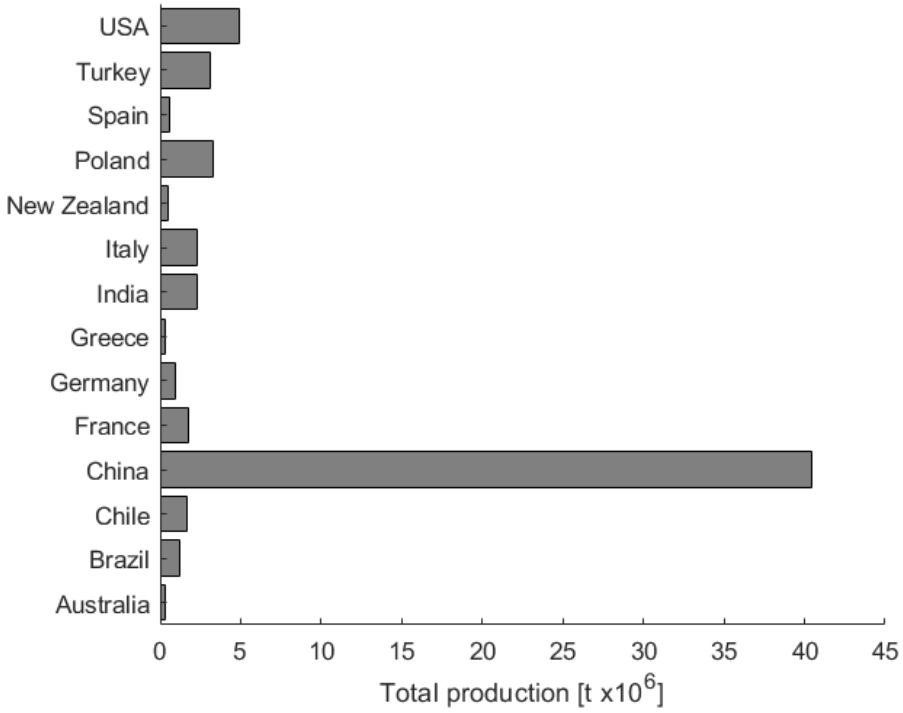

Figure 2: Average apple production (grey bar) of the 14 countries with the world‘s highest apple production (2015-2019). (FAOSTAT; access 22. April, 2021)

The apple belongs to the Rosaceae family and started to be cultivated and popularized in the daily diet about 10,000 years ago. Apples have been classified in the Maloideae subfamily because they produce pome type fruits. They originated from southwest of China, Kazakhstan and Kirgizia, and from there spread via the historic Silk Road to the Near East, and from there through the Greeks and Romans to Europe. Malus *sieversii* is regarded as the major progenitor of the domesticated apple, hybridizing with the M. hupehensis Borkh. (in China), M. baccata Borkh. (in Caucasus), and M. sieboldii (in Asia) and with M. turkmenorum and M. sylvestris Mill. (in Europe (Badenes and Byrne, 2012; Pereira-Lorenzo et al., 2018). However, the number of species in the genus Malus is still not completely defined. Harris et al., (2002) identified 55 species based on the classification of Phillips et al., (1990). Zhi-Qin (1999), classified 30-35 species, whereas 27 primary, 5 secondary species with 11 Malus hybrids have been reported by Forsline et al., (2010). Among others, the most cultivated and developed varieties are: Fuji kikiu, Firiki, Gala Shinga, Gala, Golden Delicious, Granny Smith, Jonagold, Mutsu, Odysseus, Pink Lady, Red Delicious, Red chief, Starking Delicious, Super Red chief. Furthermore, the color (green, red, yellow), toughness, taste or harvest day, are some of the macroscopic characteristics which can be used to distinguish apple varieties.

During the annual life cycle of the apple, the trees alternate between winter dormancy and the vegetative period, which is divided in the following main phases (Meier, 2001):

- Dormancy: leaf buds and thicker inflorescence buds closed and covered by dark brown scales
- Beginning of bud break: first green leaf tips just visible.
- Mouse-ear stage: Green leaf tips 10 mm above the bud scales; first leaves separating.
- Beginning of shoot growth: axes of developing shoots visible.
- Flower buds visible (still closed).
- Pink bud stage: flower petals elongating; sepals slightly open; petals just visible.
- Full bloom.
- Fruit size up to 10 mm; fruit fall after flowering.
- Fruit about half final size.
- Fruit ripe for harvest.

Over the winter period, the buds of the apple tree are in dormancy. A specific number of chill units needs to be accumulated for bud sprouting (bud break) and, therefore, the full bloom date. Flowering lasts for approximately 10 days, and during this period a temperature higher than 15 ^{o}C is required, with the most adequate temperature being 20 - 25 ^{o}C. However, this depends significantly on the micro-climate, the latitude and the variety. Pereira-Lorenzo (2018) mentioned that the full bloom date can vary from 3 to up to 6 months between apple cultivars, classifying them according to the chill unit requirements in six classes, and correlated a shorter rest period with lower growth. Varieties with low chilling hour requirements are usually selected in temperate climate, whereas in areas of adequate winter chilling, cold hardiness is often a concern as is later blooming to avoid spring frosts (Labuschagné et al., 2003). However, global warming, during the last decade, revealed new challenges to apple producers such as new pathogens or sunburn susceptibility.

After pollination and fertilization of the egg cells in each of the ovules at the base of the flower, cell division takes places for 3-4 weeks approximately. Fruit thinning in the latter stage, as well as temperature during development can improve fruit size. After petal fall, the ovary starts to expand, signifying the initiation of the cell expansion period during which the fruit stores metabolites and energy in the form of starch or sugars, continuously increasing until late in the season. The fruit starts to form by gaining weight each day until harvest. The growth rate is influenced by temperature and it usually declines before harvest. The harvest date ranges from middle of August to late October and mostly depends on thecultivar. Finally, the leaves fall in autumn signifying the begin of winter dormancy.

Early stages of cell division and late stages of cell expansion contribute the most in fruit growth as well as in the final fruit diameter (Corelli-Grappadelli and Lakso, 2004; Scorzal et al., 2019). The size of cells has generally little to no impact on fruit size, whereas the opposite applies to cell number (Sablowski and Carnier Dornelas, 2014). An apple measuring 65-70 mm in diameter (average) can reach 50 million cells (Malladi and Hirst, 2010), however the number can vary according to the variety, reaching 37-59 and 54 million cells in Empire and Gala, respectively (Costa et al., 2001; Goffinet et al., 1995). Malladi and Hirst (Malladi and Hirst, 2010) reported that cell expansion rate and consequently final fruit size is determined by cell division magnitude during the first 30 days after full bloom. On the other hand, air temperature is related to the fruit growth rate. More specifically, low temperatures,

at cell division, can lead to small size fruits with low growth rates at cell expansion (Corelli-Grappadelli and Lakso, 2004; Warrington et al., 1999). Furthermore, temperatures above 19 ^{o}C can reduce ovule elongation producing smaller fruits (Tromp and Borsboom, 1994). At the same time, anthocyanin content can be limited by temperatures > 17 °C temperatures (Yamada et al., 1988). Warrington et al. (1999) proved that expansion rates were highly temperature-responsive only during the cell-division 40 days after pollination. Fruit expansion was 10 times greater at a mean temperature of 20 °C than at a mean of 6 °C.

The ratio of fruit length to diameter is usually referred to as fruit shape. However, this ratio is very sensitive to temperature, with more elongated fruits being produced when temperatures as measured by degree days above 5°C between full bloom and harvest are relatively low, and rounder fruits being produced in warmer climates (Westwood, 1978). Desirable elongated shape is a determined parameter in apple marketing and in customer recognition of the variety when choosing an apple to purchase.

Another external quality factor is skin color which is mainly attributed to anthocyanins, i.e., glycosides of anthocyanidins. The final red color of apples is a function of anthocyanins, chlorophylls and carotenoids (Lister et al., 1994). Among other varieties, Gala is distinguished for high anthocyanin pigmentation resulting in red colour strips on the skin. Consumer preference in apple fruits is subjective, however redder fruits are usually chosen because consumers associate their appearance to a better internal quality and higher sugars, a fact confirmed by quality analyses (Hamadziripi et al., 2014). A profound environmental factor that stimulates the anthocyanins in fruit skin is the integral of sunlight irradiation and the time this irradiation takes place. Red coloration development is improved under cooler temperatures. Anthocyanin accumulation in fruit skin is highly depended on the carbohydrates sink. However, global warming during the past decades resulted in high temperatures and consequently increased respiration loss of carbohydrates, suppressing the pigment development (Red blush). Additionally, enhanced temperatures in sub epidermal tissues or the outer surface of fruit can be the cause for sunburn susceptibility in apples (Ranjan et al., 2020). An evaporative cooling approach that uses overhead sprinklers to wet the fruit is a widely adopted strategy that assists in manipulating the canopy climate and reducing fruit surface temperature in apple orchards (Evans, 2004; Iglesias et al., 2002; Li et al., 2014).

As fruit matures, starch is converted into sugars which is a driven factor of internal quality of apples for consumer preference. Usually, it is expressed in total soluble solids (TSS), total acidity or TSS to acidity ratio using instruments e.g., refractometer or chemicals methods (i.e., colourimetric assay, gas-liquid chromatography) (Nath et al., 2014). TSS, acidity and firmness measurements can predict consumer acceptability, reflecting a significant variation of sweetness perception by consumers (Hoehn et al., 2003). This variation is significantly affected from fruit position on the tree, for example TSS from outer canopy in 'Starking', 'Golden Delicious' and 'Granny Smith' fruit was consistently higher over two growing seasons than from inner canopy fruit (Hamadziripi et al., 2014). In contrast, the structure and geometry of the inner canopy establishes microclimatic conditions with lower temperature and light intensity influencing negatively fruit quality (Musacchi and Serra, 2018). Fruit acidity affects taste perception and therefore stands as an important component of organoleptic quality in apple (Etienne et al., 2013; Khan et al., 2013). Similarly, fruit position within the canopy and exposure in sunlight affects the content of acidity in apples. In other words, malic acid (main organic acid in apples) in fruit flesh can be higher in apples situated in the outer canopy compared to fruits found in the inner canopy (Feng et al., 2014). On the other hand, inner canopy 'Starking', 'Golden Delicious' and 'Granny Smith' fruit had higher TA compared to fruit in the outer canopy during one growing season, with no differences being observed between the two canopy positions in another year (Hamadziripi et al., 2014).

Texture is usually evaluated by trained panels on sensory evaluation methods and combined with instrumental measures. Apple firmness, juiciness and absence of mealiness are the most preferred textural traits by consumers (Brookfield et al., 2011). Flesh firmness is usually measured by a penetrometer, or pressure tester, a device that measures the resistance of the peeled flesh to the penetration of a metal probe (approx. 8 mm depth,). Recently, non-destructive methods have been introduced for fruit quality assessment in order to evaluate a greater number of fruit samples over time (Zude et al., 2006) and speed up the sorting step, eliminating undesired fruits (Abbott, 1999). In respect to firmness, the majority of non-destructive methods consist of acoustic methods (Kim et al., 2009). Another non-destructive technology is hyperspectral scattering imaging based on NIR spectroscopy (Wang et al., 2012).

2. Objectives

The aim of this study was to contribute to the methodology for extracting tree structural parameters and apply the methods for assessing the spatio-temporal responses of apple trees in the orchard. In order to accomplish this aim, the following objectives should be fulfilled.

.

- Enabling the detection of tree positions and tree segmentation in commercial apple orchard by means of 3D point cloud, and validate the method by assessing the LiDAR uncertainty on a portable instrumentation in field conditions.
- Analysis of individual tree point clouds by estimating structural parameters accuracy of singularized tree.
- Enabling the measurement of LA by means of 3D point cloud obtained with terrestrial LiDAR system.
- Quantifying the impact of LA in daily tree water needs in different ECa areas of an orchard.
- Investigating the seasonal growth of LA and volume in commercial apple orchard, and evaluate their response to ECa.
- Analyzing the effect of LA and ECa as determinants for predicting fruit quality.
- Detecting 3D apples points based on reflectance and geometric features in foliated and defoliated trees.
- Development of a fruit segmentation methodology for measuring fruit size in defoliated trees at different growth stages, and evaluate the accuracy of this methodology on foliated trees.

3. Materials and Methods

3.1. *Site description*

The study was conducted in two apple orchards: the experimental station of ATB (0.5 ha) in Marquardt (Latitude: 52.466274° N, Longitude: 12.57291° E) and in three commercial orchards located in Altlandsberg (3 ha) (Latitude: 52.607340° N, Longitude: 13.816763° E), in Markendorf (1 ha) (Latitude: 52.283° N, Longitude: 4.458° E), and in Glindow (Latitude: 52.923 ° N, Longitude: 10.576° E), in the region of Brandenburg, in Germany. The experimental field was planted with *Malus* x *domestica* Borkh 'JonaPrince' and 'Gala' in 2015, whereas the commercial orchards were planted only with the latter cultivar in 2014. Furthermore, 'Red Idared' pollinator trees each on M9 rootstock with 0.95 m distance between the trees were used in both fields. The trees were trained as central leader at spacing of 3.5 m x 1.10 m (36 rows), 3.3 m x 0.9 m (20 rows), 6m x 1m (24 rows), and 3.2 m x 0.95 m (12 rows) in Altlandsberg, in Markendorf, in Glindow, and Marquardt, respectively. All orchards were drip irrigated (max. 2 L $tree^{-1}$ d^{-1}) and managed according to the national regulations of integrated production. The experimental and the Altlandsberg orchard were located on a 3 % slope with southeast orientation, whereas an 8% slope with northeast orientation was observed in Markendorf.

The cultivation treatments carried out by the farmer were similar for each year. The time of application of the cultivation treatments varied by a few days from one year to another, depending on the weather conditions and the tree development. The cultivation tasks of the year would start between late November to early February with pruning. At the same time, removal of suckers, dead, damaged, or diseased shoots took place, while young shoots mounted through the horizontally parallel wires. To achieve variation in the number of fruit per tree in order to explore the model, each year, 60 of the selected trees were hand thinned to low (≈60 fruit $tree^{-1}$), medium (≈100 fruit $tree^{-1}$) and high (≈140 fruit $tree^{-1}$) crop loads. All trees were thinned with ammonium thiosulphate (20 % N; 15 kg ha^{-1}) at full bloom and with 6-benzyl adenine (500 g ha^{-1}) three weeks after full bloom. Soil fertilization was applied 4-5 weeks (early February) before bud break. At the same time, fungicides for the prevention of downy and powdery mildew were applied immediately after bud break. Typically, five applications were carried out till the beginning of apple ripening (early August). Weed control and soil aeration between the trees was carried out

manually, on a regular basis, at the experimental station, whereas in the commercial orchard the same cultivation tasks were performed only after full bloom.

3.2. *Soil sampling*

Soil electrical conductivity is a well-suited parameter for precision agriculture applications using the indirect method of electrical resistivity (i.e., Wenner array) to determine in-field soil properties. The electrical resistivity method introduces an electrical current into the soil through current electrodes (C1, C2) placed at the soil surface and the difference in current flow potential is measured using potential electrodes (P1, P2) that are placed in the vicinity of the current flow (Corwin and Plant, 2005) (Figure 3). Resistivity varies according to soil texture and moisture. In a hypothetical case of homogenous soil, the current flow would be radially emitted from the current source, generating equipotential surfaces perpendicular to the current flow lines and forming half spheres. In real conditions, the variation of soil texture and moisture differentiates the current flow lines, forming a more uneven pattern of equipotential lines as the current flow lines will bend at boundaries, where resistivity changes.

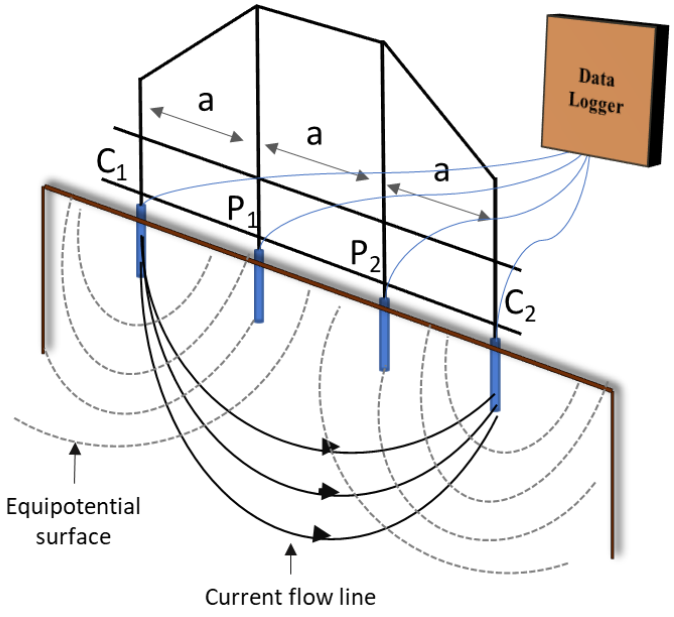

Figure 3. Schematic of Wenner array working principle

.

The four electrodes in a straight line configuration is typically referred to as Wenner array configuration. The electrodes are equidistantly spaced (Figure 3) parallel to the soil surface. As mentioned above, the two outer

electrodes (C1, C2) serve as the current or transmitter electrodes, whereas the two inner electrodes serve as the potential or receivers electrodes (P1, P2). The depth of investigation is defined by the inter-electrode spacing (a). It was set to 50 cm, which corresponds to an investigation depth of 25 cm. The measurements provided soil resistivity (Eq. 1), which were converted to ECa (Eq. 2).

$$\rho = 2\,\pi\,m\,\frac{\Delta V}{I} = 2\,\pi\,m\,R \tag{1}$$

$$ECa = \frac{1}{\rho} \tag{2}$$

where ρ represented soil resistivity (Ω m), m electrode spacing (m), ΔV difference of voltage (V), I current (A) and R resistance (Ω). The reciprocal of ρ was utilized to calculate ECa (mS m^{-1}). Data were obtained for every third tree and every second row, the values were saved by the data logger (4-Point Light, LGM, Schaufling, Germany) and analyzed in ArcGIS (10.2.2 ESRI, USA). Several studies suggest that ECa and texture relations are more stable and prevalent when soil water content is at field capacity (Auerswald et al., 2001; McCutcheon et al., 2006; Taylor et al., 2003). Therefore, the measuring date of ECa determined according to the soil moisture that derived from the weather station. The measurement was conducted each year and only in the commercial apple orchards. Specifically, in Markendorf (n = 338) and Glindow (n = 460) the measurement was conducted only after full bloom in 2018. In the case of Altlandsberg, ECa was sampled at full bloom (n = 432) and harvest (n = 425) in 2018, whereas in the following year the measurement was repeated only at full bloom (n = 435). Moreover, the elevation [m] of the Markendord orchard was acquired utilizing the RTK-GNSS system (Tagarakis et al., 2018).

After calculating the ECa map, 10 sampling locations covering the range of ECa values within the orchard were selected in Altlandsberg. Samples were collected at a 30 cm depth using an Edelman combined soil sampler. The samples were analyzed using the sedimentation method, which is based on the different settling time of different-sized particles defined as clay, silt, and sand, which make up the soil texture (Taubner et al. 2009).

Soil sampling was carried out in 10 locations guided by the range of the ECa data in Glindow in 2017. From the results of soil texture analysis, the field capacity (FC) and the wilting point were derived based on the proposed

values for typical soils in Germany (Sponagel et al., 2005). On 60 additional soil samples, cores were retrieved at 30 cm and subjected to oven-drying for 2 days at 105 °C in order to analyze bulk density and porosity(Cater et al., 2007).

3.3. *Light detection and ranging (LiDAR)*

In this study, a mobile terrestrial light detection and ranging (LiDAR) laser scanner (LMS-511, Sick AG, Waldkirch, Germany) was used to scan both sides of each individual row within the orchards (Figure 4). The LiDAR is an optical non-contact laser scanner sensor that scans the surrounding perimeter radially on a single plane using light pulses. The sensor measures in two-dimensional (2D) space in radial coordinates. The scanner's measurement method is based on the time-of-flight (ToF) principle (Figure 4). A microcontroller sends two timed pulses: a control pulse to the laser control circuit and a start pulse to the time-to- digital converter. The laser control circuit controls the laser emitter, which starts emitting the laser beam pulse. If a laser beam emitted is reflected by a target object, it returns to the photo-detector. A circuit converts the signal from the detector into a logic signal sent to the time-to- digital converter, which stops the time measurement. Thus, the position of the object is given in the form of distance and angle. A clock in the sensor's processor measures the timestamp between the transmitted and the reflected beam. The time between the emission and the reflection of the beam is proportional to the distance between the scanner and the objects. The laser beam is rotated in a specific range by an internal rotating mirror.

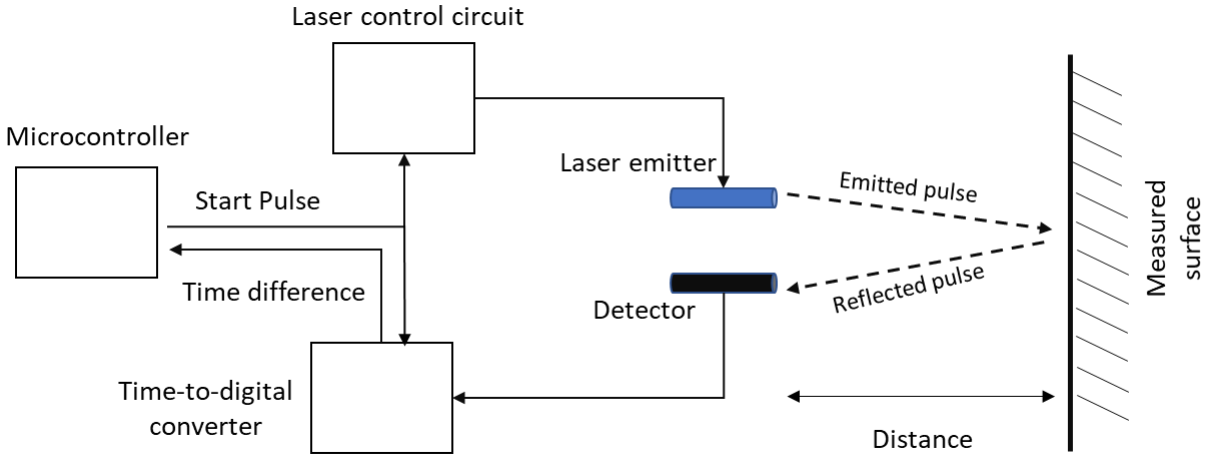

Figure 4. Overview of Time of (ToF) flight principle.

A rigid aluminium sensor-frame carrying the sensors (Figure 5a) was mounted on the three-point-hitch (front or rear) of a tractor. The LiDAR laser scanner was mounted at 1.6 m above the ground level, which corresponded to the middle height of the trees. The sensor frame was driven along the rows on both sides of the trees with an average speed of 0.13 m s^{-1}. The three-dimensional tilt of the tractor was monitored by an inertial measurement unit (IMU) MTi-G-710 (XSENS, Enschede, Netherlands), which was placed 0.24 m aside from the LiDAR. The accuracy of the sensor was 1.0° root mean square error (RMSE) for the heading at static and dynamic mode, and 0.25° RMSE and 1.0° RMSE for both pitch and roll in static and dynamic mode, respectively (Xsens Technologies, 2014). The measured data were georeferenced by an AgGPS 542 RTK-GNSS (Trimble, Sunnyvale, CA, USA) mounted at a 1.74 m height. The horizontal accuracy of the RTK-GNSS was ± 25 mm + 2 ppm and the vertical ± 37 mm + 2 ppm.

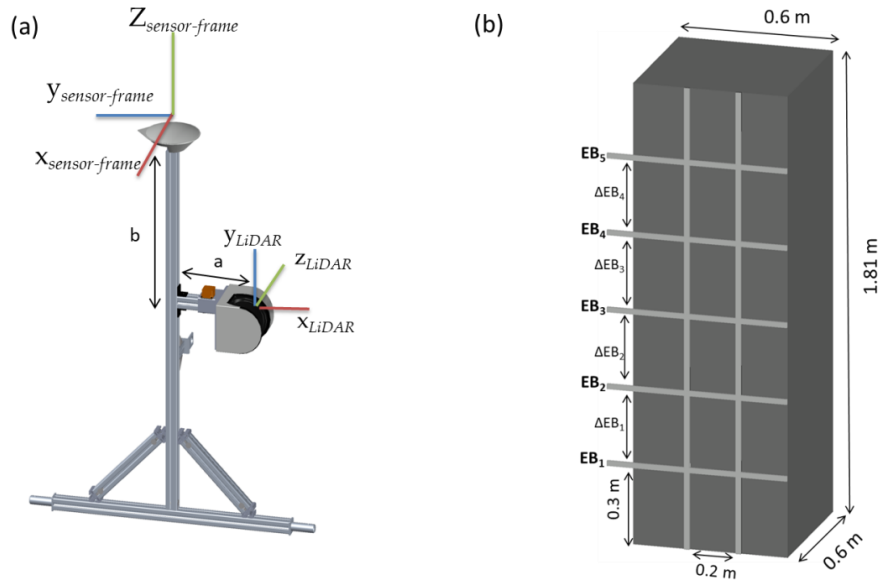

Figure 5. (a) Representation of the sensor-frame system showing the coordinate system of LiDAR and RTK-GNSS. (b) Metal box of known distances.

Two digital filters were activated to optimize the measured distance values: a fog filter that could not be avoided according to the manufacturer's setting; and a N-pulse-to-1-pulse filter, which filtered out the first reflected

pulse in cases where two pulses were reflected by two objects during a measurement (Table 1). The sensor was configured with a 0.1667° angular resolution, 25 Hz scanning frequency and a scanning angle of 190°.

Table 1. LMS 511 specification data.

Functional Data	General Data
Operating range: up to 10 m	LiDAR Class: 1 (IEC 60825-1)
Scanning angle: 190°	Enclosure rating: IP 67
Scanning frequency: 25 Hz	Temperature range: -40 ℃ to 60 ℃
Systematic error: ± 25 mm	Light source: 905 nm (near infrared)
Statistical error: ± 6 mm	Total weight: 3.7 kg
Angular resolution: 0.1667°	Laser beam diameter at the front screen: 13.6 mm

3.3.1. *Sensor Frame Analysis*

Mounting the sensors on the metal frame allowed us to measure the distances and angles between the sensors with high precision, which were utilized as inputs in point cloud reconstruction. However, uncertainty can be derived by the movement of the tractor on the soil and the vibration of the engine. Therefore, error analysis is an important factor in the calibration of a LiDAR system to establish the validity of the measurements. The calibration can be established by studying the systematic (biases) and random (uncertainty) errors of the LiDAR system on surfaces of known dimensions and material. Thus, a metal box measuring 1.81 m × 0.60 m × 0.60 m was constructed to validate the measuring uncertainty of the sensor-frame system (Figure 5b). Five bars were placed horizontally on the metal box at a 0.3 m distance from each other. The sensor-frame mounted on a tractor was applied to scan each side of the box separately at a speed of 0.13 m s^{-1}. The measurements were carried out next to the apple trees in order to simulate the real-world operating conditions.

The measured objects, hit by the laser beam, were assumed to be perfectly diffuse reflectors (Lambertian), excluding the influence of incidence angle (Calders et al., 2015; Dassot et al., 2012). Thus, the apparent signal was considered as an approximation of hemispherical reflectance. Board targets (Figure 6), coated with white barium sulphate ($BaSO_4$, CAS Number: 7727-43-7, Merck, Germany) for maximum referencing (R_{max}) and blackened urethane (S black, Avian Technologies, New London, NH, USA) for minimum (R_{min}) referencing were applied to calibrate the backscattered intensity (R_{ToF}) of the LiDAR, obtaining the R_{ToF} [%] at 905 nm for each point in the

3D point cloud (Eq. (3)).

$$R_{ToF} = \frac{R_{measured} \; R_{min}}{R_{max} - R_{min}} \tag{3}$$

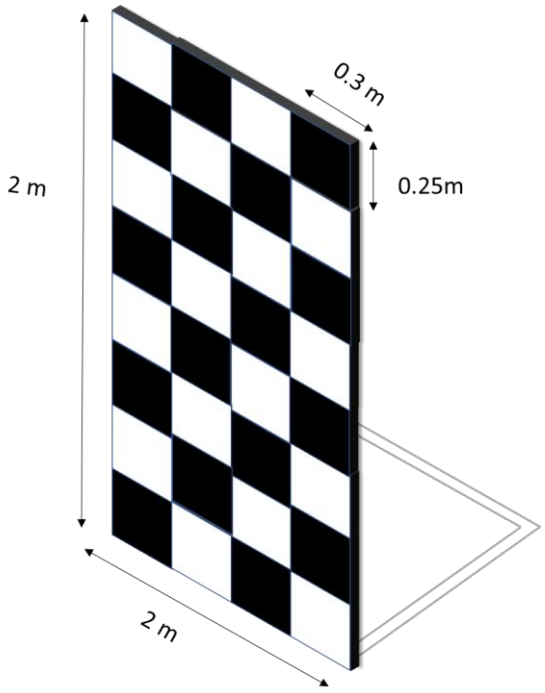

Figure 6. Schematic of board target coated with barium sulphate and blackened urethane.

The LiDAR sensor RTK-GNSS and IMU were connected to a computer for data management and storage (Figure 7). The 12 Vdc tractor battery supplied power to the LiDAR laser scanner using a 12Vdc to 24 V DC converter. USB ports were used to connect the RTK-GNSS receiver and the IMU to the computer, and an ethernet port was used for the LiDAR sensor. Software with multi-thread architecture was developed in Visual Studio (version 16.1, Microsoft, Redmond, WA, US) in order to acquire the sensor data. Parallel data acquisition was achieved by creating a dynamic thread for every connected sensor. Consequently, when the raw sensor data were read by each thread, the corresponding measurement and the time stamp from the real-time clock (1 ms resolution) were assembled into a text string. The string was stored in a text file for post-processing. The multi-threaded data acquisition of the sensors resulted in non-concurrent measurements. Therefore, the cubic spline interpolation

method was used before synchronizing time instances, based on their individual timestamps.

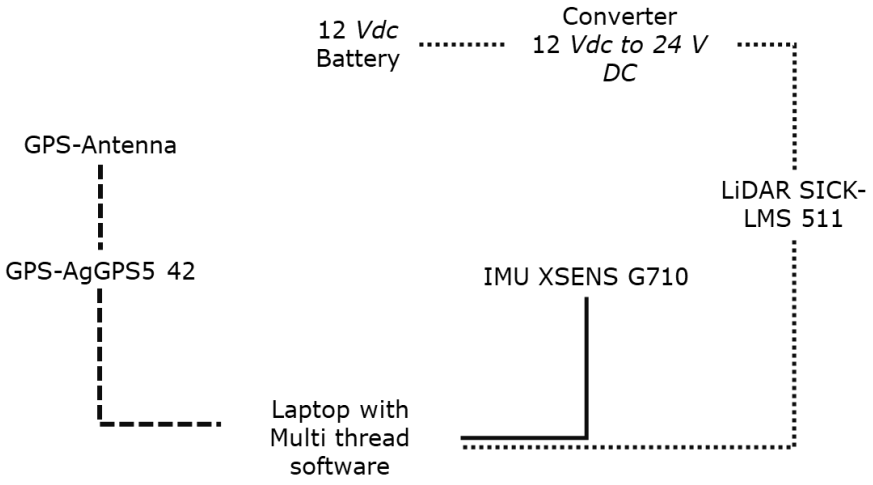

Figure 7. LiDAR, GPS receiver and computer. Scheme of communication. The dotted line indicates the connectivity of LMS 511 LiDAR with the power supply and the computer, the solid and dashed lines show the corresponding USB connections of IMU and RTK-GNSS with the computer.

3.3.2. *Acquisition dates*

Calibration of the sensor frame in real conditions and stem detection were performed at the end of fruit cell division in the experimental station of ATB located in Marquardt during early July of 2018. In the same field, data were recorded during fruit growth starting when the end of the cell division stage of fruit was reached and the cultivar-typical red blush colour (Sadar et al., 2013) appeared and on three subsequent dates, i.e., 42, 72, 104, and 120 days after full bloom ($DAFB_{42}$, $DAFB_{72}$, $DAFB_{104}$, $DAFB_{120}$, respectively) in 2020. On each measuring date, two apple trees (n = 8) were initially scanned with leaves (T_L) and then the measurement was repeated with the plants defoliated (T_D). After scanning, the total number of apples on the tree was counted. After harvest, the fruit's diameter (D_{Manual}) was manually measured in the lab. All apples of each tree were categorized according to their growing position on the slender spindle. The wires (W) were used as borders to discriminate the apples between the ground and W_1 ($\Delta W_{1\text{-}G}$); W_1 and W_2 ($\Delta W_{2\text{-}1}$); W_2 and W_3 ($\Delta W_{3\text{-}2}$); W_3 and W_4 ($\Delta W_{4\text{-}3}$).

On the other hand, the LiDAR sensor frame was used in Altlandsberg during 2018 and 2019. The trees were first scanned 10 days after bud break ($DABB_{10}$) during the stage of green tip, during the initiation of the emergence

of leaves, with further data being recorded when the end of the cell division stage of fruit was reached and the cultivar-typical red blush colour (Sadar et al., 2013) appeared, i.e. 55, 85, 115, and 140 days after budbreak ($DABB_{55}$, $DABB_{85}$, $DABB_{115}$, $DABB_{140}$, respectively). On each measuring date, four apple trees (n = 4) were manually defoliated to investigate the relation between the points per tree (PPT) and the leaf area (LA_{Manual}). The trees were scanned before and after defoliation. The leaves were measured with a desktop scanner (Scanjet 4850, HP, USA) and their surface as estimated by counting the green pixels was analyzed, considering pixels per leaf, with a script written Matlab script (2018b, Mathworks, Natick, MA, USA). An area of 6241 pixels in the image equaled an area of 1 cm^2.

In Markendorf, measurements were obtained from every second row of trees (n = 1109). A cylindrical boundary was projected around the estimated stem positions to segment each individual tree as proposed in sub-chapter 2.5.7 (N. Tsoulias et al., 2019b). Subsequently, V_{LiDAR} spatio-temporal variability of the segmented tree point clouds was estimated during full bloom ($V_{LiDAR, FB}$), fruit set ($V_{LiDAR, FS}$) and before harvest ($V_{LiDAR, BH}$). The measurements of $V_{LiDAR, FB}$, $V_{LiDAR, FS}$ and $V_{LiDAR, BH}$ were carried out 10, 31 and 81 days after full bloom (DAFB), respectively.

Table 2. Corresponding phenological dates on LiDAR type of measurement in each field. Days after full bloom (DAFB), Days after bud break (DABB).

Field	Phenological Stage (DAFB-DABB)	Measurement (Year)
Marquardt	Cell division ($DAFB_{52}$)	Stem detection-Frame calibration (2018)
	End of Cell division ($DAFB_{42}$)	
	Cell expansion ($DAFB_{72}$)	Fruit detection (2020)
	Fruit ripening ($DAFB_{105}$)	
	Harvest ($DAFB_{120}$)	
Altlandsberg	Cell division ($DABB_{55}$)	Leaf area model-Growth analysis (2018-2019)
	Cell expansion ($DABB_{85}$)	
	Fruit ripening ($DABB_{115}$)	
	Harvest ($DABB_{140}$)	
Markendorf	Full bloom ($DABB_{10}$)	Volume growth analysis (2018)
	Fruit set ($DAFB_{31}$)	
	Before harvest ($DAFB_{81}$)	

3.4. *Weather data*

The meteorological data were recorded by the weather station (IMT 280, Pessl, Austria) located inside the commercial orchards. The station recorded air temperature (T), relative humidity (RH), wind speed (u), solar radiation (R_n) and stored all data in the database http://technologygarden.atb-potsdam.de. The potential evapotranspiration (ET_0) was estimated according to Penman–Monteith equation, (Eq. (4)).

$$ET_0 = \frac{0.408\ s\ (R_n - G) + \gamma \frac{900}{T_m+273}\ u(e_s - e_a)}{s + \gamma\ (1 + 0.34\ u)} \quad (4)$$

with the daily net radiation at the surface [R_n (MJ m^{-2} day)], soil heat flux [G (MJ m^{-2} day)], which was assumed to be zero on the daily scale (Allen et al. 1998), and daily average air temperature [T_m (°C)] (Eq. (5))

$$T_m = \frac{(T_{max} + T_{min})}{2} \quad (5)$$

with T_{max} and T_{min} representing the maximum and minimum daily air temperatures, respectively, the average wind speed at 2 m above the surface [u (m s^{-1})]; the saturation vapour pressure [e_s (kPa)] and the actual vapour pressure [e_a (kPa)]. Additionally, γ represented the psychrometric coefficient (kPa °C^{-1}) and s (kPa °C^{-1}) was the slope of the saturation vapour pressure at T_m. The estimates of the net radiation and the aerodynamic terms were based on the FAO-56 paper (Allen et al. 1998).

3.5. *Soil available water content*

The ET_0 (mm day^{-1}) provided by the weather station was multiplied with the soil water stress co-efficient (K_s), the basal crop coefficient (K_{cb}) and added in the soil surface evaporation coefficient (K_e) for the calculation of the crop evapotranspiration (ET_c), as proposed FAO-56. Two cases of ET_c were tested in the present study (Eqs. (6)-(7)) which were obtained by considering, (i) the reference data tabulated in FAO (Allen et al. 2005) for the entire orchard and (ii) the leaf area based on the LiDAR data ($ET_{C,\ LiDAR}$) as shown below.

$$ET_{C,RF} = (K_{s,RF}\, K_{cb,RF} + K_e)\, ET_0 \quad (6)$$

$$ET_{C,LA} = (K_{s,RF}\, K_{cb,LA} + K_e)\, ET_0 \quad (7)$$

The basal crop coefficient $K_{cb,RF}$was estimated according to the tabulated values from FAO ($K_{cb,RF}$) (Allen et al., 1998), and based on the leaf area values derived from the LiDAR ($K_{cb,LiDAR}$). Changes in vegetation and ground cover mean that the K_{cb} varies during the growing period. According to FAO (Allen et al., 1998) K_{cb} trend can be described by minimum three values during the season. Therefore, the K_{cb} was in all cases calculated for three phenological stages: The value for the initial-season ($K_{cb,ini}$) from bud break till full bloom, for mid-season ($K_{cb,mid}$) from full bloom till harvest period and for end-season $K_{cb,end}$ from harvest period till defoliation.

During the initial season ($K_{cb,ini}$), the constant value of 0.8 was used, as suggested by FAO (Allen et al., 1998; Paço et al., 2012), and applied in all cases ($K_{cb,RF}$, $K_{cb,LA}$). The tabulated values were utilized for $K_{cb,RF}$, from cell division till harvest, set at 1.20 ($K_{cb,mid,RF}$) and from harvest till leaf drop at 0.85 $K_{cb,end,RF}$, respectively (Allen et al. 1998; Table 12). However, for the stages after full bloom, the values were adjusted to the local crop parameters and daily climatic conditions (Allen et al., 1998) for $K_{cb,LA}$ (Eqs. (10)(11)).

$$K_{cb,full,mid} = K_{cb,mid,RF} + [0.04\,(u-2) - 0.004\,(RH_{min} - 45)]\,\left(\frac{h}{3}\right)^{0.3} \quad (8)$$

$$K_{cb,full,end} = K_{cb,end,RF} + [0.04\,(u-2) - 0.004\,(RH_{min} - 45)]\,\left(\frac{h}{3}\right)^{0.3} \quad (9)$$

$$K_{cb,mid} = K_{c,min} + (K_{cb,full,mid} - K_{c,min})\,(1 - e^{0.7\,LA}) \quad (10)$$

$$K_{cb,end} = K_{c,min} + (K_{cb,full,end} - K_{c,min})\,(1 - e^{0.7\,LA}) \quad (11)$$

Where u was the wind speed, RH_{min} was the mean daily minimum relative humidity (%) for initial-season, mid-season, end-season, as recorded by the weather station. Whereas h was the mean crop height of 3 ± 0.5 m. In the case of Pinova field in Glindow, the manually measured range of leaf area (LA) has been implemented (Eqs. (10)(11)). Whereas, in Gala orchard in Altlandsberg, the estimation of LA derived from the LiDAR system. The duration of the phenological stages for Gala and Pinova apple trees was set for a deciduous orchard of low altitude; the initial period lasted 23 days after bud break, mid-season 190 days, and end season 60 days.

3.6. *RAW irrigation thresholds*

The soil water stress coefficient (K_s) used in Eqs. (6)-(7), and the total (TAW) and readily available soil water content (RAW) for high depletion of water from the root zone (D_r), with $D_r > RAW$ (Pereira et al., 2015) were calculated according to Eqs. (12):

$$K_{s,RF} = \frac{TAW_{RF} - D_{r,i}}{TAW_{RF} - RAW_{RF}} \quad (12)$$

with

$$D_{r,i} = D_{r,i-1} - (P_i - RO) - I_i\, ET_{c,i} + DP_i \quad (13)$$

$$DP_i = P_i + I_i - ET_{c,i} - D_{r,i-1} \quad (14)$$

The adopted variables captured the depletion of water in the root zone $D_{r,i}$ expressed daily by an estimation (mm) (Eq (13)), the water content in the root zone at the end of the previous day [$D_{r,i-1}$ (mm)], the precipitation on day i [P_i (mm)], the runoff from the soil surface on day i [RO_i (mm)] was assumed zero, the net irrigation depth on day i that infiltrates the soil [I_i (mm)]. The irrigation events took place early in the morning, with 6 mm per day regardless of the actual weather conditions. DP_i (mm) was the water loss out of the root zone by deep percolation on day i calculated only during high precipitation (Eq. (14)**Σφάλμα! Το αρχείο προέλευσης της αναφοράς δεν βρέθηκε.**). $D_{r,i}$ was recorded for each of the sampling points according to guided sampling derived from soil ECa, considering ECa_{Low}, ECa_{Mid}, ECa_{High}.

and with

$$TAW = 1000\ (\Theta_{FC} - \Theta_{WP})\ Z \quad (15)$$

TAW (mm) was the total available soil water for the root zone assuming field-homogeneous root depth of 1 m. The volumetric water content at field capacity [Θ_{FC} ($cm^3\ cm^{-3}$)] was set according to the German soil classes (Sponagel et al., 2005) based on the soil particle size distribution measured. The Θ_{WP} was the volumetric water

content (cm^3 cm^{-3}) at wilting point (WP) that was assumed − 1.5 MPa, Z is the average root depth for the apple trees as indicated by FAO with 1 m (Eqs. (15)).

and with

$$RAW = p\ TAW \tag{16}$$

$$p = p_{tab}\ 0.04\ (5 - ET_{c,i}) \tag{17}$$

RAW (mm) (Eq. (16)) represented thresholds for water stress. It was estimated on a daily basis according to the soil texture analyses. Consequently, three thresholds were considered in the spatial water balance as shown below. The average fraction of TAW that can be depleted from the root zone before moisture stress occurs was p (Eq. (17)), where p_{tab} equaled a constant value as recommended by Allen and co-workers (Allen et al. 1998).

The estimation of K_e takes place when the soil starts to dry. In other words, when the daily cumulative depth of water depleted from the surface ($D_{e,i}$) exceeds readily evaporable water (REW). This can be defined by the soil evaporation reduction coefficient (K_r) (Eq. (18)). REW was at 8 [mm], (Allen et., al., 1998; table 12). TEW (Eq. (19)) is the maximum evaporable water, which was defined according to the soil texture analyses. Furthermore, Z_e is the depth of soil that can be dried from evaporation, which was 16 [mm] (Allen et., al., 1998; table 12).

$$K_e = K_r\ (K_{cb,full,max} - K_{cb,mid,end}) \tag{18}$$

$$K_r = \frac{TEW - De,i}{TEW - REW} \tag{19}$$

$$TEW = 1000\ (\Theta_{FC} - \Theta_{WP})\ Z_e \tag{20}$$

Consequently, two ET_c cases were implemented in the water balance (WB) of the orchard, field-homogeneously (WB_{RF}) and considering the spatial variability of plant data (WB_{LA}) in the low, mid, and high ECa regions. Initially, the range of LA found were implemented in model for calculating the WB_{LA} [mm] in the Pinova orchard. As, in Gala orchard, the estimation of WB_{LA} was based on LiDAR values and compared with the WB_{RF} according to the tabulated values from FAO (Eqs. (21)-(22)). P is the daily precipitation [mm].

$$WB_{RF} = ET_{c,\,RF} - P \quad (21)$$

$$WB_{LA} = ET_{c,\,LA} - P \quad (22)$$

3.7. *Yield*

For yield mapping, the apples were harvested manually (n = 120) and placed in plastic bags in 2018 and 2019. The plastic bags were transferred in the sorting line where the fruit number and the weight for each tree was determined (Kg tree $^{-1}$). The production of ten trees was weighed and the geographical position in the middle point of the ten trees was recorded using the RTK-GPS.

3.8. *Quality*

The position of sample trees was recorded with RTK-GNSS. For fruit quality analysis, 20 apple trees were selected in low, middle and high ECa regions (n = 60), and 10 apples were harvested from each tree on the four measuring dates (n = 2400) for each year. The fresh mass (FM) [kg] was measured by weighting each fruit from all sample trees. Soluble solids content (SSC) [%] was analysed, from juice squeezed of each fruit, with digital refractometer (Pal-1, Atago, Tokyo, Japan). Fruit diameter (D) [mm] was measured considering height and mean of two diameters for each fruit. The FM dataset was equally partitioned in three categories, between 0.01 and 0.09 kg as low, from 0.09 to 0.13 as mid and from 0.13 kg to 0.32 kg as high. The D dataset was analysed separately according to the market price data, between 40 and 65 mm as low, from 65 to 75 as mid and from 75 mm to 90 mm as high. Whereas the SSC dataset was equally divided in categories (Harker et al., 2008) 8 % - 10 % classified as low, 10 % - 11.5 % as mid, and 11.5 % - 13.5% mm as high quality.

3.9. *Data analysis*

3.9.1. *Point cloud reconstruction*

The field data was processed using mainly the Computer Vision System ToolboxTM of Matlab (2017b, MathWorks, Natick, MA, USA) and the function of the statistical outlier filter (SOR) and cloud to cloud distance (C2C) of CloudCompare (EDF R&D) for point cloud processing.

LiDAR data were filtered to consider only those detections with distance measurements between 0.05 m and 4.00 m since these were corresponded to average tree width. The resulting detections were transformed from polar to Cartesian coordinates (x_{LiDAR}, y_{LiDAR}, z_{LiDAR}). The 3D dynamic tilt orientation (yaw (ψ), pitch (θ), roll (φ)) of the sensor-frame during the tractor movement was acquired by the IMU sensor in east north up (ENU) local frame. Thus, any point of interest on the sensor-frame could be calculated using coordinate transformation. The position data, latitude (φ), longitude (λ) and the altitude (h) (LLA), which was obtained by the RTK-GNSS receiver, were expressed in the geodetic frame defined by WGS84.

The RTK-GNSS and the IMU output data had to be converted in the same coordinate system in order to be fused. The fusion was utilized in north east down (NED), since the IMU output data was already in this local coordinate system. However, the RTK-GNSS output data was converted twice, first the LLA to earth-centred earth fixed (ECEF) frame and second to the NED frame.

The conversion from the geodetic coordinates to the ECEF coordinates was performed using the following equations (Eqs. (23)-(24))

$$x_e=(\nu(\varphi)+h)\cos(\varphi)\cos(\lambda) \tag{23}$$

$$y_e=(\nu(\varphi)+h)\cos(\varphi)\sin(\lambda) \tag{24}$$

$$z_e=[\nu(\varphi)(1-e^2)+h]\sin(\varphi) \tag{25}$$

where e = 0.0818 is the first numerical eccentricity of the earth ellipsoid, $\Pi_e = [x_e, y_e, z_e]^T$ is the position in ECEF coordinates and $\nu(\varphi)$ is the distance from the earth's surface to the z-axis along the ellipsoid normal given by

$$\nu(\varphi) = \frac{\alpha}{\sqrt{1 - e^2 \sin^2 \varphi}} \tag{26}$$

where α = 6,378,137 m is the semi-major axis length of the earth. The conversion from the ECEF coordinates to the local ENU coordinates was estimated from the equation $\Pi_n = T_e^n \Pi_e$, where where $\Pi_n = [n, e, d]^T$ is the position in the local ENU coordinate system and T_e^n is the transformation matrix from the ECEF to the ENU coordinate system

$$T_e^n = \begin{bmatrix} -\sin(\lambda) & \cos(\lambda) & 0 & 0 \\ -\sin(\varphi)\cos(\lambda) & -\sin(\varphi)\sin(\lambda) & \cos(\varphi) & 0 \\ \cos(\varphi)\cos(\lambda) & \sin(\lambda)\cos(\varphi) & \sin(\varphi) & 0 \\ 0 & 0 & 0 & 1 \end{bmatrix} \tag{27}$$

The sensor-frame enabled transformations and translation, due to the known distances and angles between the sensors. The LiDAR frame was transformed into the RTK-GNSS frame by several translations (Trans (x_{axis} , -a) × Trans (y_{axis} , +b) × Trans (z_{axis} , -c)) and one rotation (Rot ('roll', $\frac{\pi}{2}$)) in order to georeference each point of the LiDAR

$$[x_{\text{sensor-frame}}, y_{\text{sensor-frame}}, z_{\text{sensor-frame}}, 1]T\ [T_{\text{LiDAR}}^{\text{sensor-frame}}] \times [x_{\text{LiDAR}}, y_{\text{LiDAR}}, z_{\text{LiDAR}}, \quad 1]T \tag{28}$$

where $T_{\text{LiDAR}}^{\text{sensor-frame}}$ is the transformation matrix from the coordinate system of the LiDAR sensor to the coordinate system of the RTK-GNSS

$$T_{\text{LiDAR}}^{\text{sensor-frame}} = \text{Rot}('\text{roll}', \frac{\pi}{2}) \times \text{Rot}('\text{yaw}', -\frac{\pi}{2}) \times \text{Trans}(y_{\text{axis}}, -a) \times \text{Trans}(z_{\text{axis}}, +b) \tag{29}$$

The general matrix form of all rotations (Rot) and translations (Trans) are shown in Eq. (30), and by substituting them in Eq. (29), a matrix form representation of the equations can be generated. The three-dimensional tilt orientations were implemented in the point cloud considering the LiDAR timestamp (*t*).

$$\text{Rot ('roll}^{'}\text{, }\varphi)=\begin{bmatrix}1 & 0 & 0 & 0\\ 0 & \cos(\varphi_t) & -\sin(\varphi_t) & 0\\ 0 & \sin(\varphi_t) & \cos(\varphi_t) & 0\\ 0 & 0 & 0 & 1\end{bmatrix},\ \text{Trans}(\text{`}x_{axis}, x_{translation})=\begin{bmatrix}1 & 0 & 0 & 0\\ 0 & 1 & 0 & 0\\ 0 & 0 & 1 & 0\\ x_{translation} & 0 & 0 & 1\end{bmatrix},$$

$$\text{Rot ('pitch}^{'}\text{, }\theta)=\begin{bmatrix}\cos(\theta_t) & 0 & \sin(\theta_t) & 0\\ 0 & 1 & 0 & 0\\ -\sin(\theta_t) & 0 & \cos(\theta_t) & 0\\ 0 & 0 & 0 & 1\end{bmatrix},\ \text{Trans}(\text{`}y_{axis}\text{'}, y_{translation})=\begin{bmatrix}1 & 0 & 0 & 0\\ 0 & 1 & 0 & 0\\ 0 & 0 & 1 & 0\\ 0 & y_{translation} & 0 & 1\end{bmatrix}, \quad (30)$$

$$\text{Rot ('yaw}^{'}\text{, }\psi)=\begin{bmatrix}\cos(\psi_t) & -\sin(\psi_t) & 0 & 0\\ \sin(\psi_t) & \cos(\psi_t) & 0 & 0\\ 0 & 0 & 1 & 0\\ 0 & 0 & 0 & 1\end{bmatrix},\ \text{Trans}(\text{`}z_{axis}\text{'}, z_{translation})=\begin{bmatrix}1 & 0 & 0 & 0\\ 0 & 1 & 0 & 0\\ 0 & 0 & 1 & 0\\ 0 & 0 & z_{translation} & 1\end{bmatrix}$$

The three-dimensional tilt of the IMU data was implemented to stabilize the orientation of the coordinate system of the sensor-frame (Eq. (31))

$$T_{LiDAR}^{ts-geo} = T_{LiDAR}^{sensor\text{-}frame} \times \text{Rot ('roll}^{'}\text{,-}\varphi) \times \text{Rot ('pitch}^{'}\text{,-}\theta) \times \text{Rot ('yaw}^{'}\text{,}\psi) \quad (31)$$

3.9.2. *Point cloud rigid registration and stitching*

The process started by implementing the SOR filter to each point cloud pair to compute first the average distance of each point to its neighbors and then reject the points that were further than the average distance considering also the standard deviation. Furthermore, the random sample consensus (RANSAC) algorithm was used to remove points that belonged to the ground. The distance threshold value between a data point and the plane was determined at 5 mm, while the slope of the field was also considered in the plane model through the implementation of the RTK-GNSS height difference of each row. As mentioned above, a plane of 5 mm height was applied in both rows to remove the soil. The RANSAC algorithm was applied in each path separately.

The pairwise pathways were pre-aligned due to the aforementioned georeferencing method of point clouds using the RTK-GNSS. The alignment of the pairwise pathways was operated with the iterative closest point algorithm

(ICP), which iteratively minimizes the distances of corresponding points. A binary search tree, where each node represents a partition of the k-dimensional space (K-d tree) was used to speed up the ICP process (Vázquez-Arellano et al., 2018b). Moreover, the local surface normal vector and the curvatures were considered as variants in the ICP to select the corresponding point. A weight factor that incorporates the difference of eigenvalues of matched values for the minimization of distances was assigned to x, y, z and the normal vector. Higher weight was assigned to the x axis, since it was the axis of the driving direction producing the highest deviation between the point cloud pairs. The maximum correspondence distance was set to 0.1 m. Thus, the ICP minimized the distance between a point and the surface of its corresponding point, or the orientation of the normal. Finally, the two sides were merged together into a single point cloud, using a voxel grid filter (1 mm × 1 mm × 1 mm).

A similar methodology was followed for the reconstruction of each individual side of the metal box. Initially, a SOR filter was used in order for the point clouds of each individual side to be denoised. Subsequently, the normal vectors and curvatures were estimated and integrated into the ICP algorithm. Thus, the edges of the sides were aligned and later merged. Each side was divided vertically and horizontally into 6 parts using a 0.3 m step in order the maximum and minimum point of each vertical part for each individual side. Whereas the width was obtained by the subtraction of the maximum and minimum width of each horizontal part.

Furthermore, the height and the width of each individual extended bar (EB) were measured. The average height difference between the EB (ΔEB) was estimated, using 4 vertical planes to obtain the difference between the minimum and maximum point.

3.9.3. *Tree row alignment*

The methodology for stem position determination relied on Vázquez-Arellano et al., (2018a). A first-order polynomial curve considering the least absolute residuals (LAR) was used to connect the reference stem positions in each row (Eq. (32))

$$y = \alpha * x + \beta \tag{32}$$

The slope of the line was utilized by rotating the merged point cloud until it was aligned with the x-axis.

3.9.4. *Tree stem estimation*

The stem position of each tree (n = 224) was defined using a real time kinematic global navigation satellite system (RTK-GNSS), whereas a wooden meter was used to estimate the tree height manually (H_{Manual}). The average width of each tree (W_{Manual}) was specified at three different heights across the x and y axis. Furthermore, the stem diameter (S_{Manual}) was measured at 0.3 m height, which was always above the grafting area and above the ground, using a tape scale. The value of the W_{Manual} in the x and y axes and of the H_{Manual} of the tree was multiplied to determine the volume of each tree (V_{Manual}).

The generated and rotated point clouds were used to acquire 3D point density histograms using a bivariate approach by pairing the x and y values of every point in the point cloud. The bivariate histogram depicts the frequency of points, which fall into each bin sized 3 cm^2. The closer to the stem position the higher the frequency.

A bivariate histogram of the entire row was used to detect the stem position, with the highest frequency. A cylinder with the coordinates of the highest peak as a base, with a 0.65 m radius and 4 m height was applied in order to bring a point density histogram within this frame. The point with the highest frequency was considered as the starting point, since it was the one with the highest probability of being a stem. The position of the next stem was estimated in both directions of the x-axis by adding the average intra row distance (0.95 m). At this point, a second cylinder, with the aforementioned dimensions and the coordinates of the next stem as the center of the base was applied. A point density histogram was used within the cylinder frame to test whether the coordinates of the next stem would remain the same or needed to be repositioned. The tree point cloud within the latter cylinder was segmented and this process was repeated for all the trees of each row.

3.9.5. *Tree height*

When each tree was segmented based on its stem position, its height was estimated by calculating the difference between the maximum and the minimum point in the z-axis (H_{LiDAR}). However, the plane that was fitted into the soil points with the RANSAC algorithm led to the classification of some plant points, which were close to the soil, as soil points (Soudarissanane et al., 2011). Therefore, the rigid transformations that were used to register the tree point clouds were implemented to align and merge the soil point clouds. The merged soil point cloud was filtered,

using the SOR filter and merged with the tree point cloud. The merged point cloud with the tree and soil information was considered as the final one and it was used for height estimation.

3.9.6. *Stem diameter*

As mentioned above, the S_{manual} was measured at a height of 0.30 m above the ground for each tree. Thus, the region between 0.05 m and 0.3 m above the soil was selected in each individual segmented tree to calculate the trunk diameter (S_{LiDAR}). The selected points were plotted in x and y-axis. A line connected the points on the boundaries with each other, creating a polygon. The k-means clustering method was applied in order to define the coordinates of the centre inside the polygon. Consequently, the maximum Euclidean distance between the centre and the boundary points was estimated and compared to the manually measured reference trunk radius.

3.9.7. *Canopy volume*

The H_{manual} of the tree and the distance of the branching point of the tree from the ground were recorded. The canopy width of each tree at height intervals of 0.5 m was measured from both sides. The cross-sectional area of each zone was calculated by multiplying the mean value of the top and bottom width measured with the corresponding height. As mentioned above, the product of the area and h_{manual} of the tree was multiplied to determine the V_{manual} (Sanz et al., 2018; Vázquez-Arellano et al., 2018a).

On the other hand, the convex hull was applied in the segmented tree point clouds. This method fits a boundary around the structure specified and calculates the volume for that region. For measuring volume with this method, an algorithm was developed using the boundary function in Matlab (Barber et al., 1996) with a shrink factor of 1 to estimate the volume.

3.9.8. *LA Estimation*

The 3D point cloud dataset was generated and processed in the Computer Vision Toolbox™ of Matlab (2018b, Mathworks, Natick, MA, USA). Random consensus was applied to filter points belonging to ground surface (Vázquez-Arellano et al., 2018b). The aforementioned rigid translations and rotations were applied on each point of the 3D cloud, while alignment of pairing tree sides was carried out with iterative closest point algorithm, using

a k-dimensional space to speed up the process. Trees were segmented based on stem position and planting distance to gain points per tree (PPT).

The geometric feature of linearity (L) and apparent reflectance intensity (R_{ToF}) derived from the 3D point cloud were used to extract points of woody parts from PPT of each segmented apple tree for all four growth stages. For this purpose, k-nearest neighbors classification method was performed on each segmented tree to analyse the local neighborhood of points $P_i = [x_i, y_i, z_i]$ in 3D. A radius (r) determined by the mean value of stem diameter, (n = 50) measured manually at $DABB_{10}$, was used to define the relevant space of neighboring points. The total number of the P_i set (N) was used to estimate the average $\tilde{P}=\frac{1}{N}\sum_{i=1}^{N}(P_i)$ of the nearest neighbours. Thus, the covariance matrix (Cov) was built after mean centering by means of subtraction of the $\tilde{P}$ value from each P_i of the nearest neighbours set (Eq. (33))

$$\text{Cov}(\mathbf{P}) = \frac{1}{N}\sum_{i=1}^{N}(P_i-\tilde{P}) \times (P_i-\tilde{P})' \quad (33)$$

The Cov was decomposed based on singular value decomposition, producing the eigenvalues (λ_1, λ_2, λ_3), which were sorted in ascending order $\lambda_1 \geq \lambda_2 \geq \lambda_3$, and the corresponding eigenvectors. The linearity of each point L(Pi) in 3D structure was calculated (eq. (34)).

$$L(P_i) = \frac{\lambda_1 - \lambda_2}{\lambda_1} \quad (34)$$

More specifically, the closer the values of L to 100, the higher the likelihood for the shape of points to be linear (Hackel et al., 2016; Lin et al., 2014). Linearity and reflectance thresholds of wood points were determined based on data measured $DABB_{10}$, when no leaves appeared in the data set, of each year. The percentage of segmented points belonging to woody parts was quantified considering the thresholds in each PPT [%]. The probability density of quantified points of wood was calculated for each date of measurement.

Before and after filtering of the woody parts, linear regression models were built to express the relationship between LA_{Manual} and (remaining) PPT, separately for each growth stage (Eqs. **Σφάλμα! Το αρχείο προέλευσης τ ης αναφοράς δεν βρέθηκε.-Σφάλμα! Το αρχείο προέλευσης της αναφοράς δεν βρέθηκε.**). The linear calibration was applied to convert PPT into LA of each segmented tree in the orchard. A leave one-out cross-validation was used to evaluate the error of calibration models for each measuring date. The performance of calibration was assessed considering adjusted coefficient of determination in calibration ($R^2_{adj,C}$) and cross-validation ($R^2_{adj,CV}$), and root mean squared error of calibration ($RMSE_C$), cross-validation ($RMSE_{CV}$).

Partial least-squares regression (PLS) was carried out to relate fruit quality parameters of both years with tree position (longitude, latitude, elevation) and (i) ECa or (ii) LA of trees. Pre-processing captured autoscaling of variables by subtracting their mean and dividing by their standard deviation. The optimum number of latent variables was selected according to minimum $RMSE_{CV}$ in leave-one-out cross validation. Resulting latent variables were used as predictors in the k-nearest neighbours (KNN) method to classify fruit quality as low, mid and high (Matlab, Version R2018b, Mathworks Inc., MA, USA). Data from 2018 was utilized to train the model. The KNN model was cross validated with the k-fold method (n = 8) to select the number of K neighbours according to lowest mean standard error. The quality classification models obtained were validated in real-world with the dataset of the following year providing an independent test set.

On each measuring date, four apple trees (n = 4) were manually defoliated to investigate the relation between the points per tree (PPT) and the leaf area (LA_{Manual}). The trees were scanned before and after defoliation. The leaves were measured with a desktop scanner (Scanjet 4850, HP, USA) using the aforementioned (sub-chapter 3.3.2) written Matlab script (2018b, Mathworks, Natick, MA, USA).

Georeferenced datasets of ECa, yield, and LA were expressed as point data. Descriptive statistics were applied to remove possible outliers, while an ordinary Kriging interpolation method was applied to interpolate points (Aggelopoulou et al., 2010). All variables were normally distributed. A spherical variogram model was fitted in ECa and yield and an exponential in the LA to interpolate the points by ordinary Kriging method. The average nearest neighbours method was utilized to set the average distance between points and define the number of neighbours (lag) in each variogram. The lag bin sizes were selected at 8 m to obtain as stable a variogram as

possible. Data were classified in three classes according to the quantile method by which each class has the same number of points. The degree of spatial dependence (SpD) was estimated (Cambardella et al., 1994). The geostatistical analysis was carried out in ArcGIS (v.10.2.1, ESRI Inc., USA). The measured parameters, initially given as point data, were joined with the grid layer by averaging the values of the points that fall in each grid cells. Hence, the samples were categorized and compared according to the ECa zones: low, mid and high.

3.9.9. *Growth analysis*

Temporal data acquisition allowed us to characterize the development of LA. Growth curves were based on mean LA values estimated for all trees. A three-parameter logistic model was used to fit growth curves of LA (Sun et al., 2018).

$$G_{LA}(t) = \frac{x_{min}\, x_{max}}{x_{min} + (x_{max} - x_{min})\, e^{-\gamma t}} \tag{35}$$

where t represented days after bud break, G(t) denoted the estimated LA at t, x_{min} was the initial value and x_{max} the upper horizontal asymptote of extracted features and γ was the acceleration and deceleration constant rate of approximation to the two asymptotes (Gottschalk and Dunn, 2005).

$$K_{LA}(t) = \frac{G_t - G_{t-\Delta t}}{\Delta t} \tag{36}$$

$$R_{LA}(t) = \frac{\ln(G_t) - \ln(G_{t-\Delta t})}{\Delta t} \tag{37}$$

where K was the growth rate of LA, G_t was the estimated LA at time t and Δt denoted the time interval. Furthermore, the relative growth rate (R_{LA}) of LA was calculated.

A cylindrical boundary was projected around the estimated stem positions to segment each individual tree in Markendorf. The estimation of V_{LiDAR} was based on the convex hull approach, fitting a boundary around the structure specified. Subsequently, the V_{LiDAR} spatio-temporal variability of the segmented tree point clouds was

estimated during full bloom ($V_{LiDAR, FB}$), fruit set ($V_{LiDAR, FS}$) and before harvest ($V_{LiDAR, BH}$). The growth trend was determined as the variation of mean V_{LiDAR} over the monitoring period in low, mid and high ECa zones. A three-parameter logistic model (3PLM) was used to fit growth curves of the three detected traits for each ECa zone (Sun et al., 2018) (Equation (38)).

$$V(t) = \frac{V_0 V_n}{V_0 + (V_n - V_0)e^{-\gamma t}} \quad (38)$$

Where $V(t)$ was the detected tree volume [m^3] at time t, V_0 was the initial horizontal of tree volume [m^3], V_n declared the upper horizontal asymptote [m^3], γ was an acceleration or deceleration parameter related to time. Furthermore, the growth rate was determined as the average change in measured V_{LiDAR} over time interval for each individual EC_a zone (Equation(39)):

$$K_v = \frac{V_t - V_{t-\Delta t}}{\Delta t} \quad (39)$$

Where K_v was the V_{LiDAR} growth rate, V_t was the measurement of V_{LiDAR} at time t and Δt the time interval between the measurements.

3.9.10. *Apple detection*

The total number of P_i within a tree's cloud was used to estimate the mean $\tilde{P}=\frac{1}{N}\sum_{i=1}^{N}(P_i)$ of the nearest neighbors.The information of the 3D local neighbourhood of points $P_i = [x_i, y_i, z_i]$ was determined using the *k*-nearest neighbours within a radius (*r*) equal to the D_{Manual} of apples (Hackel et al., 2016). After mean centering, each P_i with $\tilde{P}$ value per nearest neighbors set and decomposition of Cov (Eq. (33)), orthogonal eigenvalues were ordered according to decreasing percentage of explained variance in the data $\lambda_1 \geq \lambda_2 \geq \lambda_3$.

The eigenvalues, which represent the highest orthogonal variance of the matrix, provided the points dispersion within *k*- nearest neighbours describing the local spatial structure in 3D. The eigenvalues were normalized between 0 and 100, allowing for the comparison of different clusters. Thus, the local geometry of each P_i in the point cloud was analyzed by means of eigenvalues to illustrate the spatial structure considering its linearity (L, Eq.**Σφάλμα! Το αρχείο προέλευσης της αναφοράς δεν βρέθηκε.**) and curvature (C, eq. (40)):

$$C(P_i) = \frac{\lambda_3}{\lambda_1+\lambda_2+\lambda_3} \quad (40)$$

where L and C described the variation of linearity and curvatures for all points along the direction of the corresponding eigenvalues, respectively (Hackel et al., 2016; Lin et al., 2014). More specifically, the closer the values of L or C to 100, the higher the likelihood for the shape of points to be linear or curved, respectively. Therefore, L was used to segment the foliage and woody parts of the tree (branches, stem), while C was used to distinguish the apple points.

The data set of T_D (N = 2) was used to define the range of R_{ToF}, C and L for the class of apple (R_A, C_A, L_A) and of woody parts (R_W, C_W, L_W), while the range of leaf class for the same features (R_L, C_L, L_L) was defined in the T_L. Thresholding was performed for each class by employing the exploratory analysis of normal distribution using the probability density function to define the threshold that will distinguish the 3D points of apples from leaves and woody parts (Gené-Mola et al., 2019a; Koenig et al., 2015). The value with the highest likelihood (mode) within the R_A, C_A, and L_A classes was used as a threshold (R_{th}, C_{th}, and L_{th}). Points which fulfilled the criteria of $L_A \leq L_{th}$, $C_{th} \leq C_A$, and $R_{th} \leq R_A$ were segmented and categorized as apples. Figure 8 presents a flowchart of the protocol for apple detection and sizing using the defoliated trees (T_D).

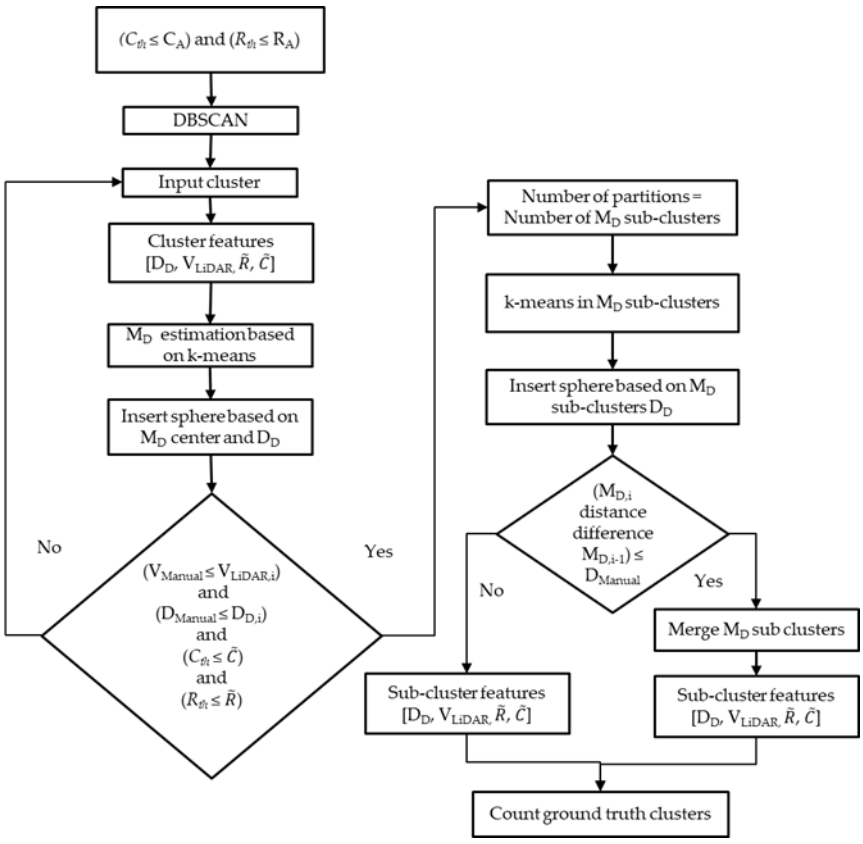

Figure 8. Flowchart showing the protocol for apple detection and sizing using defoliated trees (TD), starting with the threshold application in the registered point cloud pair, through filtering and partitioning, until the counting of ground truth centres of clusters.

Subsequently, a density-based scan algorithm (DBSCAN) (Ester et al., 1996) was applied to find the point set, using the mean D_{Manual} of apples that was found in each ΔW as a neighborhood search radius (ε) and the value 10 as a minimum number of neighbors. The value 10 resulted from manually run tests showing that less neighboring points result in random appearance of sets. The mean R_{ToF} ($\tilde{R}$) and mean C ($\tilde{C}$) for each individual set of points were extracted, while the convex hull algorithm, as utilized before in Tsoulias et al.(2019b), was applied to acquire the V_{LiDAR} of each group. The Delaunnay approach (Barber et al., 1996) was selected for triangulation, whereas a shrink factor equal to 1 was used to create a compact boundary that envelops the points. The maximum distance in x and y axes was considered as the diameter (D_D) of each point set recognized as an apple.

The *k*-means clustering was applied to count and find the fruit center (M_D) in each cluster in T_D. However, the shape variation of each apple and the clustering of more than one apples produced different C and R_{ToF}.

Consequently, the utilization of C_{th} and R_{th} values excluded points at the edge of the fruit. Therefore, a sphere was placed in each individual apple cluster, with the coordinates of M_D as the center and a radius equal with the D_D to include the filtered apple points. The *k*-means algorithm was reapplied to estimate the M_D of each cluster based on the added 3D points, while the V_{LiDAR}, $\tilde{R}$ and $\tilde{C}$ were recalculated.

The fact that more than one apples developed per inflorescence led to close appearance of 2-3 fruits in the cloud, resulting in the creation of augmented clusters with more than one apples. Thus, the clusters of 3D points within the sphere were evaluated and partitioned based on their extracted features, creating sub-clusters and defining the number of M_D. Therefore, partitioning was performed for each cluster only on the condition that the four variables, V_{LiDAR}, D_D , and $\tilde{R}$, $\tilde{C}\tilde{C}$, were close to mean values of V_{Manual} and D_{Manual} for each ΔW and R_{th}, C_{th}. The features of each sub-cluster were iteratively extracted and re-evaluated, and partitioning was continued until the sub-cluster features stopped while fulfilling the condition. Subsequently, the spheres were placed based on the M_D and the D_D of each sub-cluster. Those spheres showing a calculated distance between the M_D centres below the minimum value of D_{Manual} in each ΔW, were merged. Therefore, their M_D was redefined and their extracted features were recalculated. It should be mentioned that the M_D clusters were considered as ground truth labels for the later evaluation of the method in T_L.

Similarly, the L_{th}, C_{th}, R_{th} were applied to the same trees before their defoliation to segment the apples and find their centers (M_L) (Figure 9). The DBSCAN was used to group the segmented point, and the M_L centres were defined by the *k*-means algorithm. Furthermore, the maximum distance in the x and y axes was considered as the diameter (D_L) of each point set recognized as an apple. The partitioning condition remained unchanged using the generated features from each cluster. Thus, the features of each T_L sub-cluster were iteratively extracted and re-evaluated while fulfilling the conditions. The number of partitions was used in the *k*-means algorithm to determine the centres of M_L sub-clusters. The only difference between analysing T_D and T_L was the use of ε in T_D, whereas this manually measured fruit information remained unknown in T_L analysis.

However, in T_L, some of the apples were fully or partially covered by the leaves of the tree. In the latter case, the combination of DBSCAN and *k*-means algorithm overestimated the number of apple classes. Thus, apple

classes producing lower or equal Euclidian distance between their M_L centres compared to the minimum D_{Manual} were combined and considered as one fruit.

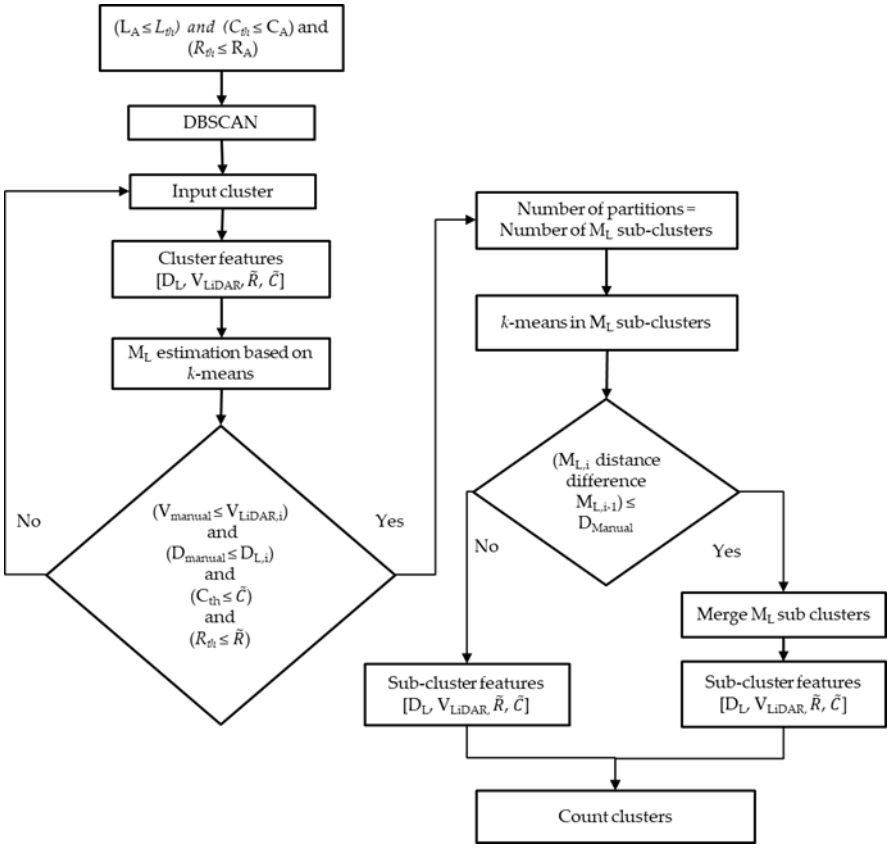

Figure 9 Flowchart showing the protocol for apple detection and sizing using foliated (TL) trees, starting with the threshold application in the registered point cloud pair, through filtering and partitioning, until the counting of centres of clusters

3.9.11. *Assessment*

The mean absolute error (MAE), the bias (MBE), the RMSE, the pearson correlation (r), the coefficient of determination (R^2) and the adjusted R^2 ($R^2_{adjusted}$), were used to estimate the measuring uncertainty and model performance in regression analysis considering the manual and the LiDAR measurements of the variables in the study (Equations (41)-(46))

$$MBE = \frac{\sum_{i=1}^{n}(y_i - \hat{y}_i)}{n} \tag{41}$$

$$MAE = \frac{\sum_{i=1}^{n}|y_i - \hat{y}_i|}{n} \tag{42}$$

$$RMSE\ [\%] = \sqrt{\frac{\sum_{i=1}^{n}(y_i - \hat{y}_i)^2}{n}} \tag{43}$$

$$r = \frac{n\sum_{i=1}^{n}(x_i\ y_i) - \sum_{i=1}^{n}(x_i)\ \sum_{i=1}^{n}(y_i)}{\sqrt{\left[n\ \sum_{i=1}^{n}(x_i^2) - (\sum_{i=1}^{n} x_i)^2\right]\ \left[n\ \sum_{i=1}^{n}(y_i^2) - (\sum_{i=1}^{n} y_i)^2\right]}} \tag{44}$$

$$R^2 = \frac{\sum_{i=1}^{n}(y_i - \hat{y}_i)^2}{\sum_{i=1}^{n}(y_i - \tilde{y})^2} \tag{45}$$

$$R^2_{adjusted} = 1 - \frac{(1-R^2)\ (n-1)}{n-p-1} \tag{46}$$

where n is the sample size, $x_{,i}$ and y_i are the individual sample points of the datasets, $\hat{y}_i$ is the predicted value of y_i, $\tilde{y}$ is the mean value of y_i and p is the number of predictors. The above equations (41- 46) were used to estimate the measuring uncertainty considering the manual and the LiDAR measurements of the metal box, stem position, tree height, stem diameter, and canopy volume and apple diameter. Whereas the pearson correlation was mainly used to evaluate the spatio-temporal relationship of plant parameters with soil properties and fruit quality.

On the other hand, calibration of the apple detection method was carried out considering data from T_D and T_L at $DAFB_{120}$ (N = 2) to define the R_{th}, C_{th} and L_{th} that describe only the apple points. Cross-validation, applying thresholds extracted at $DAFB_{120}$, was performed on the T_D and T_L data sets of the three earlier measuring dates (N

= 6). The fruit detection methodology was evaluated by calculating the accuracy, the precision, the recall, and the F1 score:

$$\text{Accuracy} = \frac{\text{TP} + \text{FP}}{\text{N}} \ [\%] \tag{47}$$

$$\text{Precision} = \frac{\text{TP}}{\text{TP} + \text{FP}} \ [\%] \tag{48}$$

$$\text{Recall} = \frac{\text{TP}}{\text{TP+FN}} \ [\%] \tag{49}$$

$$\text{F1} = \frac{2 \times \text{Precision} \times \text{Recall}}{\text{Precision} + \text{Recall}} \ [\%] \tag{50}$$

The M_D were considered as ground truth labels for the evaluation of M_L. The M_L clusters which coincide with the M_D points >50 % were considered as true positive (TP). Whereas the M_L clusters which matched <50 % were counted as false negative (FN). The clusters which revealed a V_{LiDAR} smaller than the minimum value of V_{Manual} that was found in each ΔW were categorized as false positives (FP). N denoted the total number of measurements. The values of M_D, were given as percentage.

The apple position of each individual M_L was evaluated with the M_D using the Euclidean distance, pairing the centres that revealed the minimum distance between them. Subsequently, the RMSE, the MAE, the MBE were calculated for each measuring date. Similarly, D_D was applied as ground truth for D_L.

Descriptive statistics were applied to all datasets for minimum (min), maximum (max), mean, standard deviation (SD) and coefficient of variation (CV). The descriptive statistics were carried out in Matlab (Version R2018b, Mathworks Inc., Natick, MA, USA).

4. Results and discussion

4.1. *Estimating canopy parameters based on the stem position in apple trees using a 2D LiDAR*

Tsoulias, N., Paraforos, D. S., Fountas, S., & Zude-Sasse, M. (2019). Estimating canopy parameters based on the stem position in apple trees using a 2D lidar. *Agronomy*, *9*(11), 740. Impact Factor (2021): 2.603

4.1.1. *Measuring Uncertainty of the System Applied in the Field*

After reconstructing the sides of the metal box, the LiDAR system was able to detect the slope of the soil, and the structural details of the box (Figure 10). The extended metal bars on one side were depicted, whereas their shape was also shown in the main body of S1. However, gaps of points were visible due to the sun's reflection from the metal box. The angular resolution of 0.1667° resulted in an average of 20 hits per mm^2. In total, 565 planes were recorded on S_1, S_3, and S_4 while 643 planes were recorded in S2. The ICP algorithm was utilized to align and register the sides together and then merged together (Figure 10b). The C2C function was utilized to estimate the average overlapping of the sides, revealing a mean distance error of 12 mm with a standard deviation of 0.5 mm.

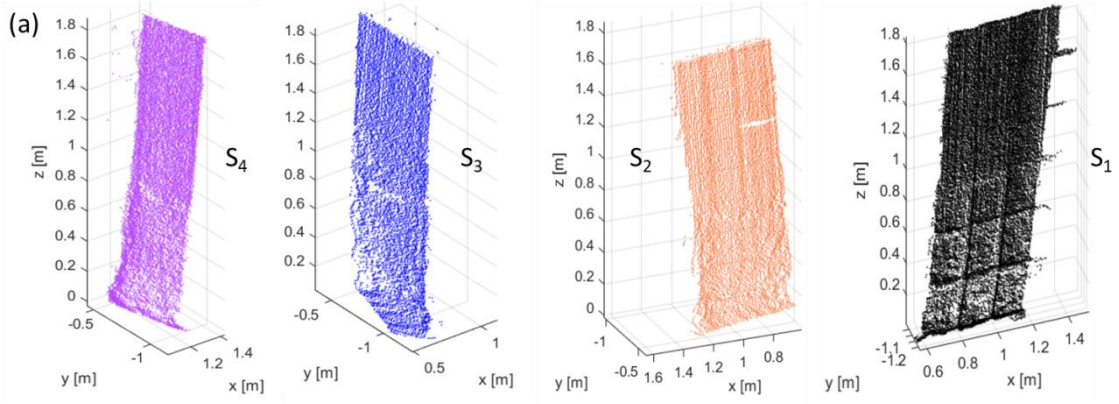

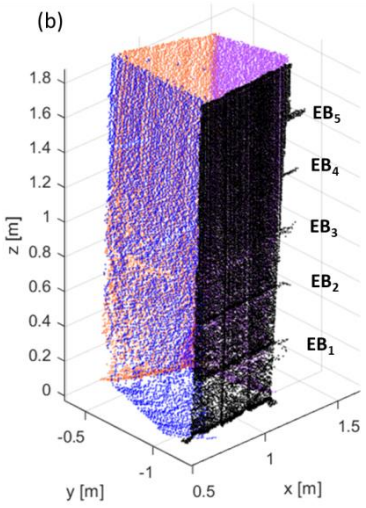

Figure 10. (a) Reconstruction of the four sides from the metal box. S_3 and S_4 are the sides parallel to the y axis, while S_1 and S_2 are the sides parallel to the x axis. (b) The resulting merged point cloud after registration and alignment of the four sides of the metal box.

The highest MAE and RMSE of height estimation was found for S_1 with 8.18 mm and 1.63%, respectively, while the highest MBE of 2.75 mm was noted at the same side (Table 3). For S_4 the lowest MAE and RMSE were depicted with 1.06 mm and 0.21 %, respectively. On the other hand, the results of the width showed generally lower MAE, while enhanced MBE was found.

Table 3. Height and width results for each side (S) of the metal box (n=6), maximum (Max), minimum (Min), standard deviation (SD), mean absolute error (MAE), bias (MBE), root mean square error (RMSE).

		Mean [m]	Max [m]	Min [m]	SD [mm]	MAE [mm]	MBE [mm]	RMSE [%]
Height	S_1	1.83	1.83	1.81	13.98	8.18	2.75	1.63
	S_2	1.80	1.81	1.79	13.34	3.00	1.75	0.60
	S_3	1.80	1.82	1.79	1.78	3.31	0.68	0.66
	S_4	1.79	1.81	1.79	5.37	1.06	-0.81	0.21
Width	S_1	0.60	0.60	0.58	2.10	4.51	2.33	0.90
	S_2	0.59	0.60	0.58	7.10	1.50	-1.5	0.30
	S_3	0.58	0.59	0.58	7.96	2.06	-4.06	0.81
	S_4	0.59	0.61	0.59	8.5	2.18	-2.22	0.43

the results regarding the extended bars (EB) on S_1 are becoming more pronounced. The measuring uncertainty increases, when considering the analysis of height and width of EB. The EB located closest to the ground, were found to be deviated to the highest extent from the actual dimensions of the bars (Table 4). The EB_4 and EB_5 were closer to the LiDAR height level and less gaps were recognized. Consequently, the measuring uncertainty was less.

The mean height of EB_5 revealed 29mm with lowest MAE of 0.2 mm and -0.2 mm MBE. The highest MBE of 2.8 mm and -2.8 mm and RMSE of 5.5 % and 5.3 % were depicted in EB_1 and EB_2, respectively.

Table 4. Estimated height and width of the extended bars (EB) (n=6), maximum (Max), minimum (Min), standard deviation (SD), mean absolute error (MAE), bias (MBE), root mean square error (RMSE).

		Mean [mm]	Max [mm]	Min [mm]	SD [mm]	MAE [mm]	MBE [mm]	RMSE [%]
	EB_1	21	30	11	7.9	2.1	−2.1	4.2
	EB_2	10	30	10	8.5	2.8	−2.8	5.6
ΔHeight	EB_3	27	29	20	4.8	0.8	−0.8	1.5
	EB_4	28	30	20	4.8	0.6	−1.5	3.2
	EB_5	29	30	28	0.9	0.2	−0.2	3.0
	EB_1	89	100	81	8.5	2.8	2.8	5.5
	EB_2	81	85	79	2.6	0.4	−2.8	5.3
ΔWidth	EB_3	104	120	85	4.8	0.8	−0.8	1.5
	EB_4	102	103	100	1.9	1.5	0.4	0.8
	EB_5	102	104	100	1.9	1.6	0.4	0.7

The mean distance between EB_1 and EB_2 (ΔEB_1) was 312.67 mm illustrating, among the other ΔEB, the lowest SD (±1.74 mm) and MAE of 1.27 mm, but also the highest MBE 3.1 mm. Furthermore, the ΔEB_3 deviate the most from the known dimensions of the metal box, with a 293 mm mean and ±6.68 mm SD. It should be mentioned that the mean values of ΔEB_2 and the ΔEB_3 were rather close with 295.2 mm and 296.8 mm, depicting a 4.77 mm and 3.17 mm MBE, respectively.

4.1.2. *Separation of trees by means of the stem position*

Each side of the row was scanned from both sides by the LiDAR system. The structure of the left side of the trees was described by the *a* and *c* pathways, while the right side from the *b* and *d* (Figure 11a, b).

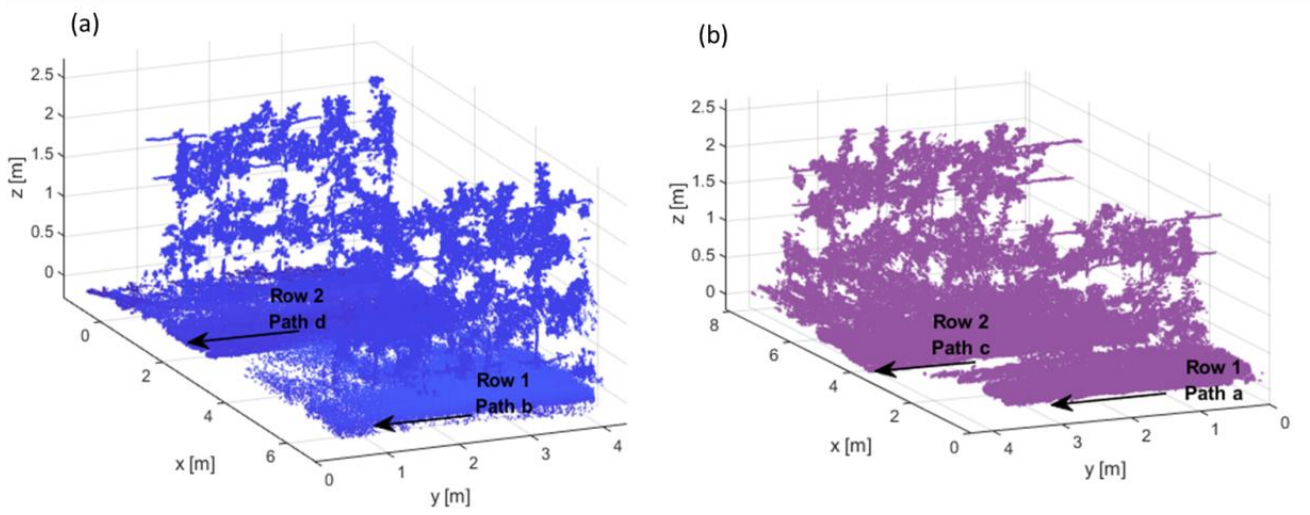

Figure 11. Representation of the point clouds were reconstructed when the LiDAR system on the tractor drove (a) through the path a, c at the left side and (b) through the path d, b at the right side of apple trees. For illustration purposes, only a part of each row was presented.

The registration and alignment of the point clouds was carried out pairwise, utilizing the ICP algorithm. The ICP algorithm was utilized in two cases: on the pairwise sides with the soil points (Figure 12a) and on the pairwise sides after the removal of soil points using RANSAC (Figure 12b) in order to evaluate which case provides a better alignment. The C2C function was used to quantify the overlapping differences. Alignment including the soil points resulted in distance error of 163.5 mm with 31.1 mm SD and 80.5 mm MBE. Removal of the soil points reduced the mean distance error of 81.6 mm with a 21.4 mm SD and lower RMSE of 0.71 % with an MBE of 5.2 mm.

The point clouds of both rows were merged into a single point cloud. The structure of the trees was clearly defined. However, it was observed that weed points above 5 mm remained within the rows (Figure 12b).

The raw data of the 3D reconstructed point cloud consisted of 18,441,933 points. The application of SOR filter reduced the point cloud by 12.17% removing 2,241,786 points. The segmentation of the soil points using RANSAC algorithm revealed that further 58.59% of the data (10,820,983 points) belonged to the soil. The remained 5,382,849 points belong to the trees representing 29.23% of the total amount of points.

The bivariate point density histogram enabled the detection of the peak of laser hits for each individual tree (Figure 13). The assumption that the stem points are concentrated in the center of the plant was based on previous studies (Vázquez-Arellano et al., 2018b; Walklate et al., 2002). Consistently, the area closer to the stem position

was assumed to appear with enhanced frequency. However, the assumption is needed confirmation considering the formation of the tree canopy and, furthermore, the analysis of the number and position of peaks can be affected by the quality of the point cloud. The potential noise or the low quality of overlapping of the point cloud could lead to more peaks since the local bin count becomes more uneven. The use of a stable bin size triggered the filtering of the peaks in the bivariate histogram and, therefore, affected the detection of the highest peak.

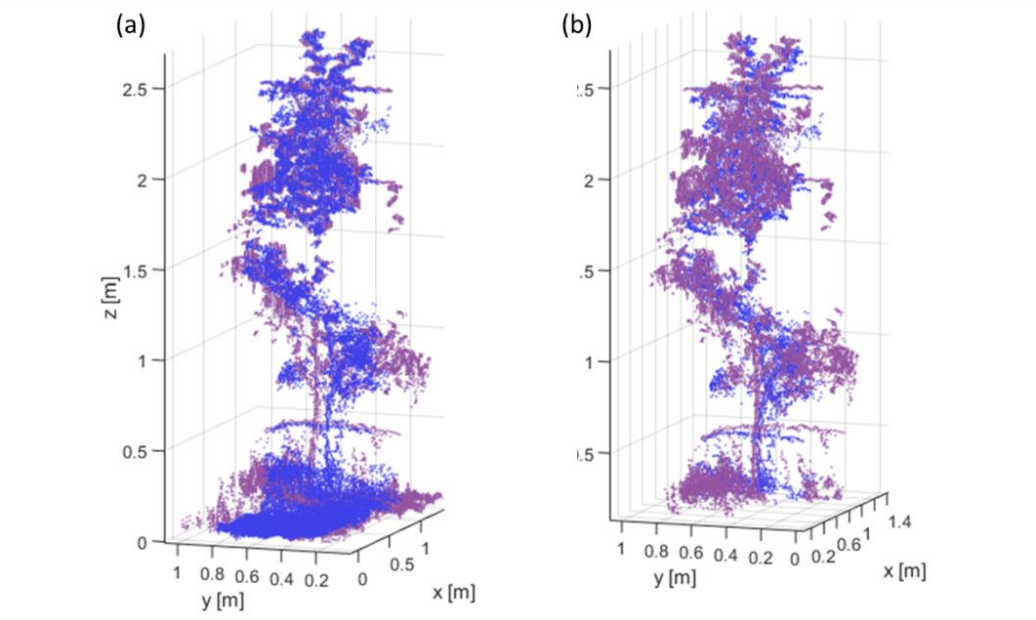

Figure 12. Registration and alignment using ICP algorithm of single tree point cloud under two cases (a) tree point cloud with soil points (b) tree point cloud after soil removal with RANSAC. The trees with the best results for each case are presented.

The coordinates of the estimated stem position were compared with the stem position, which was defined with the RTK-GNSS (Fig. 6). The estimated stem positions were closely related to the RTK stem positions, revealing a 33.7 mm MAE with 36.5 mm MBE. Despite the fact that the alignment occurred with a certain error, the algorithm was able to miss only one stem position out of 224 trees (Figure 14).

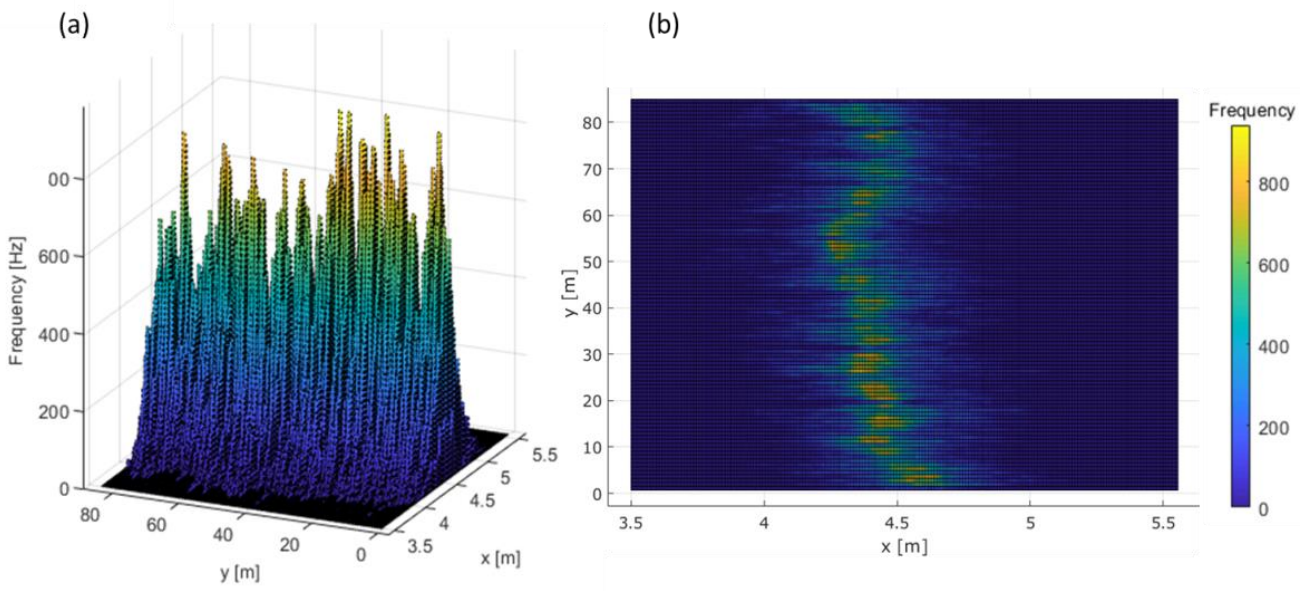

Figure 13.Result of the registration and alignment of one apple row point cloud after merging and filtering. (a) Intensity image, where the warmer squares indicate the peaks and (b) the bivariate point density histogram of the resulted row point cloud.

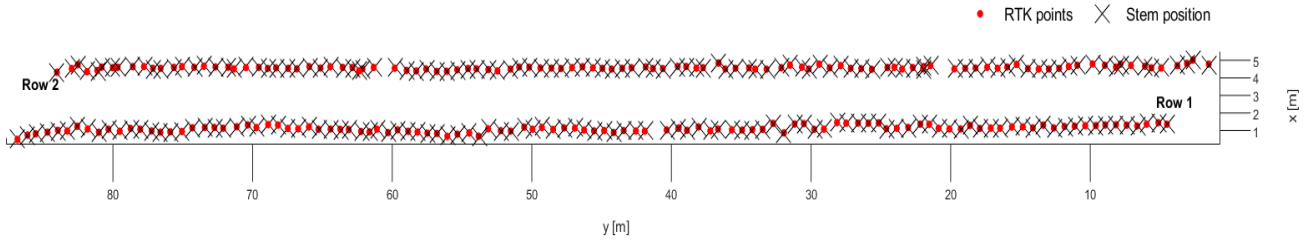

Figure 14. Estimation of tree (n = 224) stem position compared to the RTK-GNSS defined stem position

4.1.3. *Estimation of tree variables*

After the determination of stem position, the subtracted soil was merged with the point cloud of trees (Fig. Figure 15 a) to avoid loosing tree hits. The coordinates of the estimated stem position were utilized as the center for the segmentation cylinders in order to obtain the points that belonged to each individual tree. The points within the boundaries of the cylinder were segmented and considered as the tree points (Figure 15 b).

The difference between the maximum and the minimum point in the z-axis was considered to estimate the height. As was mentioned above, the radius of the cylinder was based on the manually measured average width of

the trees (n = 224). However, some tree points of long branches laid out of the cylinder resulting in an underestimation of the canopy volume. Nevertheless, this error did not reveal an underestimation of the height (Table 5).

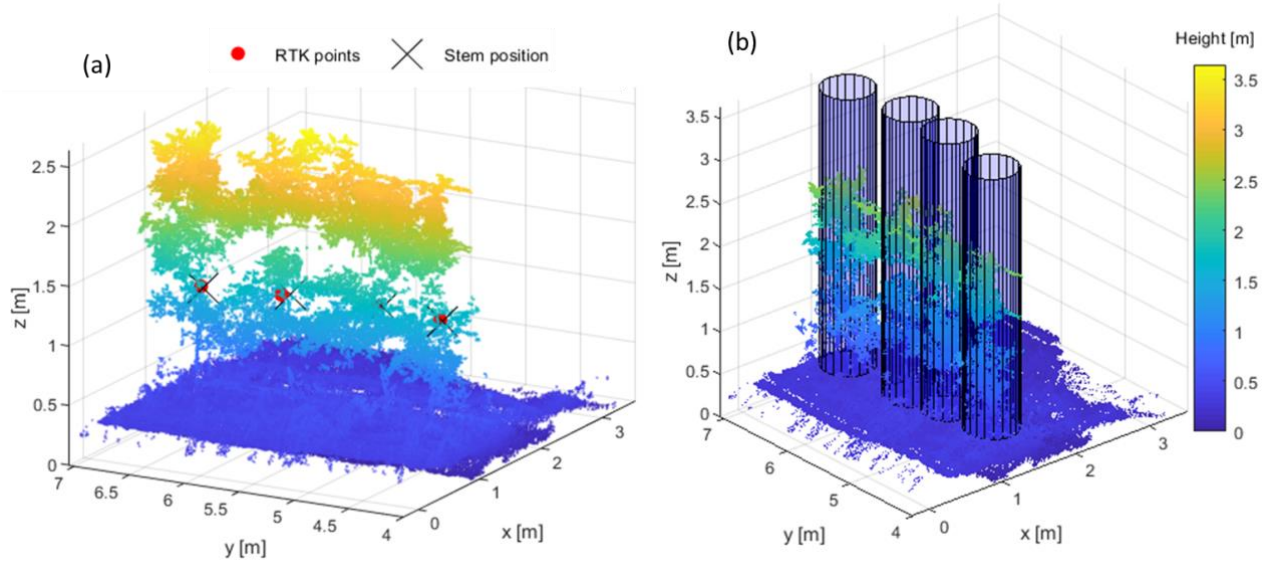

Figure 15 (a) Merged point cloud with estimated stem position and stem position defined by RTK-GNSS. For illustration purposes, only first part of row 1 is represented. (b) Projected cylinders for single tree segmentation based on the estimated stem position.

Table 5. Descriptive statistics of manual measurements of height (H_{manual}) [mm], stem diameter (S_{manual}) [mm], canopy volume (V_{manual}) [mm³] and LiDAR-based measurements H_{LiDAR}, S_{LiDAR}, V_{LiDAR} (n=224) regarding maximum (Max), minimum (Min), mean absolute error (MAE), bias (MBE), root mean square error (RMSE), coefficient of determination (R^2).

	Min	Max	Mean	MAE	MBE	RMSE (%)	R^2
H_{manual} [mm]	1900	2800	2310	5.55	0.62	5.71	0.87
H_{LiDAR} [mm]	1870	2820	2350				
S_{manual} [mm]	55	132.5	97.1	2.52	-3.75	2.23	0.88
S_{LiDAR} [mm]	63	136	99.5				
V_{manual} [m³]	0.23	1.12	0.55	5.23	5.93	4.64	0.77
V_{LiDAR} [m³]	0.38	1.05	0.58				

In the present study, the tree height profile of each row was measured manually, as the ground-truth in order to validate the results of the point cloud, pointing out a 900 mm variation in height (Table 5). The average values of manual measurements (H_{manual}) and estimated height, derived from LiDAR data (H_{LiDAR}), varied by 40 mm regarding the means comparison means. Similar values can be expected in commercial, well pruned apple orchards. The reference and estimated values were correlated, revealing an $R^2 = 0.87$ with a MAE of 5.55 mm and MBE of

0.62 mm. The RMSE of 5.7 % can be explained by the measuring uncertainty of the LiDAR as well as the uncertainty of defining the highest point of the stem elongation by means of manual measurements.

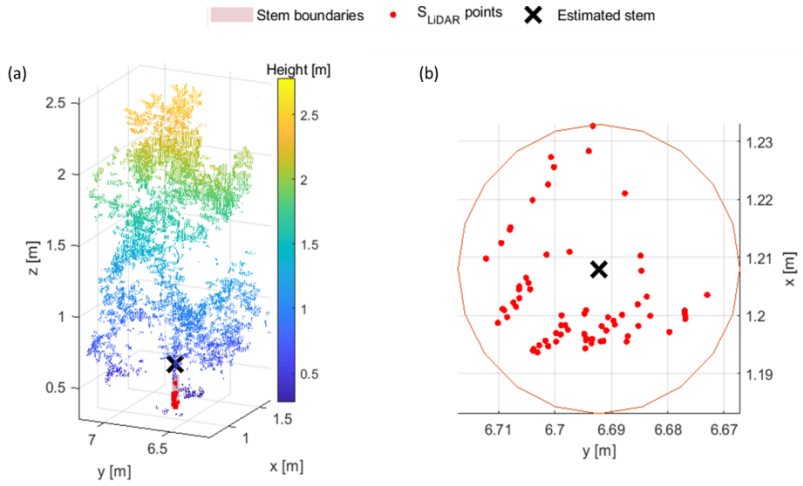

Figure 16 (a) Stem point selection marked in red between 0.1 m and 0.3 m and (b) selected stem points detected by the LiDAR (S_{LiDAR}) plotted in 2D with stem boundaries and stem position.

The section of stem between 0.10 m and 0.30 m was selected in the segmented tree point clouds to analyse the stem diameter (Figure 16). The grafting region of the cultivar and rootstock appeared always below this section. The S_{manual} and S_{LiDAR} depict 2.4 mm difference in their means, whereas 8 mm difference in minimum values was illustrated. The latter results were described by a considerable difference in the MAE of 2.52 mm and the MBE of -3.75 mm, however, reference and estimated values showed high R^2 = 0.88 and relatively low 2.23% RMSE recognizing the pertubating effects of enhanced incident angle when measuring on the extended bars of the box (Table 5).

The convex hull algorithm was used to estimate the canopy volume (Figure 17b). The boundary for each individual volume was illustrated with a different colour in order to be easily distinct. The convex hull method does not compute volume considering the gaps within the canopy, similar to ground-reference methods but instead considers the overall canopy geometry in all the zones. The manual measurement of the volume showed a strong correlation with the volume data from the segmented tree point clouds (R^2 = 0.77) (Table 5). The rough simplification of the canopy structure by the manual method based on the cylinder-fit method mainly overestimated

the actual data and the ones computed with the convex-hull algorithm. Consequently, the highest bias was found for the volume analysis (Table 5), while slightly reduced RMSE was observed compared to height estimation.

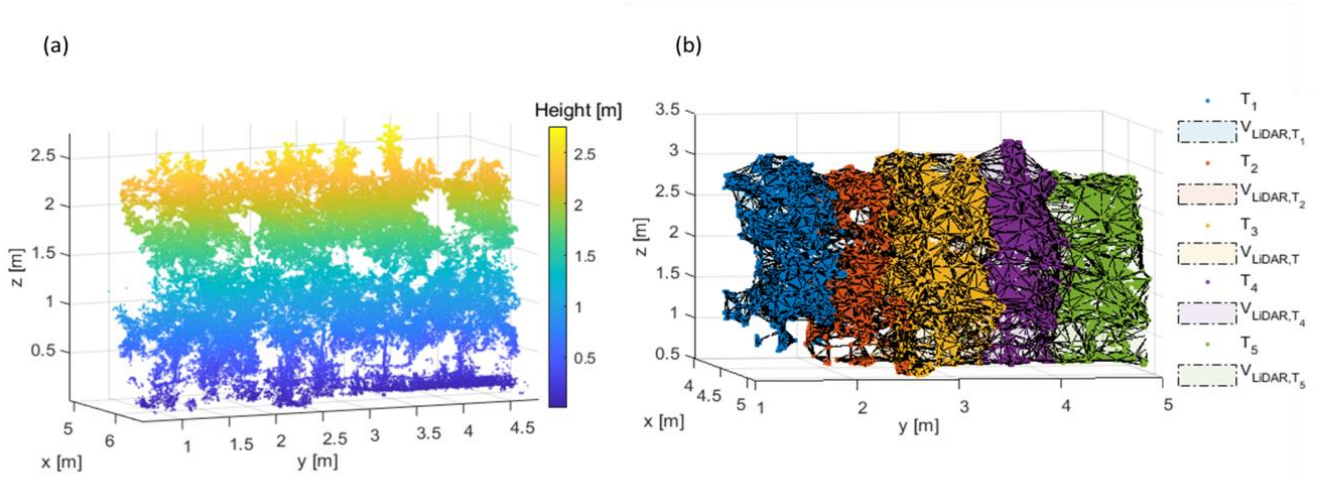

Figure 17.Point cloud of four example apple trees and visualization of convex hull method showing the canopy volume ($V_{LiDAR,T}$) of singularized tree (T_n).

4.1.4.*Discussion*

Measuring Uncertainty of the System Applied in the Field

The scanning process can basically be affected by the scanner mechanism, the atmospheric conditions and environment, the object properties and scanning geometry (Soudarissanane et al., 2011). The highest MBE and MAE have been denoted in the EB measured at high incident angle. Consequently, the point cloud quality is affected by the scanning geometry, when increased incidence angles and enhanced distances from the scanner occurred (Forsman et al., 2018; Kaasalainen et al., 2011). While the bias may be corrected, the lack of precision remains. It should be also considered that materials of high reflectance can distort the backscattered signal (Soudarissanane et al., 2011). This was the case for S_3, where 440 missing hits were found. The distortion is especially pronounced if part of the beam falls outside the target, the likelihood of which additionally depending on the angular resolution (Forsman et al., 2018). Therefore, the combination of the perturbating factors can possibly increase the MBE and MAE especially in objects of smaller dimension such as the EB. While this was an expected finding, the quantification can highlight the measuring uncertainty that can be expected in the the analysis of tree stem. Palleja et al. (2010), who mentioned that the LiDAR height misposition due to the roughness of the ground

and the oscillations of the tractor engine the trajectory during the operation, can influence the measurement errors up to 3.5%.

Separation of trees by means of the stem position

Regarding the case after removal of soil points low measuring uncertainty considering the overlapping was found (Kaasalainen et al., 2011; Sun et al., 2018). The biggest challenge of the algorithm settings was the discrimination between ground and plant points. Weeds within the trees or hanging branches close to the ground produce occlusions in the laser beam decreasing the density of soil points. RANSAC model could potentially be improved by utilizing the LiDAR backscattered reflectance to discriminate ground from plant points. Furthermore, repeating driving in both sides of the same row could increase the point density of soil points. Vázquez-Arellano et al., (2018b) have pointed out the dominance of soil hits in their 3D reconstructed point clouds, suggesting the alignment of plant points separately from the soil points.

As was prevously above, high density orchards are typically trained as slender spindle, where plant organs (e.g., branches, leaves) are significantly intervene among trees. However, as the trees in orchards are often pruned at the bottom, the trunks and parts of the stem are generally visible and act as distinct markers for separate trees. Consistently, the area closer to the stem position was assumed to appear with enhanced frequency. The use of stable bin size allowed to observe the highest peak in this area. The detected tree position was evaluated over the RTK coordinates, presenting low measuring uncertainty. In similar studies, tree segmentation was performed based on tree height changes applying hidden Markov model (Gao et al., 2020; Jagbrant et al., 2015; Underwood et al., 2016; Wellington et al., 2012). This approach mostly finds application in orchards of low density, where the boundaries of separate trees are discrete, while is not representative for estimating tree location (Bargoti et al., 2015). Bargoti (et al., 2015) presented a perception pipeline to localize and segment trees trained in V and I trellis based on individual trunk position, suggesting 99 and 98.9 % accuracy during full bloom.

Estimation of tree variables

Arellano et al. (Vázquez-Arellano et al., 2018a), with a similar method, determined the stem position in maize and acquired the height profile of the plants pointing to a MAE of 7.3 mm from the actual height. Walnuts trees

were segmented and their height was estimated considering the Min and Max values in Z axis, resulting in a significant relationship with the manual measurements ($R^2 = 0.95$) (Estornell et al., 2017). Malambo et al. (et al., 2019) utilized a similar methodology with cylinder boundaries to segment sorghum trees, reporting a correlation of r = 0.86 with RMSE = 11.4 cm.

The cylinder fitting method based on stem position for estimating the stem diameter is rather scarce in horticulture. The automatic detection that fits cylinders on stem points, has been investigated broadly in forestry (Calders et al., 2015; Dassot et al., 2012; Srinivasan et al., 2015). However, the majority of these studies employed a 3D terrestrial LiDAR, able to provide a 3D representation of stem points without moving the system and as a consequence the limitation of errors during the alignment. Moreover in forest, the tree stem has no coverage by leaves for a few meters above the ground, allowing more hits per stem and segmentation of stem points without coinciding structures.

Summarizing, the LiDAR system was able to detect geometric variables in apple trees that could be used in agricultural applications to measure structural parameters and implementation in tree-individual orchard management considering mechanical pruning, irrigation, and spraying.

4.2. *Calculating the water deficit of apple orchard by means of spatially resolved approach*

Tsoulias, N., Paraforos, D., Brandes, N., Fountas, S., Zude-Sasse, M. (2018). Calculating the water deficit of apple orchard by means of spatially resolved approach. In14th International Conference on Precision Agriculture (ICPA), 24. -27.06, Montreal, Quebec, Canada.

4.2.1. *Soil properties*

The results from soil sampling revealed that in the tested orchards the soil texture is characterized as silty sand and loamy sand. In the ANOVA analysis, with the ECa to be considered as the depended variable, it was observed that the ECa is affected by coarse silt, with F ratio = 6.3 and p = 0.09. Furthermore, the ordinary Kriging interpolation revealed that the highest values of ECa located mainly in the north and south part of the field, while the lowest values in the center of the orchard (Figure 18). Nevertheless, the soil texture analysis at 30cm showed low to middle variation (Table 6). The soil was mainly composed by sand and more specifically by middle sand, which also had a low coefficient of variance (CV = 12 %). The values of ECa varied between 10 to 27.26 mS m^{-1} characterized as low, between 27.27 to 39.22 mS m^{-1} as mid, and between 39.23 to 60 mS m^{-1}as high ECa zone.

Table 6. Descriptive statistic of soil texture. N= 20 the number of samples, providing standard deviation (SD), and coefficient of variance (CV).

	Mean	SD	Range	Minimum	Maximum	CV%
Fine silt [mg kg^{-1}]	26.00	8.12	27.00	11.00	38.00	31
Middle silt [mg kg^{-1}]	40.25	11.92	39.00	22,00	61,00	30
Coarse silt [mg kg^{-1}]	77.75	19.33	73,00	42.00	115.00	25
Fine sand [mg kg^{-1}]	302.85	60.76	228.00	153.00	381.00	20
Middle sand [mg kg^{-1}]	395.20	47.17	146.00	323.00	469.00	12
Coarse sand [mg kg^{-1}]	117.75	63.64	245.00	40.00	285.00	54

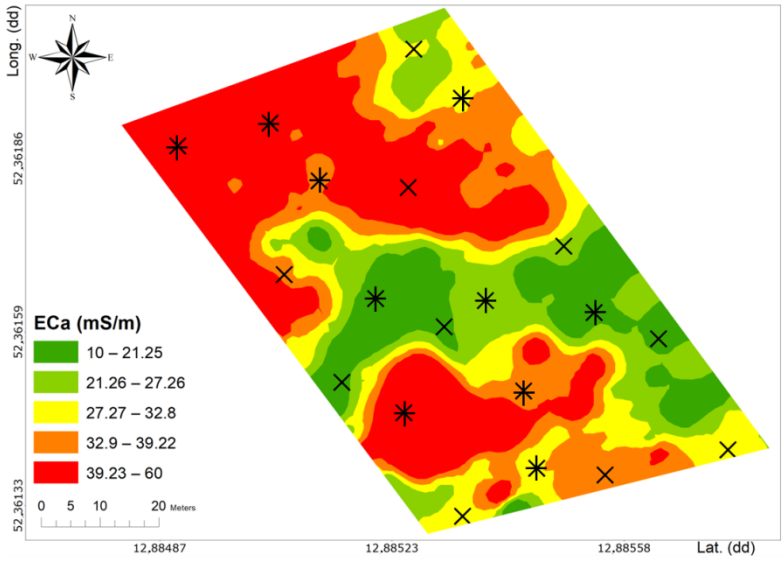

Figure 18.Thematic map of apparent soil electrical conductivity at 25 cm [mS m^{-1}]. The locations of guided soil samples at 30 cm are illustrated with crosses throughout the orchard. The locations of guided soil samples at 30 cm and LA measurement are illustrated with stars.

The mean value of bulk density was 1.08 g cm^{-3} and the mean porosity of the soil sample at 26.5%. The mean value of LA was 5.42 m^2 (Table 7). It should be noted that the values of TAW varied between 7.11 and 59.47 mm between sand and silt soils according soil texture analyses. At significance level of 5% using Pearson correlation, the soil texture partially correlated with the ECa: silt related positively (r = 0.52), while the sand was correlated negatively (r = -0.51). Furthermore, a significant correlation was observed between the ECa and the TAW r = 0.78 simply indicating that enhanced ECa areas can hold increased amount of water in the root zone. Recently, Lo investigated and correlated the spatial patterns of the available water in the root zone and the ECa (McCutcheon et al., 2006, Lo et al., 2017) confirming our results. Considering the plant response, in low ECa region the LA was 1.5 m^2, in mid ECa regions varied between 3 m^2 and 5.5 m^2, and in high ECa zone between 8 m^2 and 12 m^2., Consequently, the ECa was correlated with the LA in the present study (r = 0.80).

Table 7. Descriptive statistics for apparent soil electrical conductivity (ECa), total available water in the root zone (TAW) in 25 cm, porosity, bulk density (BD), and leaf area index (LA). N= the number of samples, providing standard deviation (SD), and coefficient of variance (CV).

	N	Mean	SD	Range	Minimum	Maximum	CV%
ECa [mS/m]	461	35.83	16.13	98.18	8.15	60	45
TAW [mm]	20	38.36	12.68	52.36	7.11	59.47	33
Porosity [%]	20	26.4	17.17	56.08	11.23	67.13	65
BD [g cm^{-3}]	20	1.08	0.19	0.60	0.87	1.47	17.98
LA[m^2]	10	5.42	3.50	9.69	1.50	11.19	65

4.2.2. *Water balance*

The precipitation rate remained low during the bud break in 2017. During full bloom, of the same year, frosts occurred, while the air relative humidity ranged between 65% and 80%, whilst in the rest of the season a decrease in the RH range was noted with values close to 90% at harvest (Figure 19).

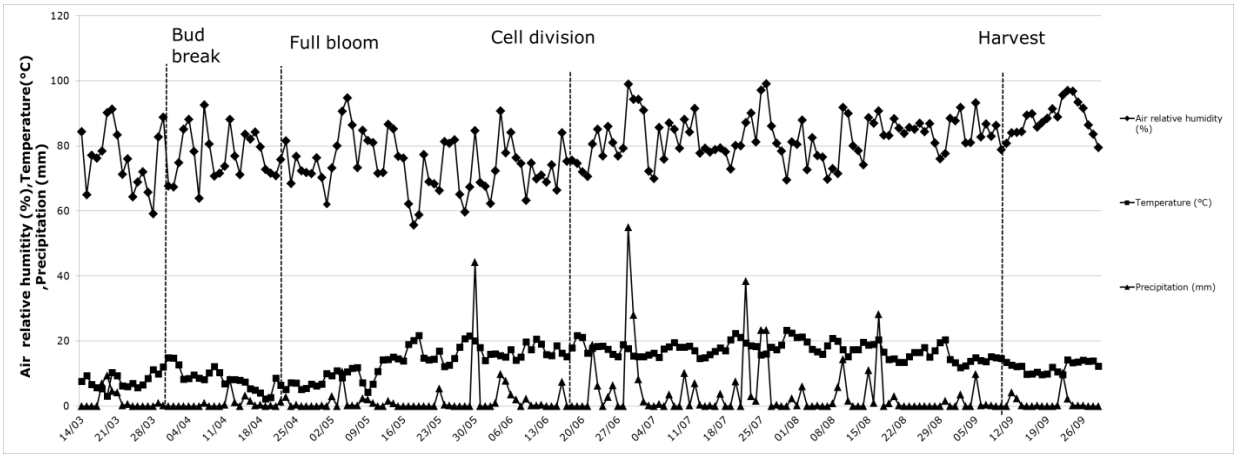

Figure 19. Daily weather conditions during the cultivation period in 2017 considering air humidity (circle), temperature (square) and precipitation rate (triangle).

The water balance model was employed to estimate the monthly water needs. The determination of the threshold according to the soil water properties and the influence of canopy size in the different ECa regions on ETc enabled the understanding of variance of spatially resolved daily water balance.

Low irrigation threshold was found for low ECa region and high irrigation threshold for high ECa area, since high ECa corresponds to enhanced volumetric water content and vice versa expressed as RAW. These two

thresholds were kept for all three ECa cases found in the orchard (Figure 20Figure 22). Furthermore, five values of LA, according to the range from the measured values, have been applied in the calculation of K_{cb} values in order to evaluate the effect of LA on the water needs in low, mid and high ECa soils.

In regions with low ECa values, the LA of 12 m^2 and 8 m^2 found steep fluctuations always above the thresholds, indicating water stress, with the highest water deficit of 180 mm after harvest period (Figure 3). The water needs for LA below 5.5 m^2 remained lower with the highest value reaching 80 mm during July. Furthermore, the reduced LA of 1.5 m^2 and 3 m^2 exceed the high threshold, corresponding to enhanced RAW, mainly during June and July.

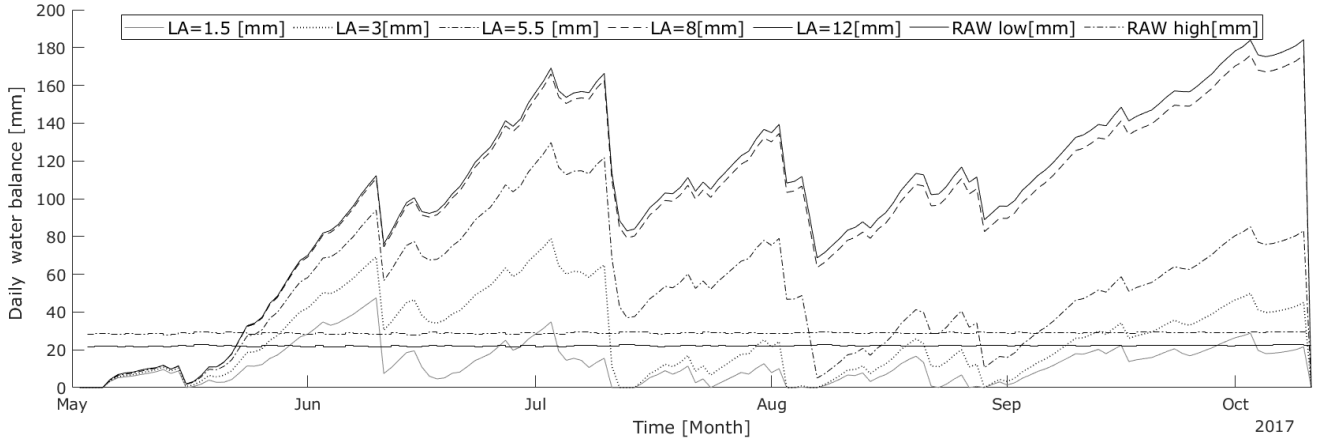

Figure 20. Simulation of LA values (1.5, 3, 5.5, 8 and 12) in Geisenheim model in low ECa regions [mm]. Readily available water content (RAW) in 80% field capacity from low ECa regions considered as two orchard-uniform thresholds values.

.

The trees from mid ECa showed reduced water deficit with the maximum value to be observed at 52.5 mm (Figure 20). More specifically, as a consequence of enhanced precipitation rate, two steep decreases have been noted during June and July in all models. The water needs of 5.5 m^2 LA and above reveal drought stress during June, July and late September. However, the trees with diminished LA of 1.5 m^2 had reduced water needs and only 3 m^2 exceeded the high and the low threshold during June, July. It should be noted that during May none of the LA values exceeded the thresholds, a fact which signifies that the trees did not face water stress in full bloom considering this mid ECa region of the orchard.

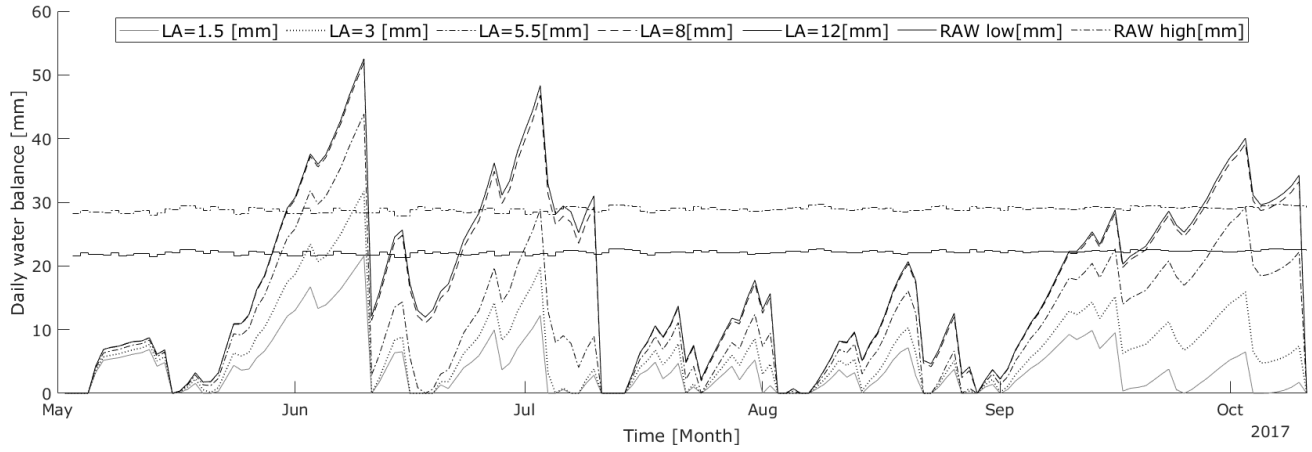

Figure 21. A Simulation of different LA values (1.5, 3, 5.5, 8 and 12) in Geisenheimer model in mid ECa regions [mm]. Readily available water content (RAW) from low ECa regions considered as thresholds values.

Trees from high ECa areas show slightly enhanced water needs compared to the mid ECa regions with maximum value around 63 mm. Similarly as in the previews graph, the pattern of water deficit for the LA remained the same. However, a slight increase in water needs of LA 5.5 m^2 and above was observed. Consequently, the water balance for these values point to drought stress between June and July and during August, which escalated during harvest period.

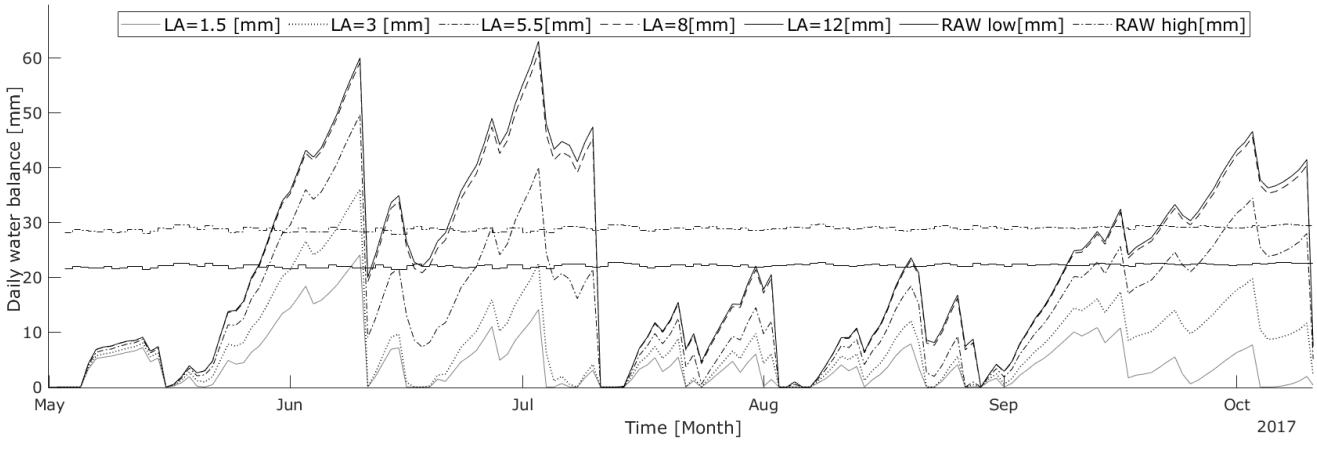

Figure 22. A Simulation of different LA values (1.5, 3, 5.5, 8 and 12) in Geisenheimer model in high ECa regions [mm]. Readily available water content (RAW) from low ECa regions considered as thresholds values.

The average monthly values from each ECa region were compared for each model. This was performed utilizing Kruskal and Wallis test, a non-parametric model used to test the differences among the models (Table 8). The

model of 1.5 m^2 and 3 m^2 LA were statistical different between low–mid ECa and low-high ECa regions ($p<0.05$), whereas no statistical significance have been observed in mid–high regions ($p = .429$, $p = .148$). However, the water balance of 5.5 m^2, 8 m^2 and 12 m^2 LA were different in all ECa regions.

Table 8. Kruskal- Wallis non parametric analysis among the water balance models for low, mid and high ECa areas.

Region	WB LA=1.5	WB LA=3	WB LA=5.5	WB LA=8	WB LA=12
Low ECa [mS/m]- Mid ECa [mS/m]	.000	.000	.000	.000	.000
Low ECa [mS/m]- High ECa [mS/m]	.000	.000	.000	.000	.000
Mid ECa [mS/m]- High ECa [mS/m]	.429	.148	.008	.024	.024

4.2.3.*Discussion*

The water demand was rapidly increased from bud break till the canopy was fully developed by the end of April. In parallel, the temperature rise and enhanced VPD increased the evapotranspiration demands. During June and July, the maximum water use takes place by the tree. A water balance experiment was utilized in citrus orchard, where researchers examined the differences on water balance of a non-irrigated area and an irrigated area at the same field (Petillo and Castel, 2007). They suggested that the variation in daily ET_c values, even in short intervals, in the same month could be due to lack of water availability to the trees or the influence of climatic conditions. Ferreira, (2017), suggested that due to the adaptation of perennial trees in soil conditions, the modeling of water balance considering the RAW and K_s need to be considered for an irrigation scheduling.

Implementing the LA in the WB showed that tree water needs can vary among ECa regions. In addition to that, the profound effect of tree structure in ET_c and consequently in water needs over the growing period was highlighted by increasing the LA. Naor et al., (2006), A positive relationship of LA with evapotranspiration rate was found in citrus and olive tree (Ayyoub et al., 2017). While the use of tree structural data such as LA over the growing season in WB can reduce the uncertainty in the estimation of daily K_c (Odi-Lara et al., 2016).

Consequently, the referenced K_c values from FAO can be optimized considering the actual plant, soil and the microclimate data from the field.

4.3. *Calculating the water deficit spatially using LiDAR laser scanner in an apple orchard*

Tsoulias, N., Paraforos, D. S., Fountas, S., & Zude-Sasse, M. (2019, July). Calculating the water deficit spatially using LiDAR laser scanner in an apple orchard. In Proceedings of the European 12th Conference of Precision Agriculture, Montpellier, France (pp. 8-11).

4.3.1. *Implementing leaf area in a water balance model*

The results from soil samples according to the guided soil sampling revealed that the soil texture was loamy sand. The highest ECa values were located in the northern extreme of the orchard while the lowest values in the middle section of the orchard (Figure 23). The values of ECa varied between 30.92 to 48.8 mS m^{-1} characterized as low, between 48.81 to 54.04 mS m^{-1} as mid, and between 54.05 to 77 mS m^{-1} as high ECa zones.

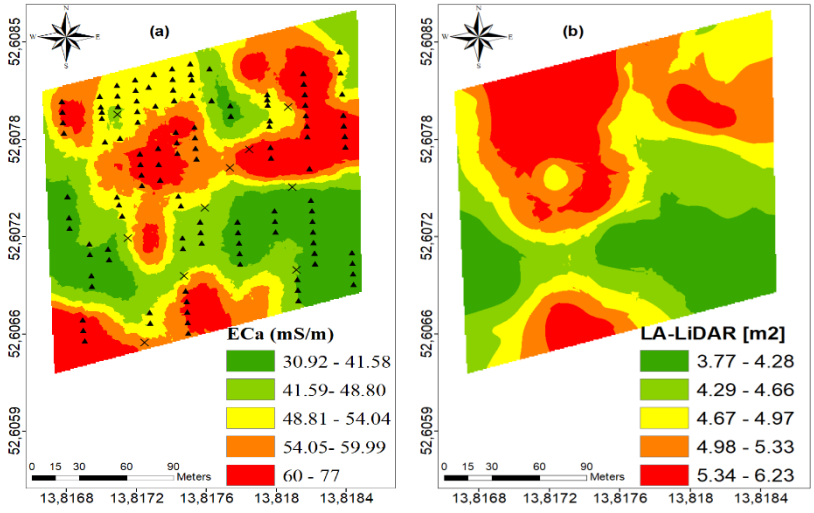

Figure 23 Spatial distribution of (a) EC_a [mS m^{-1}] and (b) LA. In ECa map the sample locations are illustrated with triangles whereas the soil samples with crosses.

Table 9. Pearson correlation between apparent soil electrical conductivity (ECa) and LA. n = the number of samples. Correlation at 0.01 level (**) and at 0.05 (*) level of significance.

	N	Low EC_a	Mid EC_a	High EC_a
LA[m^2].	28	0.74*	0.86**	0.68**

A significant correlation was revealed between the LA_{Manual} and the PPT from the six defoliated trees ($r^2 = 0.87$). The LA revealed a similar spatial distribution with ECa (Figure 24b). This was also described by a significant

correlation between the ECa and the PPT (Table 9). A result which indicates that trees in areas of high ECa can have larger canopy surface compared to low ECa areas.

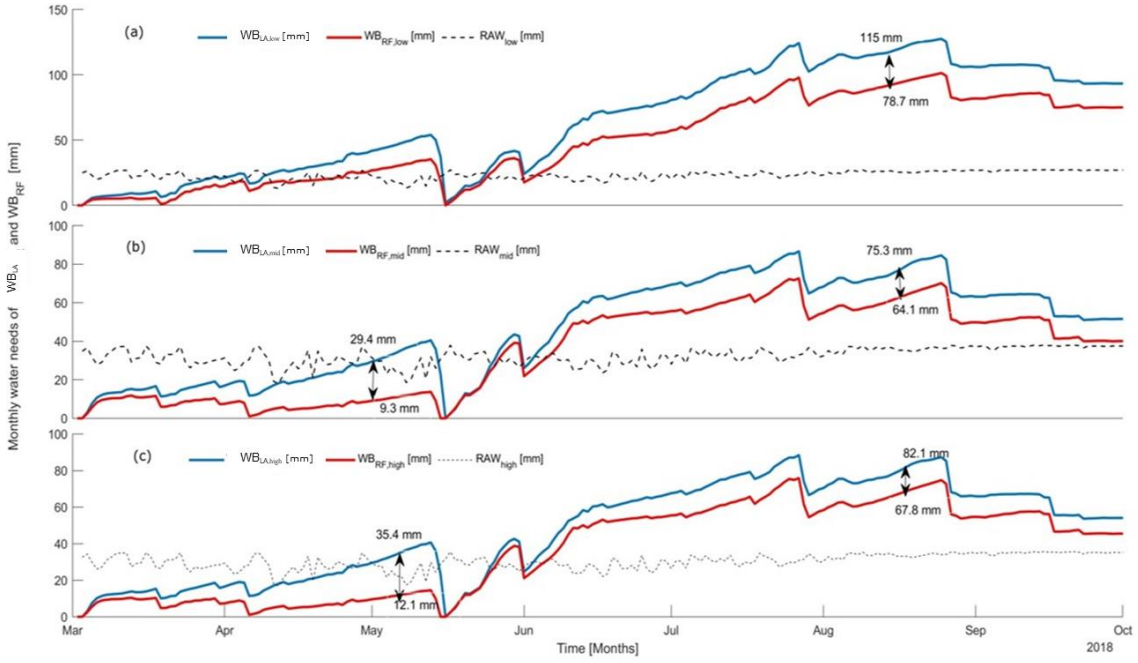

Figure 24 Water needs [mm] according to water balance model for tabulated values from FAO (WB_{RF}) and considering the leaf area per tree measured by means of LiDAR (WB_{LA}) in low (a), mid (b), and high (c) regions of soil electrical conductivity (EC_a). Readily available water content (RAW) in low (RAW_{low}), mid (RAW_{mid}) and high (RAW_{high}) EC_a region were set as thresholds, respectively.

Frosts occurred from April to May in 2018. Precipitation remained low during the full bloom. In June, precipitation height above 30 mm were recorded, representing an extremely dry year for this area (overall precipitation height: 295 mm). The air relative humidity fluctuated from 40% to 85%, between full bloom and harvest. The temperature descended, while the precipitation remained below 8 mm during harvest and leaf drop.

The highest water demands were traced during harvest in low ECa areas with 78.7 mm for WB_{RF} and 115 mm for WB_{LA} (Figure 2). The WB_{RF} dispersion around the mean was enhanced in comparison with the WB_{LiDAR}, especially in July in mid ECa areas (C.V. % = 60.52). However, none of the models showed significant variation between May and June in all ECa regions.

The results of WB_{RF} and WB_{LA} illustrate the same patterns in all ECa regions (Figure 2). A steep drop of water needs occurred in May due to increased precipitation. In low ECa areas, the water needs according to WB_{LA} overpassed the threshold (RAW_{Low}) in early June in comparison with mid and high ECa in the end of this month.

Moreover, WB_{RF} revealed 20.2 mm and 23.3 mm less water need from WB_{LA}, resulting no water stress during May, in mid and high ECa areas, respectively. Furthermore, in August and September, a difference of approximately 36.3 mm was found between WB_{LA} and WB_{RF}, in low ECa areas.

4.3.2. ***Discussion***

Scanning with the LiDAR sensor allowed to sample the 3D structure of trees at different locations of the orchard. However, extracting the points from each tree does not provides a direct indication about plant geometry or physiology. Relating the LA_{Manual} with the corresponding PPT allowed the LiDAR spatial information conversion to LA. The LA was inhomogeneous through the field, while it was shown that can be influenced at different ECa levels. The implementation of LA in the WB calculation, considering the ECa properties of the field increased water needs compared to FAO referenced values (WB_{RF}). In this study, the results revealed that trees in low EC_a areas had reduced LA and enhanced water stress. However, the WB_{LA} did not differ significantly from the WB_{RF} in all months. Ferreira (2017), pointed out that perennial trees adapt to soil conditions, and the modelling of water balance needs to take into account the plant structure, RAW and Ks coefficient based on field conditions for an irrigation scheduling.

A steady deficiency of water were illustrated after harvest, nevertheless both models remained above their thresholds. It is well known that plants reduce transpiration rate under drought stress due to physiological responses such as stomatal closure and subsequent reductions in photosynthesis rate. Furthermore, water stress adversely affects the physiological and nutritional development of crops, leading to reduced biomass, yield, and quality of crops (Rossini et al., 2013). Also, the variation in rooting depth with soil texture can affect the water needs spatially (Pérez-Pastor et al., 2014).

4.4. *Vegetative factors of tree volume per ECa level*

Tsoulias, N., S. Fountas & Zude-Sasse, M. (2021). Estimating the canopy volume using a 2D LiDAR in apple trees. virtual 4th International Symposium on Horticulture in Europe (SHE/Virtual), 8. -11.03, Stuttgart, Germany. (In print)

The EC_a ranged between 1.08 and 13.06 mS m^{-1} with 2.57 mS m^{-1} standard deviation (SD), whereas the slope varied between 0.53 and 8.80 % with 1.55% SD. The variability of EC_a (CV=34.1%) and slope (CV=2.23%) remained low. The highest values of the EC_a were mainly detected in the regions enhanced slope between 2.82 and 8.80 % (Figure 25). In fields where the slope is the dominant factor of soil formation the lower terrain, North East area of this field, is usually characterized by sediments providing enhanced water holding capacity, which can explain the enhanced ECa values (Tardaguila et al., 2011).

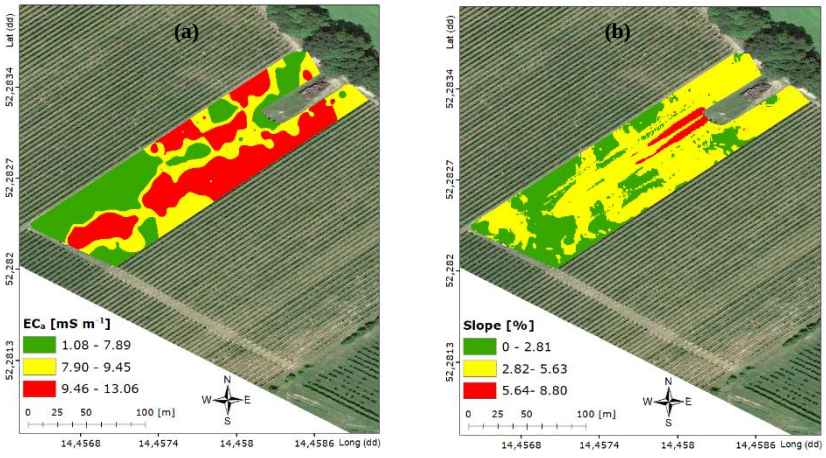

Figure 25. (a) Spatial distribution of ECa [mS m^{-1}] and (b) slope [%].

In the regions of low and middle slope, tree canopies show middle and high volume. In particular, the trees with higher canopy volume were observed in the west side of the orchard during full bloom and fruit set (Figure 26, b), whereas a second patch of the same class was traced in the east region of the field before harvest (Figure 26, c). Moreover, the lowest values of V_{LiDAR} were observed in the north and east side of the orchard. This assumption was evident by the negative correlation of V_{LiDAR} and the slope during FB (r = -0.63), FS (r= -0.66) and BH (r = -0.56) (Table 10). On the other hand, the ECa was also negatively related with the $V_{LiDAR,FB}$ (r= -0.55), and $V_{LiDAR,BH}$ (r = -0.58).

Table 10. Linear regression coefficient of apparent soil electrical conductivity (ECa) and elevation with V_{LiDAR} (n=1109) during full bloom ($V_{LiDAR,FB}$), fruit set ($V_{LiDAR,FS}$) and before harvest ($V_{LiDAR,BH}$).

	$V_{LiDAR,FB}$	$V_{LiDAR,FS}$	$V_{LiDAR,BH}$
ECa [mS m^{-1}]	-0.55	-0.45	-0.58
Slope [%]	-0.63	-0.66	-0.56

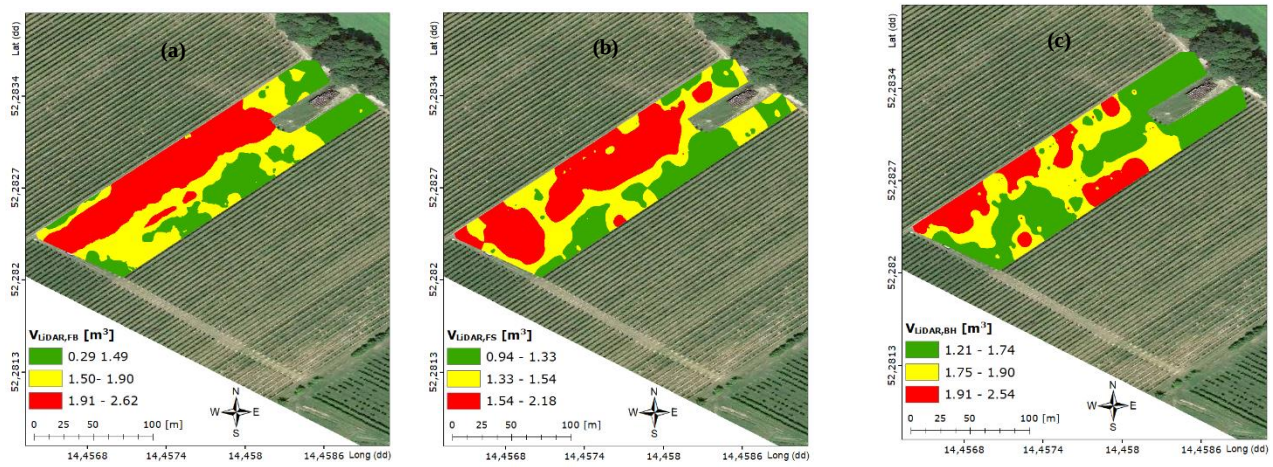

Figure 26. Spatial variability of tree canopy volume [m^3] during (a) full bloom ($V_{LiDAR,FB}$), (b) fruit set ($V_{LiDAR,FS}$) and (c) before harvest ($V_{LiDAR,BH}$).

Table 11 Tree canopy volume [m^3] during full bloom ($V_{LiDAR,FB}$), fruit set ($V_{LiDAR,FS}$) and before harvest ($V_{LiDAR,BH}$) categorized based on the soil electrical conductivity, low ($ECa_{,Low}$), mid ($ECa_{,Mid}$) and high ($ECa_{,High}$) regions. Maximum (Max), minimum (Min), standard deviation (SD), coefficient of variation (CV).

			Mean [m^3]	SD [m^3]	Min [m^3]	Max [m^3]	CV [%]
		$V_{LiDAR,FB}$	1.71	0.49	0.73	2.89	28.65
$ECa_{,Low}$	n=322	$V_{LiDAR,FS}$	1.91	0.43	0.32	3.11	22.51
		$V_{LiDAR,BH}$	1.99	0.45	0.58	2.62	22.61
		$V_{LiDAR,FB}$	1.47	0.37	0.73	2.79	25.17
$ECa_{,Mid}$	n=334	$V_{LiDAR,FS}$	1.68	0.38	0.90	2.82	22.61
		$V_{LiDAR,BH}$	1.72	0.39	0.60	2.62	22.67
		$V_{LiDAR,FB}$	1.34	0.38	0.95	2.71	28.35
$ECa_{,High}$	n=453	$V_{LiDAR,FS}$	1.67	0.44	0.81	3.20	26.34
		$V_{LiDAR,BH}$	1.70	0.45	0.64	2.85	26.47

4.4.1. *Growth rate*

In comparison with the $ECa_{,Mid}$ and $ECa_{,High}$, the apple trees in $ECa_{,Low}$ regions revealed the highest mean values of V_{LiDAR} considering all growth stages, reaching 1.99 m^3 before harvest (Table 11). The mean value $V_{LiDAR,FB}$ was increased by approximately 0.3 m^3 between FB and BH in $ECa_{,Low}$, whereas the SD ranged greatly from 0.45 to 0.49 m^3. In $ECa_{,Mid}$ regions, the mean values ranged from 1.47 to 1.72 m^3 between FB and BH, revealing also the lowest SD values among the rest EC_a regions. However, the highest rise of V_{LiDAR} was observed between FB (1.34 m^3) and BH (1.70 m^3), reaching 0.36 m^3 in $ECa_{,High}$. Furthermore, the maximum V_{LiDAR} values were detected during FS and BH from the trees of the same area, 3.20 and 2.85 m^3, respectively. Variability in all ECa areas over the growth stages (FB-BH) ranged from 22.61 to 28.65 %.

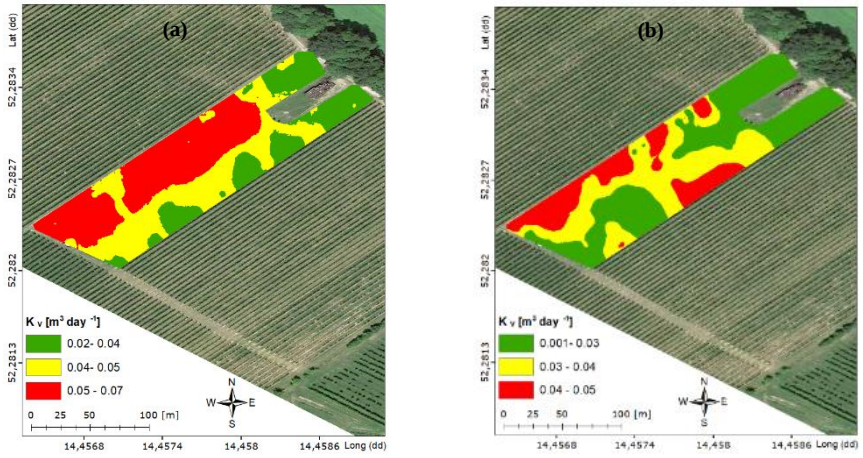

Figure 27. Spatial variability of canopy growth between (a) full bloom (FB) and fruit set (FS) and (b) fruit set (FS) and before harvest (BH).

Spatial variability of canopy volume might be affected by the heterogeneity of local topology of the orchard and the soil texture. The monitoring of canopy volume once or throughout the vegetation period allows the generation of growth maps (Figure 27). The highest tree K_v values between FB and FS were classified from 0.05 to 0.07 m^3 day^{-1} and were delineated in the west south side of the orchard, where the slope was no greater than 2.81% (Figure 27a). The areas of low K_v were mainly detected in north and east edges of the orchard, ranging from 0.02 to 0.04 m^3 day^{-1} between the cell division and harvest was observed in regions of high ECa. However, the spatial pattern of K_v between FS and BH differentiated, due to the decrease of K_v by approximately 0.01 m^3 day^{-1}

(Figure 3b). Therefore, most of the apple trees were classified with low K_v, ranging from 0.001 to 0.03 m^3 day^{-1}, which were mainly found in the north and south east side of the orchard. Overall, the mean variation of V_{LiDAR} in the three ECa levels showed different increment of growth during the vegetation period (Figure 42). The V_t curve in $ECa_{,Low}$ ($V_{t,Low}$) reached the maximum volume (2 m^3) 81 DAFB. Whereas, at the same period, the V_t curve of apple trees in $ECa_{,Mid}$ ($V_{t,Mid}$) and $ECa_{,High}$ ($V_{t,High}$) was approximately 30% lower than $V_{t,\,Low}$. The $V_{t,Mid}$ and $V_{t,High}$ reached the maximum values of 1.70 and 1.67, respectively, at the same time.

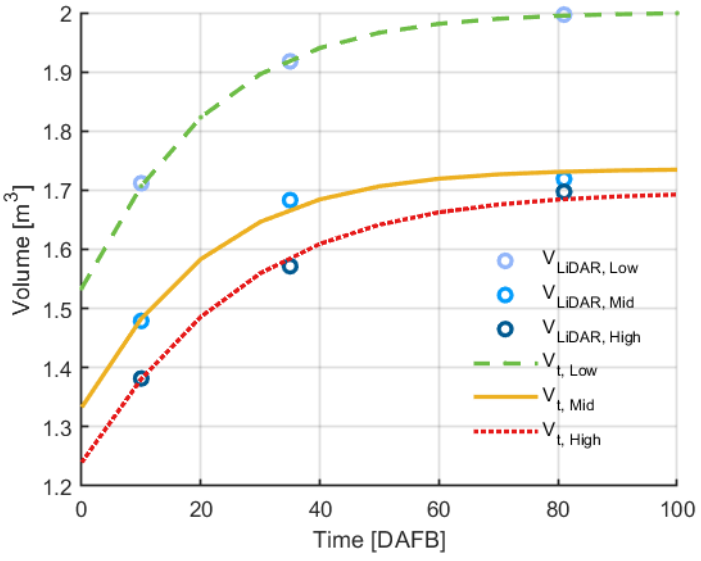

Figure 28. Averaged growth curve of canopy volume [m^3] in low ($V_{LiDAR,\,Low}$), mid ($V_{LiDAR,\,mid}$) and high ($V_{LiDAR,\,High}$) ECa regions during the developmental stages.

4.4.1. *Discussion*

Vegetative factors of tree volume per ECa level

From a macroscopic perspective, a rinse of soil was noted from the south to north part of the orchard, where the slope was reduced. The latter hypothesis was confirmed by the correlation of ECa with the slope, illustrating high values in the north-west part of the orchard. However, the V was negatively related with the latter parameters over the season, illustrating trees with higher values in areas of $ECa_{,Low}$. The opposite may have been assumed from earlier work (Käthner and Zude, 2015) in young trees and the assumption of high correlation between growth and soil water (and nutrient) content, which should be enhanced in the high ECa region. The fact that the trees can adapt

to the environmental conditions by developing deeper root systems in lower ECa soil, allowing them to have higher availability of soil water content, could possibly explain the high $V_{t,Low}$ (Tsoulias, et al., 2020). Furthermore, this assumption is likely if the water and nutrients are considered limiting factors, while in orchards with drip irrigation and fertigation, effects are outweighed. Colaço et al., (2019), observed the spatial relationship of canopy V and height with the historical yield and ECa in three different orange groves. The V was spatial and temporally related with the yield and ECa in 2 of the 3 orchards, suggesting that V information can improve the identification of management zones in yield and soil attributes.

Growth rate

Monitoring the volume of apple trees over the season spatially, enabled to estimate their growth rate (K_v). The spatial maps depicted higher K_V in the west side of the orchard the, especially between full bloom and fruit set. Recent studies in viticulture showed that vegetative and reproductive growth can have similar spatial patterns with the ECa at different growing stages. Manfrini et al., (2020) observed no affect among the spatial patterns of ECa, apple tree growth, suggesting the necessity of over time spatial plant data to improve site specific management within the orchard. On the other hand, using spatio-temporal plant data allowed to model V and increase the resolution of growth models. Whereas, shorter time intervals within the LiDAR measurements could potentially provide higher resolution in the curve per ECa level, allowing the application of site specific management. The growth of the V influences the fruit crop load and the fruit size. More specifically, the daily carbon demand of growing fruit is associated with the photosynthetic capacity and the vegetative growth of each individual tree(Robinson et al., 2017). Penzel et al., (2020) estimated the daily carbon requirement of seasonal apple growth and the associated demand of LA. In their model, the LA carbon demand calculated based on LiDAR laser hits per tree, suggesting the feasibility to predict the target fruit number and the significance of seasonal LA data in crop load management.

4.5. *Effects of soil ECa and LiDAR-derived leaf area on fruit quality and yield in the apple production*

Tsoulias, N., G. Xanthopoulos, S. Fountas & Zude-Sasse, M. (2021). Effects of soil ECa and LiDAR-derived leaf area on fruit quality in apple production. (Submitted)

4.5.1. *Wood segmentation and its impact on leaf area estimation*

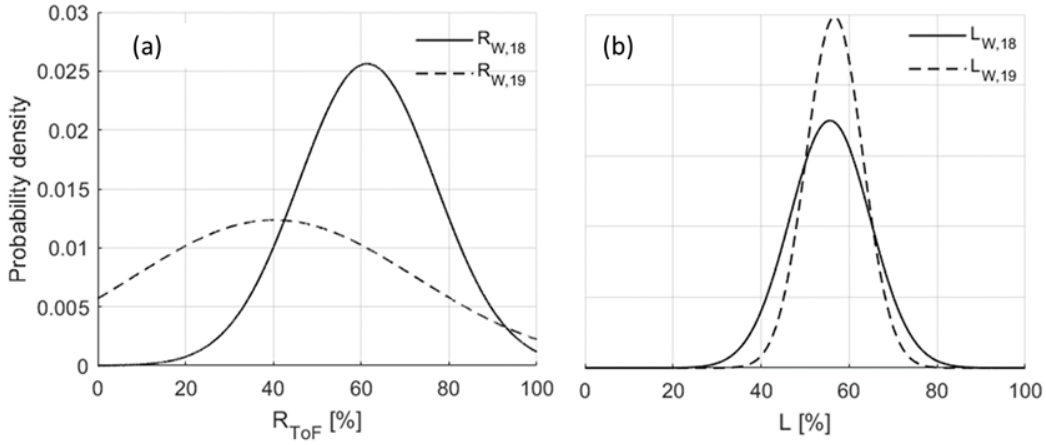

Figure 29 The probability density of wood considering (a) calibrated reflectance intensity (RW,year) [%], (b) and linearity (LW,year) [%] measured 10 days after bud break in years 2018 and 2019 (n = 16).

The probability of segmented woody parts at $DABB_{55}$ ranged between 28 % to 55 % in 2018, whereas in the following year 2019, values appeared in a broader range from 35.5 % to 65.4 % (Figure 3). Leaves expanded in terms of size during canopy development, which resulted in enhanced leaf surfaces and reduced percentage of wood parts considering the entire canopy point cloud (Figure 30a, b). In year 2018, first and second measuring date showed coinciding probability of woody parts. The mode value of woody parts marginally changed with 43 % and 44 % in $DABB_{55}$ and $DABB_{85}$, respectively. Whereas in the following year 2019, probability of wood decreased from 50 % at $DABB_{55}$ to 42 % at $DABB_{85}$ due to leaf expansion. In 2018, the probability of wood parts decreased $DABB_{115}$ showing high variation ranging from 15 % to 60 % and further decreased on $DABB_{140}$. In year 2019 the last two measuring dates $DABB_{115}$ and $DABB_{140}$ showed already coinciding patterns resulting in highest likelihood (mode) at 28.3 %.

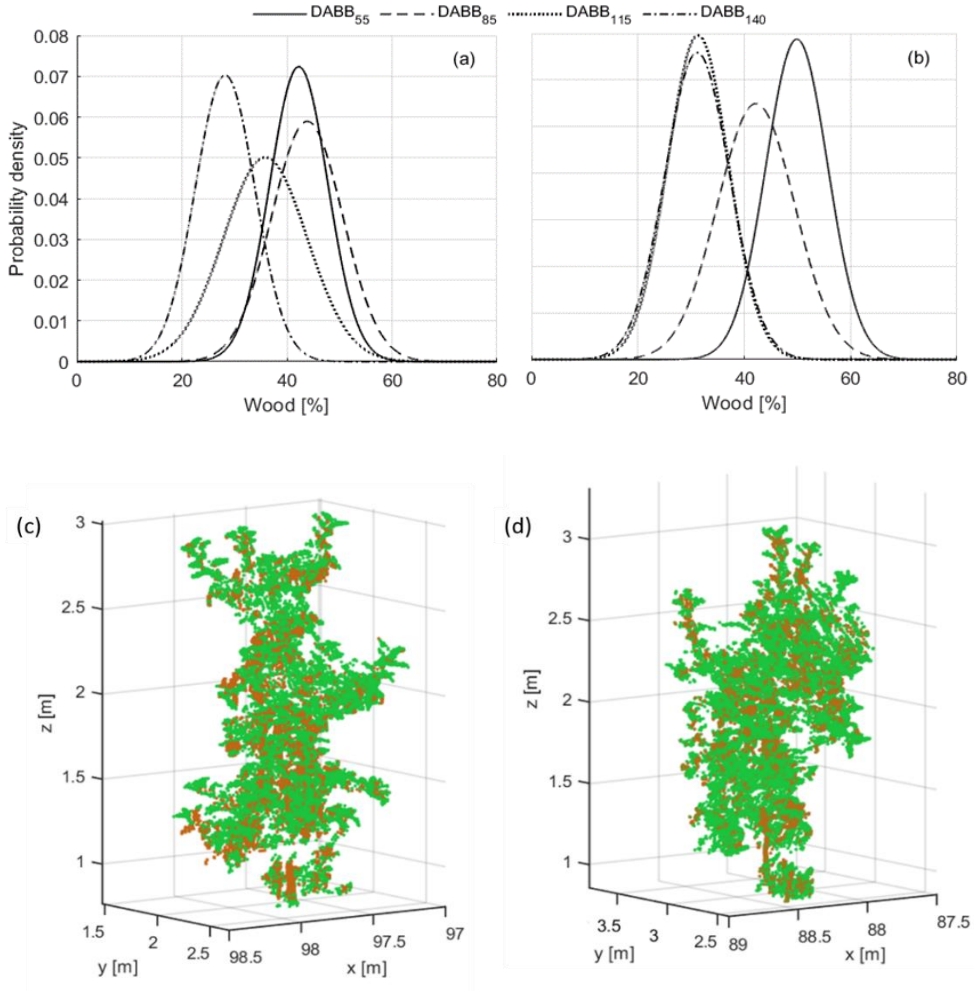

Figure 30 In years 2018 (a,c) and 2019 (b,d), subplots present the probability density of percentage of wood considering the entire tree point cloud (n = 4506) at 55, 85, 115, 140 days after bud break (DABB), and 3D point cloud of medium sized tree at the last measuring date $DABB_{140}$, when mature canopies appeared.

Destructive measurements of LA_{Manual} and points per tree excluding points of wood were used to build a linear regression model for estimating the LA of each tree from the 3D tree point clouds (Figure 31). Cross-validation of LA calibration model was performed including all phenological stages, before and after the exclusion of woody parts from tree 3D point cloud (Table 31). Retaining the wood points in the tree point cloud resulted in $R^2_{adj,\ CV}$ = 0.81 with $RMSE_{CV}$ = 7.85 %. After removal of points, which exceeded the RW and LW thresholds that are assumed to represent wood, the measuring uncertainty was reduced at 4.52 % considering RMSECV. Consequently, the LA estimation showed an enhanced $R^2_{adj,\ CV}$ = 0.92 and this model was used to calculate the LA_{LiDAR} of each tree scanned (n = 4506) in the orchard.

Table 12. Calibration and cross validation results of leaf area (LA) estimation from 3D tree point cloud (LA_{LiDAR}) and manual analysis (LA_{Manual}) (n = 32, excluding one tree as outlier, in total 31 trees) before and after removal of wood parts and considering all growth stages of both years; providing root mean squared error of calibration (RMSEc) and in leave-one-out cross validation RMSEcv), adjusted coefficient of determination of calibration ($R^2adj_{,C}$) and cross validation ($R^2_{adj,CV}$).

	$RMSE_C$ [%]	$R^2_{adj,C}$	$RMSE_{CV}$ [%]	$R^2_{adj,CV}$
with Wood	6.56	0.82	7.85	0.81
without Wood	3.31	0.95	4.52	0.92

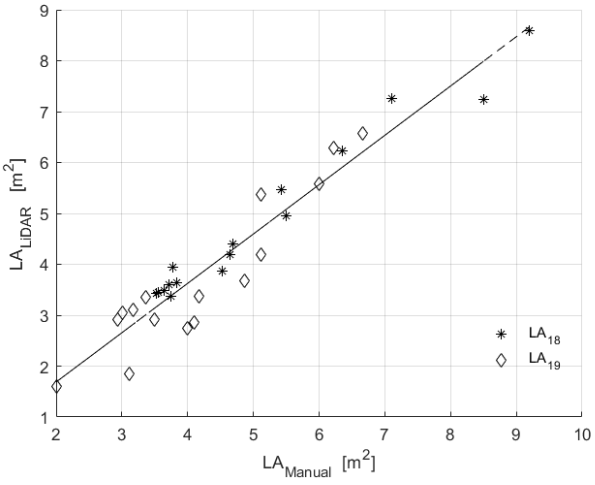

Figure 31. Linear relationship between the manual (LA_{Manual}) and LiDAR based measurements of leaf area (LA_{LiDAR}) (n = 31) after removing points of wood from entire points per tree (PPT), including all growth stages of years 2018 and 2019. LA = 0.92 × PPT

The regression model of each individual growth stage was considered to convert the points per tree (PPT) to LA after subtracting the points of woody parts of the canopy.

4.5.2.*Growth factors*

Weather conditions and soil variability were recorded, since they are determinants for yield and fruit quality. According to the daily weather data, frosts occurred at the beginning of March in 2018, during bud break, reaching -10 °C, whereas no frosts were indicated in 2019 (Figure 32). Frost in 2018 affected the vegetative growth, visible as leaf damage in early foliage development, while no effect on the flower set was observed occurring in April. During cell division of the latter year high precipitation rates > 40 mm were monitored, in contrast with 2018, which appeared as a relatively dry year.

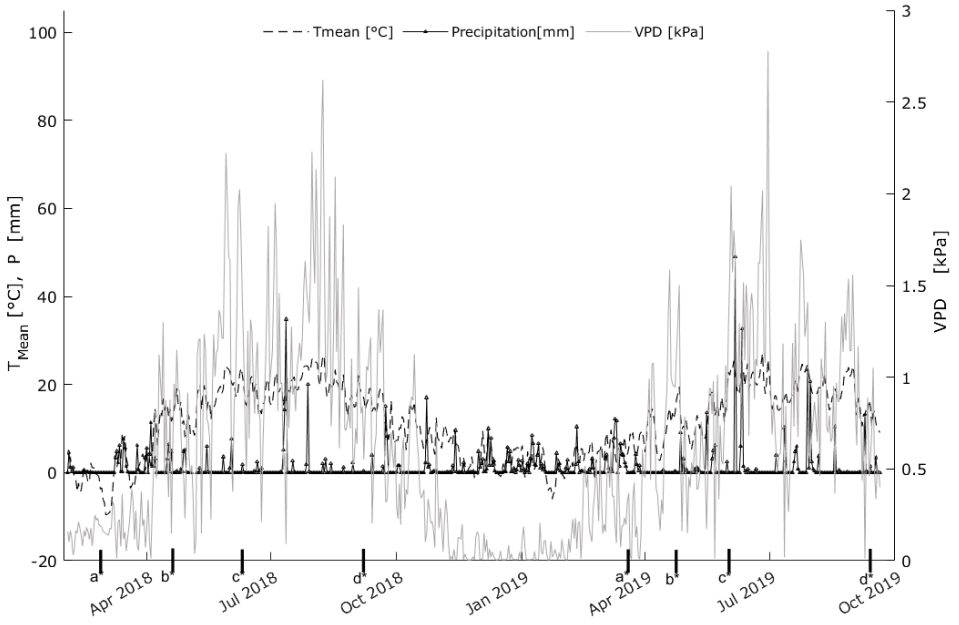

Figure 32. Daily weather conditions within the cultivation period indicating the phenological stages of the flower and fruit in 2018 and 2019. a* bud break, b* full bloom, c* cell division, d* harvest.

While weather can be considered similar in the entire orchard, the soil showed typical variability frequently found in the Brandenburg fruit growing region. The apparent soil electrical conductivity (ECa) ranged between 2.78 mS m^{-1} and 8.66 mS m^{-1} in 2018, while values appeared enhanced ranging from 4.47 mS m^{-1} to 14.85 mS m^{-1} in 2019 (Figure 33). The lowest ECa revealed in the south west and east regions, whereas highest values accumulated in the north east and south east side of the orchard in 2018. In the following year, the low ECa areas appeared in the south west side and two patches of high ECa were found diagonally in the south and north side of the orchard. From visual comparison of the two maps, the spatial correlation is evident due to extended high ECa areas in the north east side of the orchard appearing in both years. Moreover, similar coefficients of variation of ECa maps were depicted, in 2018 (CV = 20.3 %) and 2019 (CV = 20.6 %), with strong spatial dependence (Table 13).

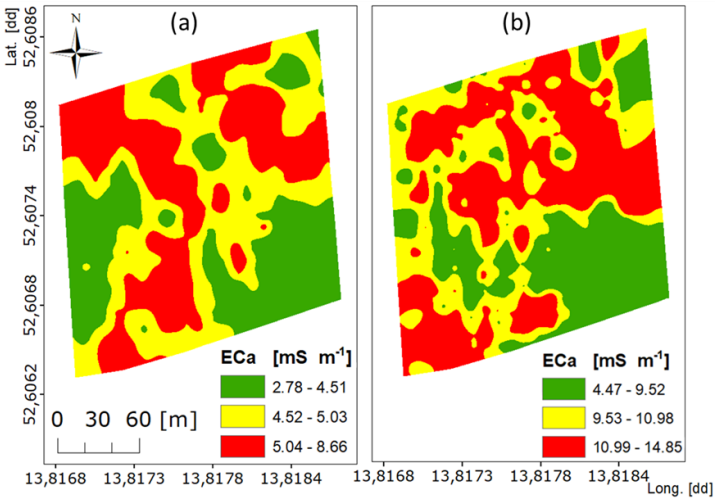

Figure 33. Spatial distribution of apparent soil electrical conductivity (ECa) [mS m-1] in (a) 2018 and (b) 2019.

Table 13. Descriptive statistics of leaf area (LA) at 55, 85, 115, 140 days after bud break (DABB), apparent soil electrical conductivity (ECa) and yield in 2018 and 2019. Standard deviation (SD), coefficient of variation (CV), spatial dependence (SpD) are provided.

		Mean	SD	CV [%]	SpD
2018	LA_{55} [m^2]	3.46	0.66	19.01	0.71
	LA_{85} [m^2]	5.58	0.43	7.71	0.65
	LA_{115} [m^2]	5.16	0.58	11.24	0.47
	LA_{140} [m^2]	6.25	0.36	5.76	0.50
	ECa [mS m^{-1}]	5.18	1.05	20.27	0.42
	Yield [kg]	14.1	0.43	30.49	0.45
	Crop load [fruit $tree^{-1}$]	92.26	27.74	30.01	0.37
2019	LA_{55} [m^2]	4.43	0.75	16.93	0.58
	LA_{85} [m^2]	6.26	0.55	8.78	0.51
	LA_{115} [m^2]	6.01	0.37	6.15	0.42
	LA_{140} [m^2]	7.15	0.28	3.91	0.45
	ECa [mS m^{-1}]	5.92	1.22	20.59	0.51
	Yield [kg]	19.1	0.48	25.36	0.48
	Crop load [fruit $tree^{-1}$]	105.2	27.4	26.05	0.42

4.5.3. *Vegetative growth*

The mean of LA increased from 3.46 m^2 to 6.25 m^2 during vegetation period 2018, whereas in the following year trees developed higher LA with 4.43 m^2 and 7.15 m^2 between $DABB_{55}$ and $DABB_{140}$, respectively (Table 13). Trees with lower LA occurred in the south and middle part of the orchard in both years (Figure 34a). Spatial patterns of high LA appeared in the west region of the orchard while the east side was characterized mainly by middle LA trees at $DABB_{85}$ (Figure 34b). Whereas in the latter growth stages trees of high LA were distributed in the west and north regions of the orchard in 2018 (Figure 34c, d).

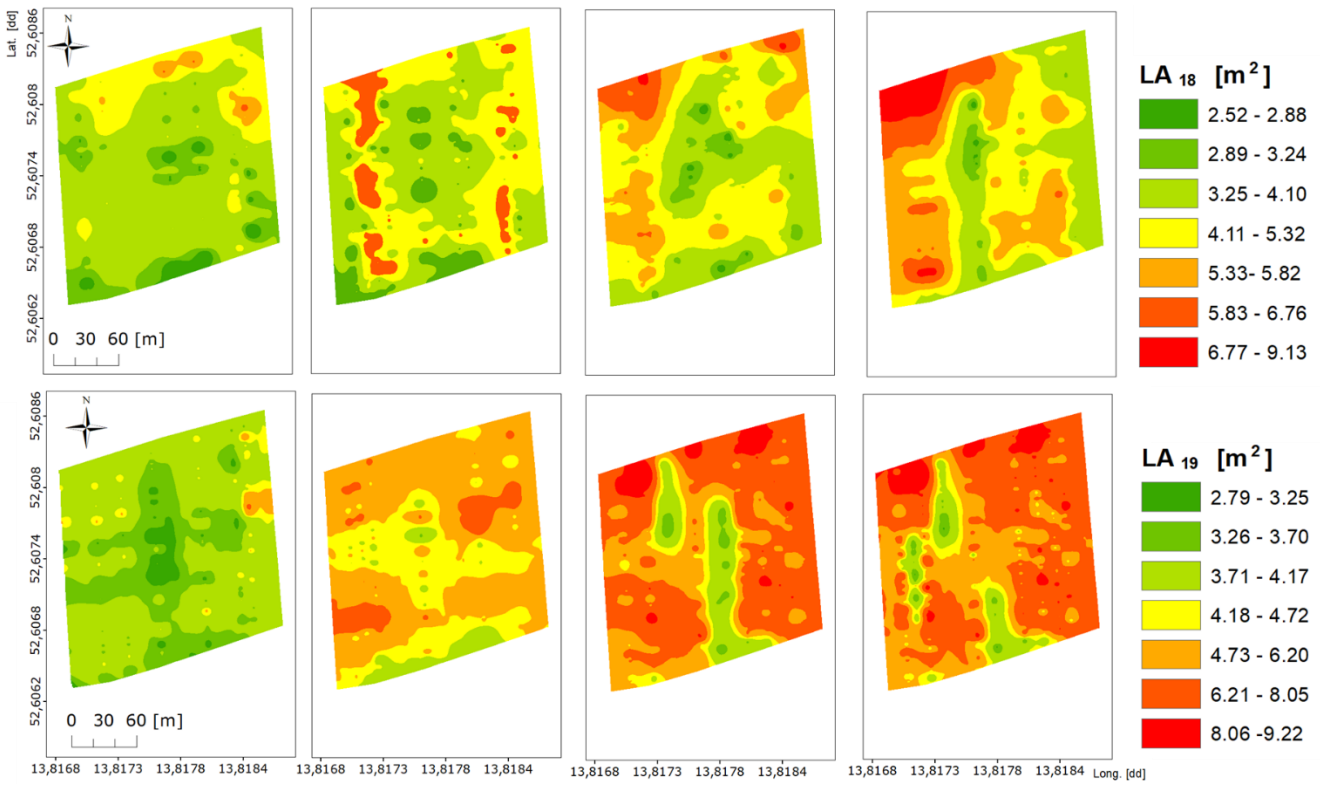

Figure 34. Spatial distribution of leaf area (LA) [m^2] (n =4506 at 55, 85, 115 and 140 days after bud break in 2018 (upper row, a-d) and 2019 (lower row, e-h).

Moreover, a correlation coefficient (r = 0.55) was observed between LA_{55} and LA_{115} in 2018, while correlation between the earlier stages of the same year was reduced. This was the period when slight frost damage was visible on the leaves, whereas, subsequently, foliage developed visually more homogeneously. In 2019, areas of low LA were initially found in the middle of the field and extended towards the south region of the field (Figure 7e). The variability found in LA_{115} matched with LA_{140} (r = 0.62). However, the highest relationship (r = 0.87) was indicated between LA_{115} in 2018 and 2019. The ECa_{18} was correlated with $LA_{140,18}$ (r = 0.53), but no consistent spatial correlation between ECa and LA was found in 2018. In the following year, correlation of ECa_{19} and LA was enhanced with r = 0.51 at $LA_{85,19}$ and r = 0.62 at $LA_{140,19}$.

4.5.4.*Growth rate*

The growth curve of LA was simulated per experimental year by a logistic model interpolating the experimental values from all trees (Figure 8). The growth curves of LA indicated that 55.4% and 62.4% of the total LA expanded until $DABB_{85}$ in 2018 ($G_{LA,18}$) and 2019 ($G_{LA,19}$), respectively (Figure 35 a).

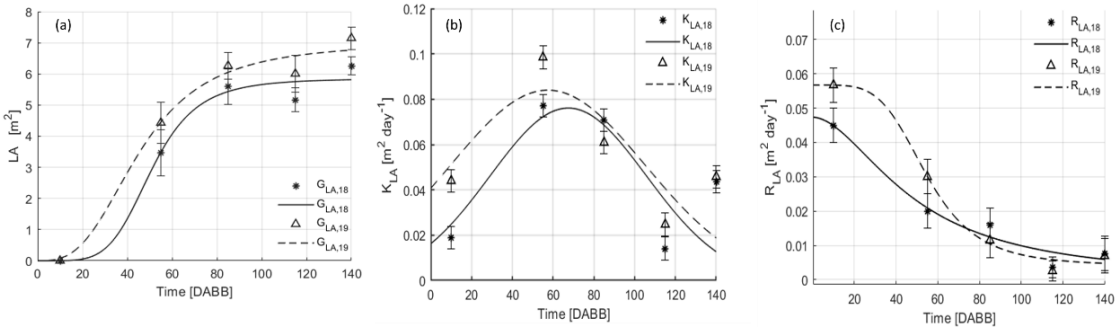

Figure 35. Analysis of leaf area (LA) in terms of (a) growth curve (G_{LA}), (b) absolute growth rate (K_{LA}) and (c) relative growth rate (R_{LA}) in 2018 and 2019.

Consistently with the hysteresis of LA growth and the occurrence of frost in March 2018, canopies were fully developed in 105 and 95 DABB during 2018 and 2019, respectively. The $G_{LA,19}$ was 13.03% higher than $G_{LA,18}$ at last measuring date ($DABB_{140}$). The impact of frost was also measurable in the $G_{LA,18}$ data (Figure 8b). Furthermore, the absolute growth rate of LA in 2018 ($K_{LA,18}$) was 0.07 m^2 day^{-1} compared to $R_{LA,19}$ = 0.10 m^2 day^{-1} in subsequent year without frost events (Figure 35 c).

4.5.5. *Yield*

Each year, yield and crop load data were obtained in tree-wise (n = 120) sorting line measurements. In total 10980 and 12508 apples were analyzed in 2018 and 2019, respectively. Similar spatial patters can be noticed when comparing the maps of yield and crop load (Figure 36). A consistent pattern of variability was visually observed between crop load maps of both years (Figure 36a,b) and yield maps comparing the two years (Figure 36c,d). Consequently, the two spatial data were correlated. The fruit yield per tree ranged between 6.77 kg and 21.71 kg in 2018. In the following year, the orchard gained higher yield reaching 32.64 kg. Low and moderate correlation

coefficients were estimated for ECa and yield as r = 0.44 and r = 0.58 in 2018 and 2019, respectively. In both years, LA at harvest, $LA_{140,18}$ and $LA_{140,19}$, appeared correlated with yield, r = 0.48 and r = 0.52, respectively.

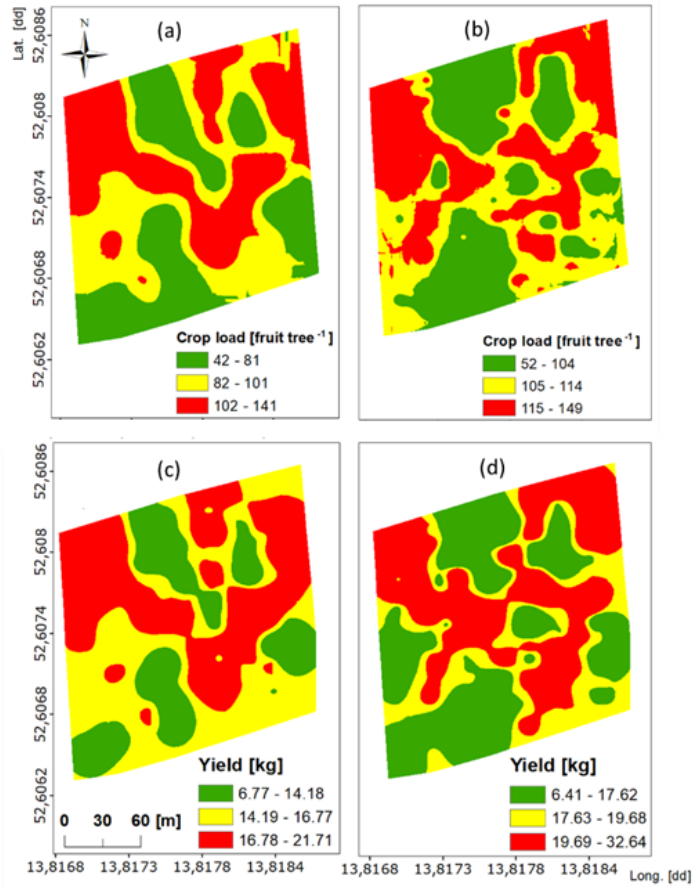

Figure 36. Spatial distribution of crop load (number of fruit per tree) (a,b) and yield [kg] per tree (c,d) (n = 120 trees) in 2018 (a,c) and 2019 (b,d).

4.5.6. *Classification of fruit quality at harvest based on soil ECa and leaf area*

Red blush colour on 100% of the fruit's surface was reached in all apples at harvest. Flesh firmness decreased over the growth stages of $DABB_{55}$ and $DABB_{140}$ from 124.3 to 76.6 N. The fresh mass (FM) revealed a mean value of 0.06 kg ±0.01 SD at $DABB_{55}$ and increased to 0.17 kg ±0.04 SD at $DABB_{140}$ in 2018. Lower values were found in the same stages of following year with 0.14 kg ±0.02 SD at harvest. Similarly fruit diameter (D) at $DABB_{140}$

was higher in 2018 (74.3 mm ±5.1 SD) compared to 2019 data (69.9 mm ±4.9 SD). In 2019, crop load was increased and consequently fruit size decreased.

Correlation between the estimated fruit quality parameters showed a moderate relationship of FM and D with highest correlation at $DABB_{55}$ (r = 0.92). In later stages the correlation decreased, but also shortly before harvest at $DABB_{140}$ FM and D were correlated (r = 0.67) due to irregular shape of the apple.

ECa was correlated with FM_{115} (r = 0.35), D_{115} (r = 0.25), and SSC_{115} (r = -0.28). The LA_{55} was correlated with FM_{55} (r = 0.72), D_{55} (r = 0.66). The LA_{115} was related with FM_{115} (r = 0.62), D_{115} (r = 0.69), and SSC_{115} (r = -0.11), while the correlations decreased at harvest stage.

No correlation was found between colour or firmness of fruit with ECa and LA. ECa revealed a low correlation with FM_{115} (r = 0.35), D_{115} (r = 0.25), and SSC_{115} (r = -0.28). The LA_{55} was correlated with FM_{55} (r = 0.72), D_{55} (r = 0.66). The LA_{115} was related with FM_{115} (r = 0.62), D_{115} (r = 0.69), and SSC_{115} (r = -0.11). However, the correlation coefficient values decreased at harvest stage.

The soil ECa and LA were applied to predict fruit FM and D at harvest stage. The leave-one-out cross validation of PLS regression model showed that the first two latent variables can predict FM and D with lowest $RMSE_{CV}$. For classification, the k-fold cross validation of KNN model indicated the lowest error with 8 neighbours.

The prediction of FM class by means of ECa revealed 31.2 % overall accuracy (Table 14). Specifically, low recall was illustrated in FM_{Mid} and FM_{High}. Furthermore, overall accuracy for D classification was slightly enhanced, reaching 48.1 %. Considering the dataset of LA, overall classification accuracy was enhanced (58.6 % and 67.9 % for FM and D, respectively) compared to the classification accuracy based on soil ECa. Lowest recall appeared for D_{Mid} (Table 14).

Table 14. Confusion matrix of fruit mass (FM), diameter (D) and soluble solid content (SSC), (n = 2400), at different days after bud break (DABB).

ECa	Predicted						
		Low	Mid	High	Precision [%]	Recall [%]	Overall Accuracy [%]
Measured	FM_{Low}	9	1	0	3.2	90.0	31.2
	FM_{Mid}	238	126	17	54.5	33.1	
	FM_{High}	37	104	70	80.5	34.1	
	D_{Low}	69	58	73	34.5	67	48.1
	D_{Mid}	12	37	101	24.7	26.2	

	D_{High}	22	46	183	72.9	51.3	
	SSC_{Low}	101	30	10	71.6	58.0	
	SSC_{Mid}	70	268	72	65.4	85.9	66.9
	SSC_{High}	3	14	33	66.0	28.7	
Predicted LA		Low	Mid	High	Precision [%]	Recall [%]	Overall Accuracy [%]
Measured	FM_{Low}	186	66	8	71.5	65.5	
	FM_{Mid}	73	113	25	53.6	48.9	58.6
	FM_{High}	25	52	54	41.2	62.1	
	D_{Low}	53	22	19	56.4	51.5	
	D_{Mid}	19	39	22	48.8	27.5	67.9
	D_{High}	31	80	316	74.0	88.5	
	SSC_{Low}	98	26	10	73.1	56.3	
	SSC_{Mid}	74	276	77	64.6	88.5	66.9
	SSC_{High}	2	10	28	70.0	24.3	

4.5.7. *Discussion*

Leaf area analysis considering the removal of Wood

The quantification of points from woody parts considering four growth stages allowed thesubtraction of wood surfaces from the tree 3D point cloud. The thresholds of linearity (>57.0 % and >57.5 % in 2018 and 2019, respectively) confirmed earlier findings (Gené-Mola et al., 2019a). The threshold considering reflectance intensity was similar in 2019 (<40 %), whereas in 2018 the mode value was enhanced in the present study. The linear relationships between LA_{Manual} and PPT for each growth stage were improved after removal of woody parts, revealing a substantial increase in LA_{55} ($R^2_{adj,CV}$ = 0.98) and LA_{140} ($R^2_{adj,CV}$ = 0.99) (Table 12). Furthermore, although the detected percentage of wood was reduced during canopy growth (Figure 30), the $RMSE_{CV}$ remained stable when estimating the LA after wood removal. However, the method has been broadly exploited in forestry (Béland et al., 2014; Vicari et al., 2019), it has been rarely applied in horticulture. The segmentation based on linearity, reflectance and also curvature were used to segment apples from leaf and branches (Gené-Mola et al., 2019a). Zhang et al. (2018) used bounding boxes for segmenting the branches in apple trees, reaching 92 % recall and 86 % accuracy when the pseudo colour and depth information were combined. The detection of cordons trajectories and shape, in the early growth stage of vines were modelled (R^2 = 0.98) to improve shoot thinning (Majeed et al., 2020). Based on the results presented on LA estimation in the present study, application of LA

information would provide an important tool in the production processes.

Spatio-temporal analysis

Spatial dependence at $LA_{55,18}$ was highest (Cambardella et al., 1994) with also high CV, which may be due to frosts, which occurred in March. Frost between bud break and full bloom can damage the vegetative buds, flower buds, or flowers, causing variability in growth patterns (Breen et al., 2016; Charrier et al., 2015). It can be also assumed that the frost impact on the vegetative buds affected the $LA_{55,18}$ resulting in high variability ranging from 2.52 - 6.76 m^2 (Figure 34a). This assumption is further supported by the delayed development of LA in 2018 compared to 2019. According to the growth curve of LA (G_{LA}) (Figure 35a) 55.4 % and 62.4 % of the total LA were developed at $DABB_{85}$, in 2018 and 2019, respectively. The inflection point of G and maximum of K also occurred earlier in 2019 compared to previous year suffering from frost. The growth rate of LA of all trees (n = 4506) indicated the full development of canopies at $DABB_{105}$ and $DABB_{95}$ in 2018 and 2019, respectively.

In the fruit growing region of federal state Brandenburg, the higher the ECa, the more vigorous the trees appear as an obvious finding (Tagarakis, Koundouras, Fountas & Gemtos, 2018), and consequently the ECa and LA are correlated. However, the correlation showed no consistence and ECa had no effect on LA_{55} and LA_{115} in both years. This can possibly be attributed to the drip irrigation system of the orchard (De Benedetto et al., 2013; Uribeetxebarria et al., 2018). Additionally, an earlier study in this orchard showed that the fruit trees adapted the rooting depth according to the ECa pattern, compensating for reduced water supply in low ECa zones (Tsoulias, Gebbers & Zude-Sasse, 2020). ECa and LA are further decoupled in commercial orchard due to adopted cultivation practises. In the present study, in both years a slight decrease of LA occurred between $DABB_{55}$, $DABB_{85}$ and $DABB_{115}$, which was assumable related to flower and fruit thinning measures and slight pruning for plant protection. However, these practises, affecting LA, are not correlated with ECa.

The LA_{140} interacted with yield of both years. Colaço and co-workers (2019) found that tree geometry can be correlated with historical yield data in citrus production, providing a determinant for delineating management zones. The relationship between spatio-temporal variability of tree vigour and yield was confirmed in pear and vineyards (Perry, Dezzani, Seavert, & Pierce, 2010; Tagarakis, Koundouras, Fountas & Gemtos, 2018). In the present study, higher values of $LA_{140,19}$ compared to $LA_{140,18}$ corresponded to enhanced yield in 2019 (r = 0.52).

From a physiological point of view, such relationship is explained by enhanced light interception and growth capacity. This holds true at least in the slender spindle trees avoiding excessive shading effects (Wünsche and Lakso, 2000). Mann et al. (Mann et al., 2011) created productivity zones using fruit yield, ultrasonically measured tree canopy volume, NDVI, elevation and apparent electrical conductivity of soil. Although all the properties were strongly correlated with yield and were able to explain the productivity of the orchard, citrus tree canopy volume and yield was most strongly correlated (r = 0.85), explaining 73% of its variation. Consequently, the correlation of LA and yield appears reasonable.

Impact of soil ECa and LA on fruit Quality

Comparing the two years of experiments, early frost events occurred in 2018 shortly before bud break, negatively affecting the vegetative growth. FM and D appeared slightly enhanced in 2018 than in 2019. The yield and also crop load followed the trend of LA, revealing lower values in 2018 compared to 2019 (Figure 36d). Consequently, higher yield in 2019 was caused by increased number of fruit per tree, while no effect of fruit size on yield can be concluded when comparing both years. Aggelopoulou et al. (2010) analyzed the spatio-temporal variability of quality in apple trees, observing no relationship between yield and fruit mass similar to the present study. As individual trees require variable intensity of crop load management, lack of tree-specific crop load management can even be seen as an important cause for heterogeneity in fruit size.

During seasonal fruit development, interaction of FM and D at different growth stages revealed the highest correlation at DABB55 (r = 0.92). The seasonal decrease of correlation between both quality parameters was expected due to non-linear relationship of FM and D in later fruit developmental stage. The SSC was autocorrelated between $DABB_{55}$ and $DABB_{85}$, but no correlation was found with ECa and LA. This may have been expected, since SSC is mainly influenced by the year and position into the canopy, i.e. exposure to light.

Despite the spatial stability of ECa patterns within the two cultivation years, no consistent correlation of ECa with FM and D was found. The absence of correlation between soil properties and fruit quality can temporally be observed in orchards (Liakos et al., 2020; Manfrini et al., 2020; Uribeetxebarria et al., 2018), which are subject to intensive management, such as irrigation, thinning, and pruning. Considering the effect of LA within one season, larger fruit size at enhanced LA to fruit ratio was reported earlier and form the basis for crop load management

(Charrier,Ngao, Saudreau & Améglio, 2015). Consistently, FM and D were correlated with LA. This has been confirmed in several studies capturing preharvest effects on postharvest quality (Teh et al., 2020).

LA of fully developed foliage of trees, crop load, and fruit quality were within the ranges of results reported by other authors for cultivars with medium size apple grown on dwarfing rootstocks (Naor et al., 1995; Xia et al., 2009). The KNN was applied to predict fruit quality parameters based on the datasets of ECa and LA. This approach was motivated by the correlation found and physiological background. The LA provided high classification accuracy considering the use of an independent test set in the validation of the model (Table 3). This can strengthen the assumption that soil properties reveal temporal stability, while trees can adapt to the conditions. Furthermore, production measures affect fruit quality, particularly through the impact on LA and correlation of LA and fruit quality as pointed out in the classification results in the present study.

4.2. *In-situ detection of apple fruit using LiDAR radiometric features*

Tsoulias, N., Xanthopoulos, G., Fountas, S., & Zude, M. (2020, November). In-situ detection of apple fruit using a 2D LiDAR laser scanner. In 2020 IEEE International Workshop on Metrology for Agriculture and Forestry (MetroAgriFor) (pp. 278-282). IEEE.

4.2.1. *LiDAR apparent reflectance*

Studying the calibrated LiDAR backscattered reflectance in defoliated trees allowed to observe possible differences between plant organs. The LiDAR reflectance was scattered at the edges of the objects, including the metal wires (WE) resulted in an R between 0 to 1% (Figure 37). Most R values for the branches and the stem were indicated between 1.1 - 47.9 % and 48.6 – 78.0 %, respectively; the apple points ranged between 78.6 - 88.0 %. The values above 90% were mostly noise and therefore removed. The R thresholds allowed distinguishing apple points from the remaining tree parts of the 3D point cloud (Figure 38b). The segmented points of WE, branches, stem and apple occupied 7.01 %, 27.07 %, 44.44 % and 17.67 % of the total amount of points in both trees, respectively.

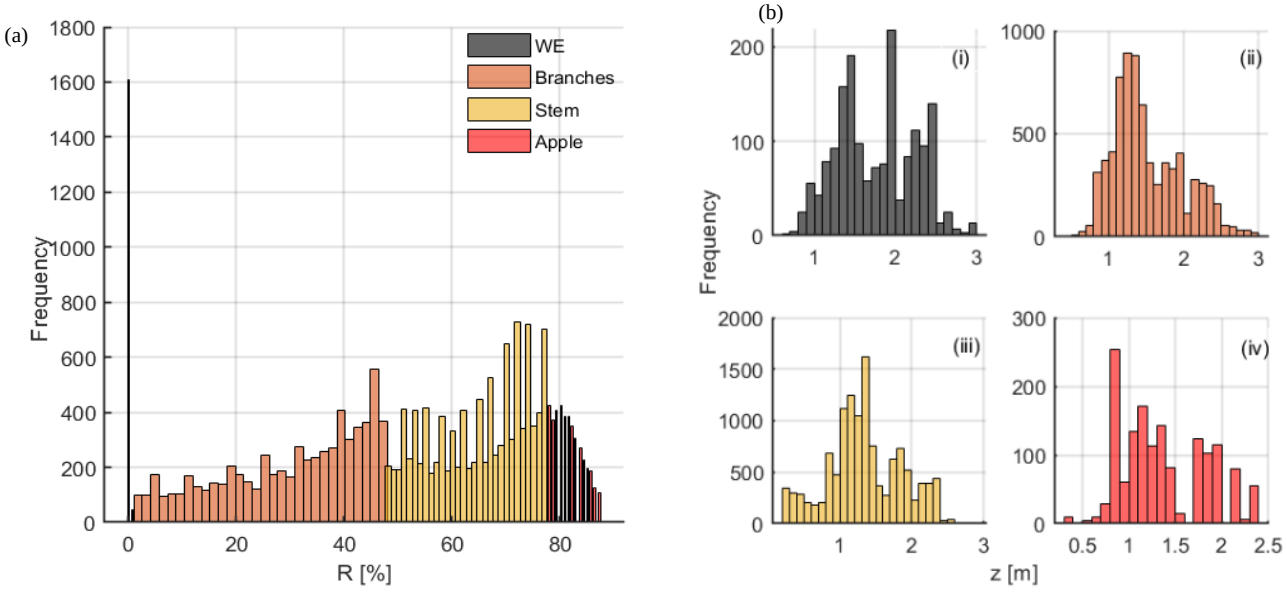

Figure 37. (a) Segmented histogram of tree parts based on the apparent reflectance (R [%]) (b) histograms of grouped R points of (i) wires and edges (WE), (ii) branches (iii) stem, and (iv) fruit along z axis [m].

The points of WE were highly distributed along z axis, revealing 59.33% coefficient of variation (CV) (Figure 37) (Table 15). Furthermore, most of the branches were found to lie between 1 and 2 m, with mean R=30.7 % and

13.2 % standard deviation (SD). A low CV of 13.0 % was found along the z axis for the fruit, indicating 73.3 % of R as the most frequent class in the 3D point cloud. However, their uneven distribution, especially between 1 and 2 m, could be a result of overlapping with the points of branches, since both classes were described by high SD (Gené-Mola et al., 2019a). On the other hand, the mean R of apple points was depicted at 81.1 % having 2.2 % SD and 2.8 % CV.

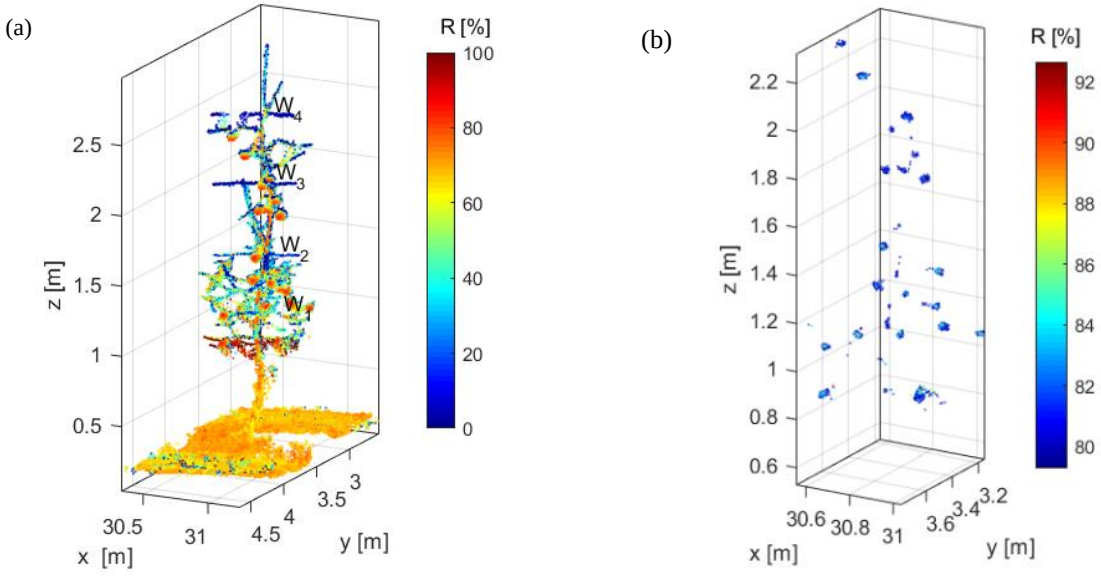

Figure 38. (a) 3D reflectance point cloud, (b) Segmented apple points after applying the reflectance threshold.

Table 15. Descriptive statistics of segmented points of wires and edges (WE), branches, stem and apples based on reflectance values including maximum (Max), minimum (Min), standard deviation (SD).

		Mean	SD	Min	Max	Median	Mode	CV
WE	[%]	0.01	0.07	0	1	0	0	59.33
Branches	[%]	30.72	13.16	1.13	47.89	33.86	47.89	42.85
Stem	[%]	65.48	8.51	48.56	77.95	67.26	73.27	13.01
Apples	[%]	81.07	2.23	78.62	87.97	80.62	78.62	2.75

4.2.2. *Fruit localization at different tree heights*

The segmented apple points were used to obtain the bivariate histograms by pairing, x with z axis and y with z

axis for each point in the point cloud (Figure 39). The local maxima appeared with approximately 18-point frequency. The combination of both bivariate histograms enabled to identify 38 out of 44 apples. The fact that the points were classified under different height allowed the comparison with the H_{manual}.

(a)

(b)

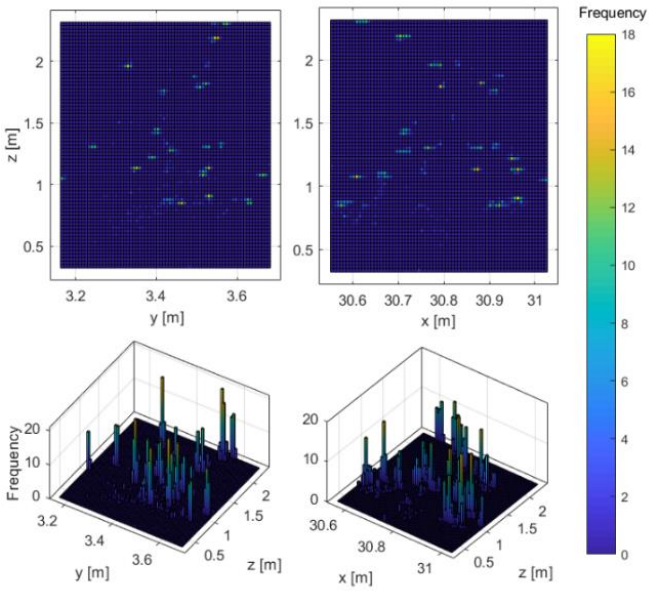

Figure 39. (a) Intensity map of apple points within y-z and x-z axis, where warmer colour indicates the local maxima and (b) the bivariate point density histogram of the resulting apple points within the y-z and x-z axis with grid resolution of 72 mm.

Applying the bivariate method each individual apple was identified in $W_{2\text{-}3}$ and $W_{3\text{-}4}$, where the apples were distributed more sparsely. More specifically, the H_{Manual} was correlated with H_{LiDAR} (R^2_{adj} = 0.72) in $W_{2\text{-}3}$ with 3.3 mm RMSE and 2.3 mm MBE (Table 16). Whereas the apples in $W_{3\text{-}4}$ area revealed a lower correlation ($R^2_{adj=}$ 0.65), with 4.2 % RMSE and 1.3 MBE.

Table 16. Descriptive statistics of manual measurements of apple height (HManual) and LiDAR-based measurements HLiDAR. capturing maximum (Max), minimum (Min), standard deviation (SD), mean absolute error (MAE), bias (MBE), root mean square error (RMSE), adjusted coefficient of determination (R2adj).

		n	Mean [mm]	SD [mm]	MBE [mm]	MAE [mm]	RMSE [%]	R^2_{adj}
$W_{G\text{-}1}$	H_{Manual}	16	73.1	4.2	0.6	4.3	5.5	0.4
	H_{LiDAR}	10	70.1	3.5				
$W_{1\text{-}2}$	H_{Manual}	12	71.1	5.6	1.7	2.7	4.3	0.4
	H_{LiDAR}	8	73.5	4.2				
$W_{2\text{-}3}$	H_{Manual}	6	69.6	1.1	2.3	2.8	3.3	0.7

	H_{LiDAR}	6	70.1	2.3				
W_{3-4}	H_{Manual}	14	74.8	6.1	1.3	3.3	4.2	0.6
	H_{LiDAR}	14	76.2	3.4				

4.2.3. *Discussion*

LiDAR apparent reflectance

The LiDAR reflectance varied among the tree elements, allowing to set discrete thresholds between the fruits and the woody parts on the tree. The points from branches and stem showed the highest range in R values, which can possibly be attributed to the dependance of the laser beam incidence angle on the target properties considering R and surface roughness. More specifically, the incidence angle increases due to the energy dispersion caused by spot spreading, while the rate of angle-dependent decay increases with the backscatter R measured at normal incidence if a regular surface is considered (Pesci and Teza, 2008). Kukko et al. (2008) presented a comprehensive experiment how backscatter intensity depends on the incidence angle using a set of natural and artificial samples. They demonstrated that the incidence angle effect is stronger for high reflectance targets. The angle effect also depends on the surface roughness of targets with a large grain size compared to the laser spot size, while reflectance other than roughness plays a stronger role for targets with small grain size (Kukko et al., 2008). However, in this study we considered apple trees as objects with perfect Lambertian distribution (Coren and Sterzai, 2006).

Regarding the laser hits along the z axis, higher frequencies were mostly observed between 1.5 and 1.7 m, where the LiDAR has been placed. However, the 3D point cloud data could restore the shape of fruit trees, providing high spatial data distribution for fruit localization.

Fruit localization at different tree heights

After applying the R thresholds, the apple points were segmented. The combination of two bivariate point density histograms allowed to study the fruit size at different heights. However, in the regions with high fruit density (W_{G-1}, W_{1-2}) the method miscounted the fruit number, depicting low correlation with the H_{Manual}. Keeping the bin size in point density histogram constant and considering only the bins connected to the regional maxima as fruits, was inevitably included less points from the outer region of the apple .The latter could be attributed in the bin size of Malambo *et al*., (2019) utilized the point density to estimate the height of sorghum panicles, reporting

a correlation coefficient of r = 0.86 with RMSE = 11.4 cm. Despite the 62.5 % and 66.7 % localization success, no correlation was indicated between H_{manual} and H_{LiDAR} in W_{G-1} (R^2_{adj} =0.45) and W_{1-2} (R^2_{adj} =0.45) areas, respectively. Tsoulias et al., (2020b) estimated the diameter of apples, at different growth stages, in foliated and defoliated tress combining the backscattered reflectance from a LiDAR and geometrical features. The LiDAR estimated diameter was related with the reference values, revealing an adjusted coefficient of determination (R^2_{adj}) of 0.95 and RMSE of 9.5% at harvest stage. When comparing the results obtained on foliated and defoliated tree's data, the maximum of 88.2% precision, 91.0% recall, and 89.5 F1 score were observed at harvest stage, where the fruit was fully developed.

4.3. *Apple shape detection based on geometric and radiometric features*

Tsoulias, N., Paraforos, D. S., Xanthopoulos, G., & Zude-Sasse, M. (2020). Apple shape detection based on geometric and radiometric features using a LiDAR laser scanner. *Remote Sensing*, *12*(15), 2481.

4.3.1. *Thresholds*

Shape geometry combined with R_{ToF} were utilized as inputs to set the threshold values under which the fruit points are found. The calibrated reflectance intensity R_{ToF} varied in the 3D point cloud of the foliated trees (Figure 3b). The R_{ToF} values of apples (R_A) and woody parts (R_W) appeared above 70 % and below 55 %. The leaves (R_L) ranged between 40 and 80 %. The C values of leaves (C_L) ranged between 35.2 % and 70 % (Figure 3c). The *C* values of apples (C_A) were observed above 50 %, whereas the points of woody parts (C_W) did not exceed 60 %. On the other hand, the L of leaves (L_L) ranged between 20 % and 80 %, while the woody parts (L_W) were scored above 60 % (.Figure ***40***d). The definition of apple class was carried out on the data set of last day's measurements at $DAFB_{120}$.

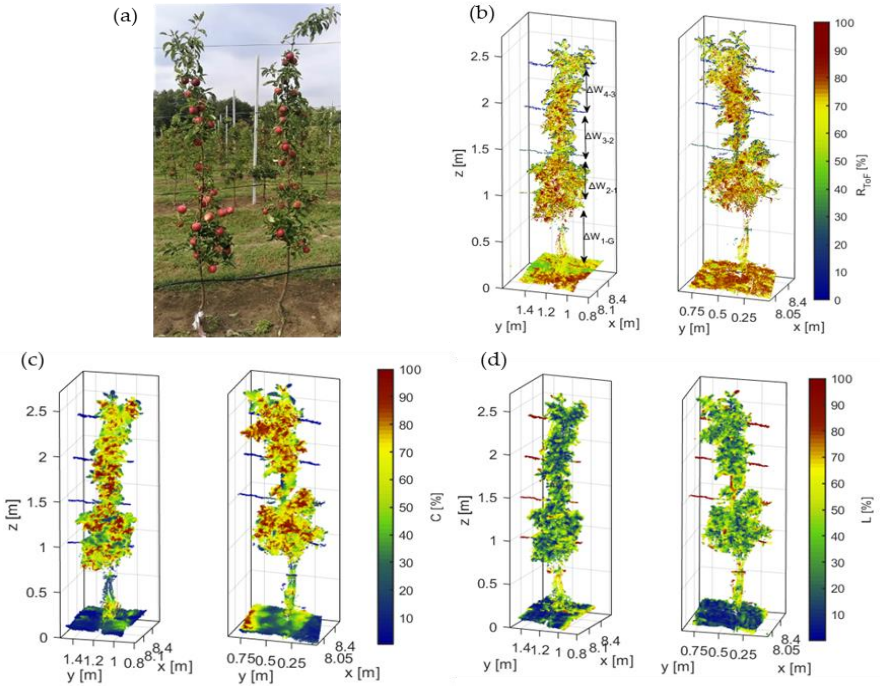

.Figure 40. Representation of 3D point clouds of (a) RGB image (b) reflectance (R_{ToF}) [%], (c) curvature (C) [%] and (d) linearity (L) [%] of trees measured before defoliation $DAFB_{120}$.

However, the occlusions of leaves and woody parts did not allow the acquisition of the full range of R_{ToF}, C, and L values of apples. Therefore, the trees that at the $DAFB_{120}$ were defoliated and scanned again with the LiDAR system (Figure 41). The R_W values ranged between 0 and 60 %, while the R_A appeared from 42 to 90 % (Figure 41b). The C_A values of apples ranged between 56 and 98 %, whereas the C_W appeared between 0.1 and 55.2% (Figure 41c). The 3D points of the latter category revealed the highest values varying between 48.8 and 98.8 %. Nevertheless, the *L* values of apple points (L_A) were more discretely ranging between 0.2 and 38.3 %. (Figure 41d).

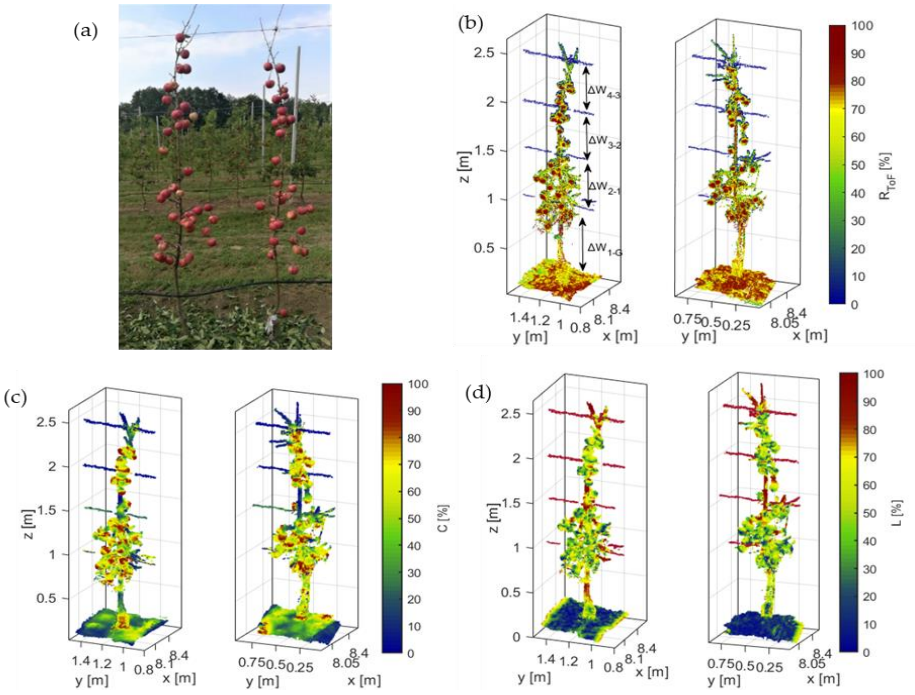

Figure 41. Representation of 3D point clouds of (a) RGB image (b) reflectance (R_{ToF}) [%], (c) curvature (C) [%] and (d) linearity (L) [%] in defoliated trees during $DAFB_{120}$.

As was mentioned above, the R values of apples could overlap with the leaves or the woody parts, while some of the surfaces may reveal similar C with apples, producing falsely clusters from leaves or woody parts. The R_W revealed a mean value of 38.2 %, standard deviation (SD) of 18.5 %. On the other hand, the R_{ToF} of leaves (R_L) and of apples (R_A) was marginally deviated (Figure 42a), while most of their values appeared from 50 to 70 % and from 65 to 71.8 %, respectively. More specifically, the mean value of R_L was indicated at 58.8 % with 12.1 % SD, and 63.2 % as the value with the highest likelihood (mode) within the class. However, the highest mean value was

obtained from the R_A class at 71.8 %, whereas the mode value (76.1 %) was utilized as R_{th} for the 'Gala' trees. Gene-Mola et al. (Gené-Mola et al., 2019b) suggested a R_{th} at 60 % for the segmentation of apples in 'Fuji' trees.

A similar pattern of the probability density of R_{ToF} was obtained in the C feature (Figure 42b). The most frequent value within the C_A was illustrated at 73.2 % (C_{th}). The C of leaves (C_L) values were partly overlapped with the C_A, revealing a mean value at 60.7 %, and 9.1 % SD. The C_W revealed a mean value of 30.1 %, with 19.4 % SD. The 3D points of L_W depicted the highest values (Figure 42c), reaching a mean value of 60.2 %, and 94.1 % as a mode value (Figure 43).

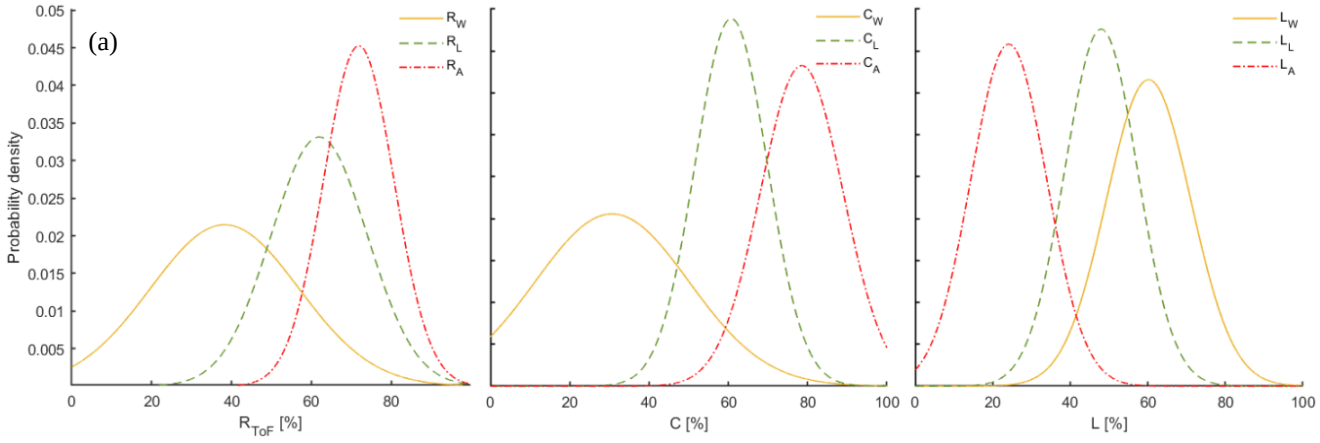

Figure 42 . The probability density of (a) calibrated reflectance intensity (R_{ToF}) [%], (b) curvature (C) [%] and linearity (L) [%] for wood, leaves and apples.

The R_A, C_A and L_A values were distinct from the residual classes, allowing the discrimination and localization of apples in the 3D point cloud. The apples were described with R_A and C_A values 76.1 % and 73.2 % (Figure 43). Therefore, the R_{th} and C_{th} were combined and used as thresholds to distinguish the apple points from woody parts. Whereas the remaining points of the latter class were removed using the L_W mode value of 15.5 % as threshold (L_{th}) (Figure 43).

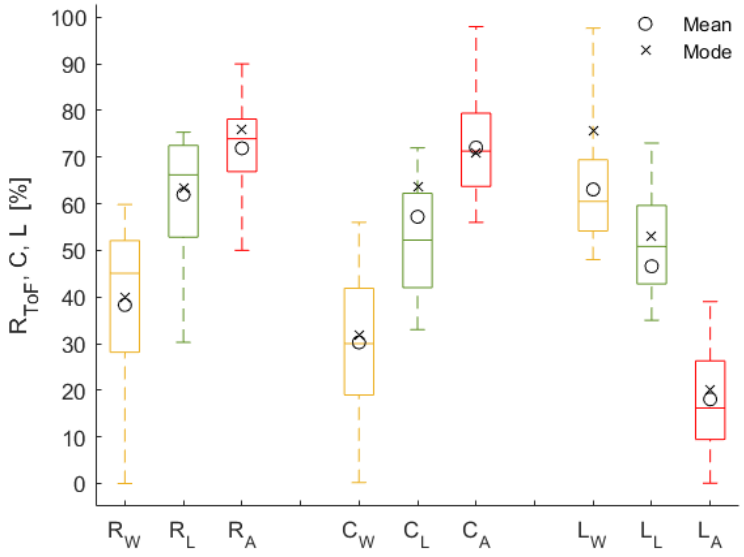

Figure 43. Box-Whisker plot of segmented points of wood (W), leaves (L) and apples (A) based on reflectance (R_{ToF}), curvature (C) and linearity (L) showing the mean and mode values, maximum, minimum, standard deviation are represented by lower and upper edges of the box, the dash in each box indicates the median.

4.3.2. *Fruit segmentation*

When performing the DBSCAN algorithm the clusters of filtered points of apples appeared in the 3D point cloud (Figure 44). Subsequently, the *k*-means partition method was applied to the points of each cluster to acquire the M_D. A sphere of variable radius based on the D_{LiDAR} of the cluster, enclosed the points of the cluster when placed at M_D. For evaluating the performance of the segmentation process in foliated trees, T_L, the data set of defoliated trees T_D was employed as ground truth. For this purpose, the M_L clusters found in T_L were compared to the clusters, M_D, found in T_D.

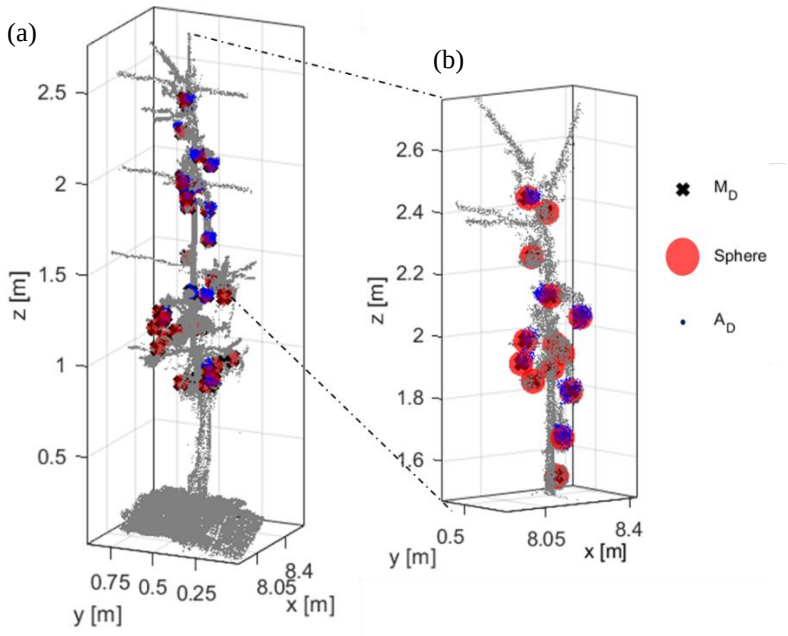

Figure 44. Apple centres detection (M_D) using sphere segmentation (b) representation of selected M_D apples classes enveloped in the sphere. The blue colour depicts the apple points of the defoliated trees (A_D)

After the localization of M_D, the estimated fruit diameter, D_{LiDAR}, was compared to the D_{Manual} for each ΔW during the growth stages (Table 17). The D_{LiDAR} was related to the D_{Manual}. In the upper sections, $\Delta W_{3\text{-}2}$ and $\Delta W_{4\text{-}3}$ of the canopies where the fruits grow more distinctly, the analysis of apple size resulted in R^2_{adj} = 0.95 with a RMSE = 3.2 %. However, high measuring uncertainty was noticed on the first two measuring dates when the fruit size was smaller, particularly in the lower sections of the trees with overlapping structures. Actually, no relation was observed on the first measuring date in $\Delta W_{1\text{-}G}$and $\Delta W_{2\text{-}1}$, presenting an MBE of 18.6 mm and 20.8 mm, respectively. Similarly, during $DAFB_{72}$ in the same areas, the MBE was raised at -29.0 mm and -30.5 mm, while their mean values differed 18.3 mm and 24.8 mm respectively. On the other hand, the highest relation was revealed in $\Delta W_{4\text{-}3}$ (R^2_{adj} = 0.95) and $\Delta W_{3\text{-}2}$ (R^2_{adj} = 0.90), during $DAFB_{104}$. Whereas, in the same stage, a less pronounced R^2_{adj} was observed in $\Delta W_{1\text{-}G}$ (R^2_{adj} = 0.55) and $\Delta W_{2\text{-}1}$ (R^2_{adj} = 0.66). The MAE decreased $DAFB_{120}$, reaching the highest error of 0.2 mm.

Table 17. Results of manually measured mean diameter (D_{Manual}) [mm] and the mean LiDAR-based measurement (D_{LiDAR}) [mm] in defoliated trees regarding mean absolute error (MAE) [mm], bias (MBE) [mm], root mean square error (RMSE) [%], and adjusted coefficient of determination (R^2adj).

		D_{Manual} [mm]	D_{LiDAR} [mm]	MBE [mm]	MAE [mm]	RMSE [%]	R^2_{adj}
$DAFB_{42}$	ΔW_{1-G}	32.0	47.6	18.6	0.4	10.8	0.46
	ΔW_{2-1}	36.1	65.1	20.8	0.7	12.0	0.45
	ΔW_{3-2}	39.2	47.9	5.9	0.5	3.6	0.69
	ΔW_{4-3}	39.3	41.2	3.1	0.6	3.2	0.74
$DAFB_{72}$	ΔW_{1-G}	66.4	48.0	-29.0	0.4	14.5	0.42
	ΔW_{2-1}	62.8	37.9	-30.5	0.5	15.8	0.38
	ΔW_{3-2}	65.6	63.7	-3.2	0.4	7.7	0.81
	ΔW_{4-3}	67.0	63.7	-3.0	0.5	5.9	0.82
$DAFB_{104}$	ΔW_{1-G}	74.8	70.3	-4.8	0.3	4.6	0.55
	ΔW_{2-1}	71.1	69.5	-3.3	0.1	4.5	0.66
	ΔW_{3-2}	69.6	68.7	-8.3	0.1	5.5	0.90
	ΔW_{4-3}	74.8	70.3	-5.2	0.2	6.1	0.95
$DAFB_{120}$	ΔW_{1-G}	69.3	67.3	-7.3	0.2	5.2	0.67
	ΔW_{2-1}	70.5	68.4	-3.2	0.1	4.8	0.74
	ΔW_{3-2}	69.7	68.6	-4.6	0.1	4.6	0.81
	ΔW_{4-3}	68.6	66.4	-7.5	0.1	4.6	0.75

As was previously mentioned, the ε of DBSCAN was based on the D_{Manual} of each ΔW during $DAFB_{120}$. That served as calibration for the modes, but also the sphere radius. Thus, earlier growth stages would be influenced by the generation of augmented clusters. Consequently, it can be assumed that the uncertainty was elevated mainly in the $DAFB_{42}$ stage, but also $DAFB_{72}$, when a lower D of the fruits was measured manually.

This uncertainty could lead in under- or over-counting of the DBSCAN clustering since the ε remained constant, and the fruit may be bigger or more small fruit are collected in one cluster. In Sun et al. (Sun et al., 2020), the wide range of size and shape of cotton boll influence the splitting operation of clusters. Furthermore, the shape of apples is not perfectly spherical producing an error in the estimation of D_{LiDAR}. Gongal et al. (Gongal et al., 2018) measured the size of apples based on the 3D coordinates from a 3D camera and they obtained a 30.9 % MAE, while the MAE decreased to 15.2 % when the pixel information from an RGB camera was considered.

Nevertheless, the present results indicate that the data set of C and R_{ToF} can enable feasible counting and sizing of apples from the 3D point cloud, allowing their discrimination even in areas with high apple density. Whereas, scanning the T_D trees from both sides enriched the 3D objectiveness of the apple size. Furthermore, the values of

C and L were described through the surface of apples, increasing the resolution in the classes, and subsequently the determination of the mode value. The acquisition of the 3D shape of apples from both sides led in the estimation D_{LiDAR} analogous to the D_{Manual}, revealing low deviations (data not shown).

4.3.3. *Evaluation*

After the determination of the M_D location, the same procedure was followed in the T_L, applying the threshold values. The detection results of M_L were evaluated for each ΔW region, considering the M_D clusters as ground truth labels (Table 18). The highest F1 score was acquired in $\Delta W_{2\text{-}1}$, reaching 84.4 %, with 85.2 % accuracy, 82.6 % precision and 86.3 % recall during $DAFB_{42}$. A less pronounced accuracy was noted in $DAFB_{72}$, with the values ranging from 65.8 to 75.1 %, while the highest values of F1 were depicted in $\Delta W_{1\text{-}G}$ (85.6 %) and $\Delta W_{3\text{-}2}$ (89.6 %). In parallel with the fruit development, the number of apple points in the 3D point cloud increased, enhancing the performance of the detection algorithm. More specifically, the precision was ranged from 81.1 to 86.6 % and the F1 between 83.7 and 92.8 % during $DAFB_{104}$. However, the highest performance was observed in $\Delta W_{4\text{-}3}$ of $DAFB_{120}$, revealing an 89.5 % F1, 88.2 % precision, and 90.9 % recall.

Table 18. Performance assessment of the localization algorithm on the segmented apple points in foliated trees (T_L) considering the apple in defoliated trees (T_D) as ground truth during the growth stages. Manually counted fruit number (N_{Manual}), counted fruit number of T_D (N_D) and true positives (TP) are given.

		NManual	ND	TP	Accuracy [%]	Precision [%]	Recall [%]	F1 [%]
$DAFB_{42}$	ΔW1-G	10	10	9	76.9	80.0	83.8	84.2
	ΔW2-1	19	18	16	85.2	82.6	86.3	84.4
	ΔW3-2	34	34	30	74.5	75.6	83.7	79.4
	ΔW4-3	17	17	15	76.9	85.0	89.4	87.1
$DAFB_{72}$	ΔW1-G	6	6	6	71.4	85.7	80.8	85.6
	ΔW2-1	15	14	12	75.1	82.8	82.3	84.8
	ΔW3-2	14	14	12	73.3	83.3	86.6	89.6
	ΔW4-3	7	7	5	65.8	71.4	83.3	76.9
$DAFB_{104}$	ΔW1-G	11	11	9	77.2	81.1	88.8	87.4
	ΔW2-1	18	18	16	84.1	85.7	81.8	83.7
	ΔW3-2	11	11	10	82.5	85.7	87.0	86.3
	ΔW4-3	12	12	11	80.2	86.6	88.5	92.8

$DAFB_{120}$	ΔW1-G	15	15	14	73.4	78.9	83.3	81.1
	ΔW2-1	32	31	28	76.4	82.2	84.2	86.4
	ΔW3-2	16	16	16	75.5	85.7	88.0	87.8
	ΔW4-3	15	15	15	88.9	88.2	91.0	89.5

Gene-Mola et al. (Gené-Mola et al., 2019a) used the reflectance and the curvature, derived from a LiDAR system, as principal features in fruit detection with slightly lower results. However, similar results have been reported from the implementation of 3D shape information with RGB vision systems, reaching a precision of 86.4 % and recall 88.9 % in fruit localization (Lin et al., 2020; Tao and Zhou, 2017). On the other hand, the woody parts in $\Delta W_{1\text{-}G}$ revealed similar R_{ToF} and C values with the apples, enhancing the FP cases and subsequently the decline of accuracy in this region. The occlusions produced by branches and leaves hide partly or totally the fruits, resulting in undercounting of apples. Mendez et al. (Méndez et al., 2019) used a LiDAR laser scanner to count the number of fruits in pruned orange trees ($R^2 = 0.63$), however, the correlation was significantly reduced (R^2=0.18) when the method was applied in unpruned trees due to occlusion by leaves.

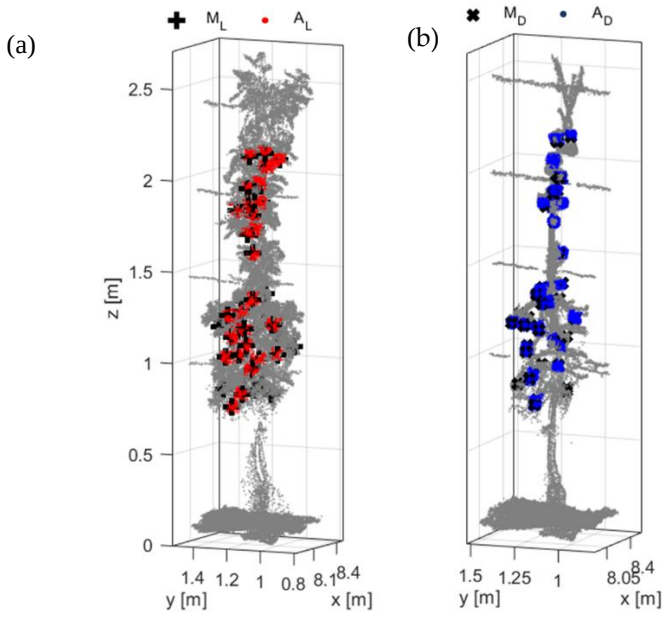

Figure 45. Representation of (a) detected centres in foliated trees (M_L) and (b) after defoliation (M_D). The red colour depicts the apple points of the foliated tree (A_L) while the blue colour show the points of the fruits in the defoliated tree (A_D).

The distance difference between the M_L and M_D was measured in each ΔW (Figure 45). The highest distance for $DAFB_{42}$ was illustrated in ΔW_{4-3} with a 37.3 % RMSE, while the mean value was illustrated at 0.5 mm with 0.6 mm SD (Table 19). The measuring uncertainty was enhanced in ΔW_{G-1}, $\Delta W_{2-1,}$ and ΔW_{3-2}, revealing an RMSE of 22.2 %, 16.8% and 11.5 % in $DAFB_{72}$, respectively. However, a less pronounced RMSE was depicted during $DAFB_{104}$, reaching a maximum value of 6.4 % in ΔW_{4-3} and a minimum value of 3.7 % in ΔW_{4-3}.

Table 19. Differences between the position of the centres of defoliated (M_D) and foliated (M_L) clusters as well as the fruit diameter estimated D_L and ground truth D_D in T_L and in T_D, respectively, regarding the standard deviation (SD) root mean square error (RMSE) [%] during the fruit growth given in days after full bloom (DAFB).

	M_D - M_L [mm]	SD [mm]	RMSE [%]	D_D-D_L [mm]	SD [mm]	RMSE [%]
$DAFB_{42}$	0.2	0.22	19.9	22.3	0.3	6.3
$DAFB_{72}$,	0.1	0.1	15.1	12.6	0.2	5.9
$DAFB_{104}$,	0.1	0.1	6.7	11.3	0.2	8.7
$DAFB_{120}$	0.1	0.1	5.7	8.7	0.1	4.9

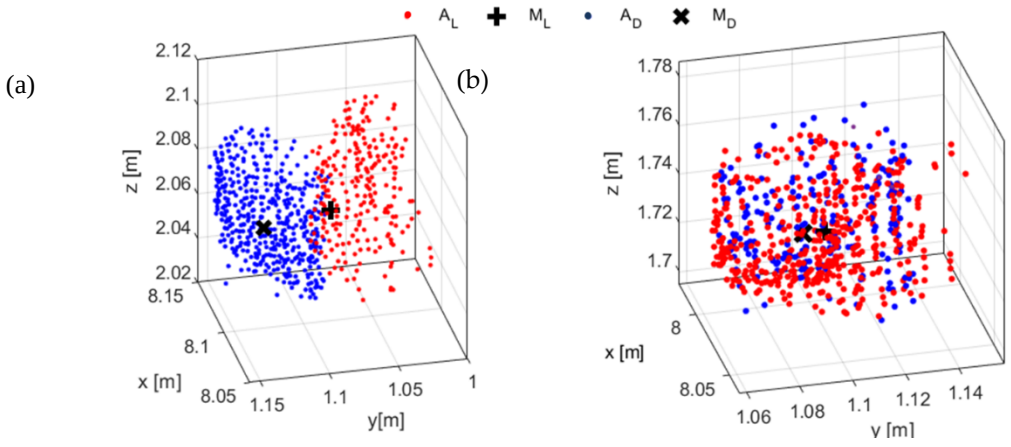

Figure 46. Representation of the (a) worst- and the (b) best-case scenario of the distance of the centre of clusters in defoliated (M_D)and foliated (M_L) during $DAFB_{120}$. The red colour depicts the apple points of the foliated trees (A_L) while the blue colour the points of the defoliated tree (A_D).

On the other hand, lower RMSE were acquired at $DAFB_{120}$ (Table 19). No differences were found between the sectors. More specifically for $DAFB_{120}$, the ΔW_{4-3} region depicted the worst-case scenario with a mean value of 0.1 mm and 8.1 % RMSE (Figure 46a). The minimum difference between the M_D and M_L was observed in ΔW_{4-3} with an RMSE of 3.7 % RMSE (Figure 46b). The growth of apples resulted in the acquisition of a higher amount

of points, generating clusters similar to the M_D. However, some of the fruits were partly or totally occluded by branches, creating smaller clusters. Thus, the use of *k*-means clustering differentiated the position of M_L centre from the M_D, increasing the measuring uncertainty.

4.3.4. *Discussion*

Thresholds

The use of a LiDAR system enabled the acquisition of tree point cloud, allowing the utilization of radiometric (R_{ToF}) and geometric features (C, L) as classifiers for fruit detection in the proposed algorithm. The apple features (R_A, C_A, L_A) were distinctively delimited from woody parts (R_W, C_W, L_W) after tree defoliation. The discrete range of R_A (42 - 90%) from the R_W (0 – 60 %) can be attributed in their different type of surface (Kaasalainen et al., 2011) and the available water content (Zhu et al., 2017) (Figure 5). Furthermore, the spherical shape of apples resulted in higher C_A values (56 – 98 %) than C_W (0.1 – 55.2 %) due to the linear shape of woody parts, while a reciprocal opposite range was observed in the correspondent classes of linearity, L_A (0.2 -38.3 %) and L_W (60.2-94.1 %). Therefore, the apples segmented from the woody parts and later clustered using the DBSCAN. Whereas, the application of sphere in each M_D enabled higher resolution in the determination of R_{th} (76.1 %), C_{th} (73.2 %) and L_{th} (15.5%), during $DAFB_{120}$. Similar value of R_{th} (60%) was suggested by Gene-Mola et al. (Gené-Mola et al., 2019b) for the segmentation of apples in 'Fuji' trees.

As was previously mentioned, the ε of DBSCAN was based on the D_{Manual} of each ΔW during $DAFB_{120}$. That served as calibration for the modes, but also the sphere radius. Thus, earlier growth stages would be influenced by the generation of augmented clusters. Consequently, it can be assumed that the uncertainty was elevated mainly in the $DAFB_{42}$ stage, but also $DAFB_{72}$, when a lower D of the fruits was measured manually.

Fruit segmentation

This uncertainty could lead in under- or over-counting of the DBSCAN clustering since the ε remained constant, and the fruit may be bigger or more small fruits are collected in one cluster. In Sun et al. (Sun et al., 2020), the wide range of size and shape of cotton boll influence the splitting operation of clusters. Furthermore, the shape of apples is not perfectly spherical producing an error in the estimation of D_D. Wang et al. (2017), combined a cascade detection and an ellipse fitting to recognize and estimate the size of mangoes, using an RGB-

D depth image. However, the not perfectly elliptical shape of fruits produced 4.9 mm and 4.3 mm RMSE in the detected height and width of fruits, respectively.Gongal et al. (Gongal et al., 2018) measured the size of apples based on the 3D coordinates from a 3D camera and they obtained a 30.9 % MAE, while the MAE decreased to 15.2 % when the pixel information from an RGB camera was considered. However, all of the aforementioned studies carried out only before harvest period, whereas there was not sufficient literature on temporal fruit detection using 3D information.

Nevertheless, the present results indicate that the data set of L, C and R_{ToF} can enable feasible counting and sizing of apples from the 3D point cloud, allowing their discrimination even in areas with high apple density. Whereas, scanning the T_D trees from both sides enriched the 3D objectiveness of the apple size. Furthermore, the values of C and L were described through the surface of apples, increasing the resolution in the classes, and subsequently the determination of the mode value. The acquisition of the 3D shape of apples from both sides led in the estimation D_D analogous to the D_{Manual}, revealing low deviations.

Evaluation

The apple clusters in T_D were used as ground truth labels. This derived from the assumption that the shape and the size of apples could be fully described due to the reduced occlusions. Mack et al. (et al., 2017) employed random sample consensus algorithm to fit a 3D sphere model in grapevine berries, reconstructing the shape of berries with 98% precision and 94% recall. However, the sphere size (D_D) was also applied in T_D as an additional step to evaluate the segmented region. In Rakun et al. (et al., 2011), a reconstructed sphere to evaluate the 3D shape of segmented voxels was employed. The apple clusters in T_D were used as ground truth labels. This derived from the assumption that the shape and the size of apples could be fully described due to the reduced occlusions. Gene-Mola et al. (Gené-Mola et al., 2019a), labelled manually the possible locations of apples in 3D point cloud, placing 3D rectangular bound boxes on each apple. Furthermore, the reflectance and the sphericity derived from a LiDAR system have been utilized as principal features in fruit detection, achieving 87.5% localization success and 0.85 F1. However, similar results have been reported from the implementation of 3D shape information with RGB vision systems, reaching a precision of 86.4 % and recall 88.9 % in fruit localization (Lin et al., 2020; Tao and Zhou, 2017). On the other hand, the woody parts in $\Delta_{W1\text{-}G}$ revealed similar R_{ToF} and C values with the apples,

enhancing the FP cases and subsequently the decline of accuracy in this region. The occlusions produced by branches and leaves hide partly or totally the fruits, resulting in undercounting of apples. Mendez et al. (Méndez et al., 2019) used a LiDAR laser scanner to count the number of fruits in pruned orange trees ($R^2 = 0.63$), however, the correlation was significantly reduced ($R^2=0.18$) when the method was applied in unpruned trees due to occlusion by leaves.

The fruit size of the calibration data set reduced the accuracy of the method, when smaller fruit size occurred. The accuracy of the proposed methodology was reduced at the first two growth stages, resulting in the lowest percentage (65.8%) in $\Delta W_{4\text{-}3}$ at $DAFB_{72}$. Stajnko et al. (et al., 2004) monitored the diameter of green apples several times during the vegetation period, combining thermal and RGB camera. The highest relation between the manually measured and detected fruit diameter ($R^2 = 0.70$) was observed at harvest stage, when the fruit reached their maximum size. Confirming, a less pronounced relation ($R^2 = 0.68$) was observed in apples of smaller size after fruit drop.

Some of the fruits were partly occluded by branches, creating smaller clusters in T_L. This deviation was presented in the high RMSE between the D_D-D_L. The growth of apples resulted in the acquisition of a higher amount of points, generating clusters similar to the M_D. However, the use of *k*-means clustering differentiated the position of M_L centre from the M_D, increasing the measuring uncertainty (Table 3). Therefore, the evaluation of distance difference between the M_L and M_D centers, allowed to quantify the possible deviations in the cluster.

5. Conclusion

5.1. *Estimating canopy parameters based on the stem position in apple trees using a 2D LiDAR*

The technical capabilities of a 2D LiDAR laser scanner to reconstruct canopy morphology in three dimensional domain and measure plant parameters were studied. To this end, chapter 3.1 presents the core component of tree segmentation and extraction of plant variables in outdoor conditions. A sensor frame platform was mounted on a tractor, tested on a box with known dimensions and applied in an apple orchard to obtain the 3D structural parameters of the trees. The LiDAR system was able to estimate simple structure of objects, with the highest RMSE of 1.63 in the case of missing hits due to reflectance of the object and increased incident angle of laser scanner with enhanced distance between laser aperture and the object. The method that was proposed was able to detect the tree stem position with an MAE of 43.7 mm and MBE of 36.5 mm.

A methodology based on a bivariate point density histogram is proposed to estimate the stem position of each tree. The cylindrical boundary was projected around the estimated stem positions to segment each individual tree. Subsequently, the height, stem diameter, and volume of the segmented tree point clouds were estimated and compared with manual measurements. The estimated stem position of each tree was defined using a real time kinematic global navigation satellite system, (RTK-GNSS) resulting in an MAE and MBE of 33.7 mm and 36.5 mm, respectively. It also provided meaningful information about the H_{LiDAR}, which was correlated strongly with the H_{manual} (R^2=0.87). Furthermore, the approach for the estimation of S_{LiDAR} indicated a high relationship with the S_{manual} (R^2=0.88). Considering the V_{manual} and the V_{LiDAR} revealed a lower correlation in comparison with the above parameters (R^2=0.77), probably due to errors in V_{manual} or the presence of weeds within the trees in the point cloud data. The convex-hull method for estimating the canopy volume was confirmed in apple trees.

5.2. *Calculating the water deficit of apple orchard by means of spatially resolved approach*

Chapter 3.2 explores the potential of estimating daily water balance model based on LA at different ECa areas. The ECa was measured at field capacity, together with soil properties, and meteorological data was recorded daily from a weather station. These values were implemented in the irrigation model for calculating the daily water needs in the crucial developmental stages: full bloom, cell division stage, and harvest. A positive correlation was observed between ECa and total available water content in the root zone ($r = 0.78$, $p < 0.05$). Furthermore, the influence of

LA on water balance was quantified, pointing to the reasonability of spatially resolved water balance. Specifically, the water balance revealed differences when considering the spatial variability of the soil and the leaf area. In the center of the orchard, the ECa values mainly were lower than in the south or in the north, while lower LA values were also detected in the center of the field. According to the soil texture analysis regions of high ECa hold enhanced amounts of water content resulting in varying, here two, thresholds. Considering the trees with high LA, enhanced water deficits were found particularly in low ECa regions and vice versa. However, the orchard had a light soil profile with high amounts of sand and silt, a fact which assist high soil evapotranspiration within the orchard, which might be reduced in heavier soils.

5.3. *Calculating the water deficit spatially using LiDAR laser scanner in an apple orchard*

The estimation of LA by means of LiDAR was confirmed. Thus, the LiDAR laser scanner system was used to estimate the leaf area per tree. Furthermore, an impact of LA and soil patterns on water needs was found in the apple orchard. The spatial dependence of LA on the ECa region was revealed. The LA correlated positively with ECa in low (r =0 .74), mid (r = 0.86), and high (r = 0.68) areas. The monthly values of the reference water balance model (WB_{RF}) based on adjusted FAO values were 36.3 mm lower than values of the model implementing LA(WB_{LA}) in low ECa regions. With LiDAR-derived plant data, land managers can improve water scheduling in fruit orchards.

5.4. *Vegetative factors of tree volume per ECa level*

The temporal variability of apple canopy volume was negatively correlated with the ECa and the slope of the orchard pointing to adaptation capacity and lack of water shortage in the irrigated orchard. It can be postulated that spatial analysis in orchards should consider the tree variability, but, different from arable, rain-fed farming, the effect of soil is diminished. However, the repeated measurements of V_{LiDAR} by means of the laser scanner allowed the estimation of Kv¬ spatially, indicating the spatial and temporal heterogeneity of Kv pointing to the potential of instrumental growth modeling and management zone delineation. In the future this should result in variable rate application not only in plant protection, but also for other tree individual managemet such as pruning, thinning, spray application of fertilizer. However, the study should be repeated considering also the variation of soil water

content at each growth stage. In parallel, daily weather data need to be added in the following studies. Whereas, the growth pattern of volume should be further studied including data from several years.

5.5. *Effects of soil ECa and LiDAR-derived leaf area on fruit quality in apple production*

The quantification of wood parts showed the high variation of canopy coverage that can be found in individual stages within the orchard. LiDAR-based estimation of leaf area (LA) was achieved by means of machine learning using the LA of defoliated trees (LA_{Manual}) with the corresponding points per tree (PPT) derived from LiDAR 3D point cloud during seasonal development of the trees. The LA models were improved when the points of woody parts were removed, especially at LA_{85} ($R^2_{adj,CVC}$ = 0.95, $RMSE_C$ = 4.67 %) and LA_{115} ($R^2_{adj,CV}$ = 0.99 , $RMSE_C$ = 2.71 %).

The spatio-temporal analysis of LA showed that the later patterns of LA_{115} and LA_{140} were stable, despite the frost in 2018, which reduced the growth of LA in early stages as well as crop load and yield. The temporal stability of ECa interacted with the $LA_{140,18}$ (r = 0.53) and $LA_{85,19}$ (r = 0.62), but correlation showed no consistent relationship. The seasonal growth analysis of LA followed similar patterns within the two years, depicting the highest K_{LA} between $DABB_{55}$ and $DABB_{115}$. The growth rate of LA was temporally interpolated by a sigmoid growth function quantifying the full development of canopies at $DABB_{105}$ and $DABB_{95}$ in 2018 and 2019, respectively

The implementation of LA information in the KNN fruit quality classification increased the overall classification accuracy compared to KNN model based on ECa. Classification accuracy in the test set validation based on ECa was 39.7 %, whereas classification based on LA resulted in 63.3 %. The prediction of quality parameters from the LA can greatly support variable rate application in apple orchards given that growers are able to tailor input requirements to local yield goals. Moreover, the results suggest the value of LA data in decision support systems aimed at optimizing orchard management practices, particularly addressing the impact of orchard management on fruit quality in the context of precision horticulture.

5.6. *In-situ detection of apple fruit using LiDAR radiometric feature*

Tree structure variables such as the LA or V can influence the number and size of fruits on the tree. Yield monitoring systems in fruit production mostly rely on color features, making the discrimination of fruits challenging due to varying light conditions. Thus, the potential of LiDAR backscattered reflectance (R_{ToF}) in fruit segmentation. An intensity analysis of tree elements was performed, obtaining mean intensity values of 28.9%, 29.1%, and 44.3% for leaves, branches and trunks, and apples, respectively. These results suggested that the R_{ToF} parameter can be useful to detect apples. A four-step fruit detection algorithm was developed to localize and estimate the height (H_{LiDAR}) and diameter (D_{LiDAR}) of fruits. A mean detection success of 92.5% was obtained in relation to the total amount of fruits on the defoliated trees during the stages of fruit development. A mean correlation of $R^2 = 0.83$ was obtained for H_{Manual} and H_{LiDAR}, whereas a less pronounced link was observed between D_{LiDAR} and D_{Manual} ($R^2 = 0.72$) during fruit development. The mean detection success was decreased to 70.5% when the fruit detection algorithm was applied to the foliated trees. From the experimental results it was concluded that LiDAR-based technology and, particularly, its intensity information has potential for remote apple detection and 3D localization. However, the less pronounced accuracy in foliated trees has led to the creation of a more advance method.

5.7. *Apple shape detection based on geometric and radiometric features*

The LiDAR system was employed to obtain a 3D point cloud of apple trees during fruit development. The LiDAR system was used to scan apple trees before (T_L) and after defoliation (T_D) four times during seasonal tree growth. An apple detection method based on calibrated apparent backscattered reflectance intensity (R_{ToF}) and geometric features, capturing linearity (L) and curvature (C) derived from the LiDAR 3D point cloud, is proposed. The thresholds for distinguishing apples from the remaining canopy resulted from a data set consisting of foliated, T_L, and defoliated trees, T_D, avoiding the coinciding geometric and radiometric features of leaf and fruit. The proposed methodology of sphere in T_D increased the resolution in the determination of threshold values of R_{th} (76.1 %), C_{th} (73.2 %) and L_{th} (15.5 %) that define the apple points. Whereas, the M_D clusterswere considered as ground labels, while the fruit size, D_D, illustrated the highest correlation (R^2_{adj} =0.95) with D_{Manual} fruit size in

$\Delta W_{4\text{-}3}$ at $DAFB_{104}$. However, the uncertainty was increased in the first two growth stages, while the highest was observed in $\Delta W_{2\text{-}1}$ at $DAFB_{72}$ (15.8 % RMSE and 10.5 mm MAE), due to the generation of augmented clusters of the smaller apples. The apple detection algorithm was developed to generate the M_D and M_L of apple clusters on trees. The M_L values were evaluated by means of the M_D clusters, resulting in 89.5 % F1 with 91.0 % recall and 88.2 % precision in $\Delta W_{2\text{-}1}$ at $DAFB_{120}$. Whereas, as a further step of evaluation, the estimated distance between the centres of M_D and M_L revealed a 0.1 mm mean deviation with 5.7 % RMSE at $DAFB_{120}$. Moreover, at the same growth stage, the minimum difference between D_D and D_L was observed, reaching 8.7 mm with 9.5 % RMSE. The method presented, shows promising results for in situ yield monitoring using a 2D LiDAR system. Further research should be carried out, to test the method in different apple varieties having less spherical shape in order to identify and tackle possible deviations of geometric and reflectance values.

6. General discussion

6.1. *Estimating canopy parameters based on the stem position in apple trees using a 2D LiDAR*

Investigating the potential of 3D data in fruit trees presents some specific characteristics as compared to 2D approaches. Contrary to arable crops, the growth of most of the perennial trees takes place in 3D space. This should be taken into consideration when 2D based remote sensing technologies are employed to monitor fruit trees. Specifically, the objectiveness of the acquired data is limited, given that these technologies cannot, due to their nature, include all the information of tree individuals. This is one of the main reasons why the LiDAR laser scanner was chosen to monitor and extract 3D plant parameters.

Aiming to scan with the LiDAR tree rows throughout the whole orchard, a sensor-frame was constructed and mounted on a tractor. Subsequently, data from an RTK-GNSS, an IMU, and the LiDAR were fused to calculate the 3D tree profiles in absolute coordinates. Sensor frames mounted on vehicle platforms have been widely used in agriculture to acquire 3D data (Underwood et al., 2016; Vázquez-Arellano et al., 2018a; Hobart et al., 2020). By utilizing the presented methodology, the sensing system could be carried by other agricultural vehicles, while stem detection was independent of the vehicle that was carrying all the required sensors. Beside the LiDAR laser scanner, the inertial measurement unit (IMU) was recording the three-dimensional tilt (roll, pitch, yaw) of the sensor frame, whereas the RTK-GNSS was providing georeference of these data. A critical task was to develop the proper methodology to store and synchronize the data, since all sensors had a different output frequency. Thus, a multi-thread architecture software was developed in Visual Studio (16.1, Microsoft, Redmond, WA, US) for data acquisition purposes The provided time-stamps eased post-processing where the cubic spline interpolation method was used to calculate sensor values in synchronized time instances.

Nevertheless, the process of using raw multi-sensor data to reconstruct 3D surface geometry can be influenced by uneven ground conditions, vibrations originated from the tractor engine or the vehicle speed, parameters that can lead to measuring uncertainty. Scanning an object of simple structure and of known dimensions, such as a metal box, in field conditions allowed researchers to quantify the measuring uncertainty of the sensor frame. It was shown that driving at 0.5 km h^{-1}, the MAE was 8.18 mm and the MBE was 2.75 mm, representing an RMSE of 1.63% due to gaps in the point cloud and increased incident angle with enhanced distance between the laser aperture

and the object. Whereas, studying the uncertainty in smaller objects, such as the metal bars, an RMSE <1 % with an MAE of 0.8- 1.6 mm was observed in the bars closer to the LiDAR height.

Addressing measurements on tree rows differs from single objects, because the position of tree individuals is not defined. Several methods have been developed to tackle this problem in fruit trees, either clustering each tree using convex hull (Auat Cheein et al., 2015), semi-Markov model (Underwood et al., 2016) or following a row wall approach (Escolà et al., 2017). The latter can extract the variability of tree information in the row, however, it does not provides the number and position of trees. On the other hand, clustering approaches are not applicable in high density apple orchards, since the boundaries among trees are not well defined. This is the reason why a tree segmentation methodology was developed to estimate plant variables for each individual tree. Assessing the accuracy of the detected tree position with the RTK-GNSS resulted in an MAE and MBE of 33.7 mm and 36.5 mm, respectively.

The 3D points of tree individuals do not provide plant information. Therefore, plant manual measurements should be exploited and utilized as reference parallel to the LiDAR data. The comparison of manual measurements to LiDAR based measurements from 224 trees, revealed significant correlation with respect to low measuring uncertainty, indicating the adequacy of LiDAR sensor to estimate simple and more complex structural parameters of fruit trees. However, plant structure is not fixed, instead, it varies according to the different stages of plant growth over the season. Therefore, LiDAR measurements should be calibrated based on manual measurements from the corresponding growth stage of the plant. In particular, manual measurements should be carried out at different heights that cover the tree profile. Since LiDAR scans radially, objects closer to sensor level are described with a greater amount of LiDAR scanning points. Further research should be conducted on the optimum sampling density of a calibration dataset to establish a robust correlation with LiDAR data.

6.2. *Calculating the water deficit of apple orchard by means of spatially resolved approach*

The implementation of LiDAR data of LA was chosen because it can be implemented in the calculation of daily tree water needs. Both orchards depicted loamy sand soil texture, depicting high coefficient of variation. In practice, soil spatial variability, among other factors. results in significant differences in orchards (Fountas et al. 2011; Uribeetxebarria et al. 2018). As mentioned above, soil texture is a major determinant of water holding

capacity, therefore a soil texture map can be used to establish an efficient irrigation plan. However, a sufficient number of samples must be taken to map the full range of soil variability, although this is typically cost prohibitive in commercial applications. Nonetheless, ECa mapping has proven to be an effective tool to describe soil spatial variability in orchards (Aggelopooulou et al., 2013; Vatsanidou et al., 2017). With the use of a four-electrode Wenner array, ECa was acquired spatially, allowing the definition of low, mid and high ECa areas within the orchards. In soil soils characterized by salinity lackness or low solubility of salts, it has been shown that ECa can be used to capture soil texture and soil moisture content information (Hunsaker et al., 2015). It is well established that, plants can access soil water through their root system, but this is mediated by soil texture and the plants' ability to extract the water. Therefore, readily available water content (RAW) was daily estimated and utilized as a threshold in the WB at each ECa region. In both orchards, the daily RAW in low ECa areas was reduced, while in high ECa regions the opposite happened. Knowledge of RAW is a factor of major significance as it indicates the threshold before the beginning of water stress (Jensen et al., 1990; Allen et al., 1998).

6.3. *Calculating the water deficit spatially using LiDAR laser scanner in an apple orchard*

However, tree water needs are affected also by morphological and physiological parameters, such as the development stage, height and leaf area. The hypothesis was initially confirmed in chapter 3.2, when the daily tree water needs were increased according to the range of manually sampled LA and height at different ECa regions. More specifically, trees of high LA in low ECa regions presented high water demands, indicating that ETc is affected by the spatial information pertaining to soil and plants, and should therefore be considered in the estimation of WB.

Many regional meteorological networks provide reference or potential ET estimates, but these are not local in the sense that they may only consider ET estimates at the scale of square kilometers, county boundaries, or for entire regions, and are often based on either remotely sensed data (Anderson et al., 2012; Knipper et al., 2019) or on sparse networks of meteorological stations (Gowda et al., 2008). However, the unique microclimate that can be created in individual orchards in combination with the heterogeneity of tree structural parameters, requires higher resolution in the calculation of ET. The suggested values of Kc from FAO do not fulfill the aforementioned requirements, especially in perennial trees where plant development takes place in 3D. This was confirmed in

chapter 3.3 when the suggested values from FAO were implemented in WB, indicating significantly lower daily water needs from the WB of LiDAR. Extracting the LA from the 3D point cloud at different ECa areas increased the resolution in the WB model. Thus, spatial information of plant parameters should be considered during the calculation of WB in orchards, since the implementation of 3D data in the WB can increase the temporal resolution and allow us to observe the plant responses with respect to environmental conditions, soil properties and fruit quality spatially.

6.4. *Vegetative factors of tree volume per ECa level*

Mounting a LiDAR sensor frame on ground vehicles gives us the opportunity to acquire 3D spatial data, while temporal information can be acquired by repeating the measurement over the growing stages of fruit trees. As mentioned above, reconstructing 3D point clouds from fruit trees does not necessarily provide any information about the plant status. In other words, 3D plant information should not be considered as a reference in the later process for extracting plant information. Instead, 3D data needs to be calibrated with related manual measurements from the tree (e.g LA, height, brunch width, stem diameter) at each measuring date. Constructing robust relationships between the latter parameters over the growth stages would provide clarity in the interpretation of spatio-temporal responses of plant physiology. For example, in chapter 3.6 the width and height of trees were temporally measured to estimate the V_{Manual} and calibrate the V_{LiDAR}. Whereas, in the following chapter, several trees (n = 32) were defoliated at each measuring date to build a relationship converting PPT to LA. A similar methodology was proposed by Sanz et al., (2018) who defoliated various perennial trees in different phenological stages to develop a linear model that uses the estimated volume from a LiDAR laser scanner as input to predict the LA.

6.5. *Effects of soil ECa and LiDAR-derived leaf area on fruit quality in the apple production*

However it should be considered if the sensor data really represent in which extent the manual measurements. In the case of LA, it was obvious that 3D point clouds of the segmented trees include points from woody part, leaves and the fruits. Forestry applications adopt LiDAR's backscattered reflectance intensity (R_{ToF}) and geometric features such as the linearity (L) and others, based on decomposed eigen values of the covariance matrix, to

discriminate LA from woody parts of trees (Ma et al., 2016; Xi Zhu et al., 2018). Thresholding methodology by means of R_{ToF} and L was proposed to segment and label tree point cloud components as LA or wood (Wang et al., 2018). Beland et al. (2014) suggested a voxel methodology to develop thresholds based on R_{ToF} frequency for retrieving the LA per tree. The results are sensitive to voxel size, and voxel size is influenced by occlusion. Hackel et al. (2016) analysed several geometric features, including L, to extract and select contour surfaces. Their method was based in the eigen values, eigen vectors and the angles (e.g. tangle) of points in 3D space. Similarly, Lin et al. (2014) calculated geometric features using a weighted principle component analysis (PCA) along with geometric median. In each point is assigned a weight to represent its spatial contribution in the weighted PCA and to estimate the geometric median, which can be regarded as a localized centre of a certain shape. However, LA analysis by means of LiDAR laser scanning needs to be further advanced for application in orchards, particularly in early season after bud break, when the percentage of wood surfaces is high compared to the trees foliage.

Thus, before using PPT to predict the LA, it should be considered that LA_{Manual} contains only the leaves that have been defoliated. Due to this fact, in Chapter 3.7, points from woody parts (e.g. stems, branches) were segmented from each individual tree. The method was based on the thresholding approach, which was part of the fruit detection methodology, using *L* and reflectance R_{ToF} to segment the woody parts from the point cloud.

The first derivate of wood segmentation was the quantification of woody parts over the season. The bare points of wood materials can be used as an indication of canopy coverage variation. Whereas their potential spatial interpretation can be implemented for the optimization of selective or site specific pruning applications. Karkee and Adhikari (2015) explicitly state that these traits could be used to develop pruning rules, showcasing preliminary success on tall spindle apple trees (Karkee et al., 2014). Recently, Li et al. (2017) proposed an adaptive extracting method of tree skeleton based on the point cloud data with a terrestrial laser scanner, and obtained consistent tree structure to identify unwanted branches in fruit trees for automated, selective pruning. Furthermore, in Medeiros et al.(, 2017), a laser sensor was used to collect observation data of fruit trees aiming for automatic dormant pruning, with the results showing that the system is able to identify the primary branches with an average accuracy of 98% and estimate their diameters with an average error of 0.6 cm. Mapping the pruning wood can be related with the early vigor in vie and utilized as a predictor with historical yield (Tagarakis et al., 2018).

On the other hand, segmenting woody parts from the point cloud allowed the optimization of the prediction of LA. Especially at $DABB_{55}$ ($R^2_{adj,C}$ = 0.97) and $DABB_{140}$ ($R^2_{adj,C}$ = 0.92), where wood materials were more profound on trees and when LA was fully developed. Furthermore, the spatial interpretation of the latter variable revealed similar spatial patterns between the two seasons, which was confirmed by several correlations. Similar correlations with ECa were partly found, indicating that trees can adapt LA according to the type of soil. Opposite results have been reported between ECa and LA in plums (Käthner et al., 2017).Nonetheless, the inextricable relation of LA with the final yield (Wagenmakers and Callesen, 1995; Wünsche and Lakso, 2000), which mainly lies in the intercepted light, was noted only at $DABB_{140}$ in 2019. As mentioned above, frosts occurred in February 2018, which delayed plant development and presumably led to yield reduction in the same year. Studies conducted in New Zealand showed that fruit growth is affected by daily temperature regimes: smaller fruit were produced from trees growing in low temperature conditions (Warrington et al., 1999). Especially in the first 40 days after full bloom (DAFB), low temperatures induce small fruit production. Stanley et al. (2000) identified a positive relationship between fruit size and growing degree-days accumulated in the first 50 DAFB.

On the other hand, the utilization of ECa and LA datasets to predict fruit quality (FM, D, SSC) was relatively limited. In general, in commercial orchards several cultivation tasks, such as soil fertilization, drip irrigation, pruning, crop load management are applied intensively, reducing the impact of soil and canopy geometry on fruit quality. Soil properties are characterized by temporal stability and low spatial variability, however, the latter it might be high to observe the effect on fruit level. In commercial apple trees no relation was found between fruit quality and ECa (Aggelopoulou et al., 2010; Manfrini et al., 2020), while similar results were indicated in plums (Käthner and Zude-Sasse, 2015). Similarly, in a commercial olive orchard, spatial variation in soil characteristics (nutrients, pH, and penetration resistance) revealed no relationship with yield time series, possibly due to extreme biennial bearing and bad prunning in olives (Fountas et al., 2011).

On the other hand, the LA collected information presented a more profound accuracy regarding fruit quality prediction. Therefore, the interaction of fruit quality with 3D plant structure should be highly considered and further studied in the future. Penzel et al. (2020) implemented a LiDAR laser scanner to model the daily demand of LA per fruit, showing that the fruit bearing capacity of individual trees varied according to the total leaf area of each

tree. However, sources of the managerial effects on production may be diverse and could range from different treatments between the two sections during block establishment, different management within this season or possibly different management in previous seasons. With perennial systems it is possible for management effects to linger for several years, for example, a different pruning strategy in year 1 will affect canopy and fruit development in year 2 and so on. As shown in this study, 3D data can be used to monitor and model tree geometry with high accuracy, presenting potential for the prediction of fruit quality. Future studies should focus on the time intervals of LiDAR measurements and define the resolution in order to bolster and facilitate the prediction of fruit quality. This is a key part of any spatial analysis and the next step in developing a spatial management strategy for the orchard, such as targeting differential, spatial, pruning, thinning and/ or harvesting strategies based on variable fruit set and maturity patterns to meet market targets.

6.6. *In-situ detection of apple fruit using LiDAR radiometric features*

In the proposed detection algorithm, with reflectance being the principal feature, showed that apples have higher reflectance than woody parts at 905 nm. The points from branches and stem showed the highest range in R values, which can possibly be attributed to the dependance of the laser beam incidence angle on the target properties considering R and surface roughness. In this study, plant materials including such as apples, leaves and woody parts have been assumed to be Lambertian scatters. Incidence angle effect on LiDAR backscatter intensity has been studied for about a decade with monochromatic laser scanners (Kaasalainen et al., 2011; Pesci and Teza, 2008). The laser beam wavelength effects of incidence angle were recently discussed by in the case of LiDAR laser scanning, suggesting that the differences in incidence angles were similar at different near-infrared wavelengths (Gaulton et al., 2013).

The bivariate histograms allowed to classify the segmented in x-z and y-z axis. The points binned within a uniform grid, chosen to cover the range of each axis and reveal the underlying shape of the distribution. Nonetheless, the latter approach reduced the resolution of fruit detection. Specifically, binning the points decreased the resolution that is provided by the 3D point cloud. The limitation became more obvious in the center of tree canopy where fruit density was increased. However, the H_{LiDAR} was correlated with the H_{Manual}, especially in the upper region of the tree where fruit were more distinct.

6.7. *Apple shape detection based on geometric and radiometric features*

The point cloud segmentation, fruit detection and counting approaches presented in this chapter can be applied to other orchards, based on data recorded over different seasons. The usefulness of 3D data in horticulture relies on the fact that fruit trees have a complex architecture that a 2D approach often fails to fully describe. The objectiveness that is provided by 3D renders fruit segmentation approaches flexible and adaptable to a wide range of classification problems.

Most of fruit detection systems in horticulture are based either on RGB or RGB-D images which are subjected to extensive light varying conditions in the field. Consequently, a larger amount of data is required to create and train a more convoluted classification architecture that can predict the nonlinear produced uncertainty from light variation. Some of the studies were undertaken in more controlled sunlight conditions (afternoon or dawn) where sunlight was reduced (Gené-Mola et al., 2019b; Z. Wang et al., 2017). However, farming applications take place in daytime, therefore the developed systems should ideally comply accordingly. In contrast, the LiDAR laser beam is not affected by lighting conditions as it relies on infrared wavelength (905 nm), providing 3D point clouds of high density.

The segmentation method of this study was based on the backscattered reflectance of the LiDAR and 3D geometrical features. However, supervised segmentation requires training examples, provided as a reference 3D point cloud, denoting the indicative values of shape and reflectance that a candidate fruit region should fulfill. Instead of labelling part of the data set in the foliated point cloud, it was preferred to manually defoliate each tree and use its point cloud as reference. This allowed us to acquire more discrete thresholds in radiometrical and geometrical features (R_A, C_A and L_A), but also estimate the position error for each individual fruit between the ideal (defoliated) and the realistic (foliated) case. A sensitivity analysis should be performed in future work to estimate the uncertainty of the inputs of the methodology.

The method could be characterized as a hybrid, because fruit detection relies on manual measurements. Following this approach, occlusions due to branches or leaves were avoided in the reference apple clusters. Fruit level labelling techniques should be adopted in the future for the evaluation of detection performance. Whereas

reverse engineering techniques such as 3D digitizers could be used in the future to reduce the time during fruit labeling.

An alternative process would be to label parts of the foliated point cloud and utilize them as training examples. This approach is relatively common in fruit detection algorithms irrespective of their data origin (e.g. 2D, 3D) (Gené-Mola et al., 2019a; Jia et al., 2020; Wu et al., 2020). The creation of a fruit detection system which can estimate fruit size at different growth stages (Figure 47) requires ground truth measurements, self-sufficient from the sensors, that can evaluate fruits over the stages.

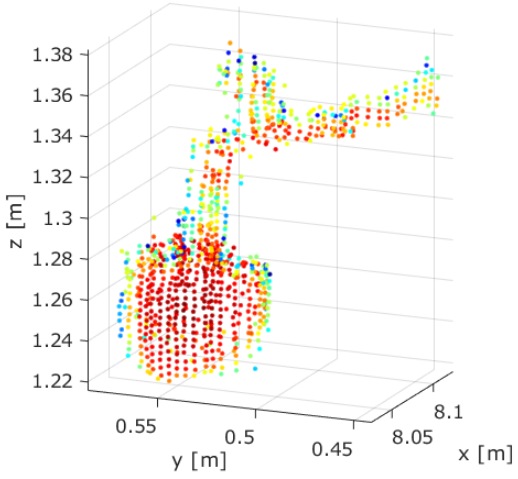

Figure 47. Apple fruit segmented from the tree 3D point cloud 120 days after full bloom, fruit size is 69.7 mm (Zude-Sasse1 et al., 2021)

Besides, combining manual measurements at different heights of the tree with 3D information can improve the assessment of the detected fruit number. From a physiological perspective, the presence or absence of fruit on apple trees has a major effect on their photosynthetic performance and growth rate (Corelli-Grappadelli and Lakso, 2004; Penzel et al., 2020). On the one hand, fruit detection results can be utilized to produce a pipeline that predicts the yield spatially (Bargoti and Underwood, 2017), nonetheless, most of the yield maps are the product of single measurements before harvest (Bramley and Ouzman, 2019; Gutiérrez et al., 2019). At this specific period, the cultivation practices that can be applied by farmers are limited, since most of the fruit growth has taken place. On the other hand, monitoring of fruit growth over the season and exploitation of the resolution provided by 3D data can be employeed to model the relationship of structural parameters (e.g. LA) with fruit number at different heights

on the tree. Thus, cultivation tasks such as late thinning would be able to be carried out by the farmer site specifically in order to produce apples of similar shape. Adjusting the crop load by thinning is an important factor of fruit quality through the alteration of the fruit:leaf ratio. Thinning modifies the carbohydrate availability and has a strong effect on fruit size, quality at harvest and return bloom. It is proven that thinning has a strong effect on source-sink relationships, in fact fruitlets are competing for carbon among themselves and growing shoots (Flore and Lakso, 2011).

7. Contributions

This thesis developed a framework for utilizing 3D data in apple trees, which is a crucial component of future precision horticulture. The proposed algorithms and systems, advance the state-of-the-art in LiDAR processing of orchard data to provide generalizable and principled approaches to estimating, mapping and modelling structural parameters. Additionally, 3D sensors are becoming smaller, smarter and cheaper. Therefore, technology breakthroughs are possible if enough research is commercialized since it is already economically justified to use 3-D sensors for producing agricultural products. The advantage of 3D data in fruit trees, is precisely the enhanced perception to describe not only the tree geometry, but also exploit their complex interaction with soil, microclimate, and fruit quality, spatio-temporally as was shown in the later chapters.

To date, there is scarce information regarding the extraction of 3D data from fruit trees in high density orchards by means of precision horticultural techniques. In this study, a tree segmentation pipeline was proposed utilizing a LiDAR laser to detect geometric variables that could be implemented in tree-individual orchard management, specifically mechanical pruning, irrigation, and spraying. The method contributed in trials on sweet cherries (Saha et al., 2020) and apple (Penzel et al., 2020) trees facilitating the data analysis process with respect to point cloud reconstruction and tree segmentation.

There is also limited information on how 3D structure could be implemented in the estimation of tree water needs. Spatial information of tree structure (LA, height) from different ECa regions was combined with weather data to produce a daily water balance model. The results of the mappings and the processing of the data provided high spatio-temporal resolution in water balance which was used for the estimation of tree water needs at different ECa levels. Thus, the estimation of daily water needs could be adjusted to the micro-conditions of individual orchards, improving the quality that is provided by FAO without having an impact on production.

Despite the physiological relationship of fruit yield and quality with vegetative growth of perennial trees, their spatial interaction during the growth season has been rarely investigated. In this study, applications of LiDAR laser scanning of apple trees addressed monitoring of 3D canopy variables at different growth stages. Specifically, the effect of ECa in the growth of tree volume was analyzed spatially. Moreover, LA models were presented at different growth stages of two consecutive seasons and utilized to express LA spatially. The soil-climatic properties and the

yield were exploited to study the interaction with the growth of LA. According to the measurements of the physiology of apple trees, having a clear picture of the properties of each part of the orchards helps make decisions for its management. Furthermore, the LA dataset performed better than the ECa in the prediction of fruit quality parameters. In parallel, the estimation of LA, based on the proposed methodology, was contributed as input for modelling the fruit bearing capacity in Pinova trees (Penzel et al., 2020).

A novel fruit segmentation method was proposed based on the LiDAR's backscattered reflectance (905 nm) and geometrical features. This allowed us to overcome limitations of RGB systems in 2D and 3D, which are mainly affected by light variations. Moreover, working in a 3D space enabled the identification of geometric tree features, such as shape and size, aiming at fruit localization. A new pipeline process which exploits ground truth labels based on in situ measurements (defoliation, fruit diameter) was proposed. Thus, information from leaves, fruits and woody parts could be acquired with higher resolution, increasing the segmentation accuracy of fruits. In parallel, the size of fruits could be monitored at different stages of apple tree growth. Finally, this study could be integrated in the development of a Decision Support System (DSS) for the development of a decision support system and for the optimization of site-specific management in apples orchards.

8. Future work

The components of this thesis are designed to address future machine vision under the challenging environmental conditions in high density apple orchards. This conditions have led to significant quantified improvements in accuracy and estimation of 3D informatin across the different stages of tree and fruit. Regarding tree segmentation, the accuracy of the proposed methodology should be evaluated at different plant density orchards and cultivars, since different fruit sphericities will test the accuracy of the proposed methodology. Moreover, further research needs to be done with the use of clustering algorithms for single plant segmentation (e.g. Euclidian, max-flow/min-cut theorem, region growing segmentation) so that parts of the canopy are not cut off from the tree point cloud, and that plants at a later growth stage can be analyzed. Also, non-rigid registration and alignment need to be explored to reduce the effect of miscellaneous errors that reduce overlapping between point cloud pairs.

The proposed framework of fruit detection is intended to be used by growers and agronomists to optimise decision making at the farm. It therefore enables the next stage of research, which involves designing data driven operational strategies that leverage the understanding of spatial distribution of fruit number at different tree heights to optimize tasks such as crop load management and selective harvesting. In addition, fruit growth variation should be modelled at different positions on the tree in relation to the microclimate properties within the canopy (e.g. radiation, humidity, temperature). The ability to associate the number and quality of fruits to individual trees and rows across orchard blocks helps maintain a database that could be systematically updated throughout the seasons and cultivation years, which will enable a quantified experimental approach to test the benefits of fully data driven decision-making at the orchard.

In the context of precision horticulture in perennial trees, further advances should focus on the impact of canopy management such as pruning, flower and fruit thinning on 3D derived structural parameters (e.g. LA, V). It would also be important to further monitor the structural parameters spatio-temporally at different perennial trees and study the impact of soil properties on their growth and fruit quality. Moreover, the inner relation of structural parameters with fruit quality at fruit growth stages should be further observed. The promising results of fruit prediction accuracies using LA could potentially be improved by providing more datasets from fruit growth stages.

The whole process of a complete precision agriculture cycle that was mentioned in the introduction could be improved by the implementation of 3D technology in perennial trees (Figure 48). Specifically, the first step concerns data acquisition, where plants would be monitored over the growth stages and be supported by microclimate, soil data and manual measurements. Therefore, temporal data of high spatial resolution would be processed and analyzed to extract plant information. The main advantage of this stage and of 3D data is that various information regarding the tree (e.g.LA, height, volume) or the fruit (fruit size) can be extracted from the same data set. The dataset could be further supported with the extraction of soil information (e.g. ECa), intensity of canopy management (pruning thinning etc.) and weather data.

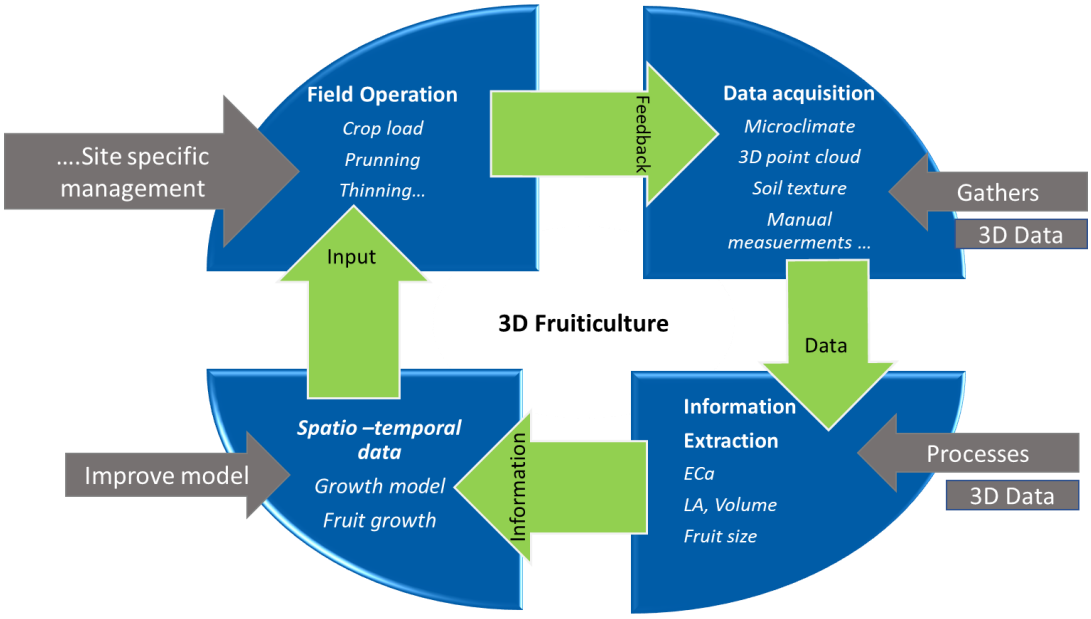

Figure 48. Cycle of fruiticulture based on 3D data.

The primary aim of the extracted information will aim toward their integration to physiological models. Therefore, fruit and tree growth would be modelled with respect to the fruit's spatial position on the tree or the tree's spatial position within the orchard. Increasing the resolution of the model would allow us to better comprehend the spatial interaction among the variables. Moreover, model derivatives would be the input of a DSS facilitating site specific applications such as selective harvesting, pruning, thinning. Whereas the 3D core of the data can potentially improve variable rate applications of fertilizers, pesticides and irrigation. The improvement of

the whole process would depend on model prediction, where its database could be systematically updated throughout the seasons and over multiple years, but mainly the feedback from the farmer or the worker who apply cultivation tasks site-specifically. 3D data and processing techniques in agriculture can help to bridge the gap between the artificial intelligence and the real world since, rapid prototyping and digital agriculture by generating physiological models derived from scanned data. Furthermore, the ability to transfer models based on different 3D sensors and/or sensor configurations needs to be examined, as it would allow more flexibility in hardware configuration without requiring repeated efforts for training. The applicability of transfer learning could potentially encourage the development a public database containing pre-learned models, allowing the deployment to new orchards without the need for extensive data labelling. Therefore, enables the next stage of research, which involves designing data driven operational strategies based on 3D data that leverage from the understanding of tree spatial distribution, to optimise tasks such as irrigating, thinning, pruning, and harvesting.

9. References

Aggelopooulou, K., Castrignanò, A., Gemtos, T., De Benedetto, D., 2013. Delineation of management zones in an apple orchard in Greece using a multivariate approach. Comput. Electron. Agric. 90, 119–130. https://doi.org/10.1016/j.compag.2012.09.009

Aggelopoulou, K.D., Pateras, D., Fountas, S., Gemtos, T.A., Nanos, G.D., 2011. Soil spatial variability and site-specific fertilization maps in an apple orchard. Precis. Agric. 12, 118–129. https://doi.org/10.1007/s11119-010-9161-x

Aggelopoulou, K.D., Wulfsohn, D., Fountas, S., Gemtos, T.A., Nanos, G.D., Blackmore, S., 2010. Spatial variation in yield and quality in a small apple orchard. Precis. Agric. 11, 538–556. https://doi.org/10.1007/s11119-009-9146-9

Alexandridis, T.K., Panagopoulos, A., Galanis, G., Alexiou, I., Cherif, I., Chemin, Y., Stavrinos, E., Bilas, G., Zalidis, G.C., 2014. Combining remotely sensed surface energy fluxes and GIS analysis of groundwater parameters for irrigation system assessment. Irrig. Sci. 32, 127–140. https://doi.org/10.1007/s00271-013-0419-8

Ali, H., Lali, M.I., Nawaz, M.Z., Sharif, M., Saleem, B.A., 2017. Symptom based automated detection of citrus diseases using color histogram and textural descriptors. Comput. Electron. Agric. 138, 92–104. https://doi.org/10.1016/j.compag.2017.04.008

Ampatzidis, Y.G., Vougioukas, S.G., Bochtis, D.D., Tsatsarelis, C.A., 2009. A yield mapping system for hand-harvested fruits based on RFID and GPS location technologies: Field testing. Precis. Agric. 10, 63–72. https://doi.org/10.1007/s11119-008-9095-8

Anastasiou, E., Balafoutis, A., Darra, N., Psiroukis, V., Biniari, A., Xanthopoulos, G., Fountas, S., 2018. Satellite and proximal sensing to estimate the yield and quality of table grapes. Agric. 8, 94. https://doi.org/10.3390/agriculture8070094

Anastasiou, E., Castrignanò, A., Arvanitis, K., Fountas, S., 2019. A multi-source data fusion approach to assess spatial-temporal variability and delineate homogeneous zones: A use case in a table grape vineyard in Greece. Sci. Total Environ. 684, 155–163. https://doi.org/10.1016/j.scitotenv.2019.05.324

Anderson, M.C., Allen, R.G., Morse, A., Kustas, W.P., 2012. Use of Landsat thermal imagery in monitoring evapotranspiration and managing water resources. Remote Sens. Environ. 122, 50–65. https://doi.org/10.1016/j.rse.2011.08.025

Anderson, N.T., Underwood, J.P., Rahman, M.M., Robson, A., Walsh, K.B., 2019. Estimation of fruit load in mango orchards: tree sampling considerations and use of machine vision and satellite imagery. Precis. Agric. 20, 823–839. https://doi.org/10.1007/s11119-018-9614-1

Arad, B., Balendonck, J., Barth, R., Ben-Shahar, O., Edan, Y., Hellström, T., Hemming, J., Kurtser, P., Ringdahl, O., Tielen, T., van Tuijl, B., 2020. Development of a sweet pepper harvesting robot. J. F. Robot. 37, 1027–1039. https://doi.org/10.1002/rob.21937

Arnó, J., Escolà, A., Vallès, J.M., Llorens, J., Sanz, R., Masip, J., Palacín, J., Rosell-Polo, J.R., 2013. Leaf area index estimation in vineyards using a ground-based LiDAR scanner. Precis. Agric. 14, 290–306. https://doi.org/10.1007/s11119-012-9295-0

Åstrand, B., Baerveldt, A.J., 2002. An agricultural mobile robot with vision-based perception for mechanical weed control. Auton. Robots 13, 21–35. https://doi.org/10.1023/A:1015674004201

Auat Cheein, F.A., Guivant, J., Sanz, R., Escolà, A., Yandún, F., Torres-Torriti, M., Rosell-Polo, J.R., 2015. Real-time approaches for characterization of fully and partially scanned canopies in groves. Comput. Electron. Agric. 118, 361–371. https://doi.org/10.1016/j.compag.2015.09.017

Auerswald, K., Simon, S., Stanjek, H., 2001. Influence of soil properties on electrical conductivity under humid water regimes. Soil Sci. 166, 382–390. https://doi.org/10.1097/00010694-200106000-00003

Ayyoub, A., Er-Raki, S., Khabba, S., Merlin, O., Ezzahar, J., Rodriguez, J.C., Bahlaoui, A., Chehbouni, A., 2017. A simple and alternative approach based on reference evapotranspiration and leaf area index for estimating tree transpiration in semi-arid regions. Agric. Water Manag. 188, 61–68. https://doi.org/10.1016/j.agwat.2017.04.005

Badenes, M.L., Byrne, D.H., 2012. Fruit breeding, Fruit Breeding. https://doi.org/10.1007/978-1-4419-0763-9

Baeten, J., Donné, K., Boedrij, S., Beckers, W., Claesen, E., 2008. Autonomous fruit picking machine: A robotic apple harvester, in: Springer Tracts in Advanced Robotics. pp. 531–539. https://doi.org/10.1007/978-3-540-75404-6_51

Bak, T., Jakobsen, H., 2004. Agricultural Robotic Platform with Four Wheel Steering for Weed Detection. Biosyst. Eng. 87, 125–136. https://doi.org/10.1016/j.biosystemseng.2003.10.009

Bakker, T., Van Asselt, K., Bontsema, J., Müller, J., Van Straten, G., 2006. An autonomous weeding robot for organic farming, in: Springer Tracts in Advanced Robotics. pp. 579–590. https://doi.org/10.1007/978-3-540-33453-8_48

Balafoutis, A.T., Beck, B., Fountas, S., Tsiropoulos, Z., Vangeyte, J., van der Wal, T., Soto-Embodas, I., Gómez-Barbero, M., Pedersen, S.M., 2017. Smart Farming Technologies – Description, Taxonomy and Economic Impact. pp. 21–77. https://doi.org/10.1007/978-3-319-68715-5_2

Barber, C.B., Dobkin, D.P., Huhdanpaa, H., 1996. The Quickhull Algorithm for Convex Hulls. ACM Trans. Math. Softw. 22, 469–483. https://doi.org/10.1145/235815.235821

Bargoti, S., Underwood, J.P., 2017. Image Segmentation for Fruit Detection and Yield Estimation in Apple Orchards. J. F. Robot. 34, 1039–1060. https://doi.org/10.1002/rob.21699

Bargoti, S., Underwood, J.P., Nieto, J.I., Sukkarieh, S., 2015. A pipeline for trunk localisation using LiDAR in trellis structured orchards, in: Springer Tracts in Advanced Robotics. pp. 455–468. https://doi.org/10.1007/978-3-319-07488-7_31

Barnea, E., Mairon, R., Ben-Shahar, O., 2016. Colour-agnostic shape-based 3D fruit detection for crop harvesting robots. Biosyst. Eng. 146, 57–70. https://doi.org/10.1016/j.biosystemseng.2016.01.013

Bauriegel, E., Herppich, W., 2014. Hyperspectral and Chlorophyll Fluorescence Imaging for Early Detection of Plant Diseases, with Special Reference to Fusarium spec. Infections on Wheat. Agriculture 4, 32–57. https://doi.org/10.3390/agriculture4010032

Bawden, O., Kulk, J., Russell, R., McCool, C., English, A., Dayoub, F., Lehnert, C., Perez, T., 2017. Robot for weed species plant-specific management. J. F. Robot. 34, 1179–1199. https://doi.org/10.1002/rob.21727

Beder, C., Bartczak, B., Koch, R., 2007. A comparison of PMD-cameras and stereo-vision for the task of surface reconstruction using patchlets, in: Proceedings of the IEEE Computer Society Conference on Computer Vision and Pattern Recognition. https://doi.org/10.1109/CVPR.2007.383348

Behmann, J., Mahlein, A.K., Rumpf, T., Römer, C., Plümer, L., 2015. A review of advanced machine learning methods for the detection of biotic stress in precision crop protection. Precis. Agric. https://doi.org/10.1007/s11119-014-9372-7

Béland, M., Baldocchi, D.D., Widlowski, J.L., Fournier, R.A., Verstraete, M.M., 2014. On seeing the wood from the leaves and the role of voxel size in determining leaf area distribution of forests with terrestrial LiDAR. Agric. For. Meteorol. 184, 82–97. https://doi.org/10.1016/j.agrformet.2013.09.005

Béland, M., Widlowski, J.L., Fournier, R.A., Côté, J.F., Verstraete, M.M., 2011. Estimating leaf area distribution in savanna trees from terrestrial LiDAR measurements. Agric. For. Meteorol. https://doi.org/10.1016/j.agrformet.2011.05.004

Bellvert, J., Marsal, J., Girona, J., Gonzalez-Dugo, V., Fereres, E., Ustin, S.L., Zarco-Tejada, P.J., 2016. Airborne thermal imagery to detect the seasonal evolution of crop water status in peach, nectarine and Saturn peach orchards. Remote Sens. 8. https://doi.org/10.3390/rs8010039

Ben-Gal, A., Agam, N., Alchanatis, V., Cohen, Y., Yermiyahu, U., Zipori, I., Presnov, E., Sprintsin, M., Dag, A., 2009. Evaluating water stress in irrigated olives: Correlation of soil water status, tree water status, and thermal imagery. Irrig. Sci. 27, 367–376. https://doi.org/10.1007/s00271-009-0150-7

Berni, J.A.J., Zarco-Tejada, P.J., Suárez, L., Fereres, E., 2009. Thermal and narrowband multispectral remote sensing for vegetation monitoring from an unmanned aerial vehicle. IEEE Trans. Geosci. Remote Sens. 47, 722–738. https://doi.org/10.1109/TGRS.2008.2010457

Blasco, J., Aleixos, N., Roger, J.M., Rabatel, G., Moltó, E., 2002. Robotic weed control using machine vision. Biosyst. Eng. 83, 149–157. https://doi.org/10.1006/bioe.2002.0109

Blum, A., 2017. Osmotic adjustment is a prime drought stress adaptive engine in support of plant production. Plant Cell Environ. 40, 4–10. https://doi.org/10.1111/pce.12800

Bochtis, D.D., Sørensen, C.G., Jørgensen, R.N., Nørremark, M., Hameed, I.A., Swain, K.C., 2011. Robotic weed monitoring. Acta Agric. Scand. Sect. B Soil Plant Sci. 61, 202–208. https://doi.org/10.1080/09064711003796428

Bosilj, P., Duckett, T., Cielniak, G., 2018. Connected attribute morphology for unified vegetation segmentation and classification in precision agriculture. Comput. Ind. 98, 226–240. https://doi.org/10.1016/j.compind.2018.02.003

Bourodimos, G., Koutsiaras, M., Psiroukis, V., Balafoutis, A., Fountas, S., 2019. Development and field evaluation of a spray drift risk assessment tool for vineyard spraying application. Agric. 9. https://doi.org/10.3390/agriculture9080181

Bramley, R.G.V., Ouzman, J., 2019. Farmer attitudes to the use of sensors and automation in fertilizer decision-making: nitrogen fertilization in the Australian grains sector. Precis. Agric. 20, 157–175. https://doi.org/10.1007/s11119-018-9589-y

Braud, I., Varado, N., Olioso, A., 2005. Comparison of root water uptake modules using either the surface energy balance or potential transpiration. J. Hydrol. 301, 267–286. https://doi.org/10.1016/j.jhydrol.2004.06.033

Breen, K.C., Tustin, D.S., Palmer, J.W., Hedderley, D.I., Close, D.C., 2016. Effects of environment and floral intensity on fruit set behaviour and annual flowering in apple. Sci. Hortic. (Amsterdam). 210, 258–267. https://doi.org/10.1016/j.scienta.2016.07.025

Brodu, N., Lague, D., 2012. 3D terrestrial lidar data classification of complex natural scenes using a multi-scale dimensionality criterion: Applications in geomorphology. ISPRS J. Photogramm. Remote Sens. 68, 121–134. https://doi.org/10.1016/j.isprsjprs.2012.01.006

Bufton, J.L., 1991. Airborne lidar for profiling of surface topography. Opt. Eng. 30, 72. https://doi.org/10.1117/12.55770

Bustan, A., Dag, A., Yermiyahu, U., Erel, R., Presnov, E., Agam, N., Kool, D., Iwema, J., Zipori, I., Ben-Gal, A., 2016. Fruit load governs transpiration of olive trees. Tree Physiol. 36, 380–391. https://doi.org/10.1093/treephys/tpv138

Calderón, R., Navas-Cortés, J.A., Lucena, C., Zarco-Tejada, P.J., 2013. High-resolution airborne hyperspectral and thermal imagery for early detection of Verticillium wilt of olive using fluorescence, temperature and narrow-band spectral indices. Remote Sens. Environ. 139, 231–245. https://doi.org/10.1016/j.rse.2013.07.031

Calders, K., Newnham, G., Burt, A., Murphy, S., Raumonen, P., Herold, M., Culvenor, D., Avitabile, V., Disney, M., Armston, J., Kaasalainen, M., 2015. Nondestructive estimates of above-ground biomass using terrestrial laser scanning. Methods Ecol. Evol. 6, 198–208. https://doi.org/10.1111/2041-210X.12301

Cambardella, C.A., Moorman, T.B., Novak, J.M., Parkin, T.B., Karlen, D.L., Turco, R.F., Konopka, A.E., 1994. Field-Scale Variability of Soil Properties in Central Iowa Soils. Soil Sci. Soc. Am. J. 58, 1501–1511. https://doi.org/10.2136/sssaj1994.03615995005800050033x

Candiago, S., Remondino, F., De Giglio, M., Dubbini, M., Gattelli, M., 2015. Evaluating multispectral images and vegetation indices for precision farming applications from UAV images. Remote Sens. 7, 4026–4047. https://doi.org/10.3390/rs70404026

Carrara, M., Comparetti, A., Febo, P., Orlando, S., 2004. Spatially variable rate herbicide application on durum wheat in Sicily. Biosyst. Eng. 87, 387–392. https://doi.org/10.1016/j.biosystemseng.2004.01.004

Catania, P., Comparetti, A., Febo, P., Morello, G., Orlando, S., Roma, E., Vallone, M., 2020. Positioning accuracy comparison of GNSS

receivers used for mapping and guidance of agricultural machines. Agronomy 10. https://doi.org/10.3390/agronomy10070924

Cater, M., Parkin, G., Culley, J., Hao, X., Ball, B., 2007. Soil Density and Porosity, in: Soil Sampling and Methods of Analysis, Second Edition. https://doi.org/10.1201/9781420005271.ch57

Chang, C.L., Lin, K.M., 2018. Smart agricultural machine with a computer vision-based weeding and variable-rate irrigation scheme. Robotics 7. https://doi.org/10.3390/robotics7030038

Charrier, G., Ngao, J., Saudreau, M., Améglio, T., 2015. Effects of environmental factors and management practices on microclimate, winter physiology, and frost resistance in trees. Front. Plant Sci. https://doi.org/10.3389/fpls.2015.00259

Chen, C., Neill, K., Wichman, D., Westcott, M., 2008. Hard red spring wheat response to row spacing, seeding rate, and nitrogen. Agron. J. 100, 1296–1302. https://doi.org/10.2134/agronj2007.0198

Clay, D.E., Kitchen, N.R., Byamukama, E., Bruggeman, S.A., 2018. Calculations supporting management zones, in: Practical Mathematics for Precision Farming. pp. 123–135. https://doi.org/10.2134/practicalmath2017.0024

Clay, D.E., Shanahan, J.F., 2011. GIS applications in agriculture: Volume two: Nutrient management for energy efficiency, GIS Applications in Agriculture: Volume Two: Nutrient Management for Energy Efficiency.

Cohen, Y., Alchanatis, V., Prigojin, A., Levi, A., Soroker, V., Cohen, Y., 2012. Use of aerial thermal imaging to estimate water status of palm trees. Precis. Agric. 13, 123–140. https://doi.org/10.1007/s11119-011-9232-7

Colaço, A.F., Molin, J.P., 2017. Variable rate fertilization in citrus: a long term study. Precis. Agric. 18, 169–191. https://doi.org/10.1007/s11119-016-9454-9

Colaço, A.F., Molin, J.P., Rosell-Polo, J.R., Escolà, A., 2019. Spatial variability in commercial orange groves. Part 2: relating canopy geometry to soil attributes and historical yield. Precis. Agric. 20, 805–822. https://doi.org/10.1007/s11119-018-9615-0

Colaço, A.F., Molin, J.P., Rosell-Polo, J.R., Escolà, A., 2018. Application of light detection and ranging and ultrasonic sensors to high-throughput phenotyping and precision horticulture: Current status and challenges. Hortic. Res. 5. https://doi.org/10.1038/s41438-018-0043-0

Colaço, A.F., Trevisan, R.G., Karp, F.H.S., Molin, J.P., 2020. Yield mapping methods for manually harvested crops. Comput. Electron. Agric. 177. https://doi.org/10.1016/j.compag.2020.105693

Corelli-Grappadelli, L., Lakso, A.N., 2004. Fruit development in deciduous tree crops as affected by physiological factors and environmental Conditions, in: Acta Horticulturae. https://doi.org/10.17660/ActaHortic.2004.636.52

Coren, F., Sterzai, P., 2006. Radiometric correction in laser scanning. Int. J. Remote Sens. 27, 3097–3104. https://doi.org/10.1080/01431160500217277

Corwin, D.L., Plant, R.E., 2005. Applications of apparent soil electrical conductivity in precision agriculture. Comput. Electron. Agric. https://doi.org/10.1016/j.compag.2004.10.004

Costa, G., Corelli-Grappadelli, L., Bucchi, F., 2001. Studies on apple fruit abscission and growth as affected by cytokinins, in: Acta Horticulturae. pp. 243–251. https://doi.org/10.17660/actahortic.2001.557.31

Courault, D., Seguin, B., Olioso, A., 2005. Review on estimation of evapotranspiration from remote sensing data: From empirical to numerical modeling approaches. Irrig. Drain. Syst. 19, 223–249. https://doi.org/10.1007/s10795-005-5186-0

Dammer, K.H., 2016. Real-time variable-rate herbicide application for weed control in carrots. Weed Res. 56, 237–246. https://doi.org/10.1111/wre.12205

Dassot, M., Colin, A., Santenoise, P., Fournier, M., Constant, T., 2012. Terrestrial laser scanning for measuring the solid wood volume,

including branches, of adult standing trees in the forest environment. Comput. Electron. Agric. 89, 86–93. https://doi.org/10.1016/j.compag.2012.08.005

De-An, Z., Jidong, L., Wei, J., Ying, Z., Yu, C., 2011. Design and control of an apple harvesting robot. Biosyst. Eng. 110, 112–122. https://doi.org/10.1016/j.biosystemseng.2011.07.005

De Benedetto, D., Castrignano, A., Diacono, M., Rinaldi, M., Ruggieri, S., Tamborrino, R., 2013. Field partition by proximal and remote sensing data fusion. Biosyst. Eng. 114, 372–383. https://doi.org/10.1016/j.biosystemseng.2012.12.001

Dodd, I.C., Egea, G., Watts, C.W., Whalley, W.R., 2010. Root water potential integrates discrete soil physical properties to influence ABA signalling during partial rootzone drying. J. Exp. Bot. 61, 3543–3551. https://doi.org/10.1093/jxb/erq195

Ebrahimi, M.A., Khoshtaghaza, M.H., Minaei, S., Jamshidi, B., 2017. Vision-based pest detection based on SVM classification method. Comput. Electron. Agric. 137, 52–58. https://doi.org/10.1016/j.compag.2017.03.016

Enclona, E.A., Thenkabail, P.S., Celis, D., Diekmann, J., 2004. Within-field wheat yield prediction from IKONOS data: A new matrix approach. Int. J. Remote Sens. 25, 377–388. https://doi.org/10.1080/0143116031000102485

Escolà, A., Martínez-Casasnovas, J.A., Rufat, J., Arnó, J., Arbonés, A., Sebé, F., Pascual, M., Gregorio, E., Rosell-Polo, J.R., 2017. Mobile terrestrial laser scanner applications in precision fruticulture/horticulture and tools to extract information from canopy point clouds. Precis. Agric. 18, 111–132. https://doi.org/10.1007/s11119-016-9474-5

Ester, M., Kriegel, H.-P., Sander, J., Xu, X., 1996. A Density-Based Algorithm for Discovering Clusters in Large Spatial Databases with Noise, in: Proceedings of the 2nd International Conference on Knowledge Discovery and Data Mining. pp. 226–231.

Estornell, J., Velázquez-Martí, A., Fernández-Sarría, A., López-Cortés, I., Martí-Gavilá, J., Salazar, D., 2017. Estimación de parámetros de estructura de nogales utilizando láser escáner terrestre. Rev. Teledetec. 2017, 67–76. https://doi.org/10.4995/raet.2017.7429

Evans, R.G., 2004. Energy balance of apples under evaporative cooling. Trans. Am. Soc. Agric. Eng. 47, 1029–1037. https://doi.org/10.13031/2013.16576

Feng, F., Li, M., Ma, F., Cheng, L., 2014. Effects of location within the tree canopy on carbohydrates, organic acids, amino acids and phenolic compounds in the fruit peel and flesh from three apple (Malus 3 domestica) cultivars. Hortic. Res. 1. https://doi.org/10.1038/hortres.2014.19

Fernandez-Gallego, J.A., Kefauver, S.C., Gutiérrez, N.A., Nieto-Taladriz, M.T., Araus, J.L., 2018. Wheat ear counting in-field conditions: High throughput and low-cost approach using RGB images. Plant Methods 14. https://doi.org/10.1186/s13007-018-0289-4

Ferreira, M.I., 2017. Stress coefficients for soil water balance combined with water stress indicators for irrigation scheduling of woody crops. Horticulturae 3, 38. https://doi.org/10.3390/horticulturae3020038

Fitzgerald, G.J., 2010. Characterizing vegetation indices derived from active and passive sensors. Int. J. Remote Sens. 31, 4335–4348. https://doi.org/10.1080/01431160903258217

Flore, J.A., Lakso, A.N., 2011. Environmental and Physiological Regulation of Photosynthesis in Fruit Crops, in: Horticultural Reviews. pp. 111–157. https://doi.org/10.1002/9781118060841.ch4

Flynn, E.S., Dougherty, C.T., Wendroth, O., 2008. Assessment of pasture biomass with the normalized difference vegetation index from active ground-based sensors. Agron. J. 100, 114–121. https://doi.org/10.2134/agronj2006.0363

Forouzanmehr, E., Loghavi, M., 2012. Design, development and field evaluation of a map-based variable rate granular fertilizer application control system, in: Agricultural Engineering International: CIGR Journal. pp. 255–261. https://doi.org/10.13031/2013.29807

Forsline, P.L., Aldwinckle, H.S., Dickson, E.E., Luby, J.J., Hokanson, S.C., 2010. Collection, Maintenance, Characterization, and

Utilization of Wild Apples of Central Asia, in: Horticultural Reviews. pp. 1–61. https://doi.org/10.1002/9780470650868.ch1

Forsman, M., Börlin, N., Olofsson, K., Reese, H., Holmgren, J., 2018. Bias of cylinder diameter estimation from ground-based laser scanners with different beam widths: A simulation study. ISPRS J. Photogramm. Remote Sens. 135, 84–92. https://doi.org/10.1016/j.isprsjprs.2017.11.013

Fountas, S., Aggelopoulou, K., Bouloulis, C., Nanos, G.D., Wulfsohn, D., Gemtos, T.A., Paraskevopoulos, A., Galanis, M., 2011. Site-specific management in an olive tree plantation. Precis. Agric. 12, 179–195. https://doi.org/10.1007/s11119-010-9167-4

Fountas, S., Anastasiou, E., Xanthopoulos, G., Lambrinos, G., Manolopoulou, E., Apostolidou, S., Lentzou, D., Tsiropoulos, Z., Balafoutis, A., 2015. Precision agriculture in watermelons, in: Precision Agriculture 2015 - Papers Presented at the 10th European Conference on Precision Agriculture, ECPA 2015. pp. 209–215. https://doi.org/10.3920/978-90-8686-814-8_25

Fountas, S., Mylonas, N., Malounas, I., Rodias, E., Santos, C.H., Pekkeriet, E., 2020. Agricultural robotics for field operations. Sensors (Switzerland). https://doi.org/10.3390/s20092672

Gan, H., Lee, W.S., Alchanatis, V., Ehsani, R., Schueller, J.K., 2018. Immature green citrus fruit detection using color and thermal images. Comput. Electron. Agric. 152, 117–125. https://doi.org/10.1016/j.compag.2018.07.011

Gao, G., Xiao, K., Jia, Y.C., 2020. A spraying path planning algorithm based on colour-depth fusion segmentation in peach orchards. Comput. Electron. Agric. 173. https://doi.org/10.1016/j.compag.2020.105412

Garcia-Lamont, F., Cervantes, J., López, A., Rodriguez, L., 2018. Segmentation of images by color features: A survey. Neurocomputing 292, 1–27. https://doi.org/10.1016/j.neucom.2018.01.091

García Petillo, M., Castel, J.R., 2007. Water balance and crop coefficient estimation of a citrus orchard in Uruguay. Spanish J. Agric. Res. 5, 232–243. https://doi.org/10.5424/sjar/2007052-243

Gaulton, R., Danson, F.M., Ramirez, F.A., Gunawan, O., 2013. The potential of dual-wavelength laser scanning for estimating vegetation moisture content. Remote Sens. Environ. 132, 32–39. https://doi.org/10.1016/j.rse.2013.01.001

Gavioli, A., de Souza, E.G., Bazzi, C.L., Guedes, L.P.C., Schenatto, K., 2016. Optimization of management zone delineation by using spatial principal components. Comput. Electron. Agric. 127, 302–310. https://doi.org/10.1016/j.compag.2016.06.029

Gebbers, R., Lück, E., Dabas, M., Domsch, H., 2009. Comparison of instruments for geoelectrical soil mapping at the field scale. Near Surf. Geophys. 7, 179–190. https://doi.org/10.3997/1873-0604.2009011

Geipel, J., Link, J., Wirwahn, J.A., Claupein, W., 2016. A programmable aerial multispectral camera system for in-season crop biomass and nitrogen content estimation. Agric. 6. https://doi.org/10.3390/agriculture6010004

Gené-Mola, J., Gregorio, E., Guevara, J., Auat, F., Sanz-Cortiella, R., Escolà, A., Llorens, J., Morros, J.R., Ruiz-Hidalgo, J., Vilaplana, V., Rosell-Polo, J.R., 2019a. Fruit detection in an apple orchard using a mobile terrestrial laser scanner. Biosyst. Eng. 187, 171–184. https://doi.org/10.1016/j.biosystemseng.2019.08.017

Gené-Mola, J., Vilaplana, V., Rosell-Polo, J.R., Morros, J.R., Ruiz-Hidalgo, J., Gregorio, E., 2019b. Multi-modal deep learning for Fuji apple detection using RGB-D cameras and their radiometric capabilities. Comput. Electron. Agric. 162, 689–698. https://doi.org/10.1016/j.compag.2019.05.016

Giles, D.K., Delwiche, M.J., Dodd, R.B., 1988. Electronic Measurement of Tree Canopy Volume. Trans. Am. Soc. Agric. Eng. 31, 264–272. https://doi.org/10.13031/2013.30698

Goffinet, M.C., Robinson, T.L., Lakso, A.N., 1995. A comparison of Empire' apple fruit size and anatomy in unthinned and hand-thinned trees. J. Hortic. Sci. 70, 375–387. https://doi.org/10.1080/14620316.1995.11515307

Gokturk, S.B., Yalcin, H., Bamji, C., 2004. A time-of-flight depth sensor - System description, issues and solutions, in: IEEE Computer

Society Conference on Computer Vision and Pattern Recognition Workshops. https://doi.org/10.1109/CVPR.2004.291

Gongal, A., Amatya, S., Karkee, M., Zhang, Q., Lewis, K., 2015. Sensors and systems for fruit detection and localization: A review. Comput. Electron. Agric. 116, 8–19. https://doi.org/10.1016/j.compag.2015.05.021

Gongal, A., Karkee, M., Amatya, S., 2018. Apple fruit size estimation using a 3D machine vision system. Inf. Process. Agric. 5, 498–503. https://doi.org/10.1016/j.inpa.2018.06.002

Gonzalez-Dugo, V., Hernandez, P., Solis, I., Zarco-Tejada, P.J., 2015. Using high-resolution hyperspectral and thermal airborne imagery to assess physiological condition in the context of wheat phenotyping. Remote Sens. 7, 13586–13605. https://doi.org/10.3390/rs71013586

González-González, M.G., Gómez-Sanchis, J., Blasco, J., Soria-Olivas, E., Chueca, P., 2020. CitrusYield: A dashboard for mapping yield and fruit quality of citrus in precision agriculture. Agronomy 10. https://doi.org/10.3390/agronomy10010129

Gottschalk, P.G., Dunn, J.R., 2005. The five-parameter logistic: A characterization and comparison with the four-parameter logistic. Anal. Biochem. 343, 54–65. https://doi.org/10.1016/j.ab.2005.04.035

Gowda, P.H., Chavez, J.L., Colaizzi, P.D., Evett, S.R., Howell, T.A., Tolk, J.A., 2008. ET mapping for agricultural water management: Present status and challenges. Irrig. Sci. https://doi.org/10.1007/s00271-007-0088-6

Gu, Z., Qi, Z., Burghate, R., Yuan, S., Jiao, X., Xu, J., 2020. Irrigation Scheduling Approaches and Applications: A Review. J. Irrig. Drain. Eng. 146, 04020007. https://doi.org/10.1061/(asce)ir.1943-4774.0001464

Gutiérrez, S., Wendel, A., Underwood, J., 2019. Ground based hyperspectral imaging for extensive mango yield estimation. Comput. Electron. Agric. 157, 126–135. https://doi.org/10.1016/j.compag.2018.12.041

Haberle, J., Svoboda, P., 2015. Calculation of available water supply in crop root zone and the water balance of crops. Contrib. to Geophys. Geod. 45, 285–298. https://doi.org/10.1515/congeo-2015-0025

Hackel, T., Wegner, J.D., Schindler, K., 2016. Contour detection in unstructured 3D point clouds. Proc. IEEE Comput. Soc. Conf. Comput. Vis. Pattern Recognit. 2016-Decem, 1610–1618. https://doi.org/10.1109/CVPR.2016.178

Haghverdi, A., Leib, B.G., Washington-Allen, R.A., Ayers, P.D., Buschermohle, M.J., 2015. Perspectives on delineating management zones for variable rate irrigation. Comput. Electron. Agric. 117, 154–167. https://doi.org/10.1016/j.compag.2015.06.019

Hamadziripi, E.T., Theron, K.I., Muller, M., Steyn, W.J., 2014. Apple compositional and peel color differences resulting from canopy microclimate affect consumer preference for eating quality and appearance. HortScience 49, 384–392. https://doi.org/10.21273/hortsci.49.3.384

Hamuda, E., Mc Ginley, B., Glavin, M., Jones, E., 2017. Automatic crop detection under field conditions using the HSV colour space and morphological operations. Comput. Electron. Agric. 133, 97–107. https://doi.org/10.1016/j.compag.2016.11.021

Harker, F.R., Kupferman, E.M., Marin, A.B., Gunson, F.A., Triggs, C.M., 2008. Eating quality standards for apples based on consumer preferences. Postharvest Biol. Technol. 50, 70–78. https://doi.org/10.1016/j.postharvbio.2008.03.020

Harris, S.A., Robinson, J.P., Juniper, B.E., 2002. Genetic clues to the origin of the apple, in: Trends in Genetics. pp. 426–430. https://doi.org/10.1016/S0168-9525(02)02689-6

Hedley, C., Ekanayake, J., Roudier, P., Road, R., Street, G., Zealand, N., 2009. Wireless Soil Moisture Sensor Networks for Precision. Landcare Res. Massey Univ. 1–10.

Hedley, C.B., Bradbury, S., Ekanayake, J., Yule, I.J., Carrick, S., 2010. Spatial irrigation scheduling for variable rate irrigation. Proc. New Zeal. Grassl. Assoc. 97–101. https://doi.org/10.33584/jnzg.2010.72.2831

Hedley, C.B., Yule, I.J., 2009. A method for spatial prediction of daily soil water status for precise irrigation scheduling. Agric. Water Manag. 96, 1737–1745. https://doi.org/10.1016/j.agwat.2009.07.009

Heil, K., Schmidhalter, U., 2012. Characterisation of soil texture variability using the apparent soil electrical conductivity at a highly variable site. Comput. Geosci. 39, 98–110. https://doi.org/10.1016/j.cageo.2011.06.017

Herppich, W.B., Mempel, H., Geyer, M., 2001. Osmotic and elastic adjustment, and product quality in cold-stored carrot roots (Daucus carota L.). Gartenbauwissenschaft 66, 20–26.

Herrero-Huerta, M., González-Aguilera, D., Rodriguez-Gonzalvez, P., Hernández-López, D., 2015. Vineyard yield estimation by automatic 3D bunch modelling in field conditions. Comput. Electron. Agric. 110, 17–26. https://doi.org/10.1016/j.compag.2014.10.003

Hobart, M., Pflanz, M., Weltzien, C., Schirrmann, M., 2020. Growth height determination of tree walls for precise monitoring in apple fruit production using UAV photogrammetry. Remote Sens. 12. https://doi.org/10.3390/rs12101656

Hoehn, E., Gasser, F., Guggenbühl, B., Künsch, U., 2003. Efficacy of instrumental measurements for determination of minimum requirements of firmness, soluble solids, and acidity of several apple varieties in comparison to consumer expectations. Postharvest Biol. Technol. 27, 27–37. https://doi.org/10.1016/S0925-5214(02)00190-4

Hsu, S.S., Chen, W.C., Lo, Y.K., Cheng, J.S., Yeh, J.H., Cheng, H.H., Chen, J.S., Chang, H.T., Jiann, B.P., Huang, J.K., Jan, C.R., 2004. Effect of the antidepressant maprotiline on ca2+ movement and proliferation in human prostate cancer cells. Clin. Exp. Pharmacol. Physiol. 31, 444–449. https://doi.org/10.1111/j.1440-1681.2004.04024.x

Hunink, J.E., Contreras, S., Soto-García, M., Martin-Gorriz, B., Martinez-Álvarez, V., Baille, A., 2015. Estimating groundwater use patterns of perennial and seasonal crops in a Mediterranean irrigation scheme, using remote sensing. Agric. Water Manag. 162, 47–56. https://doi.org/10.1016/j.agwat.2015.08.003

Hunsaker, D.J., French, A.N., Waller, P.M., Bautista, E., Thorp, K.R., Bronson, K.F., Andrade-Sanchez, P., 2015. Comparison of traditional and ET-based irrigation scheduling of surface-irrigated cotton in the arid southwestern USA. Agric. Water Manag. 159, 209–224. https://doi.org/10.1016/j.agwat.2015.06.016

Iglesias, I., Salvia, J., Torguet, L., Cabús, C., 2002. Orchard cooling with overtree microsprinkler irrigation to improve fruit colour and quality of "Topred Delicious" apples. Sci. Hortic. (Amsterdam). 93, 39–51. https://doi.org/10.1016/S0304-4238(01)00308-9

Ishimwe, R., Abutaleb, K., Ahmed, F., 2014. Applications of Thermal Imaging in Agriculture—A Review. Adv. Remote Sens. 03, 128–140. https://doi.org/10.4236/ars.2014.33011

Jagbrant, G., Underwood, J.P., Nieto, J., Sukkarieh, S., 2015. LiDAR based tree and platform localisation in almond orchards, in: Springer Tracts in Advanced Robotics. pp. 469–483. https://doi.org/10.1007/978-3-319-07488-7_32

Janareva, L.F., 1978. Application of remote sensing methods in thematic mapping. Commun. Biometry Crop Sci.

Jensen, M.E., Allen, R.G., 2016. Evaporation, evapotranspiration, and irrigation water requirements, Evaporation, Evapotranspiration, and Irrigation Water Requirements. https://doi.org/10.1061/9780784414057

Ji, W., Zhao, D., Cheng, F., Xu, B., Zhang, Y., Wang, J., 2012. Automatic recognition vision system guided for apple harvesting robot. Comput. Electr. Eng. 38, 1186–1195. https://doi.org/10.1016/j.compeleceng.2011.11.005

Jia, W., Zhang, Y., Lian, J., Zheng, Y., Zhao, D., Li, C., 2020. Apple harvesting robot under information technology: A review. Int. J. Adv. Robot. Syst. https://doi.org/10.1177/1729881420925310

Jones, H.G., 1999. Use of thermography for quantitative studies of spatial and temporal variation of stomatal conductance over leaf surfaces. Plant, Cell Environ. 22, 1043–1055. https://doi.org/10.1046/j.1365-3040.1999.00468.x

Jørgensen, R.N., Sørensen, C.G., Pedersen, J.M., Havn, I., Jensen, K., Søgaard, H.T., L.B., S., 2007. Hortibot: A system design of a robotic tool carrier for high-tech plant nursing. CIGR Ejournal IX, Manuscript ATOE 07 006.

Kaasalainen, S., Jaakkola, A., Kaasalainen, M., Krooks, A., Kukko, A., 2011. Analysis of incidence angle and distance effects on terrestrial laser scanner intensity: Search for correction methods. Remote Sens. 3, 2207–2221. https://doi.org/10.3390/rs3102207

Kamilaris, A., Kartakoullis, A., Prenafeta-Boldú, F.X., 2017. A review on the practice of big data analysis in agriculture. Comput. Electron. Agric. https://doi.org/10.1016/j.compag.2017.09.037

Karkee, M., Adhikari, B., 2015. A method for three-dimensional reconstruction of apple trees for automated pruning. Trans. ASABE 58, 565–574. https://doi.org/10.13031/trans.58.10799

Karkee, M., Adhikari, B., Amatya, S., Zhang, Q., 2014. Identification of pruning branches in tall spindle apple trees for automated pruning. Comput. Electron. Agric. 103, 127–135. https://doi.org/10.1016/j.compag.2014.02.013

Karkee, M., Steward, B.L., Tang, L., Aziz, S.A., 2009. Quantifying sub-pixel signature of paddy rice field using an artificial neural network. Comput. Electron. Agric. 65, 65–76. https://doi.org/10.1016/j.compag.2008.07.009

Kashani, A.G., Olsen, M.J., Parrish, C.E., Wilson, N., 2015. A review of LIDAR radiometric processing: From ad hoc intensity correction to rigorous radiometric calibration. Sensors (Switzerland) 15, 28099–28128. https://doi.org/10.3390/s151128099

Käthner, J., Ben-Gal, A., Gebbers, R., Peeters, A., Herppich, W.B., Zude-Sasse, M., 2017. Evaluating spatially resolved influence of soil and tree water status on quality of European plum grown in semi-humid climate. Front. Plant Sci. 8, 1–10. https://doi.org/10.3389/fpls.2017.01053

Käthner, J., Zude-Sasse, M., 2015. Interaction of 3D soil electrical conductivity and generative growth in Prunus domestica. Eur. J. Hortic. Sci. 80, 231–239. https://doi.org/10.17660/eJHS.2015/80.5.5

Khan, M.J., Khan, H.S., Yousaf, A., Khurshid, K., Abbas, A., 2018. Modern Trends in Hyperspectral Image Analysis: A Review. IEEE Access. https://doi.org/10.1109/ACCESS.2018.2812999

Khan, Z., Rahimi-Eichi, V., Haefele, S., Garnett, T., Miklavcic, S.J., 2018. Estimation of vegetation indices for high-throughput phenotyping of wheat using aerial imaging. Plant Methods 14. https://doi.org/10.1186/s13007-018-0287-6

Kitchen, N.R., Sudduth, K.A., Myers, D.B., Massey, R.E., Sadler, E.J., Lerch, R.N., Hummel, J.W., Palm, H.L., 2005. Development of a conservation-oriented precision agriculture system: Crop production assessment and plan implementation. J. Soil Water Conserv. 60, 421–430.

Kitić, G., Tagarakis, A., Cselyuszka, N., Panić, M., Birgermajer, S., Sakulski, D., Matović, J., 2019. A new low-cost portable multispectral optical device for precise plant status assessment. Comput. Electron. Agric. 162, 300–308. https://doi.org/10.1016/j.compag.2019.04.021

Knipper, K.R., Kustas, W.P., Anderson, M.C., Alfieri, J.G., Prueger, J.H., Hain, C.R., Gao, F., Yang, Y., McKee, L.G., Nieto, H., Hipps, L.E., Alsina, M.M., Sanchez, L., 2019. Evapotranspiration estimates derived using thermal-based satellite remote sensing and data fusion for irrigation management in California vineyards. Irrig. Sci. 37, 431–449. https://doi.org/10.1007/s00271-018-0591-y

Koenig, K., Höfle, B., Hämmerle, M., Jarmer, T., Siegmann, B., Lilienthal, H., 2015. Comparative classification analysis of post-harvest growth detection from terrestrial LiDAR point clouds in precision agriculture. ISPRS J. Photogramm. Remote Sens. 104, 112–125. https://doi.org/10.1016/j.isprsjprs.2015.03.003

Kounalakis, T., Triantafyllidis, G.A., Nalpantidis, L., 2018. Image-based recognition framework for robotic weed control systems. Multimed. Tools Appl. 77, 9567–9594. https://doi.org/10.1007/s11042-017-5337-y

Kühn, J., Brenning, A., Wehrhan, M., Koszinski, S., Sommer, M., 2009. Interpretation of electrical conductivity patterns by soil properties and geological maps for precision agriculture. Precis. Agric. 10, 490–507. https://doi.org/10.1007/s11119-008-9103-z

Kukko, A., Kaasalainen, S., Litkey, P., 2008. Effect of incidence angle on laser scanner intensity and surface data. Appl. Opt. 47, 986–992. https://doi.org/10.1364/AO.47.000986

Kunz, C., Weber, J.F., Peteinatos, G.G., Sökefeld, M., Gerhards, R., 2018. Camera steered mechanical weed control in sugar beet, maize and soybean. Precis. Agric. 19, 708–720. https://doi.org/10.1007/s11119-017-9551-4

Kuo, K., Itakura, K., Hosoi, F., 2019. Leaf segmentation based on k-means algorithm to obtain leaf angle distribution using terrestrial LiDAR. Remote Sens. 11. https://doi.org/10.3390/rs11212536

Kurtulmus, F., Lee, W.S., Vardar, A., 2011. Green citrus detection using "eigenfruit", color and circular Gabor texture features under natural outdoor conditions. Comput. Electron. Agric. 78, 140–149. https://doi.org/10.1016/j.compag.2011.07.001

Labuschagné, I.F., Louw, J.H., Schmidt, K., Sadie, A., 2003. Budbreak Number in Apple Seedlings as Selection Criterion for Improved Adaptability to Mild Winter Climates. HortScience 38, 1186–1190. https://doi.org/10.21273/hortsci.38.6.1186

Lasisi, L.S., Chris, C.R., 2021. An Overview of Global Navigation Satellite and Augmentation Systems. Recent Dev. Eng. Res. Vol. 11 60–74. https://doi.org/10.9734/bpi/rder/v11/6733d

Lauri, P.-É., Marceron, A., Normand, F., Dambreville, A., Regnard, J.-L., 2014. Soil water deficit decreases xylem conductance efficiency relative to leaf area and mass in the apple. J. Plant Hydraul. 1, e003. https://doi.org/10.20870/jph.2014.e003

Lee, K.H., Ehsani, R., 2009. A Laser Scanner Based Measurement System for Quantification of Citrus Tree Geometric Characteristics. Appl. Eng. Agric. 25, 777–788. https://doi.org/10.13031/2013.28846

Lesch, S.M., Corwin, D.L., Robinson, D.A., 2005. Apparent soil electrical conductivity mapping as an agricultural management tool in arid zone soils. Comput. Electron. Agric. 46, 351–378. https://doi.org/10.1016/j.compag.2004.11.007

Li, L., Peters, T., Zhang, Q., Zhang, J., 2014. Modeling apple surface temperature dynamics based on weather data. Sensors (Switzerland) 14, 20217–20234. https://doi.org/10.3390/s141120217

Li, R., Bu, G., Wang, P., 2017. An Automatic Tree Skeleton Extracting Method Based on Point Cloud of Terrestrial Laser Scanner. Int. J. Opt. 2017. https://doi.org/10.1155/2017/5408503

Liaghat, S., Balasundram, S.K., 2010. A review: The role of remote sensing in precision agriculture. Am. J. Agric. Biol. Sci. https://doi.org/10.3844/ajabssp.2010.50.55

Liakos, K.G., Busato, P., Moshou, D., Pearson, S., Bochtis, D., 2018. Machine learning in agriculture: A review. Sensors (Switzerland). https://doi.org/10.3390/s18082674

Liakos, V., Smith, E., Fountas, S., Nanos, G., Kalfountzos, D., Gemtos, T., 2020. On-Farm Evaluation of Variable Rate Fertilizer Applications Using Yield-Based Mathematical Formulae in a Greek Apple Orchard. Int. J. Fruit Sci. 20, S48–S65. https://doi.org/10.1080/15538362.2019.1702135

Lin, C.H., Chen, J.Y., Su, P.L., Chen, C.H., 2014. Eigen-feature analysis of weighted covariance matrices for LiDAR point cloud classification. ISPRS J. Photogramm. Remote Sens. 94, 70–79. https://doi.org/10.1016/j.isprsjprs.2014.04.016

Lin, G., Tang, Y., Zou, X., Xiong, J., Fang, Y., 2020. Color-, depth-, and shape-based 3D fruit detection. Precis. Agric. https://doi.org/10.1007/s11119-019-09654-w

Lindblom, J., Lundström, C., Ljung, M., Jonsson, A., 2017. Promoting sustainable intensification in precision agriculture: review of decision support systems development and strategies. Precis. Agric. 18, 309–331. https://doi.org/10.1007/s11119-016-9491-4

Linker, R., Cohen, O., Naor, A., 2012. Determination of the number of green apples in RGB images recorded in orchards. Comput. Electron. Agric. 81, 45–57. https://doi.org/10.1016/j.compag.2011.11.007

Lister, C.E., Lancaster, J.E., Sutton, K.H., Walker, J.R.L., 1994. Developmental changes in the concentration and composition of flavonoids in skin of a red and a green apple cultivar. J. Sci. Food Agric. 64, 155–161. https://doi.org/10.1002/jsfa.2740640204

Lo, T., Heeren, D.M., Mateos, L., Luck, J.D., Martin, D.L., Miller, K.A., Barker, J.B., Shaver, T.M., 2017. Field characterization of field capacity and root zone available water capacity for variable rate irrigation. Appl. Eng. Agric. 33, 559–572. https://doi.org/10.13031/aea.11963

Ma, L., Zheng, G., Eitel, J.U.H., Moskal, L.M., He, W., Huang, H., 2016. Improved Salient Feature-Based Approach for Automatically Separating Photosynthetic and Nonphotosynthetic Components WZhu, X., Wang, T., Skidmore, A. K., Darvishzadeh, R., Niemann, K. O., & Liu, J. (2017). Canopy leaf water content estimated using terrest. IEEE Trans. Geosci. Remote Sens. 54, 679–696. https://doi.org/10.1109/TGRS.2015.2459716

Mack, J., Lenz, C., Teutrine, J., Steinhage, V., 2017. High-precision 3D detection and reconstruction of grapes from laser range data for efficient phenotyping based on supervised learning. Comput. Electron. Agric. 135, 300–311. https://doi.org/10.1016/j.compag.2017.02.017

Majeed, Y., Karkee, M., Zhang, Q., Fu, L., Whiting, M.D., 2020. Determining grapevine cordon shape for automated green shoot thinning using semantic segmentation-based deep learning networks. Comput. Electron. Agric. 171. https://doi.org/10.1016/j.compag.2020.105308

Malambo, L., Popescu, S.C., Horne, D.W., Pugh, N.A., Rooney, W.L., 2019. Automated detection and measurement of individual sorghum panicles using density-based clustering of terrestrial lidar data. ISPRS J. Photogramm. Remote Sens. 149, 1–13. https://doi.org/10.1016/j.isprsjprs.2018.12.015

Malczewski, J., 2006. GIS-based multicriteria decision analysis: A survey of the literature. Int. J. Geogr. Inf. Sci. 20, 703–726. https://doi.org/10.1080/13658810600661508

Malladi, A., Hirst, P.M., 2010. Increase in fruit size of a spontaneous mutant of “Gala” apple (Malus×domestica Borkh.) is facilitated by altered cell production and enhanced cell size. J. Exp. Bot. 61, 3003–3013. https://doi.org/10.1093/jxb/erq134

Manfrini, L., Corelli Grappadelli, L., Morandi, B., Losciale, P., Taylor, J.A., 2020. Innovative approaches to orchard management: Assessing the variability in yield and maturity in a “Gala” apple orchard using a simple management unit modeling approach. Eur. J. Hortic. Sci. 85, 211–218. https://doi.org/10.17660/eJHS.2020/85.4.1

Mann, K.K., Schumann, A.W., Obreza, T.A., 2011. Delineating productivity zones in a citrus grove using citrus production, tree growth and temporally stable soil data. Precis. Agric. 12, 457–472. https://doi.org/10.1007/s11119-010-9189-y

Matese, A., Di Gennaro, S.F., 2015. Technology in precision viticulture: A state of the art review. Int. J. Wine Res. https://doi.org/10.2147/IJWR.S69405

McBratney, A., Whelan, B., Ancev, T., Bouma, J., 2005. Future directions of precision agriculture, in: Precision Agriculture. pp. 7–23. https://doi.org/10.1007/s11119-005-0681-8

McCutcheon, M.C., Farahani, H.J., Stednick, J.D., Buchleiter, G.W., Green, T.R., 2006. Effect of Soil Water on Apparent Soil Electrical Conductivity and Texture Relationships in a Dryland Field. Biosyst. Eng. 94, 19–32. https://doi.org/10.1016/j.biosystemseng.2006.01.002

Medeiros, H., Kim, D., Sun, J., Seshadri, H., Akbar, S.A., Elfiky, N.M., Park, J., 2017. Modeling Dormant Fruit Trees for Agricultural Automation. J. F. Robot. 34, 1203–1224. https://doi.org/10.1002/rob.21679

Mehta, S.S., Burks, T.F., 2014. Vision-based control of robotic manipulator for citrus harvesting. Comput. Electron. Agric. 102, 146–158. https://doi.org/10.1016/j.compag.2014.01.003

Meier, U., 2001. Growth stages of mono- and dicotyledonous plants, BBCH Monograph. https://doi.org/10.5073/bbch0515

Méndez, V., Pérez-Romero, A., Sola-Guirado, R., Miranda-Fuentes, A., Manzano-Agugliaro, F., Zapata-Sierra, A., Rodríguez-Lizana, A., 2019. In-field estimation of orange number and size by 3D laser scanning. Agronomy 9. https://doi.org/10.3390/agronomy9120885

Moltó, E., Martín, B., Gutiérrez, A., 2000. Design and testing of an automatic machine for spraying at a constant distance from the tree canopy. J. Agric. Eng. Res. 77, 379–384. https://doi.org/10.1006/jaer.2000.0621

Montgomery, B., Dragićević, S., Dujmović, J., Schmidt, M., 2016. A GIS-based Logic Scoring of Preference method for evaluation of land capability and suitability for agriculture. Comput. Electron. Agric. 124, 340–353. https://doi.org/10.1016/j.compag.2016.04.013

Mulla, D.J., 2013. Twenty five years of remote sensing in precision agriculture: Key advances and remaining knowledge gaps. Biosyst. Eng. https://doi.org/10.1016/j.biosystemseng.2012.08.009

Musacchi, S., Serra, S., 2018. Apple fruit quality: Overview on pre-harvest factors. Sci. Hortic. (Amsterdam). https://doi.org/10.1016/j.scienta.2017.12.057

Nagy, A., 2015. Thermographic Evaluation Of Water Stress In An Apple Orchard. J. Multidiscip. Eng. Sci. Technol. 2, 3159–40.

Naor, A., Box, P.O., Klein, I., Doron, I., Agriculture, M., 1995. Stem Water Potential and Apple Size. J. Am. Soc. Hortic. Sci. 120, 577–582.

Naor, A., Gal, Y., Peres, M., 2006. The inherent variability of water stress indicators in apple, nectarine and pear orchards, and the validity of a leaf-selection procedure for water potential measurements. Irrig. Sci. 24, 129–135. https://doi.org/10.1007/s00271-005-0016-6

Nath, P., Bouzayen, M., Mattoo, A.K., Pech, J.C., 2014. Fruit ripening: Physiology, signalling and genomics, Fruit Ripening: Physiology, Signalling and Genomics. https://doi.org/10.1079/9781845939625.0000

O'Connell, M.G., Goodwin, I., Dunn, G.M., 2006. Towards a better understanding of crop water requirement in orchards: A case study from the Goulburn Valley. Aust. J. Exp. Agric. 46, 405–412. https://doi.org/10.1071/EA04009

Odi-Lara, M., Campos, I., Neale, C.M.U., Ortega-Farías, S., Poblete-Echeverría, C., Balbontín, C., Calera, A., 2016. Estimating evapotranspiration of an apple orchard using a remote sensing-based soil water balance. Remote Sens. 8. https://doi.org/10.3390/rs8030253

Okamoto, H., Lee, W.S., 2009. Green citrus detection using hyperspectral imaging. Comput. Electron. Agric. 66, 201–208. https://doi.org/10.1016/j.compag.2009.02.004

Oldoni, H., Silva Terra, V.S., Timm, L.C., Júnior, C.R., Monteiro, A.B., 2019. Delineation of management zones in a peach orchard using multivariate and geostatistical analyses. Soil Tillage Res. 191, 1–10. https://doi.org/10.1016/j.still.2019.03.008

Paço, T.A., Ferreira, M.I., Rosa, R.D., Paredes, P., Rodrigues, G.C., Conceição, N., Pacheco, C.A., Pereira, L.S., 2012. The dual crop coefficient approach using a density factor to simulate the evapotranspiration of a peach orchard: SIMDualKc model versus eddy covariance measurements. Irrig. Sci. 30, 115–126. https://doi.org/10.1007/s00271-011-0267-3

Palleja, T., Tresanchez, M., Teixido, M., Sanz, R., Rosell, J.R., Palacin, J., 2010. Sensitivity of tree volume measurement to trajectory errors from a terrestrial LIDAR scanner. Agric. For. Meteorol. 150, 1420–1427. https://doi.org/10.1016/j.agrformet.2010.07.005

Peeters, A., Zude, M., Käthner, J., Ünlü, M., Kanber, R., Hetzroni, A., Gebbers, R., Ben-Gal, A., 2015. Getis-Ord's hot- and cold-spot statistics as a basis for multivariate spatial clustering of orchard tree data. Comput. Electron. Agric. 111, 140–150. https://doi.org/10.1016/j.compag.2014.12.011

Pelletier, G., Upadhyaya, S.K., 1999. Development of a tomato load/yield monitor. Comput. Electron. Agric. 23, 103–117. https://doi.org/10.1016/S0168-1699(99)00025-3

Peñuelas, J., Filella, L., 1998. Technical focus: Visible and near-infrared reflectance techniques for diagnosing plant physiological status.

Trends Plant Sci. 3, 151–156. https://doi.org/10.1016/S1360-1385(98)01213-8

Penzel, M., Lakso, A.N., Tsoulias, N., Zude-Sasse, M., 2020. Carbon consumption of developing fruit and the fruit bearing capacity of individual RoHo 3615 and Pinova apple trees. Int. Agrophysics 34, 409–423. https://doi.org/10.31545/INTAGR/127540

Peralta, N.R., Costa, J.L., Balzarini, M., Castro Franco, M., Córdoba, M., Bullock, D., 2015. Delineation of management zones to improve nitrogen management of wheat. Comput. Electron. Agric. 110, 103–113. https://doi.org/10.1016/j.compag.2014.10.017

Pereira-Lorenzo, S., Fischer, M., Ramos-Cabrer, A.M., Castro, I., 2018. Apple (Malus spp.) breeding: Present and future, in: Advances in Plant Breeding Strategies: Fruits. pp. 3–29. https://doi.org/10.1007/978-3-319-91944-7_1

Pereira, L.S., Allen, R.G., Smith, M., Raes, D., 2015. Crop evapotranspiration estimation with FAO56: Past and future. Agric. Water Manag. 147, 4–20. https://doi.org/10.1016/j.agwat.2014.07.031

Pérez-Pastor, A., Ruiz-Sánchez, M.C., Domingo, R., 2014. Effects of timing and intensity of deficit irrigation on vegetative and fruit growth of apricot trees. Agric. Water Manag. 134, 110–118. https://doi.org/10.1016/j.agwat.2013.12.007

Perez-Ruiz, M., K., S., 2012. GNSS in Precision Agricultural Operations, in: New Approach of Indoor and Outdoor Localization Systems. https://doi.org/10.5772/50448

Perry, E.M., Dezzani, R.J., Seavert, C.F., Pierce, F.J., 2010. Spatial variation in tree characteristics and yield in a pear orchard. Precis. Agric. 11, 42–60. https://doi.org/10.1007/s11119-009-9113-5

Pesci, A., Teza, G., 2008. Effects of surface irregularities on intensity data from laser scanning: An experimental approach. Ann. Geophys. 51, 839–848. https://doi.org/10.4401/ag-4462

Phipps, J.B., Robertson, K.R., Smith, P.G., Rohrer, J.R., 1990. A checklist of the subfamily Maloideae (Rosaceae). Can. J. Bot. 68, 2209–2269. https://doi.org/10.1139/b90-288

Poblete, T., Ortega-Farías, S., Moreno, M.A., Bardeen, M., 2017. Artificial neural network to predict vine water status spatial variability using multispectral information obtained from an unmanned aerial vehicle (UAV). Sensors (Switzerland) 17. https://doi.org/10.3390/s17112488

Pozdnyakova, L., Giménez, D., Oudemans, P. V., 2005. Spatial analysis of cranberry yield at three scales. Agron. J. 97, 49–57. https://doi.org/10.2134/agronj2005.0049

Prakash, A., 2000. Thermal remote sensing: concepts, issues and applications. … Arch. Photogramm. Remote Sens. XXXIII, 239–243.

Prins, A.J., Van Niekerk, A., 2020. Crop type mapping using LiDAR, Sentinel-2 and aerial imagery with machine learning algorithms. Geo-Spatial Inf. Sci. 1–13. https://doi.org/10.1080/10095020.2020.1782776

Rains, G.C., Thomas, D.L., Perry, C.D., 2002. Pecan mechanical harvesting parameters for yield monitoring. Trans. Am. Soc. Agric. Eng. 45, 281–285. https://doi.org/10.13031/2013.8518

Rakun, J., Stajnko, D., Zazula, D., 2011. Detecting fruits in natural scenes by using spatial-frequency based texture analysis and multiview geometry. Comput. Electron. Agric. 76, 80–88. https://doi.org/10.1016/j.compag.2011.01.007

Ranjan, R., Khot, L.R., Peters, R.T., Salazar-Gutierrez, M.R., Shi, G., 2020. In-field crop physiology sensing aided real-time apple fruit surface temperature monitoring for sunburn prediction. Comput. Electron. Agric. 175. https://doi.org/10.1016/j.compag.2020.105558

Raun, W.R., Solie, J.B., Stone, M.L., Martin, K.L., Freeman, K.W., Mullen, R.W., Zhang, H., Schepers, J.S., Johnson, G. V., 2005. Optical sensor-based algorithm for crop nitrogen fertilization. Commun. Soil Sci. Plant Anal. 36, 2759–2781. https://doi.org/10.1080/00103620500303988

Ravetti, L., Robb, S., 2010. Continuous mechanical harvesting in modern Australian olive growing systems. Adv. Hortic. Sci. 24, 71–77. https://doi.org/10.1400/132345

Reiser, D., Sehsah, E.S., Bumann, O., Morhard, J., Griepentrog, H.W., 2019. Development of an autonomous electric robot implement for intra-row weeding in vineyards. Agric. 9. https://doi.org/10.3390/agriculture9010018

Reyniers, M., Vrindts, E., De Baerdemaeker, J., 2006. Comparison of an aerial-based system and an on the ground continuous measuring device to predict yield of winter wheat. Eur. J. Agron. 24, 87–94. https://doi.org/10.1016/j.eja.2005.05.002

Ringdahl, O., Kurtser, P., Edan, Y., 2019. Evaluation of approach strategies for harvesting robots: Case study of sweet pepper harvesting: Category: (5). J. Intell. Robot. Syst. Theory Appl. 95, 149–164. https://doi.org/10.1007/s10846-018-0892-7

Roberson, D., Davidoff, J., Davies, I., 2000. Color categories are not universal: Replications and new evidence from a stone-age culture. J. Exp. Psychol. Gen. 129, 369–398. https://doi.org/10.1037/0096-3445.129.3.369

Robinson, T.L., Lakso, A.N., Greene, D.W., 2017. Precision crop load management: The practical implementation of physiological models, in: Acta Horticulturae. pp. 381–390. https://doi.org/10.17660/ActaHortic.2017.1177.55

Rodríguez-Pérez, J.R., Plant, R.E., Lambert, J.J., Smart, D.R., 2011. Using apparent soil electrical conductivity (ECa) to characterize vineyard soils of high clay content. Precis. Agric. 12, 775–794. https://doi.org/10.1007/s11119-011-9220-y

Rosell, J.R., Llorens, J., Sanz, R., Arnó, J., Ribes-Dasi, M., Masip, J., Escolà, A., Camp, F., Solanelles, F., Gràcia, F., Gil, E., Val, L., Planas, S., Palacín, J., 2009. Obtaining the three-dimensional structure of tree orchards from remote 2D terrestrial LIDAR scanning. Agric. For. Meteorol. 149, 1505–1515. https://doi.org/10.1016/j.agrformet.2009.04.008

Rosell Polo, J.R., Sanz, R., Llorens, J., Arnó, J., Escolà, A., Ribes-Dasi, M., Masip, J., Camp, F., Gràcia, F., Solanelles, F., Pallejà, T., Val, L., Planas, S., Gil, E., Palacín, J., 2009. A tractor-mounted scanning LIDAR for the non-destructive measurement of vegetative volume and surface area of tree-row plantations: A comparison with conventional destructive measurements. Biosyst. Eng. 102, 128–134. https://doi.org/10.1016/j.biosystemseng.2008.10.009

Rossini, M., Fava, F., Cogliati, S., Meroni, M., Marchesi, A., Panigada, C., Giardino, C., Busetto, L., Migliavacca, M., Amaducci, S., Colombo, R., 2013. Assessing canopy PRI from airborne imagery to map water stress in maize. ISPRS J. Photogramm. Remote Sens. 86, 168–177. https://doi.org/10.1016/j.isprsjprs.2013.10.002

Rupnik, R., Kukar, M., Vračar, P., Košir, D., Pevec, D., Bosnić, Z., 2019. AgroDSS: A decision support system for agriculture and farming. Comput. Electron. Agric. 161, 260–271. https://doi.org/10.1016/j.compag.2018.04.001

Rustia, D.J.A., Lin, C.E., Chung, J.Y., Zhuang, Y.J., Hsu, J.C., Lin, T. Te, 2020. Application of an image and environmental sensor network for automated greenhouse insect pest monitoring. J. Asia. Pac. Entomol. 23, 17–28. https://doi.org/10.1016/j.aspen.2019.11.006

Sablowski, R., Carnier Dornelas, M., 2014. Interplay between cell growth and cell cycle in plants. J. Exp. Bot. https://doi.org/10.1093/jxb/ert354

Sadar, N., Urbanek-Krajnc, A., Unuk, T., 2013. Spektrofotometriškai ivertinto pigmentu kiekio sveikuose obuoliuose ir jo ryšio su vaisiu kokybe tyrimu apžvalga. Zemdirbyste 100, 105–111. https://doi.org/10.13080/z-a.2013.100.014

Saha, K.K., Tsoulias, N., Zude-Sasse, M., 2020. Assessment of measurement uncertainty when using 2D mobile laser scanner to estimate tree parameters. Landtechnik 75, 270–277. https://doi.org/10.15150/lt.2020.3251

Saldaña, N., Cabrera, J.M., Serwatowski, R.J., Gracia, C., 2006. Yield mapping system for vegetables picked up with a tractor-pulled platform. Spanish J. Agric. Res. 4, 130–139. https://doi.org/10.5424/sjar/2006042-185

Sanchez, L.A., Sams, B., Alsina, M.M., Hinds, N., Klein, L.J., Dokoozlian, N., 2017. Improving vineyard water use efficiency and yield with variable rate irrigation in California. Adv. Anim. Biosci. 8, 574–577. https://doi.org/10.1017/s2040470017000772

Sanz, R., Llorens, J., Escolà, A., Arnó, J., Planas, S., Román, C., Rosell-Polo, J.R., 2018. LIDAR and non-LIDAR-based canopy parameters to estimate the leaf area in fruit trees and vineyard. Agric. For. Meteorol. 260–261, 229–239. https://doi.org/10.1016/j.agrformet.2018.06.017

Saudreau, M., Sinoquet, H., Santin, O., Marquier, A., Adam, B., Longuenesse, J.J., Guilioni, L., Chelle, M., 2007. A 3D model for simulating the spatial and temporal distribution of temperature within ellipsoidal fruit. Agric. For. Meteorol. 147, 1–15. https://doi.org/10.1016/j.agrformet.2007.06.006

Schueller, J.K., Whitney, J.D., Wheaton, T.A., Miller, W.M., Turner, A.E., 1999. Low-cost automatic yield mapping in hand-harvested citrus. Comput. Electron. Agric. 23, 145–153. https://doi.org/10.1016/S0168-1699(99)00028-9

Scorzal, R., May, L.G., Purnell, B., Upchurch, B., 2019. Differences in Number and Area of Mesocarp Cells between Small- and Large-fruited Peach Cultivars. J. Am. Soc. Hortic. Sci. 116, 861–864. https://doi.org/10.21273/jashs.116.5.861

Scotford, I.M., Miller, P.C.H., 2004. Combination of Spectral Reflectance and Ultrasonic Sensing to monitor the Growth of Winter Wheat. Biosyst. Eng. 87, 27–38. https://doi.org/10.1016/j.biosystemseng.2003.09.009

Shaner, D.L., Khosla, R., Brodahl, M.K., Buchleiter, G.W., Farahani, H.J., 2008. How well does zone sampling based on soil electrical conductivity maps represent soil variability? Agron. J. 100, 1472–1480. https://doi.org/10.2134/agronj2008.0060

Shaver, T.M., Khosla, R., Westfall, D.G., 2011. Evaluation of two crop canopy sensors for nitrogen variability determination in irrigated maize. Precis. Agric. 12, 892–904. https://doi.org/10.1007/s11119-011-9229-2

Silwal, A., Davidson, J., Karkee, M., Mo, C., Zhang, Q., Lewis, K., 2016. Effort towards robotic apple harvesting in Washington State, in: 2016 American Society of Agricultural and Biological Engineers Annual International Meeting, ASABE 2016. https://doi.org/10.13031/aim.20162460869

Sishodia, R.P., Ray, R.L., Singh, S.K., 2020. Applications of remote sensing in precision agriculture: A review. Remote Sens. 12, 1–31. https://doi.org/10.3390/rs12193136

Smith, R.J., Baillie, J.N., 2009. Defining precision irrigation: A new approach to irrigation management. Irrig. Drain. Conf. 1–6.

Solanelles, F., Escolà, A., Planas, S., Rosell, J.R., Camp, F., Gràcia, F., 2006. An Electronic Control System for Pesticide Application Proportional to the Canopy Width of Tree Crops. Biosyst. Eng. 95, 473–481. https://doi.org/10.1016/j.biosystemseng.2006.08.004

Soudarissanane, S., Lindenbergh, R., Menenti, M., Teunissen, P., 2011. Scanning geometry: Influencing factor on the quality of terrestrial laser scanning points. ISPRS J. Photogramm. Remote Sens. 66, 389–399. https://doi.org/10.1016/j.isprsjprs.2011.01.005

Sponagel, G.W., Hartmann, K.J., Hartwich, R., Janetzko, P., Joisten, H., Kühn, D., Sabel, K.J., Traidl, R.H., 2005. Bodenkundliche Kartieranleitung (German Manual of Soil Mapping, KA5), German Manual of Soil Mapping, KA5. In Bundesanstalt für Geowissenschaften und Rohstoffe, Schweizerbart Hannover.

Srinivasan, S., Popescu, S.C., Eriksson, M., Sheridan, R.D., Ku, N.W., 2015. Terrestrial laser scanning as an effective tool to retrieve tree level height, crown width, and stem diameter. Remote Sens. 7, 1877–1896. https://doi.org/10.3390/rs70201877

Stajnko, D., Lakota, M., Hočevar, M., 2004. Estimation of number and diameter of apple fruits in an orchard during the growing season by thermal imaging. Comput. Electron. Agric. 42, 31–42. https://doi.org/10.1016/S0168-1699(03)00086-3

Sudduth, K.A., Kitchen, N.R., Wiebold, W.J., Batchelor, W.D., Bollero, G.A., Bullock, D.G., Clay, D.E., Palm, H.L., Pierce, F.J., Schuler, R.T., Thelen, K.D., 2005. Relating apparent electrical conductivity to soil properties across the north-central USA. Comput. Electron. Agric. 46, 263–283. https://doi.org/10.1016/j.compag.2004.11.010

Sullivan, D.G., Shaw, J.N., Rickman, D., 2005. IKONOS Imagery to Estimate Surface Soil Property Variability in Two Alabama Physiographies. Soil Sci. Soc. Am. J. 69, 1789–1798. https://doi.org/10.2136/sssaj2005.0071

Sun, S., Li, C., Chee, P.W., Paterson, A.H., Jiang, Y., Xu, R., Robertson, J.S., Adhikari, J., Shehzad, T., 2020. Three-dimensional photogrammetric mapping of cotton bolls in situ based on point cloud segmentation and clustering. ISPRS J. Photogramm. Remote Sens. 160, 195–207. https://doi.org/10.1016/j.isprsjprs.2019.12.011

Sun, S., Li, C., Paterson, A.H., Jiang, Y., Xu, R., Robertson, J.S., Snider, J.L., Chee, P.W., 2018. In-field high throughput phenotyping and cotton plant growth analysis using LiDAR. Front. Plant Sci. 9, 1–17. https://doi.org/10.3389/fpls.2018.00016

Tagarakis, A., Liakos, V., Fountas, S., Koundouras, S., Gemtos, T.A., 2013. Management zones delineation using fuzzy clustering techniques in grapevines. Precis. Agric. 14, 18–39. https://doi.org/10.1007/s11119-012-9275-4

Tagarakis, A.C., Koundouras, S., Fountas, S., Gemtos, T., 2018. Evaluation of the use of LIDAR laser scanner to map pruning wood in vineyards and its potential for management zones delineation. Precis. Agric. 19, 334–347. https://doi.org/10.1007/s11119-017-9519-4

Tao, Y., Zhou, J., 2017. Automatic apple recognition based on the fusion of color and 3D feature for robotic fruit picking. Comput. Electron. Agric. 142, 388–396. https://doi.org/10.1016/j.compag.2017.09.019

Tardaguila, J., Baluja, J., Arpon, L., Balda, P., Oliveira, M., 2011. Variations of soil properties affect the vegetative growth and yield components of "Tempranillo" grapevines. Precis. Agric. 12, 762–773. https://doi.org/10.1007/s11119-011-9219-4

Taylor, J.A., Praat, J.P., Bollen, A.F., 2007. Spatial variability of kiwifruit quality in orchards and its implications for sampling and mapping. HortScience 42, 246–250. https://doi.org/10.21273/hortsci.42.2.246

Taylor, J.C., Wood, G.A., Earl, R., Godwin, R.J., 2003. Soil factors and their influence on within-field crop variability, Part II: Spatial analysis and determination of management zones. Biosyst. Eng. 84, 441–453. https://doi.org/10.1016/S1537-5110(03)00005-9

Teh, S.L., Coggins, J.L., Kostick, S.A., Evans, K.M., 2020. Location, year, and tree age impact NIR-based postharvest prediction of dry matter concentration for 58 apple accessions. Postharvest Biol. Technol. 166. https://doi.org/10.1016/j.postharvbio.2020.111125

Testa, G., Gresta, F., Cosentino, S.L., 2011a. Dry matter and qualitative characteristics of alfalfa as affected by harvest times and soil water content. Eur. J. Agron. 34, 144–152. https://doi.org/10.1016/j.eja.2010.12.001

Testa, G., Gresta, F., Cosentino, S.L., 2011b. Dry matter and qualitative characteristics of alfalfa as affected by harvest times and soil water content. Eur. J. Agron. 34, 144–152. https://doi.org/10.1016/j.eja.2010.12.001

Tremblay, N., Wang, Z., Ma, B.L., Belec, C., Vigneault, P., 2009. A comparison of crop data measured by two commercial sensors for variable-rate nitrogen application. Precis. Agric. 10, 145–161. https://doi.org/10.1007/s11119-008-9080-2

Tromp, J., Borsboom, O., 1994. The effect of autumn and spring temperature on fruit set and on the effective pollination period in apple and pear. Sci. Hortic. (Amsterdam). 60, 23–30. https://doi.org/10.1016/0304-4238(94)90059-0

Trought, M.C.T., Bramley, R.G.V., 2011. Vineyard variability in Marlborough, New Zealand: Characterising spatial and temporal changes in fruit composition and juice quality in the vineyard. Aust. J. Grape Wine Res. 17, 72–78. https://doi.org/10.1111/j.1755-0238.2010.00119.x

Tsoulias, N., Gebbers, R., Zude-Sasse, M., 2020a. Using data on soil ECa, soil water properties, and response of tree root system for spatial water balancing in an apple orchard. Precis. Agric. 21, 522–548. https://doi.org/10.1007/s11119-019-09680-8

Tsoulias, N., Paraforos, D.S., Fountas, S., Zude-Sasse, M., 2019a. Calculating the water deficit spatially using LiDAR laser scanner in an apple orchard, in: Precision Agriculture 2019 - Papers Presented at the 12th European Conference on Precision Agriculture, ECPA 2019. pp. 115–121. https://doi.org/10.3920/978-90-8686-888-9_13

Tsoulias, N., Paraforos, D.S., Fountas, S., Zude-Sasse, M., 2019b. Estimating canopy parameters based on the stem position in apple trees using a 2D lidar. Agronomy 9. https://doi.org/10.3390/agronomy9110740

Tsoulias, N., Paraforos, D.S., Xanthopoulos, G., Zude-Sasse, M., 2020b. Apple shape detection based on geometric and radiometric features using a LiDAR laser scanner. Remote Sens. 12. https://doi.org/10.3390/RS12152481

Tumbo, S.D., Salyani, M., Whitney, J.D., Wheaton, T.A., Miller, W.M., 2002. Investigation of laser and ultrasonic ranging sensors for measurements of citrus canopy volume. Appl. Eng. Agric. 18, 367–372.

Tworkoski, T., Fazio, G., Glenn, D.M., 2016. Apple rootstock resistance to drought. Sci. Hortic. (Amsterdam). 204, 70–78. https://doi.org/10.1016/j.scienta.2016.01.047

Underwood, J.P., Hung, C., Whelan, B., Sukkarieh, S., 2016. Mapping almond orchard canopy volume, flowers, fruit and yield using lidar and vision sensors. Comput. Electron. Agric. 130, 83–96. https://doi.org/10.1016/j.compag.2016.09.014

ÜNLÜ, M., KANBER, R., KOÇ, D.L., ÖZEKİCİ, B., KEKEÇ, U., YEŞİLOĞLU, T., ORTAŞ, İ., ÜNLÜ, F., KAPUR, B., TEKİN, S., KÄTHNER, J., GEBBERS, R., ZUDE, M., PEETERS, A., BEN-GAL, A., 2014. Irrigation scheduling of grapefruit trees in a Mediterranean environment throughout evaluation of plant water status and evapotranspiration. Turkish J. Agric. For. 38, 908–915. https://doi.org/10.3906/tar-1403-58

Uribeetxebarria, A., Arnó, J., Escolà, A., Martínez-Casasnovas, J.A., 2018. Apparent electrical conductivity and multivariate analysis of soil properties to assess soil constraints in orchards affected by previous parcelling. Geoderma 319, 185–193. https://doi.org/10.1016/j.geoderma.2018.01.008

Valente, D.S.M., de Queiroz, D.M., de Carvalho Pinto, F. de A., Santos, N.T., Santos, F.L., 2012. Definition of management zones in coffee production fields based on apparent soil electrical conductivity. Sci. Agric. 69, 173–179. https://doi.org/10.1590/S0103-90162012000300001

Van Henten, E.J., Van Tuijl, B.A.J., Hoogakker, G.J., Van Der Weerd, M.J., Hemming, J., Kornet, J.G., Bontsema, J., 2006. An Autonomous Robot for De-leafing Cucumber Plants grown in a High-wire Cultivation System. Biosyst. Eng. 94, 317–323. https://doi.org/10.1016/j.biosystemseng.2006.03.005

Vatsanidou, A., Nanos, G.D., Fountas, S., Baras, J., Castrignano, A., Gemtos, T.A., 2017. Nitrogen replenishment using variable rate application technique in a small hand-harvested pear orchard. Spanish J. Agric. Res. 15. https://doi.org/10.5424/sjar/2017154-10986

Vázquez-Arellano, M., Griepentrog, H.W., Reiser, D., Paraforos, D.S., 2016. 3-D imaging systems for agricultural applications—a review. Sensors (Switzerland) 16. https://doi.org/10.3390/s16050618

Vázquez-Arellano, M., Paraforos, D.S., Reiser, D., Garrido-Izard, M., Griepentrog, H.W., 2018a. Determination of stem position and height of reconstructed maize plants using a time-of-flight camera. Comput. Electron. Agric. 154, 276–288. https://doi.org/10.1016/j.compag.2018.09.006

Vázquez-Arellano, M., Reiser, D., Paraforos, D.S., Garrido-Izard, M., Burce, M.E.C., Griepentrog, H.W., 2018b. 3-D reconstruction of maize plants using a time-of-flight camera. Comput. Electron. Agric. 145, 235–247. https://doi.org/10.1016/j.compag.2018.01.002

Velandia, M., Buschermohle, M., Larson, J.A., Thompson, N.M., Jernigan, B.M., 2013. The economics of automatic section control technology for planters: A case study of middle and west tennessee farms. Comput. Electron. Agric. 95, 1–10. https://doi.org/10.1016/j.compag.2013.03.006

Verstraeten, W.W., Veroustraete, F., Feyen, J., 2008. Assessment of evapotranspiration and soil moisture content across different scales of observation. Sensors 8, 70–117. https://doi.org/10.3390/s8010070

Vicari, M.B., Disney, M., Wilkes, P., Burt, A., Calders, K., Woodgate, W., 2019. Leaf and wood classification framework for terrestrial LiDAR point clouds. Methods Ecol. Evol. 10, 680–694. https://doi.org/10.1111/2041-210X.13144

Vinh, P.Q., Ha, N.T.T., Binh, N.T., Thang, N.N., Oanh, L.T., Thao, N.T.P., 2019. Developing algorithm for estimating chlorophyll-a concentration in the Thac Ba Reservoir surface water using Landsat 8 Imagery. Vietnam J. Earth Sci. 41, 10–20. https://doi.org/10.15625/0866-7187/41/1/13542

Vitzrabin, E., Edan, Y., 2016. Adaptive thresholding with fusion using a RGBD sensor for red sweet-pepper detection. Biosyst. Eng. 146, 45–56. https://doi.org/10.1016/j.biosystemseng.2015.12.002

Vollmann, J., Walter, H., Sato, T., Schweiger, P., 2011. Digital image analysis and chlorophyll metering for phenotyping the effects of nodulation in soybean. Comput. Electron. Agric. 75, 190–195. https://doi.org/10.1016/j.compag.2010.11.003

Wachs, J.P., Stern, H.I., Burks, T., Alchanatis, V., 2010. Low and high-level visual feature-based apple detection from multi-modal images. Precis. Agric. 11, 717–735. https://doi.org/10.1007/s11119-010-9198-x

Wagenmakers, P.S., Callesen, O., 1995. Light distribution in apple orchard systems in relation to production and fruit quality. J. Hortic. Sci. 70, 935–948. https://doi.org/10.1080/14620316.1995.11515369

Walklate, P.J., Cross, J. V., Richardson, G.M., Murray, R.A., Baker, D.E., 2002. Comparison of different spray volume deposition models using LIDAR measurements of apple orchards. Biosyst. Eng. 82, 253–267. https://doi.org/10.1006/bioe.2002.0082

Wang, D., Brunner, J., Ma, Z., Lu, H., Hollaus, M., Pang, Y., Pfeifer, N., 2018. Separating tree photosynthetic and non-photosynthetic components from point cloud data using Dynamic Segment Merging. Forests 9. https://doi.org/10.3390/f9050252

Wang, J.J., Zhao, D.A., Ji, W., Tu, J.J., Zhang, Y., 2009. Application of support vector machine to apple recognition using in apple harvesting robot, in: 2009 IEEE International Conference on Information and Automation, ICIA 2009. pp. 1110–1115. https://doi.org/10.1109/ICINFA.2009.5205083

Wang, L.L., Zhao, B., Fan, J.W., Hu, X.A., Wei, S., Li, Y.S., Zhou, Q.B., Wei, C.F., 2017. Development of a tomato harvesting robot used in greenhouse. Int. J. Agric. Biol. Eng. 10, 140–149. https://doi.org/10.25165/j.ijabe.20171004.3204

Wang, Q., Nuske, S., Bergerman, M., Singh, S., 2012. Design of crop yield estimation system for apple orchards using computer vision, in: American Society of Agricultural and Biological Engineers Annual International Meeting 2012, ASABE 2012. pp. 3532–3544. https://doi.org/10.13031/2013.41901

Wang, Z., Walsh, K.B., Verma, B., 2017. On-tree mango fruit size estimation using RGB-D images. Sensors (Switzerland) 17, 1–15. https://doi.org/10.3390/s17122738

Warrington, I.J., Fulton, T.A., Halligan, E.A., De Silva, H.N., 1999. Apple fruit growth and maturity are affected by early season temperatures. J. Am. Soc. Hortic. Sci. 124, 468–477. https://doi.org/10.21273/jashs.124.5.468

Wei, M.C.F., Maldaner, L.F., Ottoni, P.M.N., Molin, J.P., 2020. Carrot Yield Mapping: A Precision Agriculture Approach Based on Machine Learning. Ai 1, 229–241. https://doi.org/10.3390/ai1020015

Wellington, C., Campoy, J., Khot, L., Ehsani, R., 2012. Orchard tree modeling for advanced sprayer control and automatic tree inventory. IEEE/RSJ Int. Conf. … 5–6.

Westwood, M.N., 1978. Temperate-zone pomology. Temp. Pomol.

Wu, G., Li, B., Zhu, Q., Huang, M., Guo, Y., 2020. Using color and 3D geometry features to segment fruit point cloud and improve fruit recognition accuracy. Comput. Electron. Agric. 174. https://doi.org/10.1016/j.compag.2020.105475

Wünsche, J.N., Lakso, A.N., 2000. The relationship between leaf area and light interceptor by spur and extension shoot leaves and apple orchard productivity. HortScience 35, 1202–1206. https://doi.org/10.21273/hortsci.35.7.1202

Xia, G., Cheng, L., Lakso, A., Goffinet, M., 2009. Effects of nitrogen supply on source-sink balance and fruit size of “Gala” apple trees. J. Am. Soc. Hortic. Sci. 134, 126–133. https://doi.org/10.21273/jashs.134.1.126

Xsens Technologies, 2014. MTi 10-series and MTi 100-series MTi User Manual. Doc. MT0605P.B.

YAMADA, H., HAMAMOTO, K., SUGIURA, A., TOMANA, T., 1988. Effect of Controlled Fruit Temperature on Maturation of Apple

Fruits. J. Japanese Soc. Hortic. Sci. 57, 173–177. https://doi.org/10.2503/jjshs.57.173

Yang, C., Everitt, J.H., Bradford, J.M., 2009. Evaluating high resolution SPOT 5 satellite imagery to estimate crop yield, in: Precision Agriculture. pp. 292–303. https://doi.org/10.1007/s11119-009-9120-6

Yang, C., Everitt, J.H., Bradford, J.M., 2007. Airborne hyperspectral imagery and linear spectral unmixing for mapping variation in crop yield. Precis. Agric. 8, 279–296. https://doi.org/10.1007/s11119-007-9045-x

Yang, G., Pu, R., Zhao, C., Xue, X., 2014. Estimating high spatiotemporal resolution evapotranspiration over a winter wheat field using an IKONOS image based complementary relationship and Lysimeter observations. Agric. Water Manag. 133, 34–43. https://doi.org/10.1016/j.agwat.2013.10.018

Ye, X., Sakai, K., Manago, M., Asada, S.I., Sasao, A., 2007. Prediction of citrus yield from airborne hyperspectral imagery. Precis. Agric. 8, 111–125. https://doi.org/10.1007/s11119-007-9032-2

Zaman, Q.U., Schumann, A.W., Miller, W.M., 2005. Variable rate nitrogen application in Florida citrus based on ultrasonically-sensed tree size. Appl. Eng. Agric. 21, 331–335.

Zarate-Valdez, J.L., Whiting, M.L., Lampinen, B.D., Metcalf, S., Ustin, S.L., Brown, P.H., 2012. Prediction of leaf area index in almonds by vegetation indexes. Comput. Electron. Agric. 85, 24–32. https://doi.org/10.1016/j.compag.2012.03.009

Zarco-Tejada, P.J., González-Dugo, V., Williams, L.E., Suárez, L., Berni, J.A.J., Goldhamer, D., Fereres, E., 2013. A PRI-based water stress index combining structural and chlorophyll effects: Assessment using diurnal narrow-band airborne imagery and the CWSI thermal index. Remote Sens. Environ. 138, 38–50. https://doi.org/10.1016/j.rse.2013.07.024

Zare, M., Drastig, K., Zude-Sasse, M., 2020. Tree water status in apple orchards measured by means of land surface temperature and vegetation index (LST-NDVI) trapezoidal space derived from landsat 8 satellite images. Sustain. 12, 1–19. https://doi.org/10.3390/SU12010070

Zhang, B., Gu, B., Tian, G., Zhou, J., Huang, J., Xiong, Y., 2018. Challenges and solutions of optical-based nondestructive quality inspection for robotic fruit and vegetable grading systems: A technical review. Trends Food Sci. Technol. https://doi.org/10.1016/j.tifs.2018.09.018

Zhang, J., He, L., Karkee, M., Zhang, Q., Zhang, X., Gao, Z., 2018. Branch detection for apple trees trained in fruiting wall architecture using depth features and Regions-Convolutional Neural Network (R-CNN). Comput. Electron. Agric. 155, 386–393. https://doi.org/10.1016/j.compag.2018.10.029

Zhang, M., Zhou, J., Sudduth, K.A., Kitchen, N.R., 2020. Estimation of maize yield and effects of variable-rate nitrogen application using UAV-based RGB imagery. Biosyst. Eng. 189, 24–35. https://doi.org/10.1016/j.biosystemseng.2019.11.001

Zhang, N., Wang, M., Wang, N., 2002. Precision agriculture - A worldwide overview, in: Computers and Electronics in Agriculture. https://doi.org/10.1016/S0168-1699(02)00096-0

Zhang, X., He, L., Zhang, J., Whiting, M.D., Karkee, M., Zhang, Q., 2020. Determination of key canopy parameters for mass mechanical apple harvesting using supervised machine learning and principal component analysis (PCA). Biosyst. Eng. 193, 247–263. https://doi.org/10.1016/j.biosystemseng.2020.03.006

Zhang, X., Zhang, J., Li, L., Zhang, Y., Yang, G., 2017. Monitoring citrus soil moisture and nutrients using an IoT based system. Sensors (Switzerland) 17. https://doi.org/10.3390/s17030447

Zhao, Y. dong, Sun, Y. rui, Cai, X., Liu, H., Lammers, P.S., 2012. Identify Plant Drought Stress by 3D-Based Image. J. Integr. Agric. 11, 1207–1211. https://doi.org/10.1016/S2095-3119(12)60116-6

Zhou, B., Elazab, A., Bort, J., Vergara, O., Serret, M.D., Araus, J.L., 2015. Low-cost assessment of wheat resistance to yellow rust through conventional RGB images. Comput. Electron. Agric. 116, 20–29. https://doi.org/10.1016/j.compag.2015.05.017

Zhou, Z.Q., 1999. The apple genetic resources in China: The wild species and their distributions, informative characteristics and utilisation. Genet. Resour. Crop Evol. 46, 599–609. https://doi.org/10.1023/A:1008747709534

Zhu, Xiaolin, Cai, F., Tian, J., Williams, T.K.A., 2018. Spatiotemporal fusion of multisource remote sensing data: Literature survey, taxonomy, principles, applications, and future directions. Remote Sens. https://doi.org/10.3390/rs10040527

Zhu, Xi, Skidmore, A.K., Darvishzadeh, R., Niemann, K.O., Liu, J., Shi, Y., Wang, T., 2018. Foliar and woody materials discriminated using terrestrial LiDAR in a mixed natural forest. Int. J. Appl. Earth Obs. Geoinf. 64, 43–50. https://doi.org/10.1016/j.jag.2017.09.004

Zhu, X., Wang, T., Skidmore, A.K., Darvishzadeh, R., Niemann, K.O., Liu, J., 2017. Canopy leaf water content estimated using terrestrial LiDAR. Agric. For. Meteorol. 232, 152–162. https://doi.org/10.1016/j.agrformet.2016.08.016

Zude-Sasse, M., Fountas, S., Gemtos, T.A., Abu-Khalaf, N., 2016. Applications of precision agriculture in horticultural crops. Eur. J. Hortic. Sci. 81, 78–90. https://doi.org/10.17660/eJHS.2016/81.2.2

Zude-Sasse1, M., Akbari2, E., Tsoulias1, N., Psiroukis3, V., Fountas3, S., Ehsani2, R., 2021. Sensing in Horticulture, in: Escolà, R.K.& A. (Ed.), Sensing Aproaches for Precision Agriculture. Springer US.

Zude, M., 2003. Comparison of indices and multivariate models to non-destructively predict the fruit chlorophyll by means of visible spectrometry in apple fruit. Anal. Chim. Acta 481, 119–126. https://doi.org/10.1016/S0003-2670(03)00070-9